Advanced membrane for water desalination and ion separation application

by

Kiyoumars Zarshenas

A thesis

presented to the University of Waterloo

in fulfillment of the

thesis requirement for the degree of

Doctor of Philosophy

in

Chemical Engineering

Waterloo, Ontario, Canada, 2023

Examining Committee Membership

The following served on the Examining Committee for this thesis. The decision of the Examining Committee is by majority vote.

External Examiner	Dr. Haiqing Lin Professor
Supervisor	Dr. Zhongwei Chen Professor
Internal Member	Dr. Mark Prtizker Professor
Internal Member	Dr. Michael Pope Associate Professor
Internal-external Member	Dr. Peter Huck Professor

AUTHOR'S DECLARATION

This thesis consists of material all of which I authored or co-authored: see Statement of Contributions included in the thesis. This is a true copy of the thesis, including any required final revisions, as accepted by my examiners. I understand that my thesis may be made electronically available to the public.

Statement of Contributions

The body of this thesis is based upon a combination of published and unpublished works.

1. Kiyoumars Zarshenas, Gaopeng Jiang, Jing Zhang, Mohd Altamash Jauhar, Zhongwei Chen, "Atomic scale manipulation of sublayer with functional TiO_2 nanofilm toward high-performance reverse osmosis membrane", Desalination, 480, 114342, 2020.

I designed and carried out the experiments, collected and analyzed the data, and wrote he final manuscript. Dr. G. Jiang assisted with methodology, and writing- review and editing. Dr. J. Zhang helped with reviewing and editing. Dr. M. Jauher assisted in conducting the Atomic layer deposition technique and Dr. Chen supervised me and reviewed the manuscript.

2. K. Zarshenas, H. Dou, S. Habibpour, A. Yu, Z. Chen, "Thin-film polyamide nanocomposite membrane decorated by polyphenol-assisted Ti_3C_2Tx MXene nanosheets for reverse osmosis", ACS Applied materials and interface, 14, 1, 1838-1849, 2022.

I designed and carried out the experiments, collected and analyzed the data, and wrote the final manuscript. Dr. H. Dou assisted with methodology, and writing – review and editing. Dr. Habibpour assisted in MXene nanosheets synthesis and methodology. Dr. Chen and Dr. Yu reviewed the manuscript.

3. K. Zarshenas, S. Habibpour, S. Khoshhal, A.Rahimpour, M.Sadrzadeh, A. Yu, Z. Chen, "Nanoscale architecture of thin film composite membrane through GONR interlayered: fill two needs with one deed", ready to submit.

I designed and carried out the experiments, collected and analyzed the data, and wrote the final manuscript. S. Habibpour assisted in Graphene oxide nanoribbon synthesis and methodology. Dr. Khoshhal helped with molecular dynamic simulation. Dr. Rahimpour and Dr. Sadrzadeh assisted with discussion and analyzing the data. Dr. Chen and Dr. Yu reviewed the manuscript.

Abstract

Population growth, contamination of fresh water, and climate change are increasing pressure on water supplies, accelerating the need for technological solutions that will improve access to clean water for drinking and sanitation. Membrane technology especially reverse osmosis (RO) and nanofiltration (NF) processes as sustainable routes for water desalination and purification are valuable from an environmental and economic standpoint. At present, RO and NF are the most energy-efficient technologies that provide us with safe and affordable drinking water, but they still need to be improved in terms of cost, affordability, and energy consumption. To achieve these improvements, advances in membrane materials are needed. The most commonly used semi-permeable membrane in RO and NF are polyamide (PA) thin-film composite (TFC) membranes which are fabricated on porous polymeric supports by in-situ polycondensation of two reactive monomers, namely polyamine and polyacyl chloride, at the interface of two mutually immiscible solvents. The main objective of my thesis was to use functional nanomaterials and nanotechnology tools to develop high-performance polyamide thin-film composite (TFC) membranes for water purification and desalination. PA-TFC membranes are flexible and the chemistry and performance of both top-layer and sublayer can be individually manipulated to maximize the overall membrane performance.

In the first phase of my doctoral thesis, for the first time, an approach of using an atomic layer deposited (ALD) monomer-affinitive titanium dioxide (TiO_2) nanofilm to modify the sublayer of TFC was proposed to form a thin, smooth, and highly cross-linked PA selective top layer. The functional TiO_2 nanofilm increases the affinity between modified sublayer and amine monomer provide a more efficient and subtle tuning of the adsorption and diffusion of amine monomer during the interfacial polymerization process. The obtained TFC membrane with optimal ALD TiO_2 coverage improved RO performance by obtaining a high permeance of 1.8 L m^{-2} h^{-1} bar^{-1} and high salt rejection rate of 96% in a dead-end process. This work reveals that coating functional nanomaterials by ALD is a practical

manipulation technique for the controllable fabrication of promising TFC membranes and the optimization of sublayer materials.

In the second phase of this thesis, we offered a facile, green, and cost-efficient approach for coating a stable layer of plant-derived polyphenol tannic acid (TA) on the surface of MXene ($Ti_3C_2T_x$) nanosheets. Then, high-performance reverse osmosis polyamide thin film nanocomposite (RO-PA-TFN) membranes were fabricated by incorporation of the modified MXene ($Ti_3C_2T_x$-TA) nanosheets in the polyamide selective layer through interfacial polymerization (IP). The strongly negative charge and hydrophilic multifunctional properties of tannic acid not only boosted the chemical compatibility between $Ti_3C_2T_x$ MXene nanosheets and polyamide matrix to overcome the formation of nonselective voids, but also generated a tight network with selective interfacial pathways for efficient monovalent salt rejection and water permeation. In comparison to the neat thin film composite (TFC) membrane, the optimum TFN ($Ti_3C_2T_x$-TA) membrane with a loading of 0.008%wt nanofiller yielded a 1.4-fold enhancement in the water permeability while maintaining at a high NaCl rejection rate of 96% in a dead-end process and enhanced anti-fouling tendency. To the best of our knowledge, this is the first research on tannic acid-modified $Ti_3C_2T_x$ MXene nanosheets and their utilization in the IP-based TFN membrane. This research offers a facile way for the development of modified MXene nanosheets to be successfully integrated into the polyamide selective layer to improve the performance and fouling resistance of thin film nanocomposite membranes.

In the last phase of this thesis, for the first time, a novel IP template, graphene oxide nanoribbons (GONR) was proposed to act perfectly in response to two needs including minimizing the funnel effect and mediating the IP reaction toward desired PA properties. The coated GONR template not only efficiently served the gutter layer role, but also properly regulated the adsorption and transport of amine monomers at the interface of GONR through manipulating electrostatic interaction, capillary rise, and nanoconfinment of IP template by different loadings of GONR. The optimized loading of GONR at

0.02 $g.m^{-2}$ resulted in a desired hybrid GONR/PA TFC NF membrane with nano-striped crumple structure beyond the PA context, an ultrathin PA nanofilm with a thickness of 15 nm, and a narrow pore size distribution and high crosslinking degree of 80% that simultaneously improve the permeability and selectivity, and successfully passed the upper bound trade-off with permeance of 21.3 $L.m^{-2}.h^{-1}.bar^{-1}$ and great rejection of 98% for Na_2SO_4 under 5 bar of pressure. This research provides a new understanding on taking the advantage of a template method thorough an optimized GONR ultrathin network to make a desired selective TFC membrane for more affordable and efficient nanofiltration and ion separation processes.

Acknowledgements

This research is a result of several years of effort and work, and it would never have been possible without the support of many people who have helped me in different ways.

First, I am deeply grateful to my family for their love and support throughout my academic journey. I especially want to thank my parents, Maria Rahimi and Faramarz Zarshenas, for their unwavering encouragement and belief in me. Their guidance and sacrifice have been invaluable to me and have helped me reach this point. I also want to thank my sisters, Rosa and Klara, for their support and understanding. Their presence in my life has been a constant source of joy and motivation.

I expressed my gratitude to my supervisor Dr. Zhongwei Chen for his mentorship. Also, thank you to Dr.Yu for her support and kindness.

I express my sincere gratitude to my committee members, Dr. Pritzker, Dr. Pope, Dr. Huck. I have used their advice for improving the quality of this work, also I have used the lab facilities of Dr. Croiset, and Dr. Ioannidis, Dr.Sadrzadeh for conducting some of the experiments in this dissertation.

I would also like to thank my lab mates, friends, and colleagues Saeed Habibpour, Ali Ghorbani Kashkooli, Gaopeng Jing, Sahar Hemmati, Mohd Altamash Jauhar, Elnaz Halakoo for supporting me whenever needed.

I express my gratitude to my awesome friends here in Waterloo and around the world, for their friendship and support. Many thanks to Novin Mehrabi, Aref Fozoni, Mahdi Fathizadeh, Parsa Pourali, Erfan Abedian Amiri, Hossein Tafaghodi, Shaghayegh Akbarpour, Iman Hassani, Sadaf Mollaei, Ehsan Haghi, Rasool Nasseri, Ali Shokati, Amir Mowla, Parnia Mehdipour, and Sadafnaz Kashi kalhori.

Lastly, I would like to express my special thanks to my wife, Sadaf Mohsenkhani, who has stood by me throughout this journey with her unconditional love. She has been my rock, my partner, and my best friend, and I am forever grateful to her for her love and for everything she has done for me.

Dedication

This thesis is dedicated to my beloved father, Faramarz Zarshenas, who taught me the value of life, perseverance, and unconditional love. He was a constant source of love, support, and encouragement throughout my life. His guidance and support have been invaluable to me throughout my academic journey. Although he is no longer with us, his influence on my life and my work will always be a source of inspiration. I dedicate this thesis to his memory, as a small token of my love and gratitude. I miss him deeply, but I am grateful for the time we had together and the many lessons he taught me. Rest in peace, Dad. You will always be in my thoughts and in my heart.

Table of Contents

Examining Committee Membership ii
AUTHOR'S DECLARATION iii
Statement of Contributions iv
Abstract v
Acknowledgements viii
Dedication ix
Table of Contents x
List of Figures xiii
List of Tables xviii
List of Abbreviations xix
Chapter 1 : Introduction 20
1.1 Overview and Motivation 20
1.2 Research objectives and scope of dissertation 21
1.3 Thesis structure 21
Chapter 2 : Background and Literature Review 23
2.1 Membrane separation processes 23
2.1.1 Reverse osmosis 23
2.1.2 Nanofiltration 24
2.2 Thin film composite membrane (TFC) 25
2.2.1 Sublayer of TFC membrane 27
2.2.2 Top layer of TFC membrane and IP reaction 27
2.3 TFC membranes properties - performance 29
2.3.1 Substrate role in IP optimization and TFC membrane properties 32
2.3.2 Interlayered-TFC (iTFC) membrane 33
2.3.3 Atomic layer deposition (ALD) 39
2.4 Incorporation of nanofillers in top layer - thin film nanocomposite (TFN) 41
2.4.1 Challenges of manufacturing the TFN membrane 42
2.4.2 Potential solutions to overcome the TFN manufacturing challenges 43
2.5 Transport mechanism in RO and NF 47

Chapter 3 : Atomic scale manipulation of sublayer with functional TiO_2 nanofilm toward high-performance reverse osmosis membrane 51
3.1 Introduction 51
3.2 Experimental 53
3.2.1 Materials 53
3.2.2 Deposition of TiO_2 film on PES sublayer and ALD condition 53
3.2.3 Polyamide thin film composite (PA-TFC) membrane preparation 53
3.2.4 Physicochemical characterization 54
3.2.5 Membrane performance test 55
3.3 Results and Discussion 56
3.3.1 ALD coating and the properties of ALD-x-TiO_2@PES sublayers 56
3.3.2 Properties of PA-TFC-x 60
3.3.3 Membrane transport properties 63
3.4 Conclusion 64
Chapter 4 : Thin-film polyamide nanocomposite membrane decorated by polyphenol-assisted $Ti_3C_2T_x$ MXene nanosheets for reverse osmosis 66
4.1 Introduction 66
4.2 Experimental Section 68
4.2.1 Materials and chemicals 68
4.2.2 $Ti_3C_2T_x$ MXene nanosheets synthesis 68
4.2.3 Modification of $Ti_3C_2T_x$ MXene nanosheets with Tannic acid 69
4.2.4 Fabrication of TFC, TFN ($Ti_3C_2T_x$), and TFN ($Ti_3C_2T_x$-TA) Membranes 69
4.2.5 Characterization 70
4.2.6 Performance test 71
4.2.7 Fouling test 71
4.3 Results and discussion 72
4.3.1 $Ti_3C_2T_x$ and $Ti_3C_2T_x$-TA characterization 72
4.3.2 Membrane Microstructure 74
4.3.3 Membrane performance 80
4.3.4 Optimization of $Ti_3C_2T_x$-TA loading 81
4.3.5 Fouling 82
4.4 Conclusion 83

Chapter 5 : Nanoscale architecture of thin film composite membrane through interlayered GONR: filling two needs with one deed 85
5.1 Introduction 85
5.2 Materials and Methods 87
5.2.1 Chemicals 87
5.2.2 GONR synthesis 87
5.2.3 GONR interlayer coating onto PES substrate 87
5.2.4 Fabrication of polyamide selective layer on the IP template 88
5.2.5 Characterization 88
5.2.6 Calculation the crosslinking degree of polyamide membrane: 90
5.2.7 Determination of the capillary rise: 90
5.2.8 Pore size distribution and molecular weight cut-off (MWCO) calculation of TFC membrane 91
5.2.9 Nanofiltration performance 92
5.2.10 Molecular dynamic simulation methods 93
5.3 Results and discussion 94
5.3.1 GONR characterization 95
5.3.2 Structure and properties of the IP template 97
5.3.3 Impact of GONR template loading on structure and properties of NF membranes 100
5.3.4 Separation performance of formed NF membranes 105
5.3.5 Dissecting the role of GONR on the IP reaction and exceptional permselectivity of iTFC02 109
5.4 Conclusion 112
Chapter 6 : Conclusion and Future work 114
6.1 General conclusions and contributions 114
6.2 Future work 115
Bibliography 117
Appendices 148
Appendix A. Supplementary material for chapter 3 148
Appendix B. Supplementary material for chapter 4 155
Appendix C. Supplementary material for chapter 5 167

List of Figures

Figure 1-1. Thesis layout 22
Figure 2-1. The filtration spectrum: relative size of materials, molecular weight cutoff ($g.mol^{-1}$) , transport mechanism, and their filtration process: adapted from[24]. 23
Figure 2-2. Schematic of osmosis and reverse osmosis system. Adapted from [25]. 24
Figure 2-3. Schematic of a thin film composite membrane.[29] 26
Figure 2-4. Schematic of formation of PA TFC membrane[35]. 27
Figure 2-5. Interfacial reaction of m-phenylendiamine (MPD) with trimesoyl chloride (TMC) and formation of network and linear crosslinked polyamide nanofilm. 28
Figure 2-6. interfacial reaction of piperazine (PIP) with trimesoyl chloride (TMC) and formation of network and linear cross-linked polyamide nanofilm. 28
Figure 2-7. The relationship between membrane structural and physicochemical properties and separation performance. Adapted from [19]. 30
Figure 2-8. Approaches on the controllable IP reaction and high-performance PA-TFC membrane over the past decade. 31
Figure 2-9. Fabrication of ultrathin PA membrane using a sacrificial interlayer. Adapted from [9]... 34
Figure 2-10. Mechanism of two-in-one strategy A) PD-ZIF-8 nanoparticles deposition, adapted from [55], (B) COF nanofibers deposition, adapted from [56]. 35
Figure 2-11. Brush-painting method for the fabrication of interlayer A) Modified SWCNT, adapted from[59], B) MXene ($Ti_3C_2X_3$), adapted from [60]. 36
Figure 2-12. Schematic demonstration of an ALD process cycle. In the first half-cycle, the substrate is exposed to a precursor and then purged. In the second half-cycle, the surface is exposed to a reactant and again purged. Adapted by [82] 40
Figure 2-13. General direction of ALD applications for overcoming the limitations of membrane preparation. Adapted by[82]. 41
Figure 2-14. TEM images of the cross-section of TFN membranes. (a) silica nanoparticles embedded (b) NaA zeolite embedded. Adapted from reference [13]. 43
Figure 2-15. Variation in performance of membrane with increase in nanofiller loading. Adapted from reference [14]. 44
Figure 2-16. Schematic of TFN membrane preparation through using TA-MoS_2 nanosheets. Adapted from reference [15]. 45

Figure 2-17. Schematic of novel interfacial polymerization approach. Adapted from reference [19]. 46
Figure 2-18. Fabrication of TFN membrane via in-situ hybridization. Adapted from reference [20]..46
Figure 2-19. (a) Schematic of electrical alignment and (b) micrographs of membranes. Adapted from reference [22]. 47
Figure 2-20. Schematic description of (a) solution-diffusion, and (b) pore-flow models[24].....49
Figure 2-21. Mass transfer region for an NF membrane. adapted from [20].....50
Figure 3-1. Schematic representation of TFC RO membrane with modified PES support layer and one ALD cycle of TiO2 deposition on the PES sublayer. 57
Figure 3-2. Properties of PES sublayer with different TiO_2 ALD cycles: (A to E) SEM surface images and AFM images (A, F) pristine PES, (B, G) ALD 10-TiO2@PES, (C, H) ALD 50-TiO_2@PES, (D, I) ALD 100-TiO_2@PES, (E, J) ALD 200-TiO_2@PES, (K) Normalized Ti Peak area in SEM-EDS spectra, (L) Ra surface roughness, and (M) water contact angle. 59
Figure 3-3. SEM and AFM image of the TFC RO membranes (A, F) PA-TFC-0, (B, G) PA-TFC-10, (C, H) PA-TFC-50, (C, H) PA-TFC-100, (E, J) PA-TFC-200. (K to P) cross-sectional SEM images: (K) Pristine PES, (L) PA-TFC-0, (M) PA-TFC-10, (N) PA-TFC-50, (O) PA-TFC-100, and (P)PA-TFC-200. 61
Figure 3-4. Dependency of properties of Polyamide top selective layer of RO TFC membranes on PES/TiO2 sublayer with different ALD cycles (A) Graph showing (Ra) surface roughness and thickness (B) Crosslinking degree. 63
Figure 3-5. Performance of PA-TFC-x RO membranes (A) Permeance, (B)Rejection. 64
Figure 4-1. self-polymerization of tannic acid at $Ti_3C_2T_x$ MXene nanosheets (a) Schematic representation of binding mechanism, (b) UV-visible spectra, (c) Zeta-potential, (d) XRD pattern for $Ti_3C_2T_x$ and $Ti_3C_2T_x$-TA, (e-i) Morphology and size properties: AFM images and height profile of (e, f) Ti3C2Tx after ultrasonication, and (h, i) $Ti_3C_2T_x$-TA, (g) DLS for $Ti_3C_2T_x$ and $Ti_3C_2T_x$-TA, (j) image of dispersion and stability of $Ti_3C_2T_x$ and $Ti_3C_2T_x$ -TA nanosheets (0.008% wt) in water after 7 days. 74
Figure 4-2. Fabrication and characterization of TFC and TFN membranes: (a)Schematic of membrane fabrication procedure and the chemical structure of TFN ($Ti_3C_2T_x$-TA) membrane, (b-i) surface morphologies: FESEM and AFM images of the PES support layer and PA selective layer (b, f, j) PES, (c, g, k) TFC, (d, h, l) TFN($Ti_3C_2T_x$-008), (e, i, m) TFN($Ti_3C_2T_x$-TA-008). 76

Figure 4-3. Chemistry and microstructure characterization of TFC and TFN membranes: (a)Dynamic water contact angle, (b) FTIR-ATR spectra, (c) Full scan XPS spectra (d) DSC curve (e-h) High resolution N1s, O1s XPS spectra for TFC, TFN($Ti_3C_2T_x$-TA-008) membranes. 79
Figure 4-4. Membranes performance: (a) Comparison between RO performance of TFC, TFN($Ti_3C_2T_x$-008), and TFN($Ti_3C_2T_x$-TA-008) membranes, (b) optimization of $Ti_3C_2T_x$-TA loading, (c) fouling resistance to BSA for TFC and TFN($Ti_3C_2T_x$-TA-008) membrane in RO process, (d) Schematic of TFN($Ti_3C_2T_x$-TA) membrane and disruption of polyamide chain when $Ti_3C_2T_x$-TA nanosheets present in the top selective layer. $Ti_3C_2T_x$-TA is chemically compatible with PA matrix due to high interfacial interaction. 83
Figure 5-1. Schematic of the procedure for fabricating the ultrathin nanostripe-like structure of hybrid GONR/Polyamide membrane; schematic of the IP process, which is tuned by confined space and capillary assisted IP, as well as electrostatic modulated IP. 95
Figure 5-2. (a) Procedure of oxidative longitudinal unzipping of MWCNTs; Characterization of GONR and MWCNTs; (b)FT-IR spectra, (c) Raman spectra, (d) XRD pattern, (e) and (f) SEM and TEM images of MWCNTs, and (g) and (h) SEM and TEM images of GONR. 96
Figure 5-3. Morphology and structure of IP template (PES, PES-GONR005, PES-GONR01, PES-GONR02, PES-GONR04, PES-GONR08): (a) optical photograph, (b) top surface SEM images, (c, d) top surface topography 2D and 3D AFM images. 99
Figure 5-4. Morphology and structure of TFC and iTFC NF membranes with different loading of GONR template: (a) top surface SEM images, (b, and c) 2D and 3D topography AFM images, (d) cross-sectional TEM images, (e) bottom surface AFM images of polyamide layer. 102
Figure 5-5. Chemistry and surface properties of TFC and iTFC NF membranes with various loadings of GONR template: (a) XPS spectra, O/N ratio, and crosslinking degree, (b) water contact angle, (c) zeta potential, (d) molecular weight cut-off (MWCO) and pore size distribution. 104
Figure 5-6. Separation performance of TFC and iTFC membranes: (a) Water permeance and Na_2SO_4 rejection of NF270 commercial membrane, pristine TFC, and iTFC NF membranes with different loading of GONR template. (b) Permeance and salt rejections of optimized NF membrane (iTFC02) (under 5 bar and 1000 ppm solution including single type of salt, Na_2SO_4, $MgSO_4$, $MgCl_2$, $CaCl_2$, NaCl), (c) Comparison of nanofiltration performance (water/Na_2SO_4 selectivity) and (d) ion sieving (NaCl/Na_2SO_4 selectivity) of iTFC membranes with hand-made polyamide TFC membrane and commercial NF membranes. The dashed black line is the upper-bound line related permeability-

selectivity trade-off, (e) The pressure resistance test and (f) long term stability during cross-flow filtration test of iTFC02 (test condition: pressure 5 bar, Na_2SO_4 concentration1000 ppm). 108
Figure 5-7. (a)Solution uptake, (b)capillary rise, (c)zeta potential of IP template with/without GONR 110
Figure 5-8. Molecular structure and considered simulation boxes in the MD simulation (a) hexane-water, (b) hexane-water-GONR systems, (c) hydrogen bonds formed among different molecules in hexane-water-GONR system, (d) obtained MSD data related to the mobility of PIP molecules, and (e) calculated diffusion coefficient of PIP with/without GONR. 112
Figure S0-1. SEM image and EDX map scanning images of membrane surfaces: (A) ALD-10-TiO2@PES, (B) ALD-50-TiO2@PES, (C) ALD-100-TiO2@PES, (D) ALD-200-TiO2@PES. 148
Figure S0-2. SEM surface images, the threshold images for SEM images, and pore size distribution of the sublayers (A)PES, (B)ALD-10-TiO2@PES, (C)ALD-50-TiO2@PES, (D)ALD-100-TiO2@PES, (E)ALD-200-TiO2@PES 149
Figure S0-3. Cross-sectional SEM images of the PA-TFC membrane fabricated on substrates with different cycles of ALD. 150
Figure S0-4. XPS survey spectra of the different TFC membranes. 151
Figure S0-5. Schematic of modification procedure of $Ti_3C_2T_x$ MXene nanosheets by TA. 155
Figure S0-6. AFM image and height profile of $Ti_3C_2T_x$ MXene naosheet before ultrasonication. 156
Figure S0-7. FESEM images (Mag = 10 KX) of pristine TFC and TFNs with different $Ti_3C_2T_x$-TA loading: (a) TFC, (b)TFN($Ti_3C_2T_x$-TA-002), (c) TFN($Ti_3C_2T_x$-TA-004), (d) TFN($Ti_3C_2T_x$-TA-008), (e) TFN($Ti_3C_2T_x$-TA-016) 157
Figure S0-8. AFM images of neat TFC and TFNs with different $Ti_3C_2T_x$-TA loading: (a)TFC, (b) TFN($Ti_3C_2T_x$-TA-002), (c) TFN($Ti_3C_2T_x$-TA-004), (d) TFN($Ti_3C_2T_x$-TA-008), (e) TFN($Ti_3C_2T_x$-TA-016). 158
Figure S0-9. Dynamic contact angle of TFC and TFN with different concentration of $Ti_3C_2T_x$-TA. 159
Figure S0-10. FTIR-ATR spectra of PES, TFC, and TFN with different concentration of $Ti_3C_2T_x$-TA. 160
Figure S0-11. Experimental dead-end set up for membrane separation tests: (1) N_2 cylinder, (2) gas regulator, (3) controlling valve, (4) pressure gauge, (5) feed tank and membrane test cell (Sterlitech HP4750), (6) magnetic stirrer, (7) permeate collector. 161
Figure S0-12. Performance comparison (pure water permeability and salt rejection) of the RO membranes in this study and literature [94,96,265,266,150,181,259–264]. 162

Figure S0-13. Schematic of cross-flow filtration setup. 167
Figure S0-14. Surface SEM images, operated images, and pore size distribution of GONR/PES substrate; (a)PES, (b)PES-GONR005, (c)PES-GONR01, (d)PES-GONR02, (e)PES-GONR04, (f)PES-GONR08. 168
Figure S0-15. AFM images (2D, and 3D) and mean roughness (Ra) of GONR/PES substrates; (a) pristine PES, (b)PES-GONR005, (c)PES-GONR01, (d)PES-GONR02, (e)PES-GONR04, (f)PES-GONR08. 169
Figure S0-16. Morphology and structure of TFC and iTFC02 membranes: (a, d) SEM cross section, (b, e) TEM cross section, (c, f) AFM back side. 170
Figure S0-17. Initial and after 5 seconds average water contact angles measurement of DI water for GONR/PES substrate with different loading of GONR. 171

List of Tables

Table 2-1. Comparison between TFC and cellulose acetate membranes. 26
Table 2-2. Summary of materials and fabrication methods of interlayer/sacrificial layer used for fabrication the PA-TFC membrane in various applications.....36
Table 3-1. Summary of properties related to affinity to amine solution for sublayers. 60
Table 5-1. Surface pore size, roughness, contact angle and pure water flux of PES-GONR template.99
Table 5-2. The energy quantities obtained from MD simulation.....111
Table S0-1: Summary of properties of sublayer. 152
Table S0-2: Pure water flux of sublayers.....152
Table S0-3: Physical properties of TFC membranes. 153
Table S0-4: XPS analysis of TFC membranes.....153
Table S0-5: Performance of commercial and lab made RO membrane.....154
Table S0-6: Surface roughness of the pristine TFC and TFNs with different $Ti_3C_2T_x$-TA loading...163
Table S0-7: Surface composition of the pristine TFC and TFNs with different $Ti_3C_2T_x$-TA loading. 164
Table S0-8: Peak area percentage of O1s and N1s for TFC and TFN($Ti_3C_2T_x$-TA-008) membrane. 165
Table S0-9: Filtration performance of TFC and TFN membranes for separation NaCl solution (2000 ppm, under a pressure of 20 bar at 25 ˚C).....166

List of Abbreviations

ATR-FTIR – Attenuated total Reflectance-Fourier transform infrared

AFM – Atomic force microscopy

DI – Deionized water

DLS – Dynamic light scattering

DMSO – Demethyl sulfoxide

IP – Interfacial polymerization

MPD – M-phenylenediamine

NF – Nanofiltration

PIP – Piperazine

PA – Polyamide

PES – Polyether sulfone

RO – Reverse osmosis

SEM – Scanning electron microscopy

TEA – Triethylamine

TMC – Trimesoyl chloride

TFC – Thin film composite

TFN – Thin film nanocomposite

TOC – Total organic carbon

TEM – Tunneling electron microscopy

XPS – X-ray photoelectron spectroscopy

XRD – X-ray diffraction

Chapter 1: **Introduction**

1.1 Overview and Motivation

Water is one of the most basic and vital components of life and one of the most important resources of our planet[1]. Due to the rapid population growth, industrialization, and climate change, preserving water quality and quantity, and providing fresh and clean water for particularly water-stressed regions are one of the world's greatest concerns[2]. This worldwide issue has motivated extensive research on the development of technologies and advanced materials. So far, extensive research has been dedicated to the development of technologies and advanced materials to increase fresh water supply by either seawater/brackish desalination or wastewater reuse. Of all current systems, the most energy efficient and technologically mature systems are pressure-driven membrane-based technologies, such as reverse osmosis (RO) and nanofiltration (NF)[2,3].

To date, the most commonly used semi-permeable membranes in RO and NF are the polyamide (PA) thin-film composite (TFC) membranes[4]. In general, a PA top selective layer is fabricated on the polymeric support layer by in-situ polycondensation of two reactive monomers, namely polyamine and polyacyl chloride, at the interface of two mutually immiscible solvents[5,6]. The highly cross-linked polyamide network enables a tight rejection of the dissolved monovalent and divalent ions in the feed solution. The polymeric support layer is usually made by phase inversion, providing mechanical strength so that TFC membranes can withstand the high applied pressure[7,8].

In industrial applications, PA-TFC membranes have been utilized for a few decades; however, the improvement of the performance of PA-TFC membranes is a long-term challenge for desalination application such as RO, and NF processes[2]. Rejection and permeability are two main membrane performance evaluation indexes. Enhanced permeability can reduce membrane area and energy consumption[9,10], and increased rejection can result in a more efficient process and greater water quality[11]. The TFC membrane performance is determined mainly by the PA active layer which is mainly responsible for rejection of solute and permeability of water and the desired component. Extensive research indicates several factors which affect the formation and physicochemical properties of the polyamide layer [6,12,13] such as monomer type and concentration ratio, curing temperature, reaction time, chemical additives concentration, and so on. The interfacial polymerization (IP) template (sublayer/interlayer) features including structural properties (i.e. pore size distribution, porosity, pore density, and roughness) and chemical properties (i.e. hydrophilicity-hydrophobicity, and the affinity/reactivity with amine or acyl chloride monomers) [7,14–18] play significant roles as well.

To achieve a desired PA-TFC membranes, researchers have devoted extensive effort to apply different techniques and materials to optimize the IP reaction and control the effective factors to tune the PA selective layer structural characteristics and chemical properties (including morphology, thickness, roughness, wettability, surface charge, pore (free volume) size and distribution, crosslinking degree, so on) [19–21]. However, a need exists to understand the IP behavior deeply and to develop high-performance PA-TFC membranes to increase the effectiveness of RO and NF by improving water permeability, selectivity, resistance to build-up of unwanted matter on the membrane surface.

1.2 Research objectives and scope of dissertation

This dissertation focuses on the development of high-performance RO and NF PA-TFC membranes for desalination and ion separation applications. To achieve this goal, the proposed research is divided into four tasks as follows:

Task1: Fabrication of conventional PA-TFC RO membrane and study of the mechanism of interfacial polymerization.

Task2: Design, synthesis, and evaluation of PA-TFC RO membranes by focusing on sublayer modification by TiO_2 atomic layer deposition.

Task3: Design, synthesis, and evaluation of PA-TFN RO membranes by blending modified MXene nanosheets in the polyamide selective layer.

Task4: Fabrication and evaluation of conventional PA-TFC NF membrane, followed by design, synthesis, and evaluation of novel hybrid TFC NF membrane using graphene oxide nanoribbon as a novel IP template.

1.3 Thesis structure

The Thesis organized into 6 chapters, as follows:

Chapter 1 provides preliminary information regarding the overview, motivation, purpose, and scope of the dissertation.

Chapter 2 will begin by presenting background information on reverse osmosis and nanofiltration and the mechanisms for separation in these processes. The approach of interfacial polymerization (IP) for polyamide (PA) membrane preparation is explained and the impacts of different parameters specifically the sublayer and interlayer on the interfacial polymerization and top selective PA layer formation are discussed. In addition, a brief description of atomic layer deposition (ALD) as a unique modification technique is presented. Moreover, the use of thin film nanocomposite (TFN) membrane for water

desalination application reviewed and the role of different fillers and challenges related to incorporation of fillers in polyamide layer are discussed.

Chapter 3 is concerned with the impact of atomic layer deposition. To fabricate high-performance PA-TFC membranes, for the first time, atomic layer deposition is used to modify the sublayer to tune its physicochemical properties to control the properties of the top selective layer by controlling the interfacial polymerization process. This novel membrane opens new opportunities for the development of high-performance RO TFC membrane in large scale.

Chapter 4 presents the development of RO TFN membranes fabricated through incorporation of the modified MXene nanosheets into to the polyamide selective layer. The effects of the amount of loading of MXene and modified MXene on the membrane performance are studied.

Chapter 5 investigates the role of novel interlayer, graphene oxide nanoribbon to produce the ultrathin hybrid GONR/polyamide layer. Five types of salts (i.e., NaCl, $CaCl_2$, Na_2SO_4, Mg_2SO_4, $MgCl_2$) are used as model multivalent and monovalent salts in this study.

Chapter 6 presents general conclusions and highlights the original contributions of the thesis work. Some recommendations for future research are also provided.

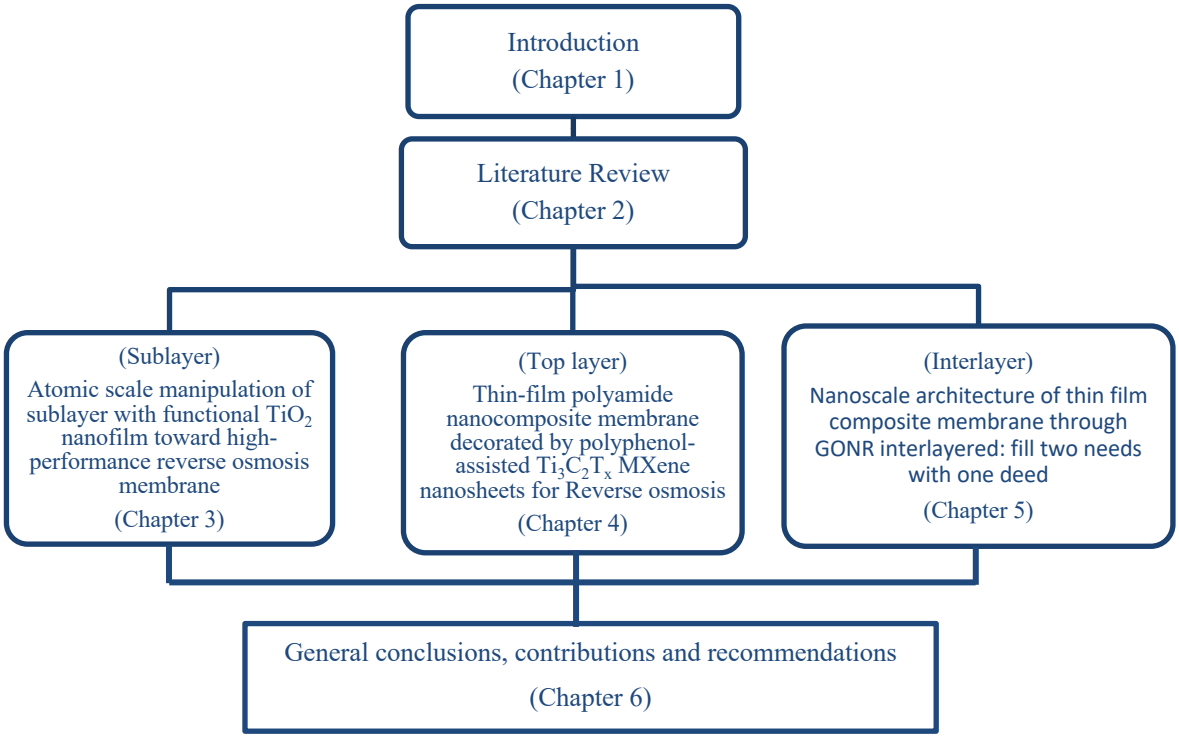

Figure 1-1. Thesis layout

Chapter 2: **Background and Literature Review**

2.1 Membrane separation processes

Membrane separation processes can be utilized in a broad range of industries such as chemical, mineral, electronics, petrochemical, pharmaceutical, biotechnology, textile, paper, food, and water purification and treatment[22]. A membrane is typically a permeable or semi-permeable thin barrier which allows the transport of certain molecules/particles while restricting the others. Depending on the type of membrane and the applied driving force for transport and separation of selected species, membrane processes are classified in various groups. **Figure 2-1** illustrates the classification of membrane separation processes, particularly for water purification the membrane processes are categorized as microfiltration (MF), ultrafiltration (UF), nanofiltration (NF), and reverse osmosis (RO) [23]. The focus of this research is on the RO and NF processes and development of high-performance thin film composite membranes (TFC) for water desalination and ion separation applications.

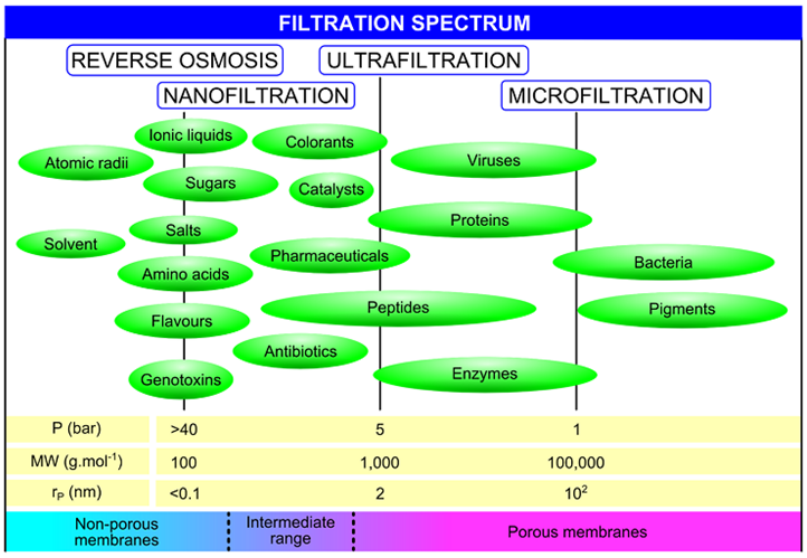

Figure 2-1. The filtration spectrum: relative size of materials, molecular weight cutoff (g.mol^{-1}) , transport mechanism, and their filtration process: adapted from[24].

2.1.1 Reverse osmosis

For many years, the ideas of "osmosis" and "reverse osmosis" have been well-known. Osmosis is the flow of solvent from a dilute solution to a concentrated solution through a semi-permeable membrane. This flow comes from the driving force generated by the difference in chemical potential of the

solvents[22]. The flow of a pure solvent to balance the concentrations of solutes on each side of a membrane generates a pressure named "osmotic pressure". Reverse osmosis is the reverse of the normal osmosis process, in which the solvent is pushed through a membrane from a high solute concentration area to low solute concentration area. **Figure 2-2** shows the processes of osmosis and reverse osmosis.

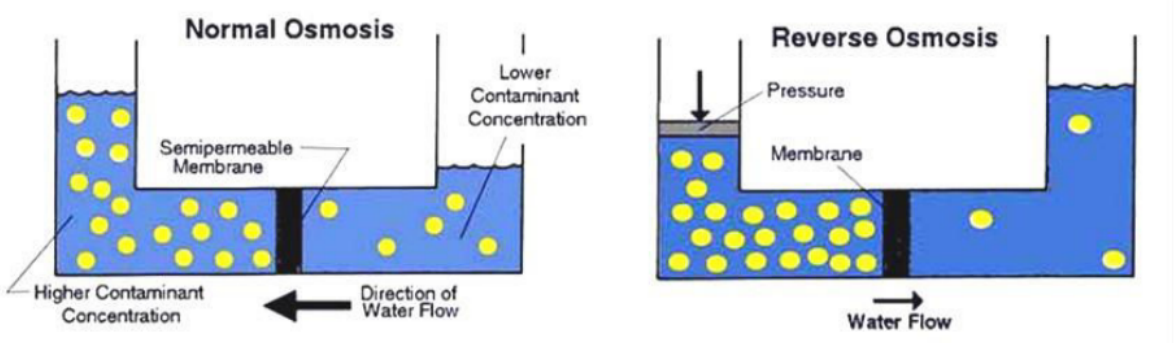

Figure 2-2. Schematic of osmosis and reverse osmosis system. Adapted from [25].

Reverse osmosis has been shown to be an effective pressure-driven process for desalination. The RO membranes are commonly considered to be nonporous, rejecting all monovalent, bivalent salts and natural organic material (NOM) from water[19]. In fact, the most common application of RO membranes is for desalination of ground and brackish water, containing 2,000 to 10,000 mg/L of total dissolved solids (TDS), and sea water, with 25,000 to 45,000 mg/L of TDS[26]. According to the World Health Organization (WHO), the maximum concentration of TDS in potable water is 600 mg/L[27]. It is estimated that almost 65% of the world's desalination plants are based on the RO process. Depending on the concentration of the salts in the feed, the water applications of RO can be categorized in the following groups: brackish water desalination, seawater desalination, and ultrapure water production and wastewater treatment. In addition to the traditional seawater and brackish water desalination processes, RO membranes have found uses in wastewater treatment, ultrapure water production, water softening, and food processing as well as many others[23].

2.1.2 Nanofiltration

Nanofiltration (NF) is one of the four types of pressure-driven membrane processes which has separation abilities between reverse osmosis (RO) and ultrafiltration (UF) and rejects molecules and ions. The goal of NF is not just desalination; it is often used for selective rejection of solutes for resource recovery or water purification. NF membranes have a nominal pore diameter in the range of 0.5 -2 nm (with a molecular weight cut-off (MWCO) in the range 200-2000 Da)[19]. NF with different pore

diameters shows diverse solute rejection properties. NF applications are determined based on the selectivity of membranes and rejection of target solutes. Typically, NF processes can be utilized for the separation of water/salt (ground water hardness removal, heavy metal ion removal, pretreatment of high salt water, scaling mitigation in industry), water/OM (NOM removal in surface water, TrOCs removal in surface water, TroC's removal in water reuse), mono/multivalent ions (extracting lithium from salt lake brine, Cl-/SO_4^{2-} separation in chlor-alkali industry), and ions/OM (resource recovery in high-salinity organics-abundant wastewaters)[19]. For the desalination (water/salt) and ion separation application, NF membranes have a greater rejection to multivalent ions such as over 90% for Ca^{2+}, Mg^{2+}, and SO_4^{2-}, but less resistance to permeation of monovalent ions such as ~23% for Cl^- and Na^+. A key advantage of NF over RO is its greater water permeability (typically > 6 $L.m^{-2}.h^{-1}.bar^{-1}$) which allows its operation at a lower pressure. Therefore, the costs of module construction and fluid pumping for NF would be less[28].

2.2 Thin film composite membrane (TFC)

At the heart of the RO and NF desalination process is a semipermeable membrane which provides separation of water and salts with the application of pressure greater than the osmotic pressure[2]. Currently, polyamide-TFC membranes dominate commercial RO/NF systems. TFC membranes have advanced dramatically since Morgan established the interfacial polymerization (IP) concept in 1965 [6]. However, this concept did not work for industrial unit until Cadotte and his colleague[5] developed a series of composite membranes in 1980. Before that, anisotropic cellulose acetate (CA) membranes, which were made of a single material with the phase inversion technique by Loeb and Sourirajan in the 1960s, were used as commercial RO membranes[23]. The advantages and disadvantages of these materials are presented in Table 2-1. Comparison between TFC and cellulose acetate Typically , PA-TFC membranes exhibit better performance than CA-based membranes because of higher water permeation flux, increased chemical and physical resistance and broader range of operating pH and temperature conditions[23].

Several advantages of TFC membranes have kept them competitive in the commercial market. Generally a polyamide thin film composite membrane consists of three layers[26], as shown in **Figure 2-3**. The ultra-thin top layer is the selective barrier responsible for the separation. This top layer is supported by a microporous sublayer which is usually an asymmetric ultrafiltration or microfiltration membrane that provides a sufficiently smooth surface to support a defect-free ultrathin top layer.

Table 2-1. Comparison between TFC and cellulose acetate membranes.

Membrane material	Advantages	Disadvantages
Thin film composite polyamide	High water flux High salt rejection High pressure compaction resistance wide pH range and temperature operation High stability to biological attack	Bad chlorine tolerance High fouling tendency
Asymmetric cellulose acetate	Low tendency to adsorption by natural organic matters (e.g. proteins) proper chlorine tolerance	Biologically degradable Severe flux decline

This is further supported by a non-woven reinforcing fabric that provides additional mechanical strength to the composite structure while offering little resistance to mass transport through the membrane[26].

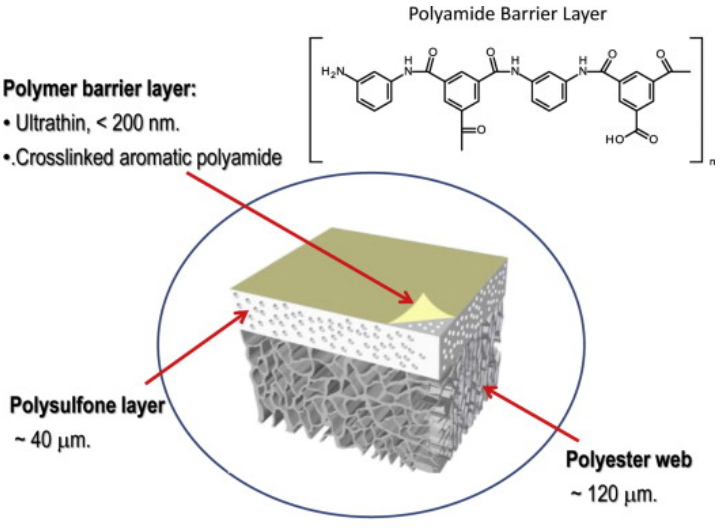

Figure 2-3. Schematic of a thin film composite membrane.[29]

2.2.1 Sublayer of TFC membrane

Porous sublayer structures for PA-TFC membrane have been fabricated from polymers such as polysulfone (PSf), polyethersulfone (PES), polycarbonate (PC), polyphenylene oxides (PEO), poly(styrene-co-acrylonitrile), poly(phthalazinone ether sulfone ketone) (PPESK), polyacrylonitrile (PAN), polyetherimide (PEI), polypropylene (PP) and others by conventional phase inversion techniques[30–33]. However, PSf and PES have been the most prevalent polymers for producing composite membranes since they are broadly accessible, comparatively cheap, easy to process, and fairly stable against thermal, mechanical, chemical and bacterial attack[34]. Note that PSf and PES are comparatively hydrophobic compared to most other polymers.

2.2.2 Top layer of TFC membrane and IP reaction

The dominant technique to produce the polyamide (PA) selective layer is interfacial polymerization. In the IP process (**Figure 2-4**), which is based on the Schotten-Baumann reaction mechanism[26], first the UF/MF substrate is immersed in an aqueous amine-rich solution, so the pores of the membrane are saturated with the first monomer. Then, the amine-loaded membrane is contacted with a water-immiscible solution, which consists of the second monomer. Therefore, at the interface of the two phases, a polycondensation reaction takes place, which forms a thin and cross-linked polyamide film with multiscale heterogeneity.

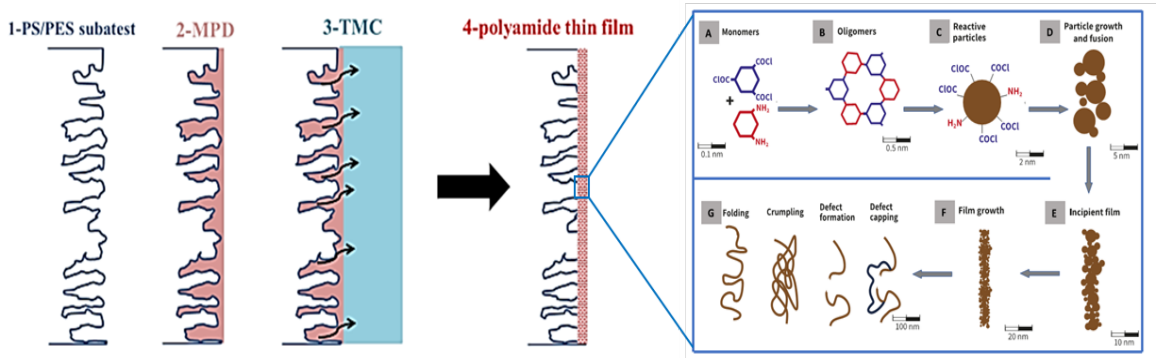

Figure 2-4. Schematic of formation of PA TFC membrane[35]**.**

Figure 2-5 & Figure 2-6 show the chemistry which involves in interfacial polymerization between water phase containing a difunctional amine and organic phase containing a trifunctional acid chloride. The most frequently used amines are m-phenylenediamine (MPD) in RO membranes and piperazine (PIP) in NF membranes, while trimesoyl chloride (TMC) is the most popular acid chloride.

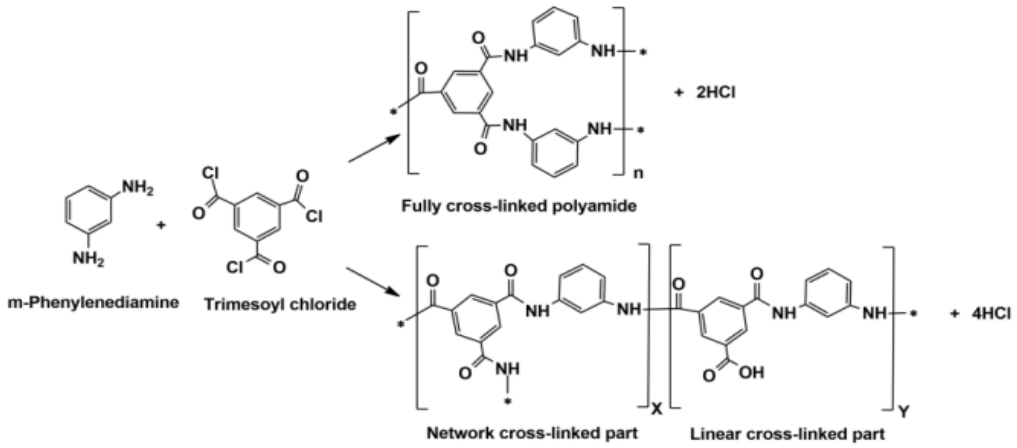

Figure 2-5. Interfacial reaction of m-phenylendiamine (MPD) with trimesoyl chloride (TMC) and formation of network and linear crosslinked polyamide nanofilm.

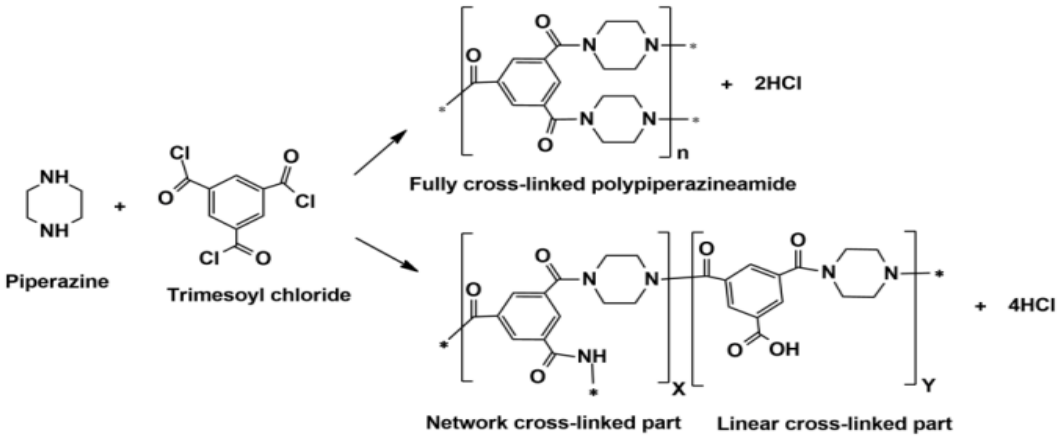

Figure 2-6. interfacial reaction of piperazine (PIP) with trimesoyl chloride (TMC) and formation of network and linear cross-linked polyamide nanofilm.

Understanding the mechanism of the IP reaction is necessary to produce the desire polyamide TFC membrane for RO and NF applications. The reaction between a diamine and acid chloride is a prevalent condensation polymerization reaction that can be finished homogenously in an appropriate reactor to produce polyamide and HCl as a by-product. However, the fabrication of polyamide by in-situ interfacial polymerization reaction contributes more complexity to the kinetics of polymerization reaction, i.e., the rate of the monomer mass transfer that directly changes the concentration of the reactive monomers in the reaction zone and thus impacts the polymerization rate and the TFC

membrane properties. It is thought that development of the PA film by the IP reaction does not follow a uniform growth. The initial step of the interfacial polymerization reaction is significantly fast, leading to an ultrathin incipient film of polyamide at the surface of sublayer. Then, the interfacial polymerization reaction moves to a slower growth step as the incipient polyamide film hinders the diffusion of the remaining MPD or PIP molecules to the reaction zone. Polymerization ultimately stops when the existing polyamide layer's mass transfer resistance becomes greater than the driving force for the MPD or PIP diffusion into the reaction zone. In this respect, the growth of polyamide on the sublayer surface is recognized as a self-limiting diffusion-controlled process[5,6]. It should also be noted that the interfacial polymerization reaction occurs primarily on the organic side of the interface because of the higher solubility of the MPD or PIP molecules in the organic phase compared to that of TMC in water[6]. Several factors can impact the IP process and kinetic of reaction including the physicochemical properties and morphology of the IP template (sublayer), the type of the reactant monomers, surfactants, chemical compounds and additives, steps of the IP, the reactant concentration and ratios, reaction time and condition, post-treatment, and the physicochemical properties of the reaction solution[19,36].

2.3 TFC membranes properties - performance

The structural and physicochemical features of a TFC membrane including thickness, roughness, pore (free volume) size, and porosity as well as chemistry, surface charge density, and hydrophilicity are easily tunable and can impact membrane selectivity, permeability or both[19,21,26] (**Figure 2-7**). Understanding the membrane property-performance relationships and how the membrane properties are affected by fabrication method and conditions would be helpful for a proper design of TFC membranes to improve the separation parameters (permeability and selectivity).

Membrane permeability can be improved by increasing its intrinsic water permeability by enhancing membrane porosity (or internal free volume), increasing water transport channels, decreasing the membrane thickness and resistance path, enlarging the effective surface area, and improving the membrane hydrophilicity[19,21,26]. The selectivity can be controlled by fine-tuning pore (free volume) size, surface chemical properties, surface charge density, and pore (free volume) size distribution. Moreover, augmenting the uniformity of pores (free volume) of membrane would be favorable to increase the selectivity of membrane. [19,21,26].

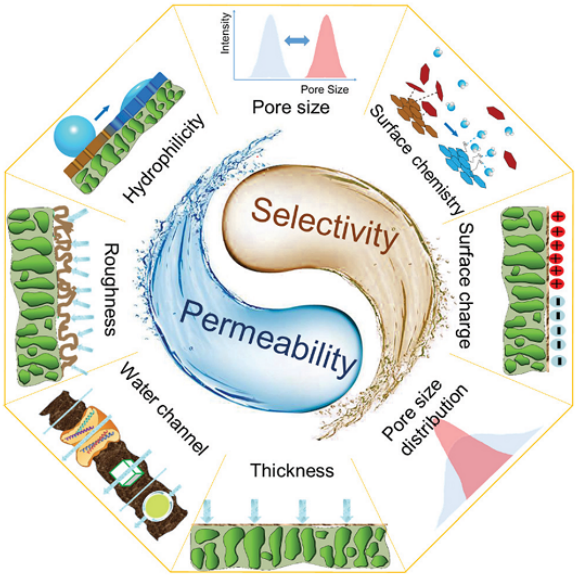

Figure 2-7. The relationship between membrane structural and physicochemical properties and separation performance. Adapted from [19].

Over the past decade, nanotechnology tools and nanomaterials have been introduced and applied to optimize and control the rapid IP process to achieve a proper design of TFC membranes with desired properties of selective layer to improve its performance [19,20,37].

In 2007, Hoek and co-workers [38] pioneered the concept of TFN membranes by incorporating the zeolite nanoparticles in the polyamide layer. Inspired by this study, several investigations were conducted to use different nanofillers to prepare the high-performance TFN membranes. In 2013, Gu and Choi et al.[39] pioneered a molecular layer by layer (LBL) technique, by changing deposition of reactive monomers on a porous support to fabricate a tunable TFC membrane. By using this technique, the PA structure and performance behavior were readily controlled. The water permeability was enhanced while salt rejection was kept similar to that achieved using the conventional IP process.

In 2015, Livingstone et. al.[9] pioneered the concept of an interlayered-TFC (iTFC) membrane by using a sacrificial interlayer of cadmium hydroxide nanowires to optimize the IP process to fabricate an ultrathin defect-free polyamide membrane with thickness around 8.4 nm. Any variation in the sublayer properties was therefore anticipated to alter the partitioning and diffusion of the MPD or PIP molecules into the reaction zone, thus changing the interfacial polymerization reaction rate, the final surface morphology and performance of the TFC membranes.

In 2018, Chowdhury et al.[40] used electro-spraying to load monomers on a substrate to tune the IP reaction. By using this technique, the structure of selective layer was effectively controlled at the nanoscale. A 3D printed polyamide membrane revealed a good perm-selectivity compared to commercial membranes.

Also, in 2018, Tan et al.[41] introduced a turning morphology to the polyamide membrane by adding polyvinyl alcohol (PVA) to the aqueous phase which slowed the diffusion of PIP amine monomers to the reaction zone by increasing the monomer interactions and solution viscosity. The PA membrane with turning structure exhibited significant separation performance due to the high-water permeability channels and higher specific area in comparison to the traditional PA morphology.

Inspired by this study, scientist learned to manipulate the structure and morphology of PA (thickness, pore size distribution, roughness, and permeation area) through a series of methods. For example, in 2020, Liang et al. [42]used surfactant as an additive to the aqueous phase to regulate the IP reaction. The surfactants self-assembled a network at the water/oil interface provides which enabled a faster and more homogenous diffusion of amine monomers. Therefore, a uniform PA layer with lower pore size distribution was formed. In 2022, Shen et al. [43] used inorganic salts to control the IP process and the nanoscale homogeneity of PA membranes. Salt addition could tune and restrict the diffusion of amine monomers to the water-hexane interface and thus form a structurally homogenous high performance PA membrane.

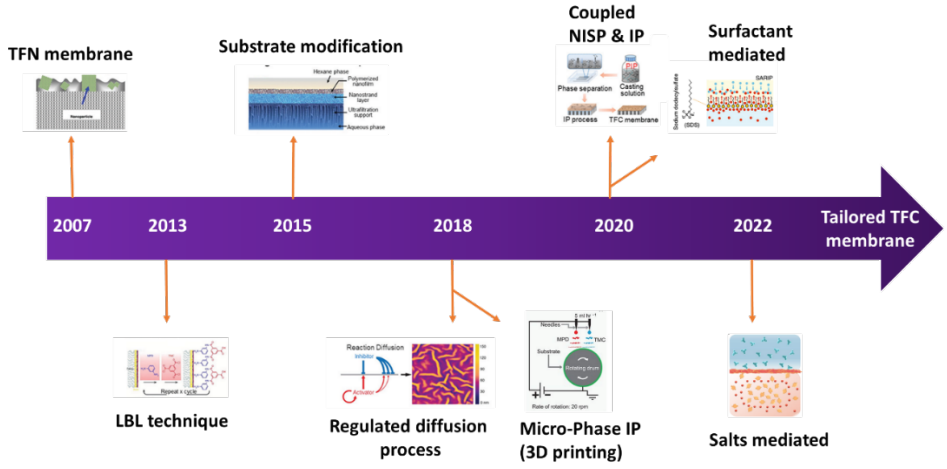

Figure 2-8. Approaches on the controllable IP reaction and high-performance PA-TFC membrane over the past decade.

2.3.1 Substrate role in IP optimization and TFC membrane properties

Based on the literature studies, physical–chemical characteristics of the support membrane including surface pore structures (including surface pore size, pore density and porosity) and surface properties (including functional group, hydrophilicity/hydrophobicity and interaction with monomers specially PIP and MPD e.g. electrostatic and van der Waals forces) are believed to be two principal factors which affect the PA composite membranes structure and then the performance for RO and NF [7,15,17,18]. Ramon et al.[17] suggested that these potential effects could be divided into two categories: (i) the sublayer surface chemistry and pore structure may impact the structure and physicochemical properties of the PA film and (ii) the pore size, porosity, and hydrophilicity of the underlying sublayer may make a significant contribution to diffusive transport through the composite structure for a specified coating film structure.

The pioneering work of Singh et al. in 2006 showed that large sublayer surface pores lead to the formation of a thinner skin layer over the sublayer and that sublayer surface pores were not completely covered with PA, resulting in a low rejection[18]. Afterwards, Hoek et al. also found that the RO membranes prepared using sublayers with small surface pores had greater rejection[7]. Shi et al.[44] thought that high sublayer surface pore density favored the fabrication of PA film with high back surface pore density and cross-linking degree, small active layer thickness and rough surface. The impacts of sublayer surface hydrophilicity-hydrophobicity (or the interaction between sublayer and MPD) on the RO membrane performance are quite complicated. Hoek et al.[7] found that hydrophilic sublayer surface or strong interaction between sublayer and MPD results in a less permeable RO membrane since the diffusion of MPD from the sublayer surface pores slows down, resulting in more PA within sublayer surface pores . Park et al.[45] found that the hydrophobicity of the sublayer surface played a critical role in fabricating a favorable top selective layer. However, the research of Lee et al. [46] indicated that it is the hydrophilicity of the sublayer surface that contributes to the formation of high flux RO membranes by favoring skin layer formation. Literature review on the role of sublayer shows the importance of sublayer properties for design of high-performance TFC-PA membrane. Thus, researchers focused their efforts to modify the conventional sublayer properties to obtain desirable properties.

2.3.1.1 Substrate modification

Modification of the sublayer can be done in two ways. One is bulk modification, such as adding hydrophilic additives including nanoparticles, and organic materials to the casting solution of sublayer.

For instance, Wang et. al.[47] fabricated a high performance RO membrane with a thin and compact PA selective layer by incorporating tannic acid into the support layer, which enhanced the hydrophilicity of the support layer, and changed the absorption/diffusion behavior of the amine and the formation of the nascent film. Bruggen et. al.[48] improved the performance of TFC RO membrane by adding TiO_2 nanoparticles as hydrophilic filler to the PES sublayer. Also, Ismail et. al. [49] potentially increased the performance of TFC membrane for FO applications by adding TiO_2 nanoparticles into PSf substrate. Liu et. al.[50] used sulfonated polysulfone (SPSf) to modify the conventional PSf ultrafiltration sublayer to obtain proper SPSf/PSf blended sublayer and fabricate a TFC RO membrane with improved separation performance.

The other approach is surface modification, such as plasma treatment, surface deposition, dip-/spin-coating, grafting, among others. For example, Kim et.al.[51] made the support membrane hydrophilic by plasma treatment to enhance not only the adhesion properties between the support and active layer, but also the RO performance of TFC membrane. Freeman et al.[52] modified the support layers of TFC membranes by depositing a polydopamine layer to increase the flux performance of TFC in the pressure-retarded osmosis processes. Cao et al.[53] fabricate a novel composite membrane by hydrophilizing the surface of the sublayer by introducing peroxide using ozone treatment by grafting acrylamide.

2.3.2 Interlayered-TFC (iTFC) membrane

One of the most interesting recent approaches to modify the substrate to use an interlayer or a sacrificial template to weaken the interference from the heterogeneous properties of the underlying substrate. Livingstone's group[9] for the first time used this unique approach to fabricate ultrathin high-performance PA membranes (**Figure 2-9**). They introduced a hydrophilic and uniform nanoporous cadmium hydroxide nanostrand sacrificial layer where the IP reaction among monomers can take place. Therefore, a freestanding ultrathin and rigid PA film with thickness of about 8.4 nm is formed. Later, inspired by this approach, researchers started using different interlayers or sacrificial templates to prepare an ultrathin high-performance PA-TFC membrane for different applications.

Table 2-2 summarizes the materials and fabrication methods of interlayer used for fabrication of PA-TFC membranes for various applications.

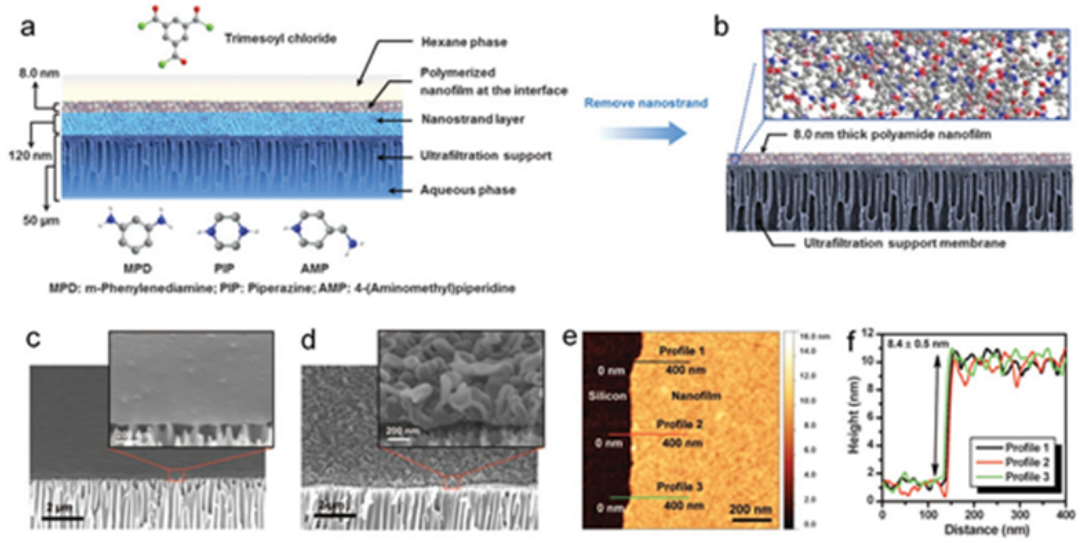

Figure 2-9. Fabrication of ultrathin PA membrane using a sacrificial interlayer. Adapted from [9].

In the interlayered-TFC approach, choosing the appropriate structure and type of materials for the interlayer or sacrificial layer are critical factors for the properties and structure of the PA layer. For example, Jin et al. [54], preloaded nanoparticles (polydopamine decorated MOF ZIF-8) as a sacrificial template on a SWCNTs/PES composite membrane to provide an irregular nanostructure and rough substrate for the formation of an ultrathin polyamide layer by interfacial polymerization. Thus, the top selective layer with a widespread crumple nanoscale structure was formed with a larger actual surface area (**Figure 2-10a**). Also, Wang et al[55]. used covalent organic framework nanofiber scaffolds as an interlayer to take advantages of the two-in-one strategy (producing ultrathin polyamide layer with increased the actual surface area) (**Figure 2-10b**). On the other hand, Tang et al[56]. by using polydopamine interlayer as a reservoir for the IP reaction, produced smooth polyamide selective layer and decreased the ridge-and-valley roughness by limiting the interfacially degassing of nanobubbles.

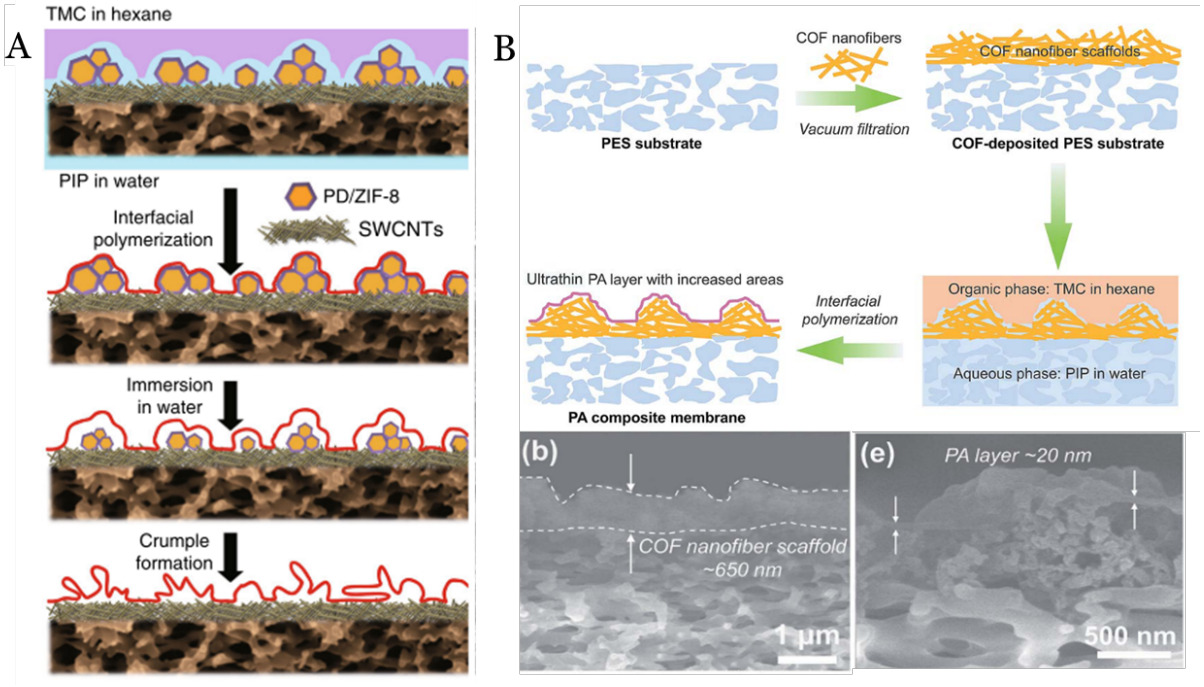

Figure 2-10. Mechanism of two-in-one strategy A) PD-ZIF-8 nanoparticles deposition, adapted from [55]**, (B) COF nanofibers deposition, adapted from** [56]**.**

The role of the interlayer and sacrificial layers for the formation of the polyamide membrane can be divided into two parts: direct impact and indirect impact. The direct impact is that it can avoid the intrusion of top layer into the substrate pores and improve adhesion strength between substrate and top layer as a gutter layer[56,57]. Indirectly, it serves the role as a reservoir or template for in-situ fabrication of top layer like interfacial polymerization. It governs the adsorption and diffusion rates of the amine monomer, interfacial polymerization reaction rate, uniformity of the distribution of the monomers. Also, the interlayer limits the interracially degassing of nanobubbles and the shaping of ridge-and-valley roughness of the selective layer. In spite of its effect on the formation of an ultrathin polyamide membrane, it facilitates the transport of permeant through a dragging effect[58].

As shown in **Table 2-2**, different methods can be used to fabricate the interlayer or sacrificial layer on top of the substrate such as vacuum filtration (simple but it provides limited area), self-polymerization (time consuming, for example PDA in air requires over 24 h), brush painting, spray coating, and so on. Scale-up potential of intermediate layer is an important element for the industrial use of polyamide membranes. Recently, spray coating and brush-painting have been shown to be practical techniques for generating a large-scale interlayer. Jin et al.[59] produced an ultrathin polyamide layer with a thickness

of 15 nm. They utilized brash-painting technique to prepare large-scale interlayer of modified SWCNT (SDBS-SWCNT) on a PES microfiltration membrane. Xie et al[60]. used brush-coating technique to prepare an MXene ($Ti_3C_2T_x$) interlayer on a microporous Nylon membrane. The properties of interlayer (thickness, pore size) are controlled by solution concentrations and painting cycles (**Figure 2-11**). Combination of brush-painting and roll-to-roll methods are used to fabricate the interlayer in the large scale and continuous form.

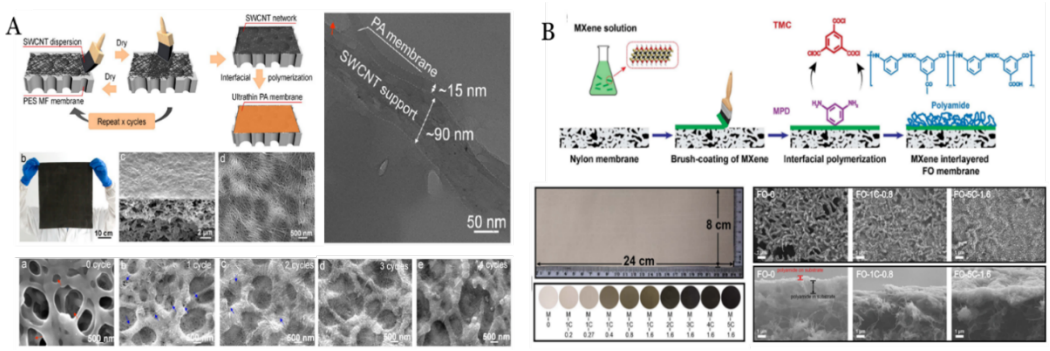

Figure 2-11. Brush-painting method for the fabrication of interlayer A) Modified SWCNT, adapted from[59]**, B) MXene ($Ti_3C_2X_3$), adapted from** [60]**.**

Table 2-2. Summary of materials and fabrication methods of interlayer/sacrificial layer used for fabrication the PA-TFC membrane in various applications.

Interlayer/ sacrificial layer	Fabrication method	Support	PA layer thickness (nm)	Application	Ref
polydopamine	Coating by pouring PDA solution	PSF	60-70	NF	[56]
CNT	Spray coated	PES MF	20	FO	[61]
PDA/GO	Self-polymerization (immersion)	Polysulfone (PS)	Higher than 100 nm	FO	[62]

Cadmium hydroxide nanostrand	Vacuum filtration	UF cross-linked polyimide XP84 Porous alumina	8	Organic solvent nanofiltration (OSN)	[9]
Chitosan nanoparticles (CSPs)	In situ	PES/SPSF UF	20	NF	[63]
COF nanofiber	Vacuum filtration	MF Polyethersulfone	20	NF	[55]
Crosslinked graphene oxide / PEI	immersion	PI	15	OSN	[64]
COFs	Vacuum filtration	Polysulfone	150	RO	[65]
MXene	Brush painting	Nylon MF (0.22 um)	-	FO	[60]
Polyphenol (tannic acid and diethylene triamine)	Codeposition Immersion in TA/DETA solution	Polysulfone UF	56.96 ± 4.4	NF	[66]
MWCNT	Vaccuum filtration	PES MF	75-90	NF	[67]
Cellulose nanocrystals (CNC)	Vaccuum filtration	polyethersulfone (PES) MF (0.22um)	Not clear (total with interlayer is 145nm)	NF	[58]
ZIF-8 nanoparticles	In-situ growth	Polysulfon UF	100-300	NF	[68]
GO/SWNCT	Vacuum filtration	Electrostatic spinning polyvinylidene fluoride (PVDF) nanofiber mat	85	FO	[69]

TiO_2	Sol-gel	α-Al_2O_3 CHF	140	PV	[70]
SWCNT	Brush painting	PES MF	15	NF	[59]
PD/ZIF-8 sacrificial layer	Vacuum filtration	SWCNT/PES	8-14	NF	[54]
SWCNT/PD	Vacuum filtration	PES MF	12	NF	[71]
Tannic Acid / Fe3+ nanoscaffold	Immersion	Polysulfon	54.9 ± 1.8	NF	[72]
PAD/COF	Immersion	PAN	11	NF	[73]
Covalent organic framework nanosheet (CONs)	Vacuum filtration	MF	7-15	NF	[74]
carbon nanotubes	Vacuum filtration	MF PES	27-53	NF	[75]
Polydopamine nanoparticle (PDA NPs)	Vacuum filtration	Electrospun polyacrylonitrile nanofiber	More than 100 nm	FO	[76]
Polydopamine (PDA)/ polyethyleneimine (PEI)	Michael addition or Schiff base reaction	UF polysulfon	Not clear	NF	[77]
SWCNT/PEI	Vacuum filtration	PES MF	34	NF	[78]
1D copper hydroxide nanofibers (CHNs)	Vacuum filtration	PAN	100 PEBAX and PDMS	GS	[79]

Aramide nanofiber hydrogel (substrate)	Non-solvent phase inversion – casing solution	-	62	NF	[80]
Tobacco Mosaic virus (TMV) protein	Vacuum filtration	Mixed cellulose esters	Not clear	NF	[81]

Based on the literature, in order to fabricate a controlled polyamide selective layer, a template with several key characteristics is required. Specifically, the template must possess high porosity, a uniform small pore size, a hydrophilic surface, and a smooth surface. These features are critical because they facilitate a homogeneous distribution of the aqueous solution, as well as accurate diffusion of the monomer onto the sublayer surface. As a result, the fabrication of the polyamide layer becomes more precise and consistent. Several studies have focused on preparing a desirable sublayer/interlayer for TFC membranes by different manipulation methods. Each has its own challenges. Undoubtedly, design of a desirable IP template needs a reliable and practical manipulation technique to provide a controllable platform for IP reaction at a large scale.

2.3.3 Atomic layer deposition (ALD)

Atomic layer deposition (ALD) is a method by which intermittent surface-limiting exposures to reactant vapors allow layer-by-layer growth of materials such as metal oxides, metals, and even organic materials. In a typical ALD cycle which is shown by **Figure 2-12**, the substrate is placed in a near-vacuum chamber filled with inert gas (i.e. N_2, Ar), and precursor vapors carried by inert gas are alternatively pulsed into the chamber. An atomic layer of precursor adsorbs on the substrate surface to subsequently react with the second one, and a purge step is performed between each pulse to remove the excess precursors. ALD can form a conformal and adjustable coating with various materials, morphologies, and size on substrates. ALD research started in the 1950s in the former USSR, and the technique was patented in 1977. In the 1990s, the semiconductors industry became interested in ALD as the technique appeared to be a effective technology for manufacturing microelectronic devices. Since then, the microelectronics industry has remained the main driver of the ALD field. Membrane engineering has recently emerged as an interesting new opportunity.

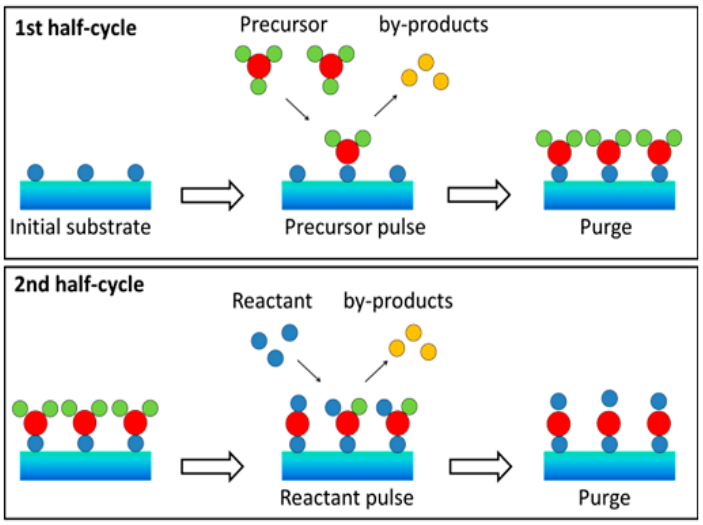

Figure 2-12. Schematic demonstration of an ALD process cycle. In the first half-cycle, the substrate is exposed to a precursor and then purged. In the second half-cycle, the surface is exposed to a reactant and again purged. Adapted by [82]

2.3.3.1 Application of ALD technology in membrane technology

Atomic layer deposition (ALD) provides a novel direction for fabricating membranes with nanoscale-controlled properties. ALD enables researchers to prepare ultrathin films with a sub-nanometer thickness control and outstanding step coverage, even on challenging structures with large aspect ratios. The ALD coatings are implemented on a broad variety of membrane sublayers, from porous polymers to inorganic ceramic template substrates. While most of the studies reported have been aimed at altering the surface physicochemical properties of the pores (hydrophilicity, organophilicity, catalytic activity, etc.) and reducing their diameter, others have been dedicated to the fabrication of selective layers with well-regulated properties. Since a main challenge for membrane manufacturers is the accurate control of both the physical and chemical nature of the membrane pore surface, the ALD method recently emerged as highly useful approach for membrane science. ALD is able to fine-tune membrane surface properties, alter the interfacial properties, and control the diameter and the aspect ratio of the pores with (sub)nanometer accuracy. In recent years, studies have investigated ALD technology to modify porous microfiltration[83], ultrafiltration[84–86], nanofiltration and reverse osmosis [87–90], including both polymeric and inorganic membranes. **Figure 2-13** shows the general direction of ALD applications for overcoming the membrane preparation limitations.

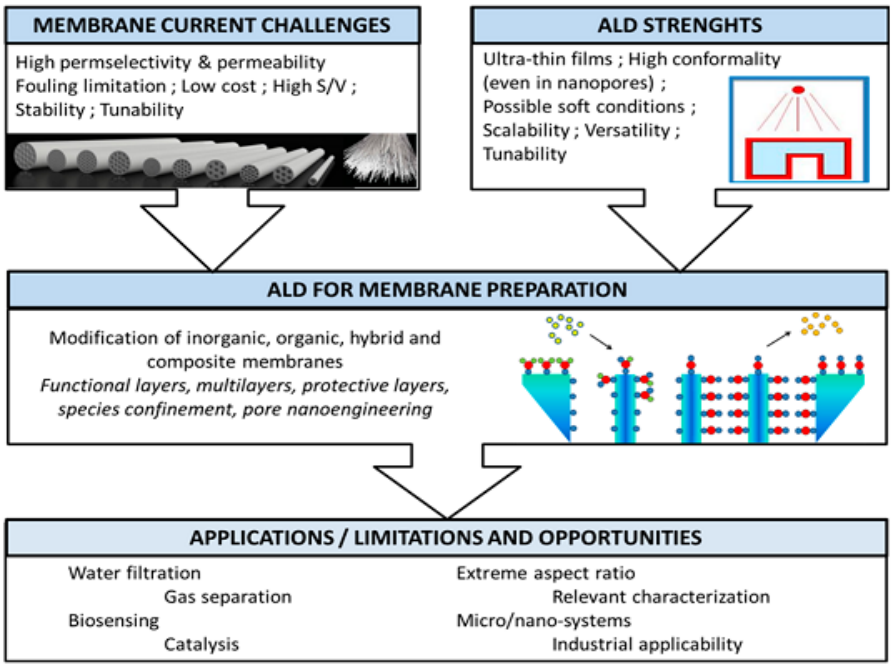

Figure 2-13. General direction of ALD applications for overcoming the limitations of membrane preparation. Adapted by[82]**.**

2.4 Incorporation of nanofillers in top layer - thin film nanocomposite (TFN)

Based on the literature, many different nanomaterials, either porous or nonporous, are used to fabricate TFN membranes[91,92]. Theoretically, nonporous nanofillers such as silver, carbon quantum dots, TiO_2, cerium oxide, and silica should decrease the TFN membrane permeability due to the reduction of effective area for water transport across the polyamide layer. On the other hand, some researchers use these nanoparticles to increase the water permeability by improving the surface hydrophilicity and free volume of the polyamide membranes. Also, contradictory results have been reported for salt rejection. For certain applications, adding a nanofiller not only improves the performance of TFN membranes, but also it has other advantages such as improved antifouling properties or higher chlorine resistance, and super hydrophilicity[93]. For instance, TiO_2 nanoparticles, in addition to enhancing the water permeability, increased the thermal stability and antifouling properties of TFN membranes[94]. Under UV light irradiation, TiO_2 releases strong oxidative species such as hydroperoxyl radicals, superoxides, and hydroxyl radicals which could hinder biofilm formation and destroy the possible microorganism[93].

Considerable research has been conducted on the preparation of ultrahigh permeable TFN membranes by using porous nanomaterials such as zeolite, MOF, CNTs, TNTs, HNTs, mesoporous silica, GO, MoS_2, and graphitic carbon nitride (gNC) nanosheets[91,95]. The molecular sieving properties of porous nanoparticles may give water molecules a favorable route via their internal pore structure. For example, zeolites (NaA) have pore diameter (4.2˚A) between that of hydrated sodium and chloride ions (8-9˚A) and water molecules (2.7˚A). Therefore these nanoparticles not only can facilitate water transport, but also they reject the hydrated salt ions[96]. Besides this molecular sieving characteristic, the charge properties and the hydrophilicity of porous nanoparticles could also lead to higher water affinity and ion repulsion because of columbic effects[91]. Recently, research has been conducted to incorporate natural water channels such as Aquaporins (AQPs) as a water channel protein, to form bio-inspired TFN membranes[97]. Although they exhibit considerable benefits, they have their own problems such as cost, stability, and compatibility of the polymer network and filler.

2.4.1 Challenges of manufacturing the TFN membrane

Many researchers have recognized the potential of polyamide TFN membranes for RO and NF applications. However, a number of challenges regarding the manufacture of TFN membrane remain. Understanding these challenges and finding solutions are the vital factors for developing high performance industrial TFN membranes. One of the critical challenges for the preparation of TFN membranes is nanoparticle agglomeration[98]. Actually, the high surface energy of nanomaterials combined with strong interactions among nanoparticles, are the main factors leading to aggregation and low dispersion of nanofiller in solutions used in the IP process[99,100]. Nanoparticle agglomeration not only reduces the active surface area, but also leads to formation of pinholes and defects in the structure of polyamide layer that can significantly deteriorate the performance of TFN membranes. For example, TEM images **(Figure 2-14)** clearly show the aggregation of nanofillers and formation of microvoids in the polyamide layers[101].

Another issue is leaching out of the nanomaterials during filtration or IP process which could be linked to the incompatibility and the absence of effective chemical interaction among organic polymer matrix and inorganic nanomaterials[95]. This problem can lower the effectiveness of the fabricated TFN membrane and reduce the efficiency of nanomaterials during the membrane fabrication.

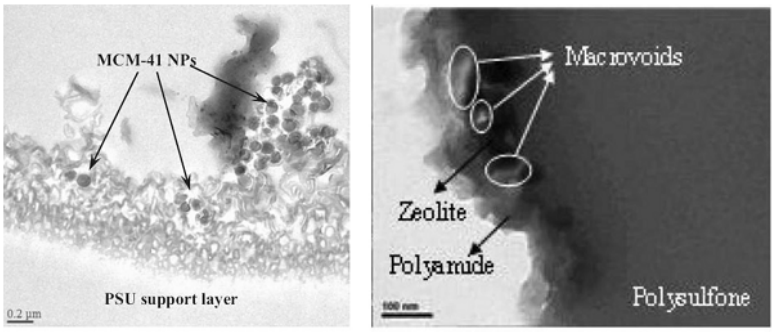

Figure 2-14. TEM images of the cross-section of TFN membranes. (a) silica nanoparticles embedded (b) NaA zeolite embedded. Adapted from reference [13].

Also, considerable quantities of nanomaterials can be wasted during the process[100]. Therefore, fabrication methods should be developed to increase the compatibility between polyamide and nanomaterials to achieve cost-efficient TFN membranes. Another challenge is related to choosing hydrophilic nanotubes (e.g., SWCNT, and MWCNT) as nanofillers for the TFN membranes instead of nanoparticles. This may lead to different resistance pathway for water molecules. **Figure 2-15** shows that the water flux and salt rejection vary inversely with the increase of CNT loading. Hydrophilic nanotubes, with the lengths of 10 to 50 μm, cannot appropriately embedded in a polyamide layer having the thickness of 100 to 500 nm. Therefore, the orientation and loading of CNT could significantly impact the performance of TFN membranes[102].

2.4.2 Potential solutions to overcome the TFN manufacturing challenges

Several approaches can be feasibly applied to solve the challenges of TFN fabrication. Surface modification of nanomaterials is a simple, and effective method that could be utilized to increase the quality of nanomaterial dispersion in non-polar organic solvents[103]. Generally, the modified nanoparticles include particular functional groups, that lead to homogenous dispersion of nanoparticles in the nonpolar organic solvent.

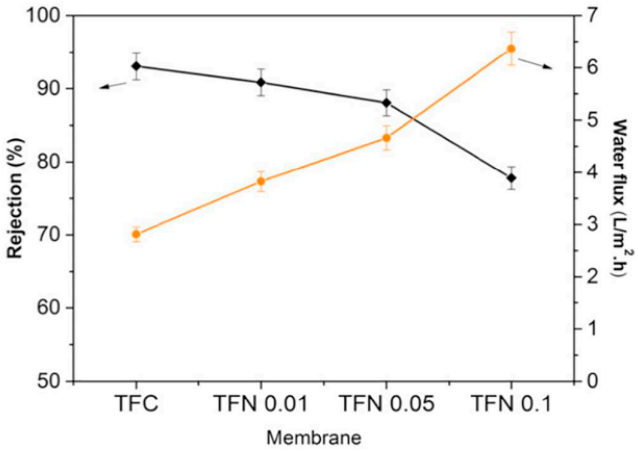

Figure 2-15. Variation in performance of membrane with increase in nanofiller loading. Adapted from reference [14].

Also, the appropriate surface modification could impart new surface characteristics to the nanoparticles and decrease the amount of agglomeration through new inter-particle interactions. Zhang et al.[104] utilized tannic acid (TA)- Fe^{3+} coordination complexes to modify the MoS_2 nanosheets and that were then embedded into the nanofiltration TFN membranes (**Figure 2-16**). Modified MoS_2 nanosheets promote covalent bonding between phenol groups and unreacted TMC groups which, during IP process, results in an increase in crosslinking degree of PA and inhibits the formation of non-selective interfacial voids.

MA et al.[105] used tannic acid (TA) to functionalize the molybdenum disulfide (MoS_2) nanosheet. TA not only contributions to the aqueous exfoliation of the bulk MoS_2 into 2D nanosheet, but also it serves as a functional molecule to alter and stabilize the MoS_2 nanosheets in aqueous solutions. Moreover, TA improves the compatibility of MoS_2 with polyamide matrix by forming covalent bond formed by the reaction between TMC and TA. Davari et. al.[106] utilized 3-aminopropyl diethoxymethylsilane (APDEMS) as an amino silane coupling agent to functionalize the nanozeolite surface. This modification enabled UZM-5 zeolite to appropriately disperse in organic solvent (e.g., hexane). Actually, the existence of functional group of amine ($-NH_2$) on the nanozeolite surface not only enables a better dispersion of nanoparticles in the organic solvent, but also simultaneously contributes forming a covalent bond with acid chloride molecules to increase the compatibility between the organic polyamide matrix and inorganic nanoparticle.

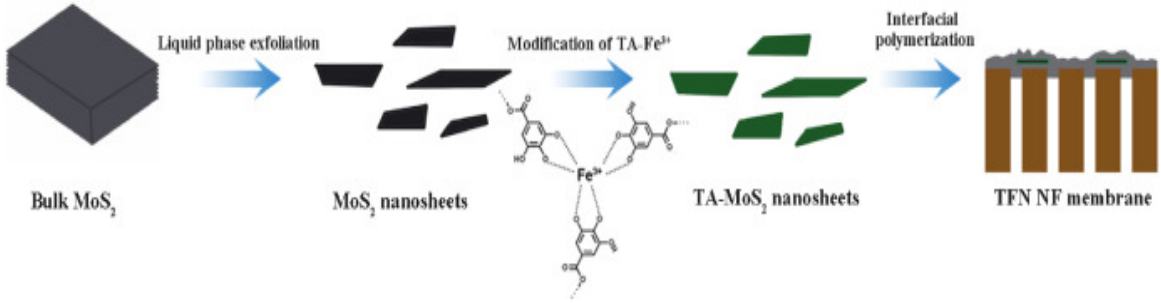

Figure 2-16. Schematic of TFN membrane preparation through using TA-MoS_2 nanosheets. Adapted from reference [15].

Also, Rajaeian et al[107] modified TiO_2 nanoparticles with the amino silane agent to decrease the adverse impact of agglomeration of nanoparticles in the polyamide membrane. A modified IP method can be a practical approach to improve the interfacial properties of composite membranes. For example, Kong et al.[108] modified the IP process by utilizing the secondary amine solution during the IP process to react with remaining acyl chloride group to reduce the potential formation of defects on the polyamide membrane (**Figure 2-17**).

Jeon et al.[109] modified the IP process by in-situ hybridization method according to dual action of reactant materials (**Figure 2-18**). The addition of the sodium dodecyl sulfate (SDS) surfactant, during the IP process, not only facilitates the formation of the PA layer, but also it stabilizes the nanofillers (silver) and transfers them to the interface where the PA layer is formed. During this modified IP process, simultaneous formation of polyamide membrane and silver nanoparticles leads to uniform embedding of nanofiller in the polyamide matrix[110].

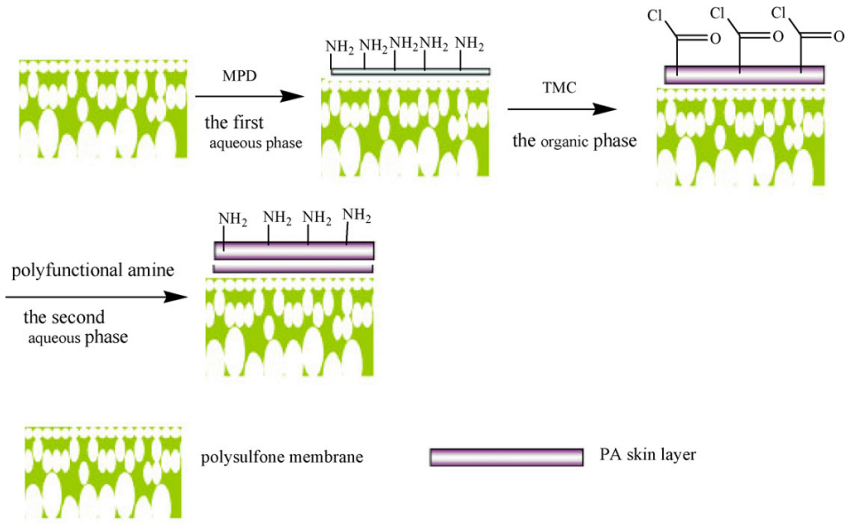

Figure 2-17. Schematic of novel interfacial polymerization approach. Adapted from reference [19].

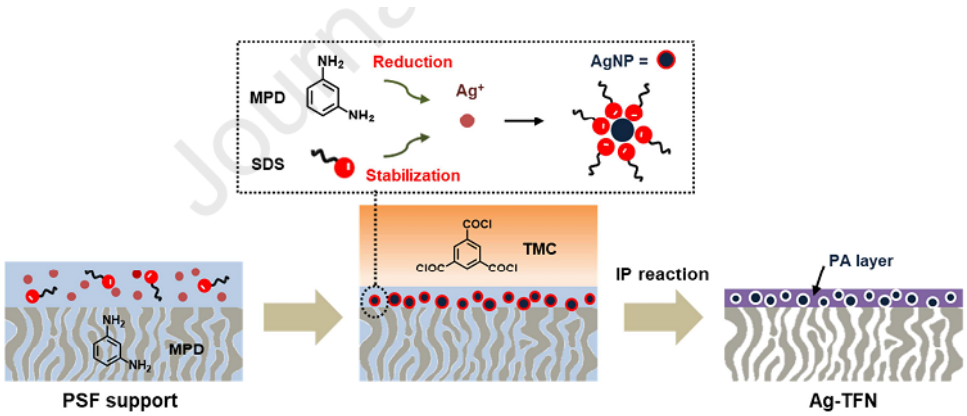

Figure 2-18. Fabrication of TFN membrane via in-situ hybridization. Adapted from reference [20].

Alignment of nanotube/fillers also could be an innovative method for fabrication of the high-performance composite membranes. Nanofiller alignment (such as CNTs), in polymer matrix, could decrease the interfacial voids among the polymer and the CNTs, and reduce the tortuosity and discontinuous route for the transport of water molecules. Wu et al.[111] applied an alternating electric field for the alignment of CNTs in a polystyrene membrane. **Figure 2-19** clearly indicates that enhancing the electric field frequency assists the CNT dispersion in the polymer matrix.

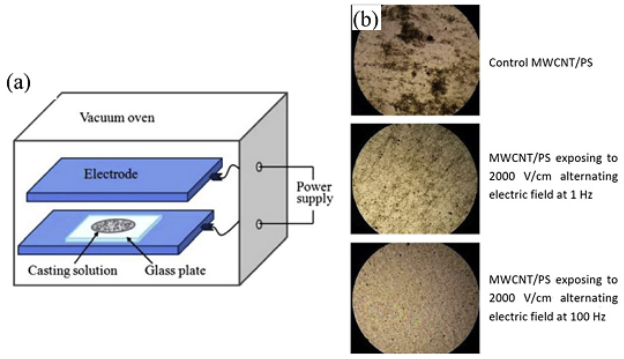

Figure 2-19. (a) Schematic of electrical alignment and (b) micrographs of membranes. Adapted from reference [22].

Also, the electro-cast membrane shows considerably less aggregation and misdistribution of nanofiller in the polymer matrix.

2.5 Transport mechanism in RO and NF

Membrane separates components due to differences in physical and chemical properties between the membrane and the solutes. Understanding the separation and transport mechanisms in RO and NF membranes will provide the guideline for rational design and unique combination of material choices to attain the desirable properties and outstanding separation performance[112]. Transport through TFC membranes is governed primarily by the ultrathin top layer where the separation between the various components of the feed solution is made. As intended, the support sublayer present little resistance to transport due to its porous nature. Although the role of the sublayer is primarily for structural support, its presence invariably plays a role in the overall performance and, as recently established, must be taken into account.

The net transport of molecules/ions is driven by gradient of pressure, temperature, and concentration across a membrane. The overall driving force can be expressed as chemical potential gradient, and the flux can be described by a simple equation:

$$J_i = -L_i \frac{d\mu_i}{dx} \qquad \textbf{Equation 2-1}$$

where $\frac{d\mu_i}{dx}$ is the chemical potential gradient of component i and L_i is a proportionality coefficient related to this chemical potential driving force.

Consider desalination process involving two components, water (w) and salt (s). The flux of water (J_w) and salt (J_s) through the membrane can be written as[23]:

$$J_w = A_w(\Delta P - \Delta\pi)$$ **Equation 2-2**

$$J_s = B_s(C_M - C_P)$$ **Equation 2-3**

where, J_w is the volumetric water flux ($m^3\ m^{-2}\ s^{-1}$), J_s is the solute mass flux ($kg\ m^2\ s^{-1}$), A_w is the pure water permeance ($m^3\ m^{-2}\ s^{-1}\ bar^{-1}$), B_s is the solute permeance ($m\ s^{-1}$), ΔP is the applied pressure difference (bar), $\Delta\pi$ is the osmotic pressure difference between the two sides of the membrane (bar), C_M and C_P are the solute concentrations at the membrane surface in the feed and permeate side ($kg.m^{-3}$), respectively. The units for the solute permeance, B_s, are obtained by dividing the solute mass flux by its driving force, which is the difference in solute concentration ΔC. Hence, it leads to the following unit ($kg\ m^{-2}\ s^{-1}\ m^3\ kg^{-1}$), and by simplifying this unit we get ($m\ s^{-1}$).

The rejection (r) which quantifies the ability of the membrane to separate salt from the feed solution is given by:

$$r = \left(1 - \frac{C_{sl}}{C_{s0}}\right) * 100\%$$ **Equation 2-4**

Generally, two model have been used to explain the mass transfer through the membrane. The solution-diffusion model is effective for describing dense membranes without pores or with extremely small pore size (less than 0.5 nm) used in RO processes.

The transport of molecules based on solution-diffusion mechanism involves three consecutive steps, that is: (1) sorption of permeant into the upstream side of the membrane; (2) diffusion of the sorbed component through the membrane under a concentration gradient; and (3) desorption from the downstream side of the membrane[22] (**Figure 2-20**). According to the solubility and diffusivity differences among permeants, separation occurs in the dense membranes.

For the porous membrane containing tiny pores from the nanoscale to microscale where the pore size ranges between 0.5 to 5 nm, such as microfiltration (MF), and ultrafiltration (UF) the pore-flow model is usually applied. This model assumed that transport occurs through the permeation pathways (pores) by the pressure driven convective flow and separation is based on the exclusion of permanents from the pores. The pore geometries (shape and size) significantly affect the mass transport of solutes and solvent. The water flux can be modeled using empirical equations based on the Hagen-Poiseuille or Carman-Kozeny equations as follows:

Consider a membrane containing a number of parallel cylindrical pores. The flux through such a membrane is given by:

$$J = (\frac{\varepsilon r_p^2}{8\tau l})(\frac{\Delta P}{\eta}) = \frac{\Delta P}{\eta R_m}$$ **Equation 2-5**

where J is the volumetric permeation flux of solvent through the membrane ($m^3.m^{-2}.\ s^{-1}$), η is the viscosity of the liquid solvent (MPa.s), ΔP is the pressure difference across the membrane, r_P is the pore radius (m), ε is the surface porosity, l is the membrane thickness (m), τ is the tortuosity of the pores and R_m , is the total resistance towards solvent flow (m^{-1}) and equal to the term $(\frac{8\tau l}{\varepsilon r_p^2})$.

For membranes which consist of closely packed spheres, the solvent flux is given by:

$$J = (\frac{\varepsilon^3}{K_{c-k} l S_m^2 (1-\varepsilon)^2})(\frac{\Delta P}{\eta}) \qquad \textbf{Equation 2-6}$$

where K_{c-k} is the Carman-Kozeny constant, which depends on the pore geometry, and S_m is the pore internal surface area per unit volume (m^2/m^3). Based on the Carman-Kozeny equation, Rm is equal to the term $K_{c-k} l S_m^2 (1-\varepsilon)^2/\varepsilon^3$.

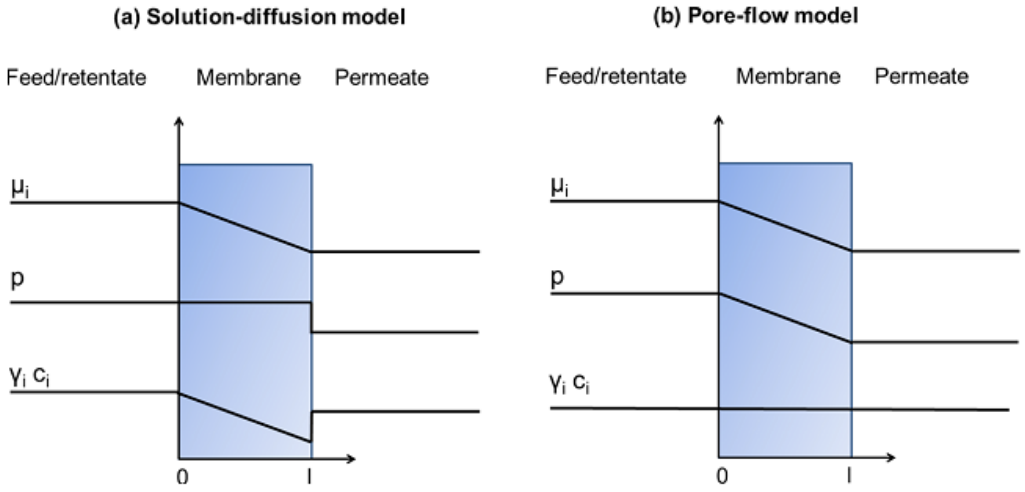

Figure 2-20. Schematic description of (a) solution-diffusion, and (b) pore-flow models[24].

An NF membrane is considered as a combination of a (porous) and a RO (nonporous) membrane. An NF membrane consists of a porous and a nonporous zone[20]. The four mass transport regions for an NF membrane are shown in **Figure 2-21**. Note that, in a real NF membrane, the boundaries between mass transfer regions are not possible to easily distinguish.

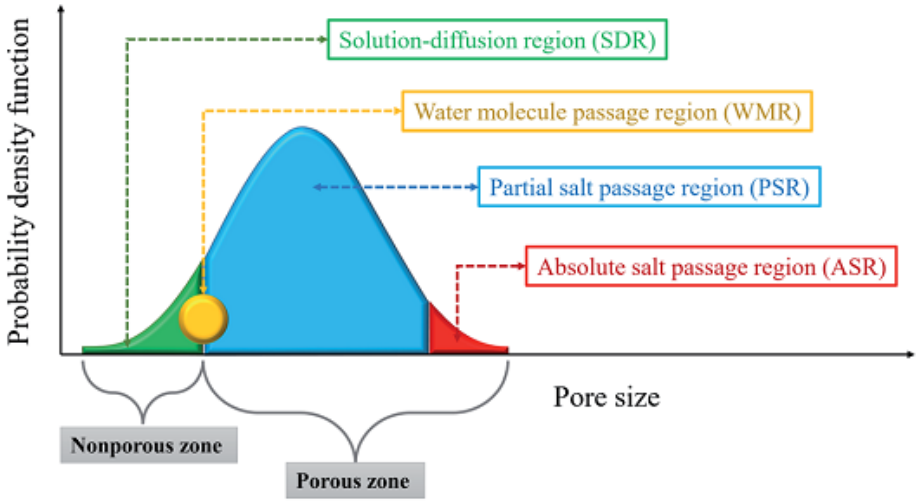

Figure 2-21. Mass transfer region for an NF membrane. adapted from [20].

The separation mechanism for NF membranes is complex and many models regarding impacts of different parameters on transport mechanism and prediction of membrane performance have been reported[19]. Traditionally, three main factors have been given for the separation of solutes by NF membrane:

Steric hindrance effects: These are related to the relative size of the solute and pore[19,23]. For example, combination of uncharged membrane and neutral solutes, or larger solute and smaller membrane pore size leads to higher rejection ratio.

Electrostatic (Donnan) effect: It depends on the phenomena of counter-ion and co-ion competition membranes. According to the relationship among charged solute and fixed membrane charge, the electrostatic interaction can be either repulsive or attractive[19,23]. For example, membrane and solute with similar charge (co-ions) yield a higher rejection rate because of the electrostatic repulsion.

Dielectric interaction effect: It is caused mainly by the difference in the dielectric constants of the membrane and water. It leads to the rejection of both neutral and charged solutes, even for a neutral membrane. Moreover, regardless of the charge sign, the dielectric effect is more noticeable for ions with more charge[19,23]. For example, multivalent ions are rejected to a higher degree than monovalent ions because of the interactions between ions, membrane, and solvent.

These three main effects are not completely independent; they can impact each other in the rejection of solutes. Also, other solute-membrane interactions include hydrogen bonding, the hydrophobic effect, and, which play roles in the rejection of solutes[19].

Chapter 3: **Atomic scale manipulation of sublayer with functional TiO_2 nanofilm toward high-performance reverse osmosis membrane**

3.1 Introduction

Water scarcity, a growing global concern, has led to a broad interest in membrane desalination technology[2]. Reverse osmosis (RO) is one of the dominant and efficient methods for generating pure water from saline water and other sources of wastewater[2,3,113]. The cutting edge choice for RO desalination are the polyamide thin film composite (PA-TFC) membranes [4,114]. In general, PA-TFC membranes are fabricated on porous polymeric supports by *in-situ* polycondensation of two reactive monomers, namely polyamine and polyacyl chloride, at the interface of two mutually immiscible solvents [5,6]. Among several synthesis factors of interfacial polymerization (IP) which impact the separation performance and the physicochemical properties of TFC membranes, the sublayer properties play one of the most significant roles[115,116]. They include structural properties (pore size distribution, porosity, pore density, and roughness) and chemical properties (hydrophilicity-hydrophobicity and the affinity/reactivity with amine or acyl chloride monomers) [7,8,14,15,17,18,48,117]. Conventional sublayers for TFC membrane consist of polymeric ultrafiltration (UF)/microfiltration (MF) membranes, which generally have poor surface wettability, rough surface, and low porosity[71]. An effective strategy to overcome these limitations is to modify a sublayer by functional nanomaterials to mediate the adsorption and diffusion rate of the amine monomer, the uniformity of both monomer distributions, and the IP reaction rate[71,115,118]. The innate properties of functional nanomaterials such as hydrophilicity, antifouling, interactive affinity, photocatalytic and others, equip the membrane with desirable properties [119].

Recently, several different manipulation methods have been proposed to modify the sublayer by functional nanomaterials. One strategy is to add inorganic and hydrophilic additive to the sublayer [47,49,120]. For instance, Wang et. al.[47] fabricated a high performance RO membrane with thin and compact PA selective layer by incorporating tannic acid into the support layer, which enhanced the hydrophilicity of the support layer, and varied the absorption/diffusion behavior of the amine and the formation of the nascent film. However, the homogenous dispersion of additive in the sublayers is challenging [115] Alternatively, the application of a specific interlayer[58,59,61,62,66,68,70,73,75,121] or sacrificial layer[9,54] was achieved via vacuum

filtration or interfacial self-assembly. For example, Livingston et al.[9] utilized a hydrophilic and uniform cadmium hydroxide nanostrand interlayer, which works as a container for the aqueous solution of the amine monomer, to regulate and optimize the formation of the skin layer with exceptional permeability. Applying sacrificing layer not only results in poor integrity between polyamide top layer and sublayer, but also makes the TFC membrane preparation procedure complicated due to additional removal steps of sacrificing layer after IP. Also, using these techniques would result in a relatively small area membrane. Therefore, the design of desirable sublayer by functional nanomaterials needs a reliable and practical manipulation strategy for controllable IP reaction at large area. Atomic layer deposition (ALD) as a versatile technology with outstanding properties[122] and feasible up-scaling[82,123,124] in membrane preparation[85–88,124], able to coat thin film of various high quality materials (inorganic metal oxides, metals, etc.) on substrates at the nanoscale with accurate thickness control, great uniform coverage and outstanding conformality.

Here, in this study, for the first time, a novel strategy of atomic scale surface modification by functional nanomaterial was proposed to tune the physicochemical properties of the sublayer to design high-performance PA-TFC membrane. Atomic layer deposition (ALD) was used to coat an ultrathin layer of monomer-affinitive TiO_2 on porous polyethersulfone (PES) sublayer. Such a novel and rational approach adapts the following advantageous features: (i) ALD offers a great uniform and size control[125] coating of TiO_2 which controllably boosts uniformity and smoothness of the sublayer at nanoscale. (ii) The ALD coated TiO_2 layer with outstanding hydrophilicity, porosity,[70,126] and stability [127–130], entirely covers the surface of the PES and firmly integrate with the PES layer [131]. Moreover, TiO_2 nanofilm's functionality of tuning up the affinity of sublayer to the amine monomer further mediates absorption/diffusion behavior of the amine monomer in the interfacial polymerization process. (iii) The optimal ALD TiO_2 coverage leads to a thin, smooth, and highly cross-linked PA selective top layer. As a result, improved RO performance was obtained for the optimal TFC in a dead-end process in terms of high permeance of 1.8 $L.m^{-2}.h^{-1}.bar^{-1}$ and high salt rejection rate of 96.1%. Atomic scale manipulation of sublayer by ALD opens a new path toward controlling IP and preparing high-performance RO membranes.

3.2 Experimental

3.2.1 Materials

As reacting monomers, trimesoyl chloride (TMC) 98% and m-phenylenediamine (MPD) 99% were provided from Sigma-Aldrich. Anhydrous Hexane (≥99%) as the organic solvent, triethylamine (TEA), sodium dodecyl sulfate (SDS), dimethyl sulfoxide (DMSO), and camphorsulfonic acid (CSA) were used as the additives and supplied from Sigma-Aldrich. PES sublayer (average pore size of 0.1 μm) was purchased from Sterlitech Co. (WA, USA). The purchased materials and membranes were used without further modification.

3.2.2 Deposition of TiO_2 film on PES sublayer and ALD condition

An ultrathin film of TiO_2 was directly coated on the PES membrane at 95 °C in an ALD system (Thermal Gemstar 6XT, Arradiance, LLC, USA). Firstly, using deionized water (DDI water), PES membranes were washed then dried for 8 h at 70 °C. Afterwards, the membrane samples were placed in the holder of an ALD system, preheated at 95° C for 30 min under vacuum (~ 30 mTorr). Each ALD cycle consisted of (1) insert a first precursor (a pulse of 700 mSec of titanium tetraisopropoxide (TTIP, $Ti(OCH(CH_3)_2)_4$) heated at 60 °C for a determined exposure time to allow the TTIP to react with the membrane surface), (2) Purging the chamber with the carrier gas (pure N_2) with a flow rate of 200 sccm to remove a remaining unreacted precursor or any by-products, (3) insert the water into the process as an oxygen reactant source (a pulse time of 22 mSec of H_2O) to form the TiO_2, and (4) again N_2 purging to remove excess water and by-products from the chamber. By repeating this cycle, TiO_2 film with the accurate thickness can be deposited on the sublayer. In this study, different ALD cycles (0, 10, 50, 100, 200) were performed on PES sublayer and the obtained modified sublayers for further IP were denoted as ALD-x-TiO_2@PES, where x means the number of ALD cycles.

3.2.3 Polyamide thin film composite (PA-TFC) membrane preparation

The PA-TFC membranes were synthesized by modified IP procedure (filtration method) via a vacuum filtration lab-scale setup[132]. In this filtration technique firstly, a 2 w/v% of MPD solution (25 mL) containing 0.1 w/v% SDS, 1 w/v% CSA, 1 w/v% TEA and 1 w/v% DMSO was poured onto the support layer. After 10 min of contact time, the MPD solution was filtered through the support layer by vacuum pressure (applied vacuum of 0.1 bar below atmosphere) to distribute MPD evenly on the surface of the support. Then, the excess solution was air-dried until no observed droplets. support membrane was contacted with the organic phase (0.15 w/v% of TMC in hexane) (25 mL) which was removed by

pouring out from the top of filtration flask, after 30 secs. Then, the membrane surface was washed by n-hexane (100 mL) to eliminate unreacted monomers. The resulting membranes were cured at 60 °C for 4 min. Lastly, using DDI water, the fabricated TFC membranes were washed to remove the remaining reactants and then placed in lightproof DDI water container for performance evaluation and characterization. The obtained TFC membranes on different ALD-x-TiO_2@PES sublayers are denoted as PA-TFC-x, where x stands for the number of ALD cycles that was applied for TiO_2 nanoparticle coating.

3.2.4 Physicochemical characterization

The surface and cross-sectional morphologies of the membranes were detected by high resolution scanning electron microscopy (SEM, LEO FESEM 1530) with an accelerating voltage of 10 KV. For the cross-sectional analysis, membranes were broken in liquid nitrogen, and gold sputtering was used for all membrane samples before Field Emission Scanning electron microscopy (FE-SEM) detection. Energy dispersive X-ray spectroscopy (EDS) attached to a FE-SEM was applied to measure elemental composition specially the total amount of Ti atoms on the modified PES support membrane. The distribution of pores of the support layer was assessed by studying FE-SEM images of the modified PES membrane utilizing the ImageJ software. To study the surface topology of the membranes, Atomic Force Microscopy (AFM) (Bruker Innova AFM, USA) was utilized in tapping-mode. At least three times each membrane sample was scanned over a surface area of 10 μm by 10 μm, then the obtained AFM data was processed using Gwyddion analysis software, eliminating the noise and calculating the root mean square (R_q) and the average (R_a) roughness values.

The elemental compositions (C, O, and N) of the TFC PA membrane surfaces were studied via an X-ray photoelectron spectroscopy (Thermal Scientific K-Alpha XPS spectrometer). The cross-linking degree can be calculated by XPS spectra. the based on the chemical formula of fully linear ($C_{15}H_{10}O_4N_2$) and fully cross-linked ($C_{18}H_{12}N_3O_3$) polyamide, the theoretical O/N ratio can be shown by:

$$\frac{O}{N} = \frac{3m + 4n}{3m + 2n} \qquad \textbf{Equation 3-1}$$

and cross-linking degree (%) of the whole PA selective layer (not only the incipient layer) can be calculated by:

$$D = \frac{m}{m + n} \times 100 \qquad \textbf{Equation 3-2}$$

where n and m are the linear and cross-linked proportion of the PA selective layer, respectively, and XPS analysis results are used to determine the values of n and m [77,133].

The surface hydrophilicity of support layer was evaluated through contact angle measurements by means of an optical instrument (OCA20, Data Physics, Germany) at room temperature. Using a motorized micro syringe, a preset 5 μL droplet of DDI water was formed at the tip of a steel needle (20 gauge, 0.603 mm in diameter) placed on the surface of membrane and images of this drop were captured by a CCD camera. Image acquisition and determination of contact angle by automated drop shape analysis (ADSA) were implemented utilizing the VCA 2500 XE equipment and software (AST Products, Billerica, MA). For each sample, the static contact angle was assessed at 5 various locations to minimize the experimental error.

Membrane partition coefficient of MPD (K_m) was measured to determine the affinity of MPD to sublayer membrane.[134] Also, the solution uptake (SU) was used to determine the amount of solution taken up by the membrane sublayer[135]. The sublayer membranes were cut into the square pieces 1.5" in length. The pieces were then immersed in 50 mL of aqueous 2 wt.% MPD solution for 10 minutes. K_m and SU can be calculated by:

$$K_m = \frac{C_{MPD}^{membrane}}{C_{MPD}^{H_2O}} = \frac{\frac{m_2 - m_0}{m_1 - m_0}}{C_{MPD}^{H_2O}} \quad \textbf{Equation 3-3}$$

$$\mathrm{SU}(\%) = \frac{m_1 - m_0}{m_0} \times 100 \quad \textbf{Equation 3-4}$$

Where m_1 depicts the sublayer weight saturated with MPD solution, m_0 and m_2 depicts the weight of dry sublayer before and after immersing in the MPD solution, respectively. Based on the Beer-Lambert law, the concentration of MPD in the water phase was measured at a certain time interval by an Ultraviolet–visible spectrophotometer (GENESYS 10S UV-Vis Thermo Fisher Scientific) using its absorbance at a wavelength of 292 nm, therefore, the MPD concentration ($\boldsymbol{C_{MPD}^{H_2O}}$) of the solution could be calculated after immersion of each sublayer.

3.2.5 Membrane performance test

Dead-end filtration system (Sterlitech HP4750 Stirred Cell) was used to investigate the rejection and pure water permeability of the prepared membranes. To pressurize the membrane cell, a nitrogen gas cylinder attached with the pressure regulator was linked to the top of container. The prepared TFC membrane was cut into the determined shape (effective area was 14.6 cm^2) and placed in the membrane cell. The solution volume was 250 ml. The membranes were initially compacted at a constant temperature of 25 °C and a trans-membrane pressure of 20 bar with DI water for approximately 1 h. After the compaction, the initial water flux was measured for 10 minutes. Permeate was gathered via

graduated cylinder for a period of time till steady condition. The pure water permeability (PWP) ($L.m^{-2}.h^{-1}.bar^{-1}$) was calculated by:

$$PWP = \frac{\Delta V}{\Delta t}\frac{1}{A_m \Delta P} \quad \textbf{Equation 3-5}$$

Where ΔP (bar) is the applied trans-membrane pressure, A_m(m^2) is the effective area of the membrane testing cell, Δt(h) is the elapsed time period of sample collection, and ΔV (L) is the volume of collected permeate. In the salt rejection test, a brackish water (2 g/L NaCl) was utilized as the feed solution. A bench conductivity meter (Hanna HI 8733) was utilized to measure the conductivity in the permeate ($\boldsymbol{\sigma}_p$) and feed ($\boldsymbol{\sigma}_f$). At least 40 ml solution was collected each time for the measurement. The membrane salt rejection calculation was performed by the conductivity ratio between the permeate solution ($\boldsymbol{\sigma}_p$) to the feed solution ($\boldsymbol{\sigma}_f$)[136].

$$R\ (\%) = \left(1 - \frac{\sigma_p}{\sigma_f}\right) \times 100 \quad \textbf{Equation 3-6}$$

For each TFC membrane, at least three similar membranes were prepared with the same procedure and were analysed to calculate the average salt rejection, pure water permeability, and the standard deviation was indicated by the error bar.

3.3 Results and Discussion

3.3.1 ALD coating and the properties of ALD-x-TiO_2@PES sublayers

As shown in **Figure 3-1**, fabrication of TFC polyamide membranes consist of the following two steps: (a) Deposition of TiO_2 layer on the PES sublayer (b) Polyamide interfacial polymerization on the modified sublayer.

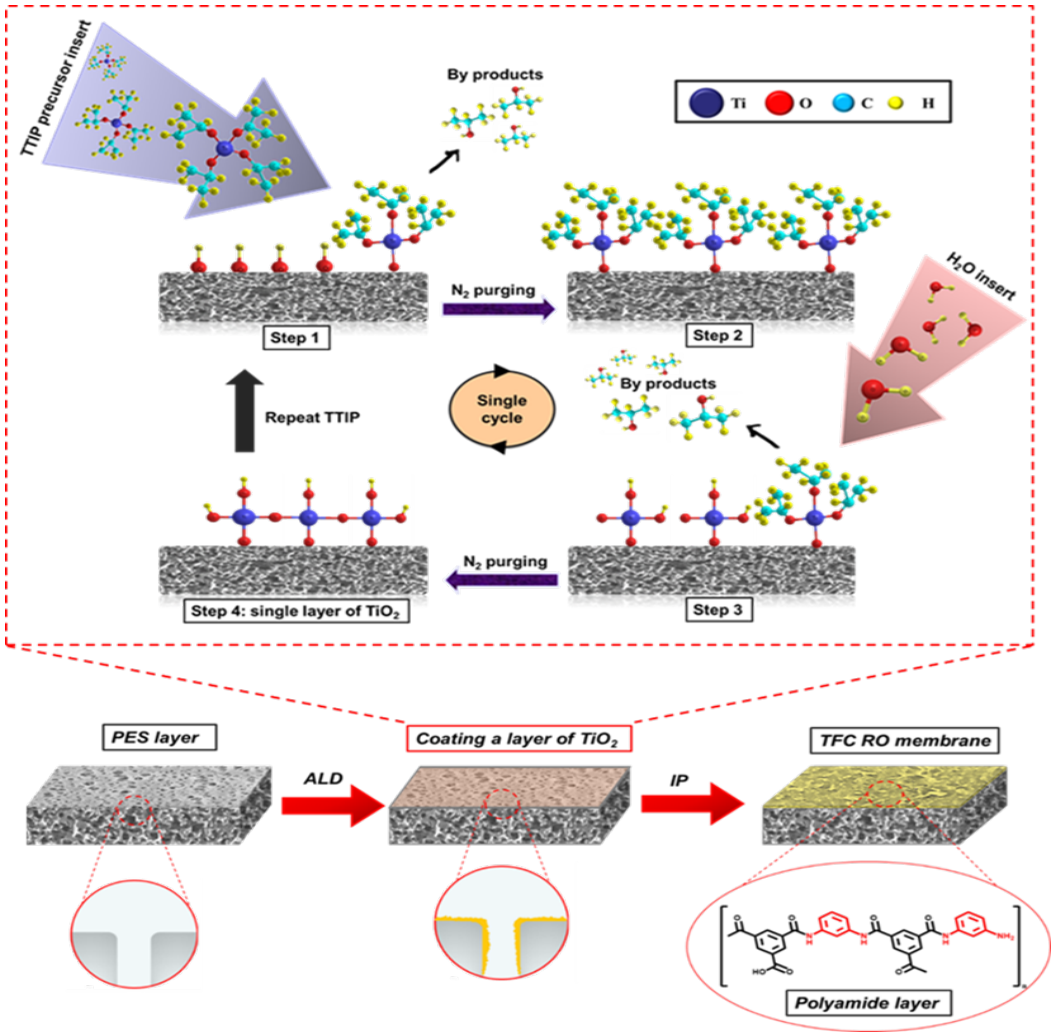

Figure 3-1. Schematic representation of TFC RO membrane with modified PES support layer and one ALD cycle of TiO2 deposition on the PES sublayer.

TiO_2 ALD nucleation growth on the PES that lacks reactive groups like hydroxyl, can be described by different mechanism[137–139] in comparison to the normal ALD growth. The PES sublayer, which has a porous surface, and TTIP are nonpolar. Therefore, TTIP is anticipated to have a decent solubility in the PES, and TTIP can adsorb to the surface of the PES and afterwards diffuse to the PES sublayer's near-surface area. During the ALD reaction, the arriving H_2O will react effectively with TTIP molecules at or near the surface of the PES sublayer and TiO_2 clusters will be formed. After the nucleation of TiO_2, the reaction for the cycle of TiO_2 ALD can be defined as below [140,141]:

$$[Ti(OH)_x]^* + Ti(OCH(CH_3)_2)_4 \rightarrow$$
$$[TiO_xTi(OCH(CH_3)_2)_{4-x}]^* + xCH(CH_3)_2OH \quad (1^{st} \text{ half reaction})$$

$$[TiO_xTi(OCH(CH_3)_2)_{4-x}]^* + 2H_2O \rightarrow$$
$$TiO_2 + [Ti(OH)_x]^* + (4-x)CH(CH_3)_2OH \quad (2^{nd} \text{ half reaction})$$

$$Ti(OCH(CH_3)_2)_4 + 2\,H_2O \rightarrow$$
$$TiO_2 + 4CH(CH_3)_2OH \quad \text{(Total reaction)}$$

By repeating the ALD cycle, an ultrathin layer of TiO_2 with the amorphous structure was obtained in the low temperature[142,143]. Figure 2K, which is proportional to the Ti EDS intensity[87], and Figure S1, which is EDS mapping of Ti element, can confirm that the amount of TiO_2 on the PES support layer increases when the ALD cycle is increased. Also, it indicates that TiO_2 deposition successfully coated on the PES support layer surface and pore walls.

Figure 3-2(A-J) shows the SEM and AFM images of ALD-x-TiO_2@PES membranes. The FE-SEM images of ALD-x-TiO_2@PES (**Figure 3-2(B-E)**) indicate almost unchanges in the surface morphology compared to the pristine membrane (**Figure 3-2A**) which may be due to conformal and uniform deposition of modified layers. Based on the growth rate of TiO_2 reported by literature in the same experimental ALD condition[140], the growth rate of TiO_2 is reported around 0.04 nm per cycle. Therefore, for ALD 200-TiO_2@PES the nominal thickness of TiO_2 is considered around 8 nm and it can be estimated that the pore size reduction is around 5 to 10 nm. Thus, the effect of these range of ALD cycle on the morphology and pore size of the sublayer can be considered negligible. According to the AFM images in **Figure 3-2(G-J)**, the homogenous deposition of TiO_2 nanoparticles clearly reduced the surface roughness of sublayers, declining from 53 nm in average for pristine PES membrane to 37 nm in average for ALD-200-TiO_2@PES (**Figure 3-2J**).

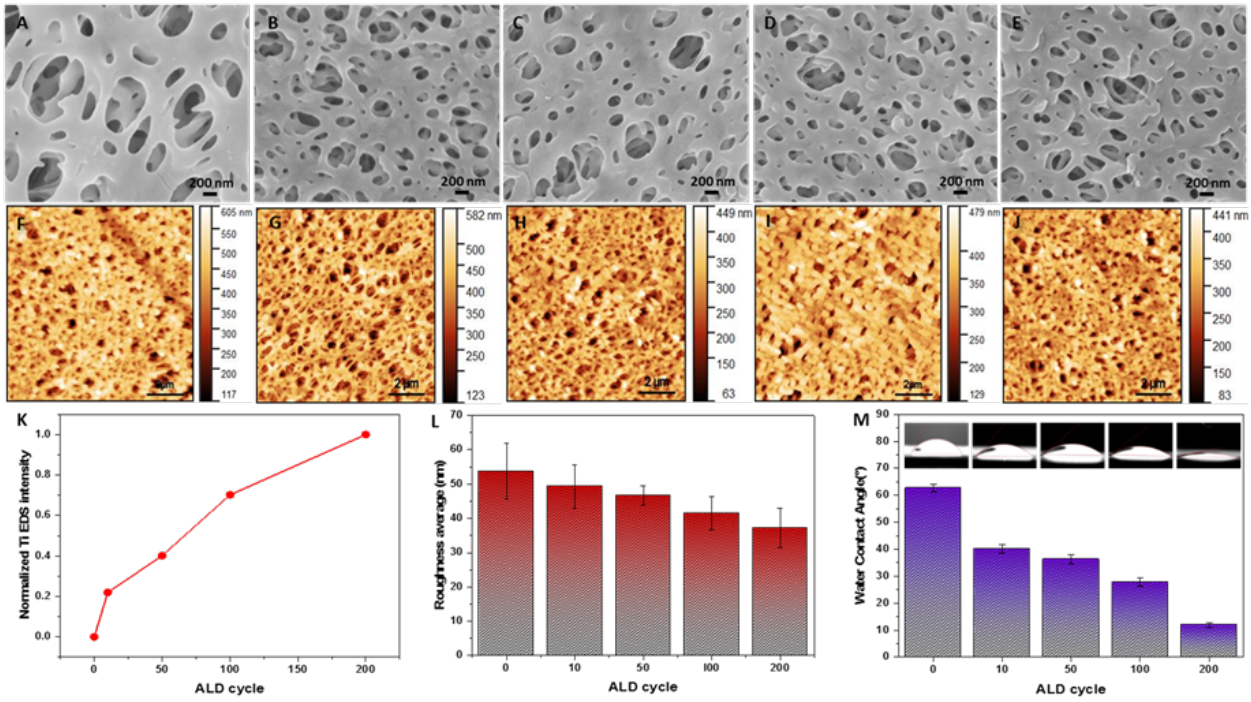

Figure 3-2. Properties of PES sublayer with different TiO_2 ALD cycles: (A to E) SEM surface images and AFM images (A, F) pristine PES, (B, G) ALD 10-TiO2@PES, (C, H) ALD 50-TiO_2@PES, (D, I) ALD 100-TiO_2@PES, (E, J) ALD 200-TiO_2@PES, (K) Normalized Ti Peak area in SEM-EDS spectra, (L) Ra surface roughness, and (M) water contact angle.

Such smooth surface of sublayer is favorable for the following IP of the PA top layer. The surface hydrophilicity was determined by the water contact angles (WCAs) measurement. WCA continuously decreased as the number of ALD cycles increased (**Figure 3-2M**). The contact angle decreased from 62 to 41 for PES membranes with 10 ALD cycles. This result showed that PES surfaces were not fully covered by TiO_2 during this stage and discrete coating of TiO_2 is on the surface of PES layer. At 200 ALD cycles, the contact angle reduced considerably to 11, because of the formation of a continuous film of TiO_2. These results suggest that the ALD-coated TiO_2 nanoparticles considerably enhance the surface wettability of the PES sublayer, which enables the amine solution to homogeneously spread on the coated support surface. The tunable wettability towards high hydrophilicity for PES sublayer via ALD coating of TiO_2 nanoparticles will further favor in the formation of the PA selective layer [47,66]. Solution uptake is measured to understand the adsorption and diffusion behavior of MPD. The solution uptake increases from 3.114% for the pristine PES sublayer to 4.781% for the ALD-200-TiO_2@PES. According to the results, PES-TiO_2 membranes absorb more MPD than pure PES membranes, which

Table 3-1. Summary of properties related to affinity to amine solution for sublayers.

Sample	Membrane partition coefficient (K_m)	solution uptake (%)
PES	0.6731	3.114
ALD-10-TiO_2@PES	1.0321	4.162
ALD-50-TiO_2@PES	0.9552	4.238
ALD-100-TiO_2@PES	1.0616	4.516
ALD-200-TiO_2@PES	1.0848	4.781

enhances the concentration of MPD in the membrane and, subsequently, increases the amount of MPD in the reaction zone for interfacial polymerization. Also, membrane partition coefficient of MPD shows the affinity of MPD to sublayer increase from 0.67 to 1.08 with increasing the ALD cycle of TiO_2 coating on the PES membrane **(Table 3-1.** Summary of properties related to affinity to amine solution for sublayers.**)**. In fact, the negatively charged TiO_2 layer leads to a strong electrostatic attraction between MPD and PES-TiO_2 layer because MPD is positively charged [144]. Also, PES-TiO_2 sublayer includes considerable amount of functional groups (hydroxyl) interacting with amine monomers via hydrogen bonds and covalent bonds[48,49,70]. Thus, there is a high affinity between MPD and PES-TiO_2, which is consistent with membrane partition coefficient of MPD results.

3.3.2 Properties of PA-TFC-x

After interfacial polymerization, the obtained PA-TFC-x membranes were imaged by FE-SEM. The selective PA layer was found to be full of folded nodular structures and randomly distributed protuberances on the uncoated PES sublayer (**Figure 3-3A**). On the contrary, the surfaces of PA-TFC-x membranes become smoother and smoother with the increased number of ALD cycles as displayed in **Figure 3-3 (B-E)**. Moreover, the population and size of nodules also decrease with the increase of the ALD cycles of the TiO_2 on the PES support layer. Similar to the surface SEM images, AFM images of the surfaces of PA-TFC-x membranes in **Figure 3-3 (F-J)** also show the decreasing trend in surface roughness. According to **Figure 3-4A**, the polyamide layer on the coated sublayer (PA-TFC-200) has the smoothest surface, exhibiting the Ra value of 54 ± 4.32 nm, 35% lower than that of PA layer on uncoated PES membrane (81.76± 14.74 nm). The change in the roughness of PA layers lies mainly in the alteration of wettability and roughness of the underlying support membrane. The aqueous solution of MPD cannot homogenously cover the uncoated PES layer due to the low wettability of the surface

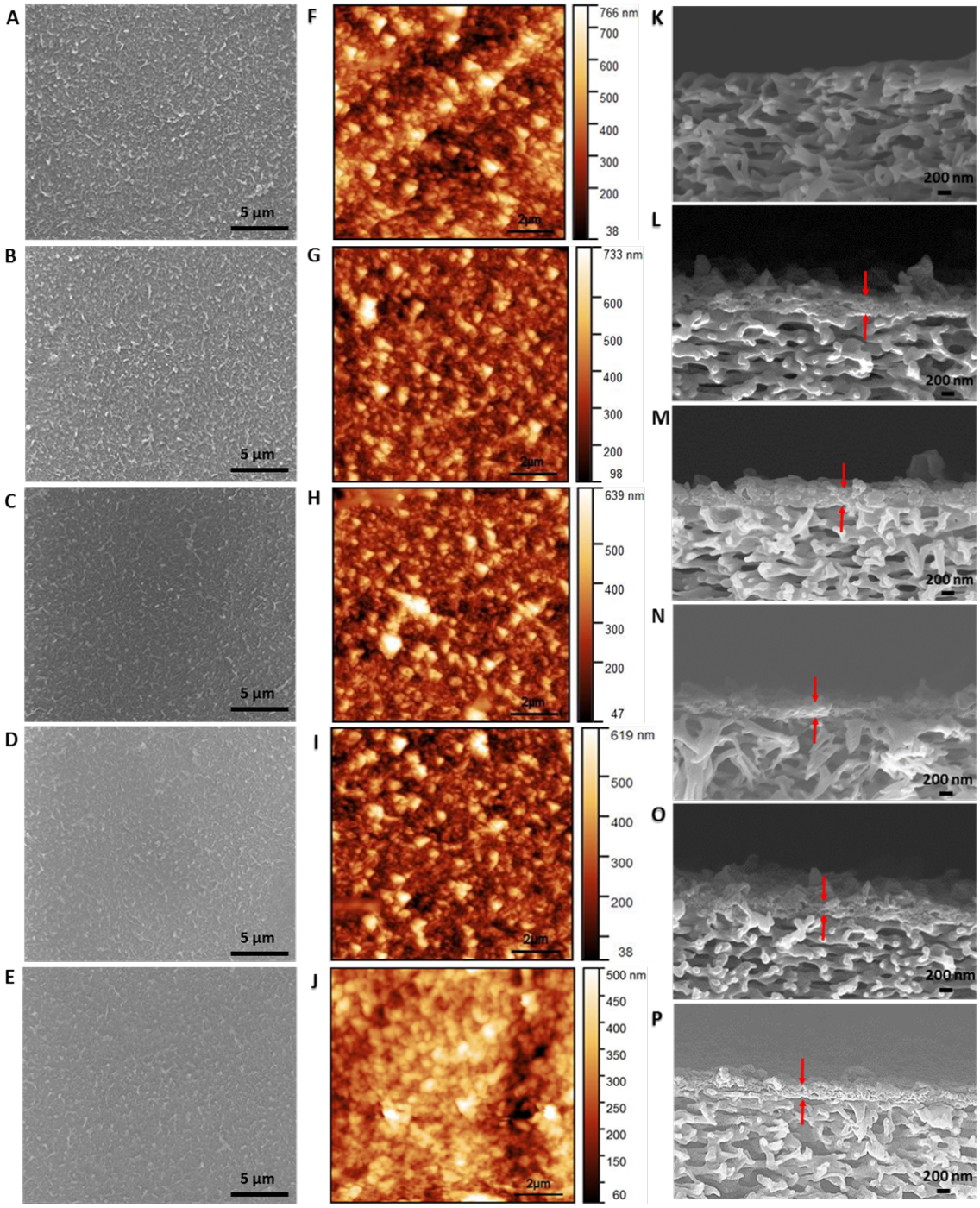

Figure 3-3. SEM and AFM image of the TFC RO membranes (A, F) PA-TFC-0, (B, G) PA-TFC-10, (C, H) PA-TFC-50, (C, H) PA-TFC-100, (E, J) PA-TFC-200. (K to P) cross-sectional SEM images: (K) Pristine PES, (L) PA-TFC-0, (M) PA-TFC-10, (N) PA-TFC-50, (O) PA-TFC-100, and (P)PA-TFC-200.

and the non-uniform diffusion of MPD during IP process, resulting in rough PA layer. As the roughness and surface wettability of ALD-x-TiO_2@PES decreases and increases, respectively, the PA layers turn into smooth, which is in agreement with the literature [66,77,131].

The continuous polyamide films were clearly observed on top of the sublayers from the cross-sectional SEM images in **Figure 3-3 (L-P)** and **Figure S0-3**. By comparison of the thickness of the PA selective layer, shown in **Figure 3-4A** and **Table S0-3**: Physical properties of TFC membranes, it is obvious that the TiO_2 coating can lessen the thickness of the PA selective layer, changing from 216.2 ± 12.57 nm for PA on pristine PES membrane to 153.6 ± 9.6 nm for PA-TFC-200. The decreased thickness of the PA layer can be ascribed to two factors, which are also accord with the kinetic model[145,146] for thin film formation which was presented by Freger[147]. Firstly, the change of IP reaction leads to the different formation of the initial nuclei of the polyamide layers. The primarily formed polyamide layer will have a high degree of crosslinking if there is more amount of MPD in the reaction zone during IP, which were approved by the solution uptake test. Then, the further diffusion of MPD will be hindered by the highly cross-linked polyamide film [66]. This nucleation could allow the thinner PA layer with smaller ridges and valleys to be fabricated. Secondly, after formation of the preliminary thin layer of polyamide, amine monomers are unceasingly released through the pores and partitioned into the organic phase[7,9]. The sublayer's affinity to MPD will affect the penetration of amine monomers through the preliminary layer. There is a high affinity between MPD and PES-TiO_2, which is consistent with membrane partition coefficient of MPD results, and contributes to a limited diffusion of amine monomers through the preliminary layer. Also, this confined and regulated amine diffusion would lead to the fabrication of the smoother and thinner selective PA layer[77].

The cross-linking degree and elemental composition of the polyamide active layer were assessed by XPS analysis. Spectra of XPS for TFC with different sublayers are shown in **Figure S0-4.** XPS survey spectra of the different TFC membranes. and the consistent values of element composition, crosslinking degree are listed in **Table S0-4**. The XPS survey spectra of TFC membranes illustrate three major peaks of oxygen (O 1s), carbon (C 1s) and nitrogen (N 1s) at the membrane surfaces as an indication of polyamide structure. The elemental composition results show that the O/N ratio of the polyamide layer declines with the increase of ALD cycle of TiO_2 on the PES support layer, indicating an increase of crosslinking degree. Based on the solution uptake test by increasing the ALD cycle of TiO_2 on the PES sublayer, the amount of amino monomer in the reaction zone increases which leads to the enhancement of polymerization efficiency and progress of the crosslinking degree of the polyamide layer that can be showed by **Figure 3-4B**.

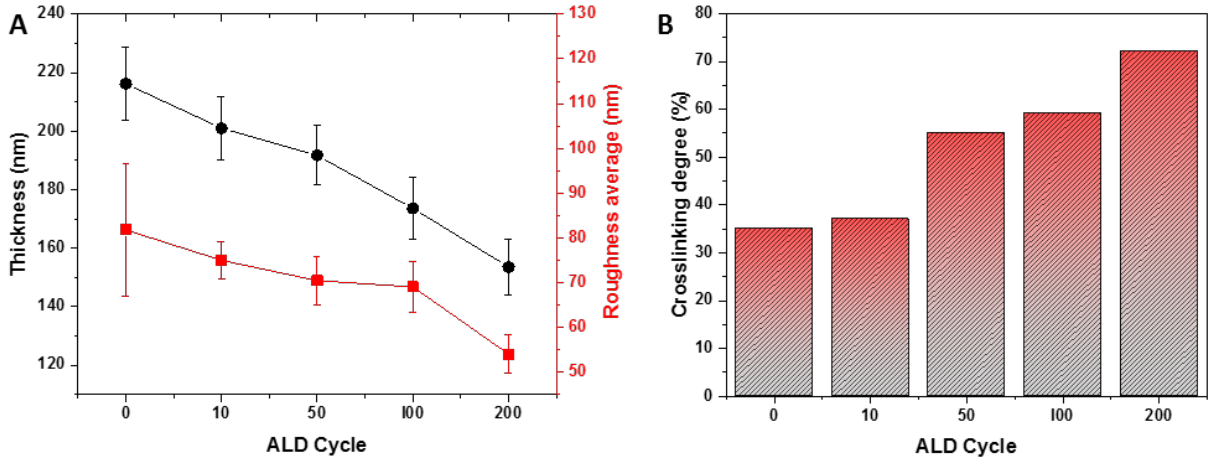

Figure 3-4. Dependency of properties of Polyamide top selective layer of RO TFC membranes on PES/TiO2 sublayer with different ALD cycles (A) Graph showing (Ra) surface roughness and thickness (B) Crosslinking degree.

Therefore, presence of TiO_2 layer on the PES sublayer increase the amount of MPD in the concentration zone and limit the diffusion rate of the MPD molecules through the IP process. As a consequence, a thin and smooth polyamide skin layer with high cross-linking density and without defect fabricated at the interface.

3.3.3 Membrane transport properties

Figure 5 depicts the performance of the PA-TFC-(0, 10, 50, 100, 200). The pure water permeation of the PA-TFC RO membrane rises from 1.4 to 1.8 $L.m^{-2}.h^{-1}.bar^{-1}$ for PA-TFC-0 to PA-TFC-100. This observation is expected because the membrane thickness, which is the main transmembrane resistance[148] , decreases with the introduction of the TiO_2 layer as displayed in the FESEM images of the cross-section (Figure 3 and Figure S3). Also, the TiO_2 coating on the surface and pores of the support layer makes the water transport path faster and thus improves the water flux. It can also be seen that the NaCl rejection gradually rises at the same time from 92.6 to 96 with the increase of the ALD cycle of the TiO_2 on the PES support from 0 to 100. This increase in rejection is because of the increase in the crosslinking degree of the PA layer and formation of the uniform and defect-free PA layer on the sublayer. Once extended the ALD cycle of TiO_2 to 200, the TFC RO membranes demonstrated a decline in NaCl rejection (~88%). This trend can be attributed to the enhanced hydrophilicity of the sublayer. As revealed in Figure 2I, when the ALD cycle is 200, the water contact angle declines below 20°. Therefore, instead of being reserved, the aqueous phase may penetrate through the sublayer which

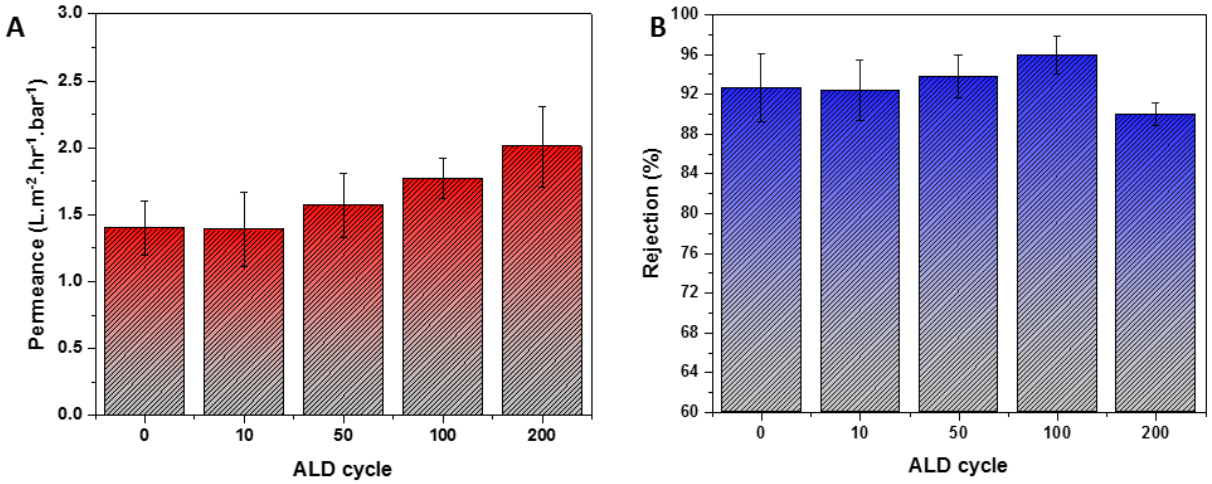

Figure 3-5. Performance of PA-TFC-x RO membranes (A) Permeance, (B)Rejection.

results in a discontinuous PA selective top layer. Accordingly, the salt rejection decreases, and the water permeation increases.

Totally, the ALD coating of TiO_2 has been shown to be an effective modification method to tune the sublayer properties and to make a favorable platform for the interfacial polymerization reaction of selective layers. The optimized ALD cycle of TiO_2, 100, leads to a PA-TFC RO membrane which had a superior performance (1.8 $L.m^{-2}.hr^{-1}.bar^{-1}$, 96.1%) compared to that of the PA-TFC membrane on the neat PES sublayer (1.4 $L.m^{-2}.h^{-1}.bar^{-1}$, 92.6%). Moreover, table S2 as a comparison between the PA-TFC-x membrane in this study and the commercial PA TFC membranes indicates that the TFC membrane with an interlayer of TiO_2 is within the range of or better than the performance of commercial membranes [38].

3.4 Conclusion

In this study, for the first time the low temperature ALD of TiO_2 as a functional nanomaterial was applied to tune the PES sublayer for developing the performance and properties of PA-TFC RO membranes via regulation of the adsorption/diffusion of amine monomer for the IP. The research results indicate that PES-TiO_2 platform leads to thin, smooth, no-defect and high cross-linked polyamide selective layer. On the other hand, it should consider a caution when the ALD technique is used because of the hydrophilicity of the coating layer, applying a large number of ALD cycles (200 cycle) will result in the discontinues polyamide layer and decline in the rejection, which is not appropriate in most applications. As a result, the TFC membranes on the sublayer with the optimum TiO_2 ALD coating

(100 cycle) exhibited the superior performance for both water permeation and salt rejection. Therefore, ALD coating of TiO_2 as a functional nanomaterial on the sublayer may be a promising candidate to prepare high performance PA TFC membranes for desalination application to employed in industry.

Chapter 4: **Thin-film polyamide nanocomposite membrane decorated by polyphenol-assisted $Ti_3C_2T_x$ MXene nanosheets for reverse osmosis**

4.1 Introduction

Thin film nanocomposite (TFN) membranes, including dispersed organic/inorganic fillers and nanoscale dense polymeric matrix, are the amended form of the thin film composite (TFC) membranes, the most common commercial reverse osmosis (RO) membranes for water desalination application[91,100]. To date, several fillers, such as metal oxide nanoparticles[38,149], carbon nanotubes[150], graphitic carbon nitride[151], graphene oxide[152,153], metal organic framework[154], and covalent organic framework[155,156] have been incorporated into the selective polymeric layer through the interfacial polymerization process to surmount the limitations of permeability-selectivity trade-off and fouling propensity of TFC membrane [91,100]. The transport mechanisms of water and solutes will be influenced by the shape/structure of nanofillers, resulting in a considerable change in separation performance. Nanoporous particles, for example, make it easier for water to enter via pore channels, but tube and sheet-like nanomaterials let water pass through nanochannels while preventing larger solutes.[157,158] Although intensive research has been conducted on the progress of the polyamide (PA) TFN membrane, there are still number of challenges on the fabrication of TFN membrane. The low affinity between polymer matrix and nanofillers could result in nanofillers agglomeration, nonhomogeneous distribution, defects and deterioration of selectivity. Moreover, applying nanofillers to offer extra transporting pathways generally threaten the selectivity due to their intrusion in the fabrication of dense PA layer[92,159]. In fact, the nanofillers with various properties not only change the internal structure (crosslinking degree and free volume) of the PA layers by impacting the interfacial polymerization (IP) process, but also alter the chemistry of the selective layer's surface by adding a large number of functional groups [160,161]. Hence, performance of TFN membranes can be regulated for various separation applications by skilfully choosing and designing the chemistry, shape, and dimension of nanofiller with thoughtful connectivity between polymer and nanofillers [162].

MXenes as a class of multifunctional two-dimensional transition metal carbides, nitrides or carbonitrides with a formula $M_{n+1}X_nT_x$ (T = -OH, –O, or – F) has attracted noticeable attention for membrane-based separation application due to fascinating properties such as hydrophilicity, diverse

surface chemistry, superior thermal and mechanical stability, high antifouling and antibacterial activity, and large surface area[163–165]. Although the privilege and benefit of MXene-based membranes, which apply MXenes as a filler[166,167] or selective layer[168,169] have been confirmed, there are still several drawbacks on MXenes such as weak ambient stability, easy restacking, and poor processability, which constrain the further scalable development of MXene-based membranes[170]. Also, an important issue regarding the production of well mixed MXene/polymer nanocomposite membrane is the interface interaction between polymeric chain and MXene nanosheets. A deficient compatibility between MXene and polymer matrix unavoidably leads to irregular morphology, interfacial defects, and poor dispersion and aggregation of MXene nanosheets, potentially deteriorating the performance of composite membranes[171]. Thus, to address these critical challenges, it is of importance to discover an appropriate and practical modification approach to boost compatibility, processability, and chemical stability and oxidation resistance of MXene nanosheets to progress the scalable implication for different applications [172–176]. Also, up to now, there is just limited research on the application of MXene or modified MXene nanosheets in the IP-based TFN membranes[166,167,177,178].

In this Research, we demonstrated a robust, green, economic and single step self-assembly approach to functionalize $Ti_3C_2T_x$ MXene nanosheets by facile assembly of plant-inspired polyphenol coating on the surface of $Ti_3C_2T_x$ nanosheets. Then, the MXene decorated TFN membrane was produced by interfacial polymerization process of two reactive monomers, polyacyl chloride (TMC) and polyamine (MPD), on the support layer (PES). To the best of author's knowledge, it is the first research of tannic acid modified $Ti_3C_2T_x$ MXene nanosheets and their utilization in the IP-based TFN membrane. Tannic acid, cost effective, environmentally friendly polyphenol which is simply produced from nature, is widely available in the market [179]. TA as a type of plant-derived polyphenol, which includes pyrogallol and catechol compounds in its structure, could readily adhere and form a uniform coating to roughly all kind of fillers through covalent and/or noncovalent interactions and self-polymerization in basic conditions [105,180–186]. The following are some of the expected benefits of $Ti_3C_2T_x$-TA nanosheets: First of all, since MXene nanosheets could readily oxidize in ambient conditions or aqueous media, TA coating with antioxidant properties could considerably improve oxidation resistance of Ti3C2Tx nanosheets and prolong the lifetime of MXene nanosheets, leading to a stable and durable composite membrane system [187,188]. Secondly, the hydrophilicity and highly negative charge of functional group of TA on the $Ti_3C_2T_x$ nanosheets not only decline the aggregation of $Ti_3C_2T_x$ nanosheets and boost their dispersion in the aqueous phase, but also improve the TFN membrane's anti-

fouling properties by increasing the repulsion among negative charged foulants and membrane[179,183]. Thirdly, TA could favorably manipulate the nanofiller/polymer interface by improving the compatibility between the PA matrix and $Ti_3C_2T_x$ nanosheets through formation of chemical crosslinking bonding (polyester) between unreacted acyl chloride groups of TMC and phenol groups of TA during IP [105,179,185]. Finally, the incorporation of $Ti_3C_2T_x$-TA nanosheets in the PA selective layer

would lead to favorable alterations in the surface morphology and hydrophilicity of the TFN membrane. The aims of this study are to (1) modify the $Ti_3C_2T_x$ MXene nanosheets by tannic acid and (2) improve the performance and antifouling properties of the TFN membranes for RO application. With the assistance of several characterization techniques, the physicochemical properties, antifouling properties and performance of TFC and TFN membrane were systematically studied.

4.2 Experimental Section

4.2.1 Materials and chemicals

Commercial flat sheet RO membrane TriSep ACM2, and PES support layer (average size of pore = 100 nm) were bought from Sterlitech Co. (WA, USA). Ti_3AlC_2 powders (MAX phase) with particle size of <38 μm, Lithium fluoride (LiF) and 12 M hydrochloric acid (HCl) purchased from Sigma Aldrich. The chemicals, tannic acid (TA, ACS reagent), Tris-buffer agents (Trizma@ base, Trizma@ HCl), m-phenyl diamine (MPD, 99%), trimesoyl chloride (TMC, 98%), anhydrous Hexane (≥99%), triethylamine (TEA), sodium dodecyl sulfate (SDS), camphor sulfonic acid (CSA), dimethyl sulfoxide (DMSO), bovine serum albumin (BSA, 96%), sodium chloride (NaCl, >99%) were provided from Sigma-Aldrich. All the above-mentioned membranes and chemicals were used as received.

4.2.2 $Ti_3C_2T_x$ MXene nanosheets synthesis

MXene nanosheets were synthesized via selective etching of the aluminum layer from the Ti_3AlC_2 MAX phase with a minimally intensive layer delamination (MILD) method. In a typical experiment, 1.6 g LiF was dissolved in 20 ml of 9 molar HCl in a Teflon container and stirred for 30 minutes. Afterward, 1 g Ti_3AlC_2 was gradually added to the solution over a period of 10 minutes and stirred for 24 hours at 37 C. Next, the acidic clay-like product was transferred to 50 ml Falcon tubes, washed copiously with distilled deionized (DDI) water, followed by centrifugation at 8000 RPM for 10 minutes. The washing process repeated until the pH level reached 5-6, and a dark green supernatant started to form. The appearance of dark green supernatant indicates that delamination of the MXene flakes

commenced. DDI water was added to the clay-like sediment and sonicated for 1 hour in a bath sonicator under argon flow to facilitate the delamination process. Argon flow started 10 minutes prior to the sonication and continued during sonication to minimize oxidation of MXene flakes via extraction of dissolved oxygen molecules from the solution. Lastly, $Ti_3C_2T_x$ suspension was centrifuged at 3500 RPM for 45 minutes, and delaminated flakes of MXene were collected and stored in the fridge for further uses. The concentration of the MXene solution was determined based on gravimetric analysis after vacuum-assisted filtration of a specific volume of delaminated MXene solution.

4.2.3 Modification of $Ti_3C_2T_x$ MXene nanosheets with Tannic acid

The MXene nanosheet was modified via the self-polymerization of TA. In a typical example, the MXene nanosheets initially was sonicated with a probe sonicator for 15 min. After that, 5 mg of MXene was dispersed in Tris buffer solution (0.01 M, pH 8.5). 10 mg of TA was dissolved in 1 ml of Tris buffer solution by vortexing for 30-45 Sec. The freshly prepared TA solution was added to MXene suspension and vigorously stirred at 25 ^oC, in the dark for 15 h. The reaction solution was centrifuged for 1 h at 16000 * g, supernatants were removed and then the modified MXene nanosheets were washed two times with deionized water for 1 h at 16000 *g each time. Finally, the $Ti_3C_2T_x$-TA nanosheets were re-dispersed in deionized water for further use. **Figure S0-5** represent the modification route of $Ti_3C_2T_x$ MXene nanosheets.

4.2.4 Fabrication of TFC, TFN ($Ti_3C_2T_x$), and TFN ($Ti_3C_2T_x$-TA) Membranes

The typical IP method was used for the fabrication of TFC and TFN membranes. The IP condition was chosen based on our previous research[189] and literature[190]. PES membranes were immersed in deionized water overnight and stabilized before using as a support layer for IP. The polyamide layer was coated on the PES layer via reaction between aqueous solution (2 w/v% of MPD, 0.1 w/v% SDS, 1 w/v% DMSO, 1 w/v% TEA, 1 w/v% CSA, and desired amount of $Ti_3C_2T_x$ or $Ti_3C_2T_x$-TA nanosheets) and organic solution (0.1 w/v% of TMC in hexane). An ultrasonic bath was used for 30 min to disperse the fillers in the aqueous solution. The PES layer was soaked and saturated with the aqueous solution for 10 min. The remained aqueous solution on the surface of membrane was wiped carefully with filter papers, and the saturated membrane kept air-dried for 5 min. After that, the organic solution was contacted with membrane surface for 30 s to conduct IP. In the next step, n-hexane (100 mL) was used to wash the membrane surface to remove unreacted remained monomers. For further polymerization and crosslinking the polyamide selective layer, the membranes were placed in oven at 60 °C for 4 min.

Finally, the residual reactants were removed by washing the fabricated polyamide membrane via DDI water and then the membranes were stored in lightproof water container for further studies. Also, the TFC membrane without using fillers was fabricated with the similar procedure. The prepared membranes were labelled as TFC (pristine), TFN ($Ti_3C_2T_x$-X), TFN ($Ti_3C_2T_x$-TA-X) membranes in which X is refer to the various loading of 0.002, 0.004, 0.008, 0.016 %wt of $Ti_3C_2T_x$ or $Ti_3C_2T_x$-TA. **Figure 4-2a** illustrate the fabrication route of polyamide membrane. The commercial TFC polyamide membrane - TriSep ACM2 was also used as a benchmark for desalination experiment.

4.2.5 Characterization

To measure the particle size and zeta potential of nanosheets, dynamic light scattering (DLS) (Malvern Zetasizer Nano instrument) was utilized. The results of DLS were averaged from three replications. an Ultraviolet–visible spectrophotometer (GENESYS 10S UV-Vis Thermo Fisher Scientific) was used to detect the absorbance peak of $Ti_3C_2T_x$ and $Ti_3C_2T_x$-TA nanosheets. Crystallinity pattern of the samples was recorded by X-Ray Diffractometer (XRD, Rigaku Miniflex 600) with the rate of 2°/min using a Cu Kα ($\lambda = 1.5405$ Å) radiation source. The surface topology of the fillers and membranes were investigated by an atomic force microscope (Bruker Innova AFM, USA) under tapping mode. Surface area of 5 μm ×5 μm of membranes were scanned more than three times. The AFM images were processed by Gwyddion and Nanoscope analysis software to eliminate the noise and calculate the roughness value (average roughness (Ra), and root mean square (Rq)). The surface morphologies of the prepared PES, TFC, and TFN membranes were studied by field emission scanning electron microscopy (SEM, LEO FESEM 1530). All of the samples were coated with a layer of gold before FESEM observation. The chemical functionalities of membranes were analyzed by Fourier Transform Infrared Spectroscopy (Nicolet-670 FTIR, Thermo Fisher, USA) under the attenuated total reflectance (ATR) mode, with the resolution of 4 cm^{-1} in the range of 600-4000 cm^{-1}. The elemental compositions and bonding information of membranes surface were measured by an X-ray photoelectron spectroscopy (Thermal Scientific K-Alpha XPS spectrometer). DSC were conducted by DSC-Q200 (TA instrument, USA) to measure the glass transition (Tg) of polyamide membranes (heating range of 25 to 400 °C with a rate of 10 °C/min under a nitrogen atmosphere). A video contact angle measurement system (VCA-2500 XE, AST products, Billerica, MA) was used to evaluate the surface wettability of membranes at room temperature. For each sample, the dynamic contact angle was measured during the 150 second at 3 different locations.

4.2.6 Performance test

The RO performance of TFC and TFN membranes were measured by using a dead-end filtration setup (Sterlitech HP4750 Stirred Cell) at ambient temperature and pressure (ΔP) of 20 bar, as defined in previous publication [189]. Prior to any measurement, the membranes were compacted for an hour with deionized water at pressure of 21 bar, then the pure water permeation of membranes were measured at pressure of 21 bar for determined time interval until steady state condition. The feed solution was a brackish water (2000 ppm NaCl). The concentration of salt in feed (C_f) and permeate (C_p) were determined by using a bench conductivity meter (Hanna HI 8733). The pure water permeance (A, $L.m^{-2}.h^{-1}.bar^{-1}$) and salt rejection (R, %) were calculated by the following equations:

$$A = \frac{\Delta V}{A_m . \Delta t . \Delta P} \quad \textbf{Equation 4-1}$$

$$R\ (\%) = \left(1 - \frac{C_p(\sigma_p)}{C_F(\sigma_F)}\right) * 100 \quad \textbf{Equation 4-2}$$

Where ΔV is the permeate mass (liter), Am is the effective area of the membrane (m2) and Δt is the permeation time (h), and ΔP is the applied trans-membrane pressure (bar). The conductivity ratio between the permeate solution (σp) (μs/cm) to the feed solution (σf) (μs/cm) determined the salt rejection. For each membrane, at least three similar membranes were fabricated with the same procedure and were analysed to report the average water permeance and salt rejection, and the standard deviation are represented by the error bar.

4.2.7 Fouling test

The antifouling properties of the membrane were analysed by using bovine serum albumin (BSA) as model foulant. After pre-compacting the membrane, the initial flux (J_0) of water through the membrane under transmembrane pressure of 20 bar was measured. Then, the membrane cell was emptied and filtration of BSA solution (1000 ppm) was conducted for 1 h and the BSA solution flux (J_{BSA}) was measured. Finally, the membrane was rinsed with DDI water and then recovered flux (J_R) was determined in the same way as initial flux measured. The following equations are applied to calculate the fouling recovery rate (FRR) and the total fouling rate (R_t):

$$FRR = \frac{J_R}{J_0} * 100\% \quad \textbf{Equation 4-3}$$

$$R_t = \left(1 - \frac{J_{BSA}}{J_0}\right) * 100 \quad \textbf{Equation 4-4}$$

Where J_R (recovered flux) is the water flux ($L.m^{-2}.h^{-1}$) after the protein filtration test, and J_{BSA} ($L.m^{-2}.h^{-1}$) is the flux of foulant solution, J_0 is the initial water flux ($L.m^{-2}.h^{-1}$). The antifouling properties of a membrane is high when the R_t is low, and the FRR is high.

4.3 Results and discussion

4.3.1 $Ti_3C_2T_x$ and $Ti_3C_2T_x$-TA characterization

The $Ti_3C_2T_x$ nanosheets were effectively modified by a rapid and simple method through coating a stable polyphenol layer on the surface of nanosheets [191,192]. TA, as one of the plant-derived polyphenol materials, which has plenty of hydrophilic -OH functional groups associated with the ten aromatic rings--five catechol groups (an aromatic ring with two linked hydroxyl groups) and five gallol groups (an aromatic ring with three connected hydroxyl groups)--was chosen[179]. As **Figure 4-1a** shows TA attaches to the surface titanium (Ti) of the $Ti_3C_2T_x$ MXene nanosheets through potential interactions: (i) by electrostatic interaction, (ii) by coordination bonds, and (iii) by hydrogen and other polar bonds[179,188,193]. Once the pH of the solution exceeds pKa of TA, it acts as a polyanion, meaning that TA can bind to a substrate through electrostatic interactions. Coordination could be another interaction; lone pair electrons from the phenolic hydroxyl group of TA offers for connecting metal centers. The Pyrogallol and Catechol groups in TA have high multivalent metal ions linking affinities through coordinating bonding. A Catechol-Titanium oxide complex (C-O-Ti), in particular, has received considerable attention. The structure of TA coordinated to $Ti_3C_2T_x$ MXene with a monodentate complex or chelating bidentate complex[194]. The constituents of TA that are not involved in coordination will interact with $Ti_3C_2T_x$ MXene surface through hydrogen bonds and other polar interactions. UV-visible, DLS, XRD, AFM analysis were conducted to indicate the successful modification of the surface of $Ti_3C_2T_x$ nanosheets by TA. The UV-visible spectrophotometry in **Figure 4-1b** shows that for $Ti_3C_2T_x$-TA nanosheets, along with the $Ti_3C_2T_x$ nanosheets characteristic absorbance peaks at 770 nm [172], additional peaks at 275 nm and 221 nm were observed, which were allocated to the n-π* and π - π* transitions of tannic acid, respectively[185]. XRD spectra of $Ti_3C_2T_x$ and $Ti_3C_2T_x$-TA are indicated in **Figure 4-1d**. After modification of $Ti_3C_2T_x$ by TA, the angle of Ti_3C_2Tx diffraction peak (002) reduced and shifted to the lower angle, accordingly, the interlayer spacing enlargement and intercalation of TA into the interlayer space in $Ti_3C_2T_x$ nanosheets. It is important to mention that the increased interlayer gap will be useful for the water transport. The size and morphology of pristine $Ti_3C_2T_x$ MXene and modified $Ti_3C_2T_x$-TA nanosheets were analyzed by

using AFM and DLS (**Figure 4-1(e-i)**, **Figure S0-6**). The DLS hydrodynamic size of pristine $Ti_3C_2T_x$ MXene after ultrasonication was 127.8± 0.24 nm and the height measured by AFM averaged approximately 1.6 nm. After the $Ti_3C_2T_x$ MXene modification, as shown in the **Figure 4-1 (f, g, and i)**, the size of $Ti_3C_2T_x$-TA became 143.1 ± 0.75 nm, the average height 13.1 nm. Therefore, it is verified that a thin coating layer formed on the $Ti_3C_2T_x$ MXene nanosheets after the TA modification. Also, the considerable difference in the zeta-potential values of $Ti_3C_2T_x$ MXene nanosheets after the TA coating shows the formation of the layer of TA on the $Ti_3C_2T_x$ MXene nanosheets surface (**Figure 4-1c**). The surface of a $Ti_3C_2T_x$ MXene nanosheets was negatively charged of -21.8±0.3 mV because of the anionic nature of terminal groups (i.e., -OH, -O, -F). Also, it can be detected that $Ti_3C_2T_x$-TA nanosheets represented the lower negative charges of -41.8±0.5 mV because of the existence of a TA layer on the $Ti_3C_2T_x$ MXene nanosheets surface. The higher negative surface charge the higher electrostatic repulsion between nanosheets which leads to more stable dispersion and good stability [195,196]. It would also improve the incorporation of $Ti_3C_2T_x$–TA in the PA selective layer and as a result develop the performance of TFN membranes. Moreover, the advantage of high negative charge of $Ti_3C_2T_x$-TA nanosheets makes the membrane superior in antifouling performance. The surface functionalization of $Ti_3C_2T_x$ nanosheets could be an efficient and practical approach to diminish the oxidation propensity of $Ti_3C_2T_x$ MXene nanosheets through formation a protection coating layer. The photograph in **Figure 4-1j** indicates the stability and dispersion of $Ti_3C_2T_x$ and Ti_3C_2Tx-TA solution after 7 days. On visual inspection, the dispersion of $Ti_3C_2T_x$ MXene nanosheets became lighter as the majority of $Ti_3C_2T_x$ MXene nanosheets oxidized to the C and TiO_2. Moreover, there was obvious precipitation of $Ti_3C_2T_x$ MXene nanosheets. $Ti_3C_2T_x$ MXene nanosheets have a high tendency for oxidization and degradation in a short period of time. The use of an antioxidant [187,197], such as tannic acid, could efficiently prevent oxidation and aggregation of $Ti_3C_2T_x$ MXene nanosheets. Overall, $Ti_3C_2T_x$ MXene nanosheets have been successfully modified with coating a multifunctional layer of TA as an effective and practical surface modification technique.

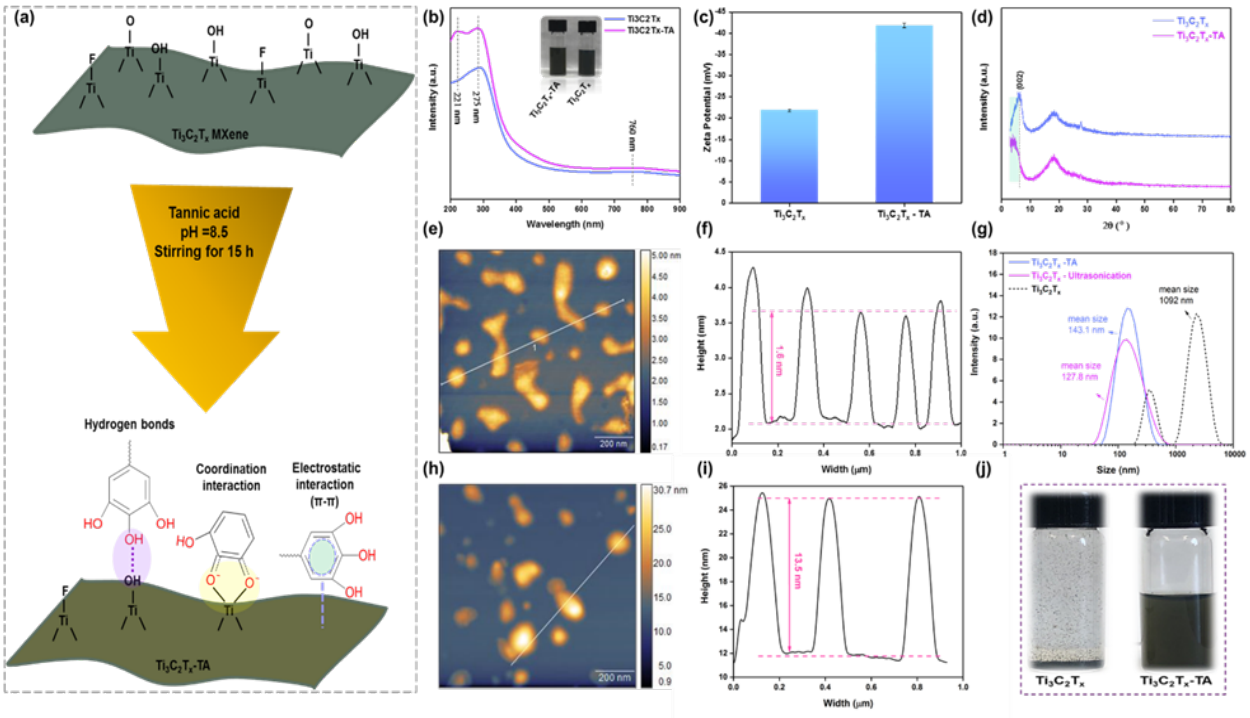

Figure 4-1. self-polymerization of tannic acid at $Ti_3C_2T_x$ MXene nanosheets (a) Schematic representation of binding mechanism, (b) UV-visible spectra, (c) Zeta-potential, (d) XRD pattern for $Ti_3C_2T_x$ and $Ti_3C_2T_x$-TA, (e-i) Morphology and size properties: AFM images and height profile of (e, f) Ti3C2Tx after ultrasonication, and (h, i) $Ti_3C_2T_x$-TA, (g) DLS for $Ti_3C_2T_x$ and $Ti_3C_2T_x$-TA, (j) image of dispersion and stability of $Ti_3C_2T_x$ and $Ti_3C_2T_x$ -TA nanosheets (0.008% wt) in water after 7 days.

4.3.2 Membrane Microstructure

PA-TFN membranes were readily formed through the IP reaction among MPD/fillers and TMC monomers on the porous PES support layer **(Figure 4-2a**). **Figure 4-2(b-i)** demonstrates the surface topology and morphology of the PES support layer, TFC, and TFN membranes. The common ridge-and-valley morphology of the PA active layer with leaf-like structure illustrates the successful interfacial polymerization among TMC and MPD, which fabricates a PA layer on the substrate. Generally, the IP reaction includes two parts: (1) formation of a loose incipient film of PA without ridge-and-valley morphology by initially diffusion of MPD monomer through the water/hexane interface to the organic phase and reaction with TMC monomer; (2) Marangoni convection boosts the MPD diffusion to react with TMC further, Marangoni effect is impacted by surface tension near the

water/hexane interface, the incorporation of $Ti_3C_2T_x$ and $Ti_3C_2T_x$-TA in aqueous phase could decrease the interface tension [198] and increase the Marangoni convection; consequently the incipient film is pushed and bended, and a dense cross-linked PA film with the ridge-and-valley structure are formed[199,200]. The presence of nanofillers in the polymerization region will affect the Marangoni convection, initial position of monomers and amine diffusion rate, and consequently the morphology and structure of PA layer will alter[104,201,202]. As **Figure 4-2(c, d)** shows, upon the incorporation the $Ti_3C_2T_x$ and $Ti_3C_2T_x$-TA nanosheets, greater leaf-like or even belt-like structures were detected. Also, according to the AFM results and the calculated RMS values in **Figure 4-2 (f-h)**, TFN membranes inclined to have a surface with higher roughness in comparison to TFC membrane. It is presumed that the MPD monomers can be attracted by H-bonding interaction of nanofillers in the aqueous phase. Therefore, the diffusion-reaction process of IP can be assisted by the locally enriched MPD in the vicinity of $Ti_3C_2T_x$ and $Ti_3C_2T_x$-TA nanosheets, thus producing bigger leaf structure on the membrane surface. Additionally, the size of nanosheets may exceed the PA layer's thickness, which gives the TFN membranes a rougher surface. A comparison between TFN($Ti_3C_2T_x$) and TFN($Ti_3C_2T_x$-TA) indicates that the ($Ti_3C_2T_x$-TA) nanosheets lead to bigger leaf structure and larger roughness features on the PA layer. The reasons may be related to plenty of functional group on the $Ti_3C_2T_x$-TA nanosheets surface in comparison to neat $Ti_3C_2T_x$ nanosheets, which could take part in the IP reaction. Moreover, the bigger average size of $Ti_3C_2T_x$-TA in comparison to the $Ti_3C_2T_x$ nanosheets, make the ridge and valley feature of the membrane surface bigger and rougher. As it is clear, the surface roughness (RMS) order is compatible with the FESEM images observation, which follows TFC < TFN($Ti_3C_2T_x$) < TFN($Ti_3C_2T_x$-TA). Also, **Figure S0-7** shows that by increasing the amount of $Ti_3C_2T_x$-TA nanosheets loading, the greater leaf-like structure were formed on the surface of membrane. Moreover, the FESEM cross-sectional images in **Figure 4-2 (j-m)** reveals that with the incorporation of nanofillers the thickness of the polyamide layer increased due to the increasing the polyamide formation rate which was confirmed with surface morphology observation. In comparison to the TFC membrane, the TFN membranes with thicker polyamide layers offer more void in their structures. Since all polymerization are exothermic, faster formation of polyamide result in faster heat generation during the IP reaction. The generated heat leads to polyamide layer with multiscale internal void structure[203]. The difference among the morphology and structure of membranes confirms the impacts of nanofillers on the IP reaction and PA layer formation.

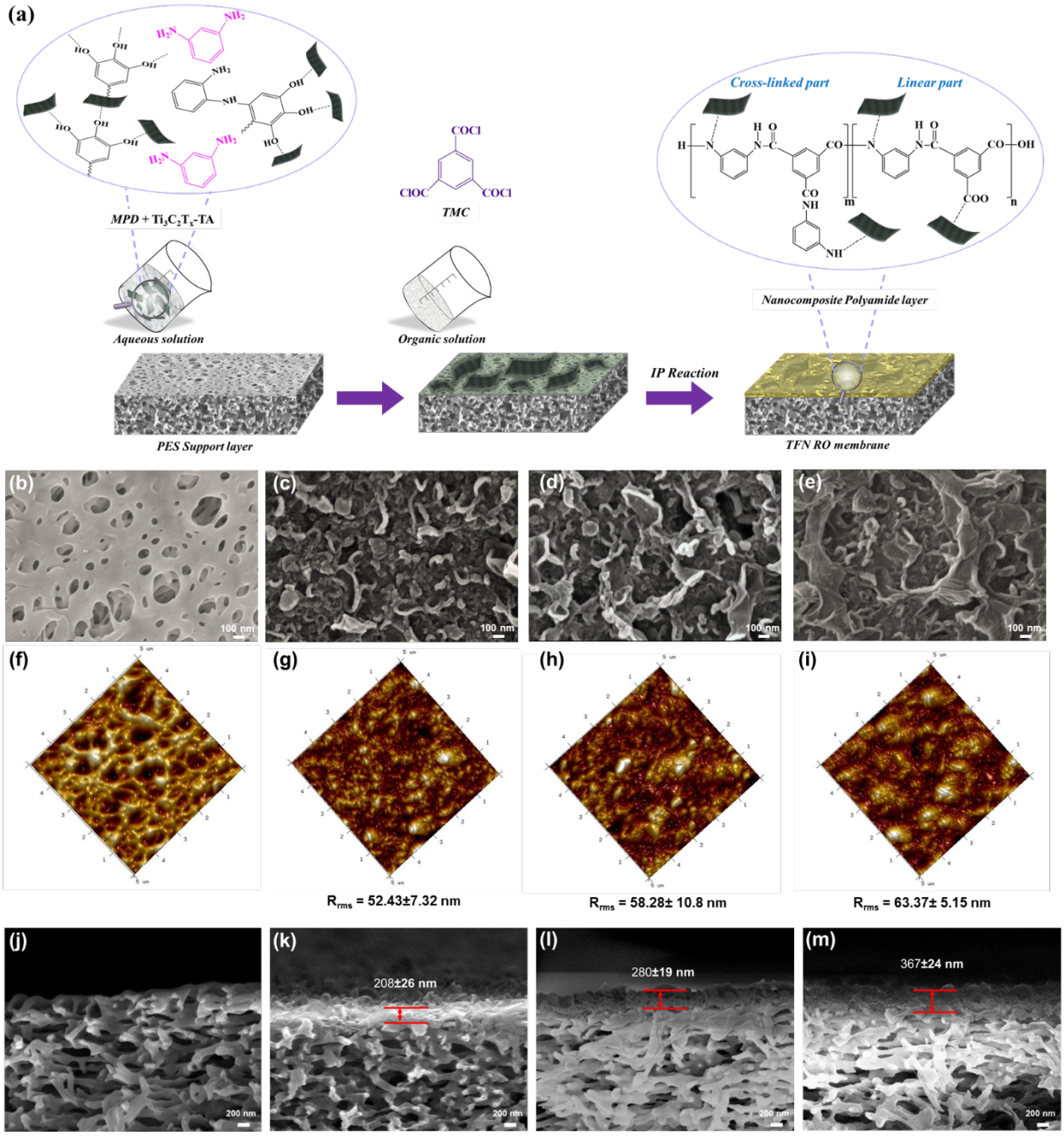

Figure 4-2. Fabrication and characterization of TFC and TFN membranes: (a)Schematic of membrane fabrication procedure and the chemical structure of TFN ($Ti_3C_2T_x$-TA) membrane, (b-i) surface morphologies: FESEM and AFM images of the PES support layer and PA selective layer (b, f, j) PES, (c, g, k) TFC, (d, h, l) TFN($Ti_3C_2T_x$-008), (e, i, m) TFN($Ti_3C_2T_x$-TA-008).

The wettability of a membrane's surface is a key factor to assess the performance of membranes. The dynamic water contact angle (WCA) of TFC and TFN membranes with various concentration of $Ti_3C_2T_x$ and $Ti_3C_2T_x$-TA nanosheets were measured to investigate the wettability of the membrane (**Figure 4-3a, Figure S0-9**). The initial WCA of the TFC membrane was 104.4° and after 150 s, it reduced to 77.8°. By introducing the nanosheets to the polyamide layer, the initial WCA of TFN($Ti_3C_2T_x$-008) and TFN($Ti_3C_2T_x$-TA-008) declined from 84.5° to 55.5°, and 97.9° to 8.3° in 150 s, respectively. When the concentration of $Ti_3C_2T_x$-TA nanosheets increased to 0.016 wt%, the time for WCA< 10° was considerably reduced to 90 s (**Figure S0-9**). The lowest WCA of TFN($Ti_3C_2T_x$-TA) is because of the presence of plenty of negatively charged groups (i.e. hydroxyl) on $Ti_3C_2T_x$-TA which provides great polarity and hydrophilicity within the PA layer. Also, based on the Wenzel model [204], for the wettable surface, rougher surface has a smaller contact angle. Therefore, the rougher surface of the TFN membrane and better dispersity of $Ti_3C_2T_x$-TA nanosheets offer more available hydrophilic spots to water molecules, which are positive to the wettability properties of the membrane and diminishes the apparent contact angle.

To analysis the surface chemistries of the PES substrate, as well as the pristine and modified PA top layers, ATR-FTIR and XPS were conducted. As represented in **Figure 4-3b**, three characteristic peaks for the fully aromatic PA layer are 1541 cm^{-1} Amide II band (C-N stretching vibration and N-H in plane bending of a –CO-NH- group), 1609 cm^{-1} Aromatic amide (C=C ring stretching vibration), and 1663 cm^{-1}Amide I band (C=O stretching vibration in a secondary amide group), which are absent in the PES spectrum [205]. Moreover, a wide range at 3200 – 3650 cm^{-1} is attributed to the O-H stretching vibration, due to hydrolysis of acid chloride groups and possible presence of functional hydroxyl group of nanosheets[104,166]. Due to the high depth of penetration of the IR beam, the identifiable peaks of PES substrate were indicated in all membranes at 1580 and 1485 cm^{-1}(stretching vibration of aromatic in-plane ring), 1410 cm^{-1}(C-C aromatic ring stretching), 1240 cm^{-1} (asymmetric stretching of C−O−C), and 1150 cm^{-1} (symmetric SO_2 stretching vibration)[205]. The $Ti_3C_2T_x$ or $Ti_3C_2T_x$-TA concentration was below 0.016 wt% when the MPD solution with concentration of 2 wt% was used for the PA layer fabrication. Therefore, because of the small amount of nanosheets loading in the PA layer, and the weak absorption nature of nanosheets, the extra characteristic peaks of nanosheets were not obviously detected in TFN membranes; the same observations were indicated in the literatures when other fillers with low concentration were added to the PA layer [183,206,207]. Meanwhile, by comparing the TFC and TFN membrane spectra, the amide I peak normalized intensity (divided by reference peak spectrum

which was considered aromatic amide peak at 1609 cm^{-1}) increased, confirming the presence of nanosheets in the PA layer.

To further study the bonding information, surface composition, and cross-linking degree network of the PA layer, XPS analysis was employed. **Figure 4-3c**, which shows the full-scan XPS spectra of membranes, indicated the PA structure with the major peaks with binding energy of 285.3 eV (C1s), 399.8 eV (N1s), and 532.1 eV (O1s)[189]. Also, there is no clear peak corresponding to the titanium element in the PA layer which is because of the low amount of $Ti_3C_2T_x$ and $Ti_3C_2T_x$-TA nanosheets in the TFN membranes. Regarding the PA layer, a lower O/N ratio offers a higher crosslinking degree[186,208]. Hence, as **Figure 4-3c** shows (O/N ratio for TFC is 1.39, TFN($Ti_3C_2T_x$-008) is 1.21, and TFN($Ti_3C_2T_x$-TA-008) is 1.19), a PA layer with a relatively denser structure and higher crosslinking degree was obtained with the incorporation of $Ti_3C_2T_x$ or $Ti_3C_2T_x$-TA nanosheets during the IP process. Also, TFN($Ti_3C_2T_x$-TA-008) membrane indicated the lowest O/N ratio due to the interfacial crosslinking among the PA network and $Ti_3C_2T_x$-TA nanosheets. To study the chemistry of the TFC and TFN ($Ti_3C_2T_x$-TA-008) membranes further, high resolution N1s, O1s XPS were represented in **Figure 4-3 (e-h)**. Three fitted peaks from deconvolution of the N1s peak spectrum were associated to 400 eV (N-C=O, amide nitrogen group), 398.5 eV (R-NH_2 primary amine from partially cross-linked MPD monomer), and 402.1 eV (–NH_3^+, quaternary amine). The peak of -NH_3^+ corresponds to the electrostatic interaction among carboxylic group and amine [202,208,209]. Two peaks from deconvolution of the O1s spectrum were assigned to 531.2 eV (-NH-C=O, oxygen in the amide linkages), and 532.6 eV (O-C=O, OH group in unlinked carboxyl group)[209,210]. To assess the crosslinking density, the ratio of carboxylic or amine groups (unreacted functional groups) to amide linkages was determined[208]. As table S3 revealed, the ratio of O-C=O / N-C=O in the O 1s peak and the ratio of R-NH_2 / N-C=O in the N1s peak for the TFN ($Ti_3C_2T_x$-TA) membrane is lower than TFC membrane, indicating that the amount of amide linkage enhanced, and as a result the crosslinking density increased. The amine group of MPD is more reactive than the hydroxyl group of TA since the bond dissociation enthalpy of N-H is lower than O-H[211].

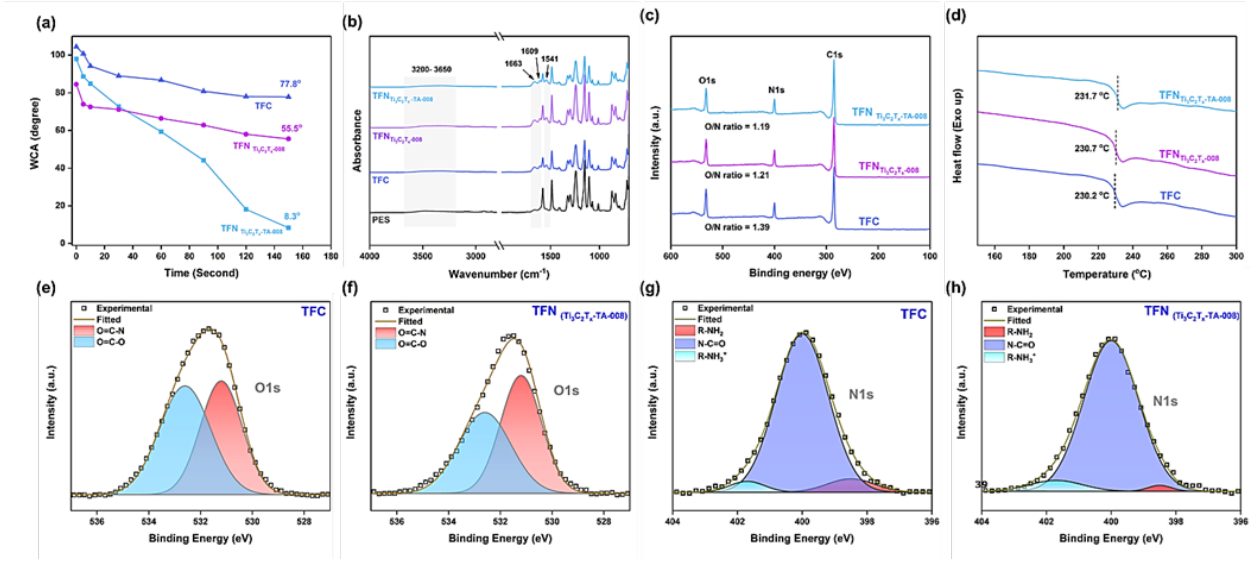

Figure 4-3. Chemistry and microstructure characterization of TFC and TFN membranes: (a)Dynamic water contact angle, (b) FTIR-ATR spectra, (c) Full scan XPS spectra (d) DSC curve (e-h) High resolution N1s, O1s XPS spectra for TFC, TFN($Ti_3C_2T_x$-TA-008) membranes.

The minimum amount of TA attached to the $Ti_3C_2T_x$ nanosheets can react with both MPD and TMC monomers[181,212], it can react with amine by Michael addition reaction, or it can serve as a reactive site for further crosslink with unreacted and remaining acid chloride, assisting the polyester bonding formation, improving the compatibility among $Ti_3C_2T_x$-TA nanosheets and the polyamide matrix. Therefore, the stability and membrane's structure could be improved by incorporation of $Ti_3C_2T_x$-TA nanosheets. More considerably, the covalent bonding among the PA network and $Ti_3C_2T_x$-TA nanosheets not only increased the PA crosslinking degree, but also limited the interfacial voids formation[104]. Also, the DSC results (**Figure 4-3d**) suggested that glass transition temperature (Tg) slightly increase after incorporation of $Ti_3C_2T_x$ nanosheets due to the lower interaction between the functional group of $Ti_3C_2T_x$ and the polymer matrix in compare to $Ti_3C_2T_x$-TA and the polyamide network. However, after adding $Ti_3C_2T_x$-TA nanosheets into the PA matrix due to the higher crosslinking degree and the restriction for the movement[213] of the PA macromolecular chain, Tg obviously increased, which revealed the presence of higher interactions and good compatibility between $Ti_3C_2T_x$-TA and PA networks.

4.3.3 Membrane performance

TFC and TFN membranes' performance were investigated by using NaCl solution (2000 ppm) under dead-end filtration mode, where a detailed procedure, and pre-compaction condition for experimental testing and apparatus of system were indicated in the **Figure S0-11** and Method. The pre-compaction causes an increase in the hydraulic resistance of the membranes, and hence, reduces the water flux by up to 20%. **Figure 4-4a** indicates that the neat TFC membrane has a fairly low water permeability and high salt rejection (1.7 $L.m^{-2}.h^{-2}.bar^{-1}$, 96.1%). The TFN membranes with a small amount of $Ti_3C_2T_x$ or $Ti_3C_2T_x$-TA (0.008 wt.%) considerably enhanced the water permeability about 1.6 and 1.4 times, respectively. Generally, the incorporation of hydrophilic nanosheets with plentiful functional group not only ameliorates the wettability of the TFN membranes, but also provides favorable spots for the hydrogen bond interaction, leading to the promotion of the solubility and diffusion of water molecules through selective PA layer. Secondly, the introduction of more water transport channels at the interface between the PA chain and nanosheets as well as the interlayer nanochannels between MXene nanosheets, supporting the low resistance water transport (**Figure 4-4d**). Moreover, the presence of TA among polyamide and $Ti_3C_2T_x$ nanosheets also provide high water affinity with the PA layer. Thus, a large amount of water molecules passes through short-cuts formed instead of transporting across the whole thickness of the cross-linked selective PA membrane, which follows the ineffective mechanism of solution-diffusion. Thirdly, the contribution of nanosheets interrupts the dense PA chains' packing by presenting further free volume for transporting of water molecules. The recent investigation using molecular dynamic simulation and positron annihilation lifetime spectroscopy, has revealed that the internal free volumes include network (4.2 – 4.8 ˚A in diameter) and aggregate (7-9 ˚A in diameter) voids [214–216]. The network void is a short distance among the PA network's segments, and the aggregate voids is a bigger space among the PA network domains (**Figure 4-4d**) [214–216]. Consequently, the augmentation of the performance of the TFN($Ti_3C_2T_x$-TA) in comparison to TFN($Ti_3C_2T_x$) and pristine TFC membranes might be related to the adequate expansion of internal voids within the PA membrane. To be specific, from membrane structural perspective, it is widely acknowledged that water permeance of TFN membranes incorporating 2D materials is mainly dependent on hydrophilicity, thickness, crosslinking degree, and surface roughness of the PA active layer. As discussed in membrane structure characterization part, after adding TA-MXene nanosheets, TFN membranes demonstrate enhance wettability, surface roughness, crosslinking degree, and thickness by comparison with TFC membrane. Among these changes, the variation of wettability, surface roughness and thickness with multiscale internal void structure can be count for the

improvement of water permeance. **Figure 4-4a** shows that although the salt rejection for the $Ti_3C_2T_x$ embedded PA layer had a drastic drop, the salt rejection for $Ti_3C_2T_x$-TA embedded PA layer stayed roughly similar to the pristine PA layer. Refer back to **Figure 4-2a**, where the layer of TA in $Ti_3C_2T_x$-TA has one end attached to the $Ti_3C_2T_x$ and the other end cross-linked with nearby PA macromolecules. Therefore, not only the proper dispersion of $Ti_3C_2T_x$-TA nanosheets, but also promising compatibility among $Ti_3C_2T_x$ and the PA matrix led to the well-maintained salt rejection. Moreover, the increase in the crosslinking degree and rigidity of TFN ($Ti_3C_2T_x$-TA), which were confirmed by XPS and DSC results, could be another reason for maintaining the same level of salt rejection.

4.3.4 Optimization of $Ti_3C_2T_x$-TA loading

According to the aforementioned results, $Ti_3C_2T_x$-TA nanosheets were chosen as a proper nano-fillers for further investigation because they cannot only improve the permeability of TFN membranes, but also maintain salt rejection properly due to the high compatibility and proper dispersity. Therefore, in order to find the best RO performance and study the optimal loading, various $Ti_3C_2T_x$-TA nanosheets loading from 0 to 0.016 wt% were applied in the polyamide layer. Supplementary Tables and figures summarize AFM, SEM, WCA, FTIR, XPS, and performance results, respectively. **Figure 4-4b** obviously indicates that the water permeation of TFN($Ti_3C_2T_x$-TA) membranes improves considerably by increasing the concentration of $Ti_3C_2T_x$-TA nanosheets loading in the PA layer. After adding $Ti_3C_2T_x$-TA nanosheets from 0 wt% to 0.008 wt%, the resultant TFN membranes indicate noticeable increase in water permeation with almost the same salt rejection in the TFC membrane. However, with an additional amount of $Ti_3C_2T_x$-TA nanosheets (0.016 wt%) in the PA layer, although the rigidity of the PA network increased and the chain mobility and segmental motion decreased through more chemical attachment between nanosheets and the polymer, the salt rejection drastically decreased possibly due to the nonselective defect formation and possible macroscale aggregation of nanosheets. Also, the performance results of TFN membranes in **Table S0-9** reveals that for TFN ($Ti_3C_2T_x$) membrane, after 0.04 %wt loading of $Ti_3C_2T_x$ nanosheets, a significant rejection drop was observed, while for TFN ($Ti_3C_2T_x$-TA), after 0.08 %wt loading of $Ti_3C_2T_x$-TA nanosheets, a smooth drop was detected. Therefore, modification of $Ti_3C_2T_x$ MXene nanosheets by TA enables us to incorporate higher amount of nanofillers in the PA selective layer due to the better dispersion and compatibility of $Ti_3C_2T_x$-TA nanosheets in comparison to pristine $Ti_3C_2T_x$ MXene nanosheets in the selective PA layer. According to the results, the TFN membrane with 0.008 wt% loading of $Ti_3C_2T_x$-TA nanosheets was selected as the best TFN membrane for further investigation.

The performance of the best TFN membranes in this research was compared with the commercial membrane (TriSep ACM2) as a benchmark. The commercial RO membrane revealed salt rejection of 95.5% with a water permeance of 2.2 $L.m^{-2}.h^{-1}.bar^{-1}$ in a dead-end mode test (P=20 bar, T=25 ˚C, Feed= 2000 ppm NaCl solution) while our best TFN membranes indicates roughly better performance (96%, 2.4 $L.m^{-2}.h^{-1}.bar^{-1}$). Also, **Figure S0-12** shows a comparison of this study with some of the previously reported TFN membranes from literature. TFN membrane at a low loading of $Ti_3C_2T_x$-TA nanosheets is within the range of or better than performance of most of the literatures. Therefore, utilizing $Ti_3C_2T_x$-TA nanosheets is considered as a proper select for the fabrication of TFN membranes with desirable performance.

4.3.5 Fouling

Fouling has historically been a bottleneck limiting the efficiency of the RO processes by degrading water quality, decreasing water flux, and rising energy usage[217]. The main reasons of fouling are related to adsorption and build-up of foulant on the surface of membrane through hydrophobic interactions, and van der Waals and electrostatic forces [218]. The **Figure 4-4c** indicates the antifouling properties of TFN ($Ti_3C_2T_x$-TA-008) and TFC membranes by FRR and R_t index which were calculated after adding the BSA as a foulant. Here, high fouling resistance is expressed in a high FRR and low Rt. The TFN ($Ti_3C_2T_x$-TA-008) membrane revealed higher flux recovery ratios and lower total flux decline ratio (FRR ~ 93%, R_t ~ 12%) in comparison to TFC membrane (FRR ~ 82 % and Rt ~ 21%). The high fouling resistance of the TFN($Ti_3C_2T_x$-TA-008) membrane could be related to the incorporation of hydrophilic and strong negative charge $Ti_3C_2T_x$-TA nanosheets in the PA layer which are confirmed by WCA and zeta potential analyses. The hydrophilicity could reduce the interaction among the membrane and foulants by boosting the hydration on the surface of membrane. Moreover, the strong negative charge could reduce the chance of an adhesion impact by improving the repulsive force to foulants [218]. Therefore, owing to the highly negative charge, hydrophilicity and antifouling properties of $Ti_3C_2T_x$-TA nanosheets, functionalized RO TFN membrane by $Ti_3C_2T_x$-TA nanosheets could successfully diminish the adhesion and accumulation of foulants on the surface of membrane. It is worth noting that the suitable antifouling properties was achieved through dead-end filtration mode which is considered as a worst-case scenario. We expect that fouling resistance would be exceptional if cross flow filtration mode is used. According to the results, TFN ($Ti_3C_2T_x$-TA) membranes can offer not only greater volume of purified water during RO process, but also have a smaller level of fouling,

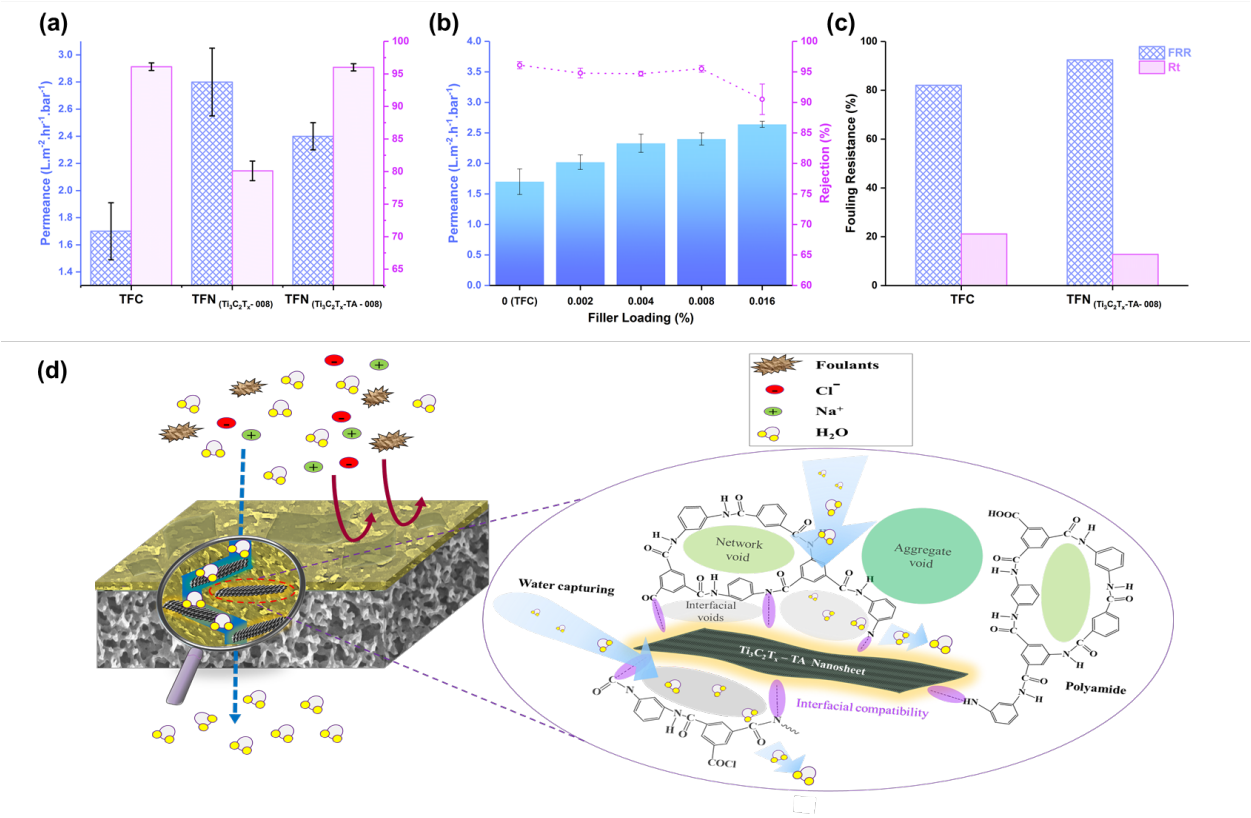

Figure 4-4. Membranes performance: (a) Comparison between RO performance of TFC, TFN($Ti_3C_2T_x$-008), and TFN($Ti_3C_2T_x$-TA-008) membranes, (b) optimization of $Ti_3C_2T_x$-TA loading, (c) fouling resistance to BSA for TFC and TFN($Ti_3C_2T_x$-TA-008) membrane in RO process, (d) Schematic of TFN($Ti_3C_2T_x$-TA) membrane and disruption of polyamide chain when $Ti_3C_2T_x$-TA nanosheets present in the top selective layer. $Ti_3C_2T_x$-TA is chemically compatible with PA matrix due to high interfacial interaction.

which can consequently decrease the membrane cleaning cycles and enhance the membrane lifespan for the industrial applications.

4.4 Conclusion

In summary, $Ti_3C_2T_x$ MXene nanosheets were successfully modified by tannic acid through facile, cost-effective, green, and robust self-polymerization method. The TA coating layer improved the chemical stability, oxidation resistance, processability, compatibility, and dispersity of $Ti_3C_2T_x$ nanosheets in the aqueous solution and polymer matrix due to the highly negative charge and hydrophilic functional group of TA. In this work, for the first time, the TFN membranes were fabricated by embedding the

$Ti_3C_2T_x$-TA nanosheets into the PA selective layer via interfacial polymerization for RO application. The importance of the role of TA and different loading of $Ti_3C_2T_x$-TA nanosheets on structure, chemistry, and performance of membrane were investigated. At the loading of 0.008 %wt of $Ti_3C_2T_x$-TA nanosheets, the TFN membrane indicates the optimal RO performance; simultaneously the permeability increased 1.4 times (2.4 $L.m^{-1}.h^{-1}.bar^{-1}$), the NaCl rejection was well maintained (~96%) and the fouling resistance improved compared to pristine TFC membrane. The $Ti_3C_2T_x$-TA nanosheets are more appropriate for the functionalization the PA selective layer compared to the pristine $Ti_3C_2T_x$ nanosheets. This is attributed to the favourable dispersion and incorporation of hydrophilic $Ti_3C_2T_x$-TA nanosheets, and promising compatibility among PA matrix and $Ti_3C_2T_x$-TA nanosheets, which leads to the selective interfacial pathways and adequate expansion of internal voids within the PA membrane. Therefore, the simple self-polymerization of TA, open a practical strategy for potential using the modified $Ti_3C_2T_x$ nanosheets for the scalable polymer nanocomposite implication. The beneficial properties of polymer nanocomposite containing modified MXene nanosheets ($Ti_3C_2T_x$-TA) including antioxidant and antibacterial properties can be practical for the development of efficient and high-performance membranes for ion separation and other application.

Chapter 5: **Nanoscale architecture of thin film composite membrane through interlayered GONR: filling two needs with one deed**

5.1 Introduction

The daunting worldwide water crisis has forced water resources management to implement an effective solution to provide sufficient clean water beyond the hydrological cycle[2,219]. In recent decades, enormous efforts have spent to develop efficient water treatment technologies to generate fresh water through wastewater reuse and desalination[2,220]. Membrane-based processes, such as reverse osmosis (RO) and nanofiltration (NF) are the most efficient and mature techniques among all existing water treatment technologies[19,26]. Polyamide-based thin film composite (PA-TFC) membranes, initially fabricated by interfacial polymerization (IP) by Cadotte in the1970s[5], are the most common commercial type for RO and NF applications[35]. It has been verified that overcoming the permeability and selectivity trade-off relationship of TFC membrane, which is restricted by the intrinsic structure and properties of the dense selective layer, result in a reduction in the capital cost, energy consumption, and footprint of RO and NF processes[28,221]. Therefore, extensive research has been focused on different strategies such as using various additives (salts[43], surfactants[42], co-solvents[222,223], and so on) in monomer solution, 3D printing[40] and electro-spraying [224] process, molecular layer-by-layer method [39,225], and incorporation nanomaterials[54,59,60,226–228] as an interlayer or fillers to obtain the desired structure beyond the PA framework and optimize the IP reaction to attain tailored selective layer features toward both rapid water transport and superior rejection[19,35].

Among the different strategies, the template method and designing of the novel IP platforms have recently received significant interest as powerful and practical approaches to efficiently improve the permselectivity of the membrane[19,21,229]. Livingstone et al.[9] pioneered the template method by applying a sacrificial layer of a cadmium hydroxide nanostrand as a hydrophilic and porous template to regulate the IP reaction rate and thereby generate an ultrathin high performance PA nanofilm with thickness of 8 nm. Later, inspired by this approach, researchers started using various interlayers or sacrificial templates such as, two-dimensional NaCl fractal nanocrystals[230], spherical polyamide dendrimer porous layer[231], amphiphilic metal-organic framework nanoflakes[227], MXene[60], MWCNTs[59], MOF[232,233], ZIF-8[54], MoS_2 [234], microporous organic nanotube[226], COF[74], GO[235], and tobacco mosaic virus porous protein nanosheet[81]. The IP template not only sometimes serves a direct role as a gutter layer [56,57] which prevents the growth of polyamide into the substrates thus reduces the hydraulic resistance and funnel effect[236] of the membrane, but also

has an indirect role on the morphology and properties of PA nanofilm by manipulating the IP reaction rate. The structure and chemistry of the IP template regulate the uniformity of distribution of the monomers, adsorption and diffusion rate of amine monomers, the heat dissipation and interfacially degassed nanobubbles, and the formation of ridge-and-valley roughness and a crumple structure[19,37,229]. Therefore, choosing the appropriate structure and chemistry of IP template to optimize the IP reaction properly and manipulate the structure and properties of PA layer, including thickness, roughness, charge density and pore size (free volume) distribution and crosslinking degree, is challenging. Also, it is important to improve our understanding of the template on the TFC-PA membrane properties and transport behavior.

Graphene oxide nanoribbons (GONR) with their unique one-dimensional structure and plentiful oxygen-containing functional groups have attracted considerable attention for nanocoating[237], fiber formation[238], and membrane fabrication as an interlayer[239] or selective layer[240,241]. Inspired by their potential for interfacial properties tuning and separation application, for the first time, we have developed a novel IP template, GONR ultrathin network, to act simultaneously in response to two needs including minimizing the funnel effect and mediating the IP reaction toward desired PA properties. The coated GONR template not only efficiently serves the gutter layer role, but also properly regulates the adsorption and transport of amine monomers at the interface of GONR by manipulating electrostatic interaction, capillary rise, and nanoconfinment of IP template by different loading of GONR. The optimized loading of GONR at 0.02 $g.m^{-2}$ results in a desired hybrid GONR/PA TFC NF membrane with nanostriped crumple structure beyond the PA context, ultrathin PA nanofilm with a thickness of 15 nm, and a narrow pore size distribution and high crosslinking degree of 80% that simultaneously improves the permeability and selectivity, and successfully passes the upper bound trade-off with permeance of 21.3 $L.m^{-2}.h^{-1}.bar^{-1}$ and rejection of 98% for Na_2SO_4 under 5 bar of pressure. This research provides a new understanding of the advantage of template method through an optimized coated of GONR ultrathin network to make a desired selective TFC membrane for more affordable and efficient water purification and ion separation processes.

5.2 Materials and Methods

5.2.1 Chemicals

PES support layer (effective pore size 0.1 μm) was purchased from Sterlitech Co (WA, USA). The MWCNT powder (OD: 20–30 nm, length: 10–30 μm, and an average surface area of 110 $m^2 \cdot g^{-1}$) utilized in this research was purchased from Cheap-Tubes Inc. The chemicals, anhydrous piperazine (PIP, 99%), trimesoyl chloride (TMC, 98%), anhydrous n-hexane (≥95%), hydrochloric acid (HCl), hydrogen peroxide (30%), phosphoric acid, sulfuric acid, potassium permanganate, sodium dodecyl sulfate (SDS) and dimethyl formamide (DMF) were acquired from Sigma-Aldrich. All the above-mentioned membranes and chemicals were used as received.

5.2.2 GONR synthesis

Graphene oxide nanoribbon (GONR) was produced using an improved version of the Hummer's method developed by James Tour and colleagues [242], which involved oxidative unzipping of multi-walled carbon nanotubes (MWCNTs). The process began by stirring 2 g MWCNTs in a mixture of sulfuric (360 ml) and phosphoric (40 ml) acids for 1 hour in an ice bath. 10 g potassium permanganate was then added gradually over 30 minutes, and the mixture was heated to 65°C and stirred for an additional 5 hours. The mixture was then cooled and mixed with 400 ml ice including 20 ml hydrogen peroxide and allowed to precipitate over 24 hours. The supernatant was separated and mixed with 400 ml hydrochloric acid (5%v/v), and the resulting solution was centrifuged and washed with hydrochloric acid (5%v/v) three times. The resulting slurry was placed in a dialysis tube until the pH reached between 6 and 7, and the resulting GONR solution was freeze-dried to obtain a GONR powder. (**Figure 5-2a**)

5.2.3 GONR interlayer coating onto PES substrate

A commercial polyether sulfone (PES) support was used as a substrate for the polyamide membrane. Solution of GONR dispersion was prepared by adding and sonicating 17.67 mg GONR powder in 20 mL of DDI water for 2 h. The interlayers were prepared by vacuum filtration selected amount of the GONR on the PES substrate membranes with filtration area of 14.41 cm^2. To form a uniform stable GONR layer, the dilution and exfoliation of GONRs was critical since GONRs can form aggregated particles and bundled scaffolds at high concentration[239,240]. After vacuum filtration for 15 h, the membrane was dried in oven at 60 °C for 30 min to remove excess water. Then the membrane was washed in ethyl alcohol for 15 min and then dried before further use. The PES/GONR templates were

denoted as PES-GONR-005 to PES-GONR-08. The number at the end is the concentration of GONR solution ($g.L^{-1}$), for example 005 corresponds to 0.005 $g.L^{-1}$.

5.2.4 Fabrication of polyamide selective layer on the IP template

The fabrication of the polyamide layer on the GONR network membrane was carried out by interfacial polymerization, using the GONR network membrane as the IP template. The reaction was conducted at room temperature. Prior to the reaction, solutions of PIP in water with a concentration of 0.25% (w/v) and TMC in n-hexane with a concentration of 0.2% (w/v) were prepared. The GONR-coated PES membrane was placed on a glass plate and the PIP solution was applied to the membrane surface for 1 minute. The excess PIP solution was then removed, and the membrane was left to sit at room temperature for 10 minutes. The TMC solution was then applied to the GONR membrane surface for 30 seconds. The excess TMC solution was then removed and the GONR network membrane was washed in n-hexane for 30 seconds and dried at 60°C for 30 minutes. The resulting polyamide membrane was stored in water at room temperature. The post-solvent-washing step removed any unreacted TMC from the surface of the nascent nanofilm and prevented further growth of the nanofilm during the post-heating process, which was necessary to achieve the desired cross-linked structure. This step helped to design nanofilms with a controlled surface charge and produced the ultrathin separation layer of the composite membrane. The fabricated hybrid GONR/PA NF membranes are denoted iTFC-005 to iTFC-08 according to the IP template names. The number at the end is the concentration of GONR solution ($g.L^{-1}$) at the template.

5.2.5 Characterization

The surface topology and roughness of various membranes (PES, PES/GONR, PES/GONR/PA) were characterized by an atomic force microscope (Bruker Innova AFM, USA). The AFM images were captured at ambient condition under tapping mode (scan rate of 0.2-1 Hz, minimum resolution of 256 points per line) with a typical tip radius of 8 nm (RTESPA-CP). The membrane surface area (5 μm ×5 μm) were scanned more than three times. The Gwyddion and Nanoscope analysis software were applied to process the AFM images by leveling and eliminating the noise and calculate the roughness value. Surface roughness was presented as root-mean-square (Rq), and average roughness (Ra). To measure the thickness, free-standing nanofilms were transferred to a silicon wafer and dried. A scratch was made to expose the wafer surface and allow measurement of the height from the silicon wafer surface to the

upper nanofilm surface. Thickness of the nanofilm was estimated from the height difference between the silicon and the nanofilm using a one-dimensional statistical function.

Field emission scanning electron microscopy (SEM, LEO FESEM 1530) with a high accelerating voltage of 5 kV and 10 kV was conducted to observe the membrane surface morphology and cross-section. For the cross-sectional study, nanofilm/membrane were soaked in ethanol, freeze-fractured in liquid nitrogen and dried quickly under dry air. All of the samples were coated with a layer of gold under a nitrogen atmosphere to achieve a minimum conductivity for reliable information before FESEM observation. Also, the cross-sectional images of the membranes were investigated by transmission electron microscopy (TEM, Philips/FEI Morgagni 268, The Netherlands) at an acceleration voltage of 80 kV. Regarding the polymeric samples, the preparation protocol included first staining in uranyl acetate and lead citrate, then embedding in spur's resin, and finally sectioning using ultramicrotome (Reichert-Jung Ultracut E, USA). To analyze the microscopic images, ImagJ software was used to process the images and measure the average pore size, pore size distribution of surface and thickness of selective membranes.

The surface wettability of the fabricated membranes was evaluated by measuring the contact angle using Krüss DSA 100 (Krüss GmbH, Germany) and FTÅ200 (First Ten Angstroms, Inc.) instruments. A sessile drop of DI water was placed on the surface of the TFC membranes, and the static contact angle was measured. The contact angle was measured at 5 different locations on each sample in order to minimize the experimental error. A video contact angle measurement system (VCA-2500 XE, AST products, Billerica, MA) was used to evaluate the surface wettability of membranes at room temperature. For each sample, the dynamic contact angle was measured over a 60 second period.

The droplet, after contacting the membrane surface, typically is involved in a two-stage diminishing process: 1) rapid infiltration into the pores at the contacting interface, 2) gradual absorption into the entire membrane because of the capillary suction of the pores.

The surface (zeta) potential of membranes was measured using Surpass Electrokinetic Analyzer (Anton Paar). Rectangular clamp cell was used to fix the membrane sample. For each test, a membrane sheet (1×2 cm) was cut and attached onto a holder by water-repellant double-sided tape, followed by fixing into the rectangular clamp cell. The system was washed with enough amount of DI water prior to each test. The pH and conductivity were calibrated before each test. 50 mM HCl and NaOH solutions were used for titration to change the pH in the system. The zeta potential values were measured over a pH range 3-10 at 25 ˚C.

The chemical properties of membranes were analysed by Fourier transform infrared spectroscopy (Nicolet-670 FTIR, Thermo Fisher, USA) under the attenuated total reflectance (ATR) mode, with a resolution of 4 cm^{-1} in the range of 600-4000 cm^{-1} after 32 scans.

The elemental compositions (carbon, oxygen, nitrogen, sulphur) and bonding information of the top 1–10 nm of the membrane surface was measured by X-ray photoelectron spectroscopy (Kratos AXIS ULTRA spectrometer) equipped with a monochromatic Al Ka X-ray source. The source was run at a power of 210 W (14 mA, 15 kV) and a hybrid lens with a spot size of 700 µm × 400 µm. Survey spectra were collected with a pass energy of 160 eV, step size of 0.4 eV, and sweep time of 100 s in the range of 0–1100 eV. High resolution spectra for C, O and N elements were collected with a pass energy of 20 eV, step size of 0.1 eV, and sweep time of 200 s.

5.2.6 Calculation the crosslinking degree of polyamide membrane:

The cross-linking degree of an interfacially polymerized PA film can be determined using the N S1and O S1 components of the photoemission spectrum with the following equations:

$$\frac{O}{N} = \frac{3n + 4m}{3n + 2m} \qquad \textbf{Equation 5-1}$$

$$Crosslinking\ Degree\ (\%) = \frac{n}{n+m} * 100\% \qquad \textbf{Equation 5-2}$$

where n and m are the fractions of cross-linked and linear parts of the PA film calculated based on the oxygen-to-nitrogen ratio (O/N) obtained from the XPS. Theoretically, the O/N ratio can indicate the level of crosslinking in a polymer film. A ratio of 1.0 corresponds to a fully cross-linked structure ($C_{18}H_{12}N_3O_3$, n=1 and m=0), while a ratio of 2.0 corresponds to a fully linear structure ($C_{15}H_{10}O_4N_2$, n=0 and m=1).

5.2.7 Determination of the capillary rise:

The modified Lucas-Washburn equation [243]was used to calculate the capillary rise (h) as a function of time for the solution in the porous media:

$$\frac{dh}{dt} = \frac{P_c r^2}{8\mu h} \qquad \textbf{Equation 5-3}$$

where r is the pore radius, μ is the liquid viscosity (1.0016 mPa.S at 20˚C) and P_c is the capillary pressure that can be calculated using the Young-Laplace equation[243]:

$$P_c = \frac{2\sigma cos\theta}{r}$$ **Equation 5-4**

where σ is the liquid surface tension (72.8 mN/m for water at 20 ˚C) and θ is the contact angle. When applied to pores such as those in the PES membrane and GONR network, the tortuosity factor (τ) should be taken into account. Therefore, the modified Lucas-Washburn equation becomes[243]:

$$h(t) = \sqrt{\frac{r\sigma cos\theta}{4\tau^2\mu}t}$$ **Equation 5-5**

For the capillary channels in the PES and PES/GONR template, θ is measured by contact angle test , τ is calculated through following equation[244]:

$$\tau = \frac{(2-\varepsilon)^2}{\varepsilon}$$ **Equation 5-6**

where ε is porosity of membrane and calculated based on the following equation[244]:

$$\varepsilon\ (\%) = \frac{W_w - W_d}{V} * 100$$ **Equation 5-7**

where W_w and W_d are the weight of wet and dry membranes (g), respectively; V= A*L, where A is the membrane surface area (cm^2), and L is the thickness of membrane (cm).

5.2.8 Pore size distribution and molecular weight cut-off (MWCO) calculation of TFC membrane

The pore size distribution of TFC membranes was determined by the rejection test using a cross-flow testing cell with an effective area of 18.5 cm^2, and a feed solution containing 200 ppm neutral organic solutes PEG with different molecular weights (MWs) (200, 300, 400, 800,1000 Da). TOC analyzer (Shimadzu, model TOC-V; detection range 3-25000 mg/L) was used to measure the amount of total organic carbon in the permeation and feed phases. Then, the PEG rejection was calculated by the following equation:

$$R = \left(1 - \frac{TOC_{permeation}}{TOC_{feed}}\right) * 100\%$$ **Equation 5-8**

The Stocks diameter (ds, m) of a PEG molecule can be calculated based on its molecular weight (MW, Da) using the following equation:

$$d_s = 33.46 * 10^{-12} * MW^{0.557}$$ **Equation 5-9**

To obtain information about the pore size distribution of TFC membranes, a log-normal probability plot was drawn by plotting the solute rejection against the PEG Stokes diameter. The best-fitting straight line and corresponding linear equation were obtained through curve fitting.

From this equation, the mean solute size (u_s) could be obtained when R=50%, and σ_g (geometric standard deviation of u_s) was determined from the ratio of d_s at R=84.13% and 50%. It is assumed that the steric and hydrodynamic interactions between the solute and the pore size can be ignored, the mean pore size (u_p) and the σ_p (geometric standard deviation about u_p) were the same as u_s and σ_g, respectively. The pore size distribution can be represented by the following probability density function:

$$\frac{dR(d_p)}{dd_p} = \frac{1}{d_p ln\sigma_p \sqrt{2\pi}} exp\left[-\frac{(\ln d_p - ln\, u_p)^2}{2(ln\sigma_p)^2}\right] \quad \textbf{Equation 5-10}$$

5.2.9 Nanofiltration performance

The NF performance of TFC membranes was tested utilizing a cross-flow set-up (Sterlitech Corporation, USA), which consists of a feed tank, membrane cell, diaphragm pump (Hydra-cell), temperature control system (ISotemp 3013, Fisher Scientifics), pressure regulator (Swagelok), and data collection software. The data were collected using a digital weighing balance (Mettler Toledo) and LabView software (National Instruments). The cross-flow setup, as shown in Figure S0-13, is designed to measure the permeate flow rate and control the temperature, pressure, and flow velocity of the feed solution.

First, the membranes were compacted under 6 bar at 25 C for 1 h, and then, the filtration tests were conducted at a trans-membrane pressure of 5 bar and at a feed flow rate of 2 L.min^{-1}. corresponding to a constant cross-flow velocity of 0.25 m/s and a laminar crossflow Reynolds number Re=730.

To calculate the pure water permeance (A, L.m^{-2}.h^{-1}.bar^{-1}), the weight of water (Δm) passing through the effective surface area of the membrane (A_m) at a specific temperature, pressure (ΔP), and time (Δt) was measured as follows:

$$A = \frac{\Delta m}{A_m . \Delta t . \rho . \Delta P} \quad \textbf{Equation 5-11}$$

where ρ is water density. To test the salt rejection of the membrane, inorganic salt solutions (Na_2SO_4, $MgSO_4$, $MgCl_2$, $CaCl_2$, and NaCl) with a concentration of 1000 ppm were utilized separately as the feed. Apparent salt rejection was calculated by measuring the salt concentration in permeate solution after 3 h filtration of 1000 ppm salt solution at 22 ˚C as follows:

$$R\ (\%) = \left(1 - \frac{C_p(\sigma_p)}{C_F(\sigma_F)}\right) * 100$$ **Equation 5-12**

The concentration of salt in feed (C_f) and permeate (C_p) were determined by using a bench conductivity meter (Hanna HI 8733), respectively, measured after 1 h filtration process. The conductivity ratio between that of the permeate solution (σ_p) and that of the feed solution (σ_f) determined the salt rejection. To evaluate the long-term stability of the NF membrane, a cross-flow test was conducted using a 2000 ppm Na_2SO_4 solution as the feed. The pressure was kept at 5 bar for a duration of 12 hours. The membrane permeance and rejection were tested at intervals of 1 hour to assess the stability of the membrane over time. Also, to further test the stability, NF membranes were evaluated under different applied pressure of 1 to 6 bar.

The water permeance of substrate (PES, PES/GONR) membranes was measured by using a dead-end filtration setup (Sterlitech HP4750 Stirred Cell) at ambient temperature and pressure (ΔP) of 1 bar.

Each membrane was tested for at least three times to report the average water permeance and salt rejection, while the standard deviation are represented by the error bar.

5.2.10 Molecular dynamic simulation methods

The molecular simulation has been conducted by applying Materials Studio software. All calculations were conducted using periodic boundary conditions and COMPASS [245] force field was used to determine partial charges and interatomic interactions for all calculations including energy minimization and dynamic runs. The molecular cutoff distance was set to 10 Å and electrostatic interactions were taken into account by the Ewald summation method with an accuracy of 10^{-4} kcal/mol. All simulations aimed at the diffusion coefficient and intermolecular interactions of PIP monomers to make the role of GONR clear in interfacial polymerization reaction.

In the first step, two simulation cells attributed to aqueous and organic phases were constructed. The aqueous simulation cell was consisted of 400 water molecules and 7 PIP monomers while the organic simulation cell constructed by 62 hexane molecules. After geometry optimization, a 100 ps dynamic run was performed under NPT ensemble (at 293 K and 1 bar) for each cell to achieve equilibrium density. The final densities of the aqueous and organic phases were obtained 0.964 and 0.659 g/cm^3, respectively. Also, to elucidate the role of GONR in the interfacial polymerization reaction, another aqueous simulation cell was prepared by adding one GONR particle to previous aqueous cell which increased the final density to 1.08 g/cm3. Afterwards, a simulation cell with 23.78 Å × 23.78 Å × 59.26 Å size for hexane-water system and a simulation cell with 23.78 Å × 23.78 Å × 58.72 Å size for hexane-

water -GONR were prepared. In the next step, the new simulation cells were relaxed by 100 ps run NPT ensemble at 293 K and 1 bar and then 3000 ps run was performed under NVT ensemble at 293 K to calculate the diffusivity of PIP monomers. The diffusion coefficient (D) of monomers was estimated using mean square displacement (MSD) calculation and Einstein's equation as follows:

$$MSD(t) = \frac{1}{N}\sum_{i=1}^{N}\left[r_i(t) - r_i(t_0)\right]^2 = A + 6Dt \qquad \textbf{Equation 5-13}$$

It is important to highlight that the last 500 ps were ignored in the diffusion coefficient calculation due to the fluctuations in this period of time.

Also, the energy of intermolecular interaction between PIP molecules and the other parts of the system (including GONR, water, and hexane molecules) was calculated by conducting an energy analysis of of the final molecular configuration (last snapshot) as follows:

$$E_{\text{int}eraction} = E_{System} - \left(E_X + E_{PIP}\right) \qquad \textbf{Equation 5-14}$$

where E_{System} is the total energy of the system, E_{PIP} is the energy of PIP molecules while the other part of the system had been removed, and E_X is the energy of the other parts of the system while PIP molecules had been omitted.

5.3 Results and discussion

Graphene oxide nanoribbon, a new one-dimensional carbon-based building block with a high aspect ratio and narrow width has a structure combines aspects of both carbon nanotubes (CNTs) and graphene oxide[246]. Due to the structure of the GONR network and its polar properties, this unique IP template provides a confined space[78] and modulated electrostatic[247] interfacial polymerization reaction. The confined structure of GONR network not only plays a role as a gutter layer to prevent the formation of polyamide film inside the pores of substrate, but also tunes the selective layer structure and properties by manipulating and limiting the transport of amine monomers through the interlayer nanocapillary channels and free volume between the loosely stacked nanoribbons facing the organic phase. Moreover, the modulated electrostatic interaction regulates the absorption and diffusion of available amine for the interfacial polymerization through the interaction between amine monomers and COOH and other oxygen functional groups at the edge and basal plane of the nanoribbons as later confirmed by MD simulation. Overall, the presence of such a unique IP template results in an ultrathin and dense hybrid GONR/polyamide selective layer with nanostripe-like structure.

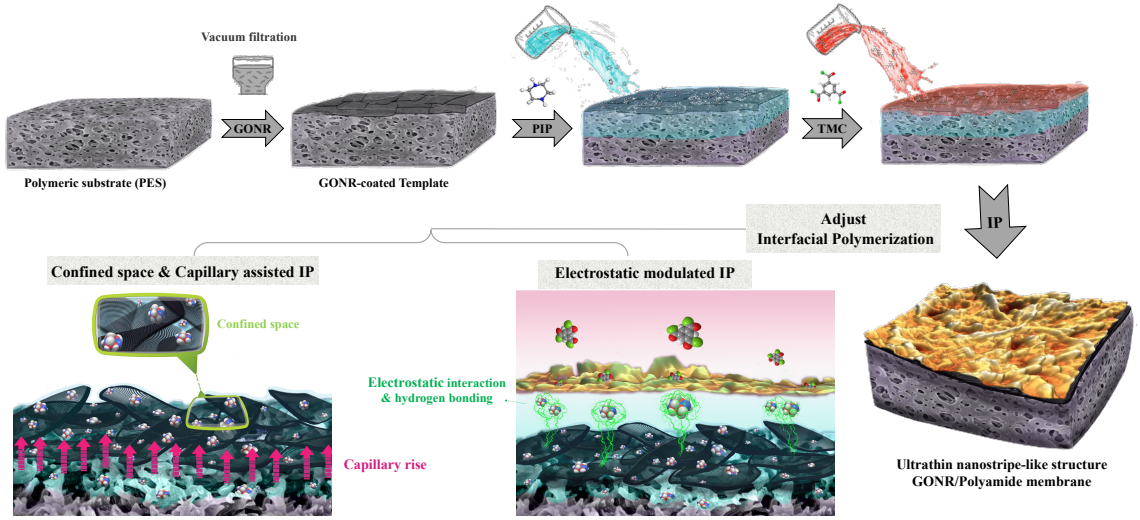

Figure 5-1. Schematic of the procedure for fabricating the ultrathin nanostripe-like structure of hybrid GONR/Polyamide membrane; schematic of the IP process, which is tuned by confined space and capillary assisted IP, as well as electrostatic modulated IP.

5.3.1 GONR characterization

The size of GONR was characterized by FESEM and high-resolution TEM. As **Figure 5-2(d-g)** shows, the tubular structure of MWCNTs with 20-30 nm diameter, properly are longitudinally unzipped and form a ribbon-like structure with the average width of 75 nm. The 2D narrow stripes of graphene oxide sheets have a width of 60-100 nm and a length of 5-15 µm. Also, the FTIR and Raman spectra **(Figure 5-2 b, c)** confirm that a successful oxidation of the sp^2 carbon regions of the MWCNTs and formation of GONR have occurred. Due to the carbon-only structure of MWCNT, no peak for a functional group appears in its FTIR spectrum, while several absorbance peaks related to oxygen-containing functional groups (including epoxy, carboxylic, and hydroxyl groups at 1049, 1733, 3387 cm^{-1}) which might be along the edge of the nanoribbon appear in the spectrum for hydrophilic GONR. Raman spectra, which provide a chemical fingerprint for carbonaceous materials, exhibits three characteristic peaks for graphene oxide nanoribbons (**Figure 5-2c)**. The G peak at approximately 1580 cm^{-1} is attributed to the presence of sp^2-bonded carbon atoms and provides a measure of the degree of graphitization or ordering. The D peak at approximately 1350 cm^{-1} is attributed to the presence of defects and structural disorder and is used to measure the level of defects or disorder. The 2D peak at approximately 2680 cm^{-1} is attributed to the presence of sp^2-bonded carbon atoms and is used to determine the number of layers and the thickness of the individual layers[248]. The I(D)/I(G) ratio is a

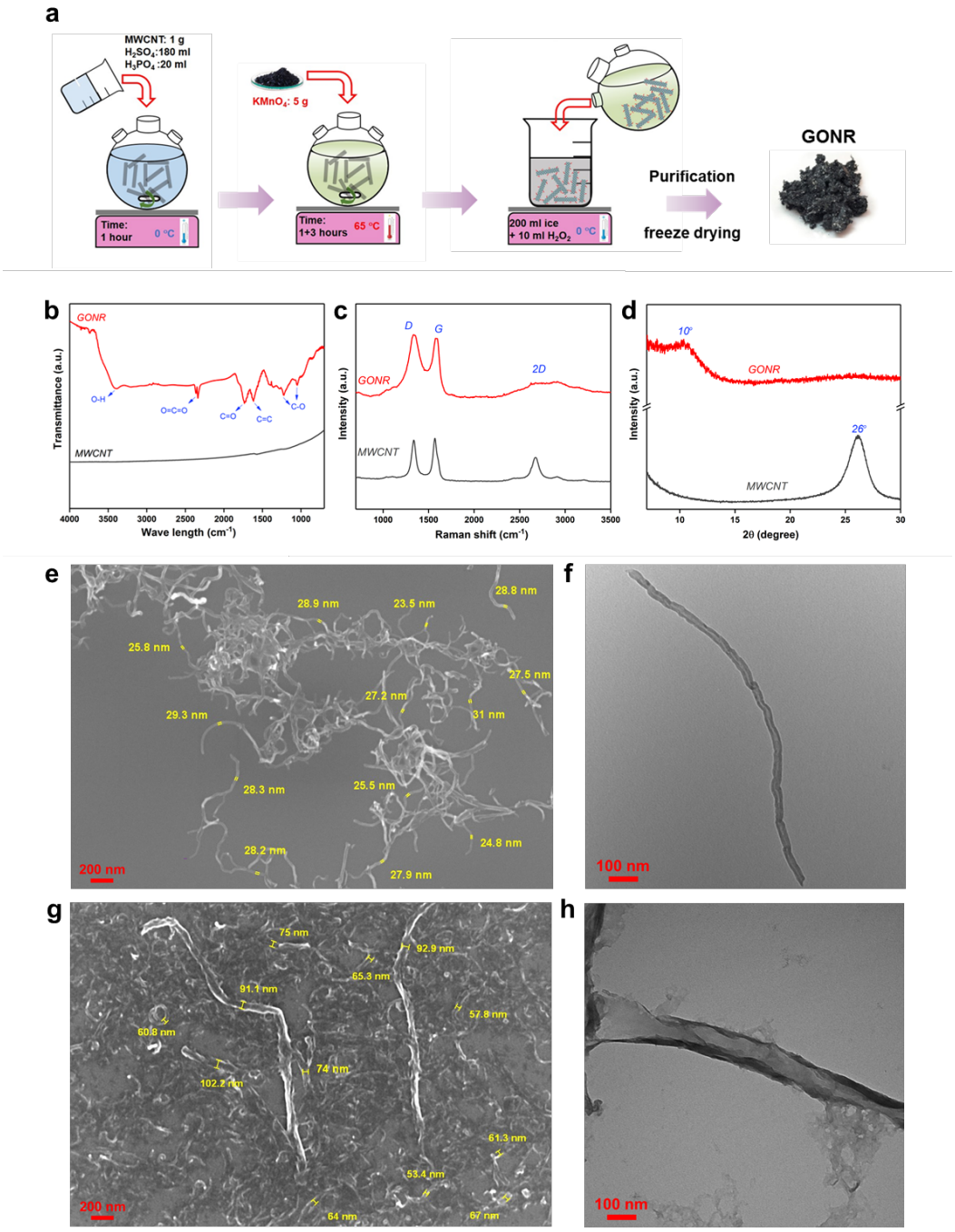

Figure 5-2. (a) Procedure of oxidative longitudinal unzipping of MWCNTs; Characterization of GONR and MWCNTs; (b)FT-IR spectra, (c) Raman spectra, (d) XRD pattern, (e) and (f) SEM and TEM images of MWCNTs, and (g) and (h) SEM and TEM images of GONR.

common ratio used to measure the degree of defects or disorder in the material[248,249]. After oxidizing and transforming MWCNT to GONR, as **Figure 5-2c** reveals, the I(D)/I(G) ratio increases from 0.95 (for MWCNTs) to 1.04 (for GONRs) due to the higher number of defects and disorder present in GONR. Also, wider G and 2D bands in the Raman spectrum for GONR, corresponding to the development of the sp^3 carbon bonding, indicates the presence of structural defects or disorder [250]. Therefore, the Raman spectrum confirms the unzipping of MWCNT with significant decrease in the purity of MWCNT. Moreover, XRD patterns (**Figure 5-2d**) shows that the crystal structure has transformed from MWCNT to GONR. For the MWCNTs, a large peak appears at 26˚ related to the interlayer spacing of MWCNT. While the GONR sample exhibits a broad peak from 8˚ to 12˚, relating to the broad range of interlayer spacing of stacked GONR. The entangled thin multilayered structure of the graphene oxide nanoribbon with abundant oxygen groups at the edge and basal planes serves as a highly permeable gutter layer that provides a tunable template for the interfacial polymerization (IP) reaction.

5.3.2 Structure and properties of the IP template

It is well-known that the IP template properties such as pore size, pore density, wettability, surface charge, chemistry, uniformity, and morphology, not only can play a role in the membrane performance, but also can impact the amine molecule distribution and absorption, further change the diffusion-reaction rate, and IP condition and result in the formation of a polyamide nanofilm[19,21,229,251]. Here, we discuss the influence of GONR loading on the PES substrate properties and further its impact on the IP and polyamide hybrid nanofilm formation in the presence of low concentration of monomers. As top-view SEM and AFM images of substrate surface show in **Figure 5-3(b, c, and d)**, the morphology and roughness of PES substrate were significantly influenced by coating of the GONR. A low loading of GONR (0.005 to 0.02 $g.m^{-2}$) results in the formation of an incomplete, dispersive and stripe-like GONR interlayer while a high loading (0.04 to 0.08 $g.m^{-2}$) causes the formation of plate-like GONR bundles and complete coverage on the surface of PES substrate. To study the influence of GONR on the morphology of substrate, the surface pore size and pore density of GONR/PES substrate surface have been determined by measuring the diagonal distance of the pores shown in the SEM images. As shown in the **Figure 5-3** and **Figure S0-14**, an increase in the loading of the GONR reduces the mean surface pore size from 116 nm to 23.98 nm and decreases the surface pore density.

The loading of GONR also leads to a smoother GONR/PES substrate, since many nanoribbons are deposited in the support pore and on its top surface. As shown in **Figure 5-3(c and d)** and **Table 5-1**,

the arithmetical mean roughness (Ra) declines from 57.9 nm for pristine PES to 31.2 nm for PES-GONR08.

Although narrow GONRs in comparison with other 2D barrier materials such as graphene oxide and graphene are more permeable [252,253], a thick and compacted plate-like GONR layer could produce a considerable resistance for water molecules. Therefore, as the loading of GONR increases, the surface pore size, surface porosity, and the surface roughness of the GORN/PES substrate decrease, producing thick and compact GONR layers. These changes in substrate morphology leads to a gradual reduction of water flux to 500 $L.m^{-2}.h^{-1}.bar^{-1}$ for the PES-GONR08 substrate (**Table 5-1**).

The wetting behavior of substrates is vital for a uniform and complete IP reaction to improve the quality of the polyamide layer. The high wettability of the substrate (small water contact angle and fast spreading of water droplet on the surface) is beneficial since it means that the substrate can uniformly and easily absorb aqueous amine solution and provides suitable template for a uniform amine monomer distribution. **Table 5-1.** Surface pore size, roughness, contact angle and pure water flux of PES-GONR indicates the average water contact angle (WCA) of the GONR/PES substrate at various loadings of GONR. It can be seen, after GONR loading, the initial WCA of substrate decreases from 70˚ for the pristine PES to 35˚ for the optimized loading (0.2 $g.m^{-2}$) of GONR. Then, with further increase of the concentration of GONR the WCA rises slightly to about 42-45˚, which could be related to lower roughness of substrate and smaller contact area, based on the Wenzel equation. In addition, after 5 seconds WCA (**Figure S0-17**) indicates the spreading and penetration of a water droplet becomes faster after loading the GONR. At optimized loading of GONR (0.2 $g.m^{-2}$), the after 5 seconds WCA decreases to 0˚, indicating that the water droplet has entirely diffused into the substrate. By raising the loading of GONR above 0.2 $g.m^{-2}$, a complete layer of GONR forms and the pores of the substrate becomes smaller (confirmed by SEM images **Figure 5-3b**). Thus, the gradual absorption step takes longer and rises to a higher value for the after 5 seconds WCA. This result confirms that the wettability of the PES-GONR template is better than that of pristine PES membrane, especially for the optimized loading of GONR due to the hydrophilic nature of GONR and introduction of abundant hydrophilic functional groups such as carboxyl and hydroxyl. In addition, such a sufficient contact between the template and the aqueous phase guarantees the controlled release of monomers, and effectiveness of electrostatic interaction between amine monomers and substrate during the interfacial reaction. Consequently, the quality of polyamide layer should improve.

Table 5-1. Surface pore size, roughness, contact angle and pure water flux of PES-GONR template.

Sample	GONR loading ($g.m^{-2}$)	Surface roughness (nm)	Average pore size (nm)	Water contact angle (°)	Pure water flux ($L.m^{-2}.h^{-1}.bar^{-1}$)
PES	0	57.9	116.23	70	3841.6
PES-GONR005	0.005	53.03	101.32	69	3633.1
PES-GONR01	0.01	49.66	74.08	60	3037.5
PES-GONR02	0.02	43.76	56.59	35	1435.4
PES-GONR04	0.04	40.99	46.32	42	973.8
PES-GONR08	0.08	31.23	23.98	50	500

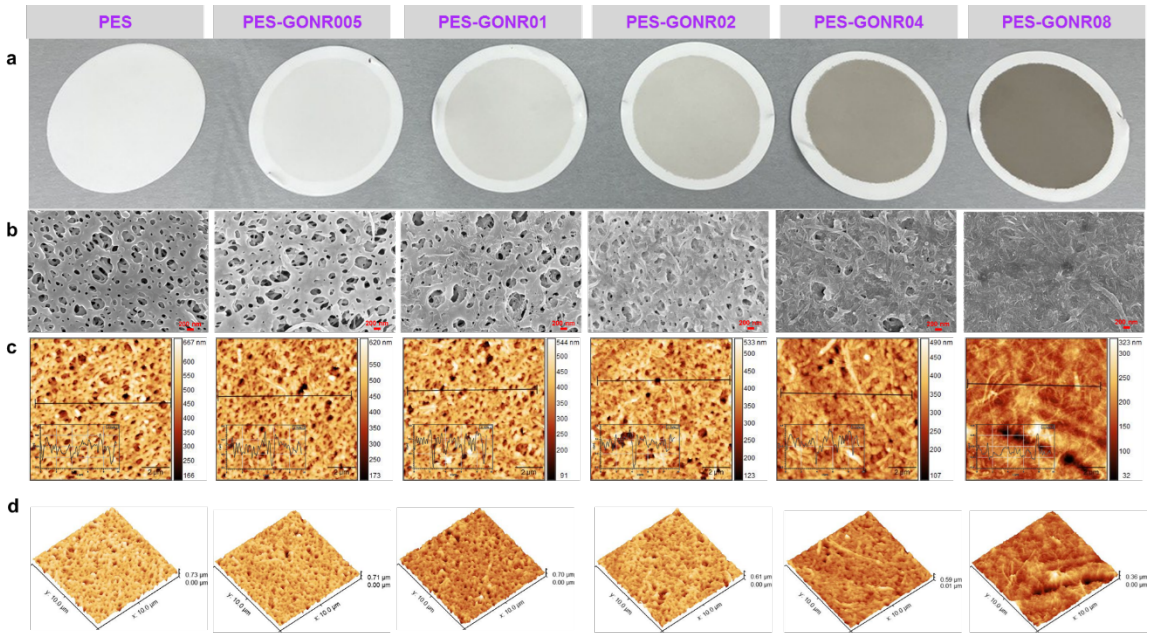

Figure 5-3. Morphology and structure of IP template (PES, PES-GONR005, PES-GONR01, PES-GONR02, PES-GONR04, PES-GONR08): (a) optical photograph, (b) top surface SEM images, (c, d) top surface topography 2D and 3D AFM images.

These results suggest that the properties of substrate and IP template could be manipulated precisely by loading various concentrations of GONR on the PES substrate. This is an advantage over the traditional support membranes which need complicated process to change their properties and structure.

5.3.3 Impact of GONR template loading on structure and properties of NF membranes

5.3.3.1 Structure and morphology

The varied properties of IP templates influence the structure and morphology of polyamide NF membranes. The impact of GONR template loading on the structure and morphology of PA membrane is studied in detail. **Figure 5-4** and **Figure S0-16** indicate the top and bottom surfaces, and cross-sectional morphology and structure of the selective layer in the TFC and iTFC NF membranes. Since low concentrations of PIP (0.25%, w/v) and TMC (0.2%, w/v) have been used for the IP process, an ultrathin continuous and roughly flat and thin PA selective layer with thickness below 40 nm has been achieved. Top surface SEM and AFM images of the TFC membrane (**Figure 5-4 a and b**) reveal that the PA layer on the pure PES substrate has a typical nodular structure and does not cover all surface pores of the substrate, but also forms inside some of the pores, as observed in the cross-sectional TEM and bottom surface AFM images (**Figure 5-4 d and e**). By increasing the GONR interlayer loading to 0.02 $g.m^{-2}$, IP template with mean pore size below 50 nm, yields a selective layer with more extensive stripe-like structure with fewer nodules shapes (**Figure 5-4 b and c**). a further increase of the GONR template loading to 0.08 $g.m^{-2}$, causes some of the larger stripes to merge together, forming wider interconnected stripes and cluster structure (**Figure 5-4 a, b**).

The bottom surface AFM images (**Figure 5-4e**) and cross-sectional TEM images (**Figure 5-4d**) and **Figure S0-16b** of the TFC and iTFC membranes clearly show the gutter layer role of GONR and the multilayered structure of the membrane, in which the presence of GONR on the PES substrate noticeably prevents the intrusion of PA inside the PES pores. As the GONR loading increases, a thicker and denser interlayer template with higher number of nanoribbons covers the PES pores, and as a result less polyamide forms inside the PES pores. The bottom surface morphology suggests that when the GONR layer becomes, thick PA forms inside and on top of the GONR network without penetration into the bottom, and the granular structure of bottom surface shifts to a stripe-like structure.

Also, the cross-sectional TEM images reveal that at low loading of GONR (0.005 g/m^{-2}), no clear interface between GONR and the PA layer appears, due to the low concentration of GONR layer. Instead, a hybrid structure similar to that of a TFN membrane involving a combination of polymeric network and nanoribbons forms. A further increase of the loading of GONR which leads to a dense and

confined network space, in addition to the hybrid structure of PA/GONR, this yields an ultrathin polyamide layer in the range of 10-30 nm on top of the hybrid PA/GONR layer (**Figure 5-4d**). The thinnest top selective layer belongs to iTFC02 which consists of hybrid part GONR/PA and pure polyamide layer on top with a thickness of 14.6±3.3 nm. The porous layer on the left side represents the PES substrate, the middle black line with a deep contrast reveals the GONR interlayer, and the thin layer with a light contrast on the right side is the polyamide layer (Figure S0-16. Morphology and structure of TFC and iTFC02 membranes: (a, d) SEM cross section, (b, e) TEM cross section, (c, f) AFM back side.). It is clear that the continuous GONR layer and confined polymerization guarantee that a continuous polyamide layer is firmly connected to the GONR interlayer without reaching into the expansive pores of the PES substrate.

With respect to surface roughness, as AFM images show (**Figure 5-4 b and c**), the iTFC membranes with different GONR templates, result in a rougher surface (~40 nm) in comparison to the pristine TFC membranes (~30 nm). By increasing the loading of GONR on the substrate surface, on the one hand, we obtain a smoother template surface; on the other hand, we have a denser and confined network available for the IP reaction. The dense interlayer with confined space and smaller pore size resists to air movement and retains the degassed nanobubbles formed on the aqueous solution side and prevents their escape through the bottom. This promotes the encapsulation of the gas bubbles by the polyamide layer and a rougher iTFC surface in comparison to that of pristine TFC membranes.

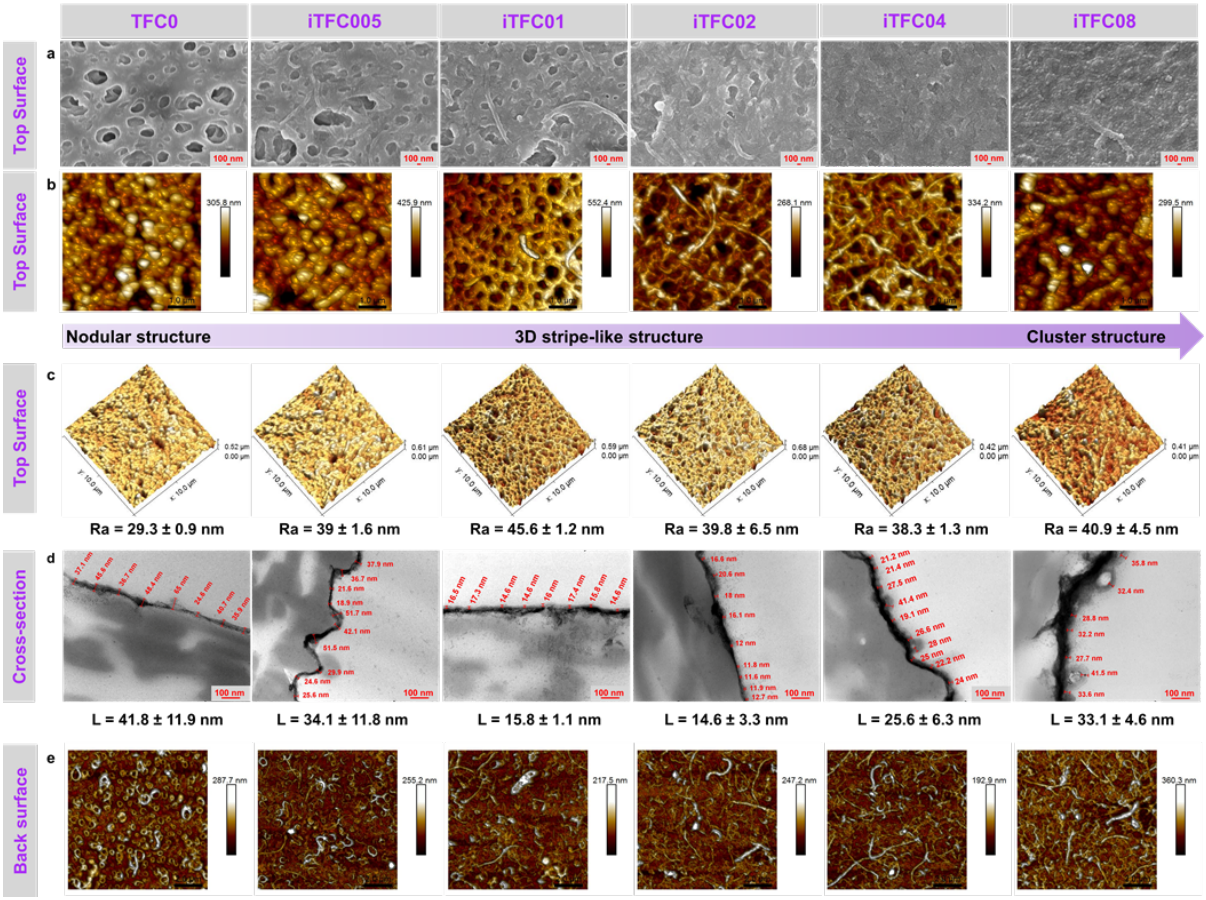

Figure 5-4. Morphology and structure of TFC and iTFC NF membranes with different loading of GONR template: (a) top surface SEM images, (b, and c) 2D and 3D topography AFM images, (d) cross-sectional TEM images, (e) bottom surface AFM images of polyamide layer.

5.3.3.2 Chemistry and surface properties

Control of the kinetic of IP reaction not only affects the PA selective layer morphology, but also influences the surface properties and chemistry of the selective layer of the NF membrane. To evaluate the effect of GONR template on the structure of NF membrane, the pore size distribution, hydrophilicity, and surface charge properties, and crosslinking degree of iTFC NF membrane with selective hybrid polyamide/GONR nanofilms have been determined at different loading of the GONR template (0, 0.01, 0.02, 0.04 $g.m^{-2}$). As shown in **Figure 5-5**, iTFC NF membranes exhibit superior surface properties including greater hydrophilicity, negative surface charge, higher crosslinking degree, and lower (free volume) pore size distribution.

The surface chemical composition and crosslinking degree of the prepared NF membranes have been determined using XPS. **Figure 5-5a** indicates XPS survey spectra and crosslinking degree of the PA selective layer for TFC and iTFC NF membranes. The C1s, O1s, and N1s peaks which are characteristic peaks of the PA layer are observed in all membranes. The crosslinking degree increases from 50.15% for the pristine TFC membrane to 71.08%, 80.15%, and 82.51% for iTFC01, iTFC02, iTFC04 membranes respectively. The boosted crosslinking degree reflects the effectiveness of the interfacial reaction and is important for the selectivity of the NF membrane. Generally, a denser template blocks heat dissipation/transfer more effectively, which could enhance the transport of amine monomer toward the organic phase[233]. Also, the thicker GONR template increases the PIP absorption and concentration of amine monomer in the interfacial reaction zone. Those factors could promote the formation of a cross-linked PA network[233,247]. The crosslinking degree of iTFC04 does not significantly increase relative to that of iTFC02, possibly due to the fact that the rates of PIP monomer adsorption and transport are only slightly different in the two cases.

The hydrophilicity of prepared NF membranes is examined by water contact angle measurements. **Figure 5-5b** indicates that the iTFC membranes have smaller contact angle in comparison to the pristine TFC membrane. The hydrophilic GONR template leads to the formation of a thinner and rougher PA layer. It is confirmed that the surface roughness can amplify the hydrophobicity or hydrophilicity of the membrane based on Wenzel's equation[254]. Hence, rougher iTFC membranes slightly improve the hydrophilicity of the formed PA layer. Also, the thinner PA layer enhances water droplet penetration, due to the better hydrophilicity of the iTFC membrane.

The rejection of charged solutes, especially multivalent ions, is greatly affected by the membrane surface charge during the NF process[19]. Surface charge properties of TFC and iTFC membranes have been evaluated by zeta potential measurement. **Figure 5-5c** shows that all prepared NF membranes are negatively charged in the pH range of 3-9 with a similar trend, which could be result from the hydrolysis of remained acyl chloride groups on the membrane surface to carboxyl groups that have a propensity to deprotonate. By increasing the loading of GONR template, the zeta potential decreases from -19.5 mV for the pristine TFC to -27.8 mV for iTFC02 under a neutral environment. A factor contributing to this trend may be the exposure of the GONR of hybrid GONR/PA layer to the solution. The highly negative surface charge of the selective layer is beneficial to improve the rejection of negative di/multi valent ions via the Donnan exclusion effect.

The pore size distribution of a membrane is an essential element determining the separation effectiveness or selectivity by the size exclusion effect[19]. To calculate the pore size distribution and

molecular weight cut-off (MWCO) of the TFC and iTFC membranes, a series of neutral molecules (PEG) with different molecular weights (200 to 1000 Da) were used. As **Figure 5-5d** indicates, by increasing the loading of GONR template, the selective layer of NF membranes indicates a molecular weight cut-off (MWCO) reduction from 265 Da to 235 Da. Also, a sharper pore size distribution is achieved with a decline in the mean pore size from 0.24 nm for pristine TFC membrane to 0.21 nm for iTFC02, which is consistent with the increase in crosslinking degree and a denser and tighter PA network of selective layer in the presence of GONR template. Therefore, the iTFC membrane provides a more efficient size exclusion effect whereby hydrated ions are rejected.

Overall, regulating the IP reaction through the GONR template results in an ultrathin nanostrips selective layer, which offers a sharper pore size distribution with smaller mean pore size, higher crosslinking density, and more hydrophilic surface with a negative charge. The optimized loading of GONR template is of great importance to improve the performance of the formed NF membrane.

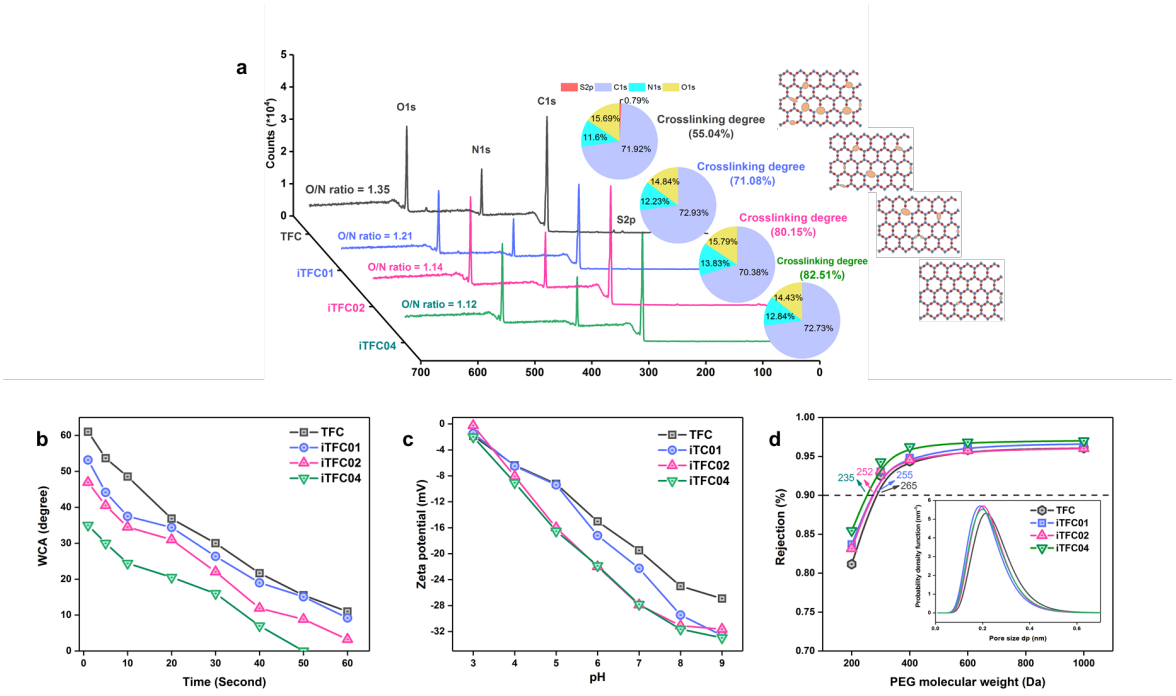

Figure 5-5. Chemistry and surface properties of TFC and iTFC NF membranes with various loadings of GONR template: (a) XPS spectra, O/N ratio, and crosslinking degree, (b) water contact angle, (c) zeta potential, (d) molecular weight cut-off (MWCO) and pore size distribution.

5.3.4 Separation performance of formed NF membranes

The separation properties of the prepared TFC and iTFC NF membranes has been investigated by separating various salt solutions containing Na_2SO_4, $MgSO_4$, $MgCl_2$, $CaCl_2$, and NaCl at concentrations of 1000 ppm in a cross-flow filtration configuration at a pressure of 5 bar. Furthermore, the relationship between the separation performance and selective layer properties is discussed.

5.3.4.1 Impact of GONR loading on NF membrane separation performance

The presence of GONR network templates on a PES substrate, positively influences NF membrane performance. **Figure 5-6a** presents the water permeability and Na_2SO_4 rejection of iTFC membranes with different loading of GONR in comparison to the pristine TFC membrane and DOW NF270 commercial membrane. By increasing the loading of GONR as a IP template, the iTFC membranes overcome the trade-off effect by improving the water permeance without sacrificing the salt rejection, and the rejection of Na_2SO_4 were above 97% for all membranes. The optimized iTFC02 membrane indicates more than 2 times water permeation compared with the traditional pristine TFC and NF270 commercial Dow membranes with a similar or higher Na_2SO_4 rejection. Based on the SEM, AFM, TEM images, and contact angles results, the increase in water flux of the iTFC with a hybrid PA/GONR selective layer is primarily related to the several desirable factors. Firstly, a reduction of the water-transfer resistance in NF membranes due to both the GONR gutter layer role, which minimizes the funnel effect of TFC membrane and prevents the formation of polyamide layer inside the PES pores, and the mediating role of GONR template in optimizing the IP process, which leads to a thinner selective layer. Secondly, the iTFC membranes have a higher effective surface area due to a rougher surface and formation of the 3D nano-striped structure of the selective hybrid GONR/PA layer. Thirdly, more hydrophilic selective layer properties and the presence of GONR water nanochannels inside the PA layer could also increase the tendency of water molecules to pass through the membrane faster. Further increase in GONR loading and forming a thicker template, leads to slight decrease of the water permeance, which could be due to the excessive stacking of the GONR layer, and thicker and denser selective layer.

For the salt rejection, the GONR IP template forms a selective layer with several desired characteristics. The crosslinking degree of the hybrid PA/GONR nanofilm, as determined by XPS measurements, is higher than that of the traditional polyamide nanofilm, which helps to improve salt rejection. The pore size distribution of the hybrid GONR/PA membrane shows that it has a smaller mean effective pore radius than that of traditional nanofilms, indicating that the hybrid PA/GONR nanofilm is more

effective at size-exclusion of ions and has a high salt rejection rate. The negative surface zeta potential of both the hybrid PA/GONR and traditional PA nanofilm also contribute to the charge exclusion effect on SO_4^{2-}, which further increases the salt rejection.

To further test the ability of the ultrathin hybrid GONR/PA membrane to separate ions, the iTFC02 membrane permeance and rejection of various monovalent and divalent salts at a concentration of 1000 ppm have been measured. The rejection ratio, as revealed in **Figure 5-6b**, decreases in the following order: Na_2SO_4 (98.2%) > $MgSO_4$ (91%) > $MgCl_2$ (74.4%) > $CaCl_2$ (70.2%) > NaCl (23.3%). The rejection results of the iTFC membrane provide further evidence of the synergistic effect of size sieving and strong Donnan exclusion. The Donnan theory predicts that the negative charges on the polyamide membranes due to deprotonation of residual carboxyl groups will repel high-valent anions and attract high-valent cations, resulting in high rejection of salt with multivalent anions and monovalent cations[19,43]. However, the low rejection of NaCl compared to $MgCl_2$ and $CaCl_2$ is due to the steric effect. The smaller hydrated ion radius of Na^+ (0.358 nm) makes it more difficult for it to pass through the selective layer.

5.3.4.1.1 Trade-off between permeability and selectivity

Selective separation between water/multivalent ions and mono/multivalent ions is vital for NF applications such as water and Na_2SO_4 recovery from wastewater in the chlor-alkali industry which contains high concentration of Na^+, Cl^-, and SO_4^{-2} ions, RO desalination pretreatment, and water softening in which low NaCl rejection prevents the unnecessary osmotic pressure build-up[19]. The NF membranes that represent high-water permeability and ion selectivity would enable an energy-efficient NF process with high quality product. The GONR template method produces ultrathin, hydrophilic, stripe-like, and highly cross-linked hybrid GONR/PA NF selective layer with narrow pore size distribution and fewer defects, suggesting an effective approach to overcome the trade-off of water permeance and Na_2SO_4 salt rejection (**Figure 5-6c**). Also, the prepared iTFC NF membranes appear to exhibit an excellent permselectivity for the challenging angstrom-level ion selectivity of mono/multivalent ions such as SO_4^{-2}/Cl^- (**Figure 5-6d**). The upper-bound line in this figure reveals the level of permeability and selectivity attained by different lab-made PIP/TMC-based NF membranes and commercial membranes[19]. The separation performance of the iTFC membrane with hybrid GONR/PA selective nanofilm surpasses the upper-bound line and achieves a better trade-off in comparison to some of the other NF membranes. The high permselectivity is related to the high Na_2SO_4 rejection (above 98%) and low NaCl rejection (about 20-30%) along with rapid water transport.

5.3.4.1.2 Stability

Nanofiltration treatment applications require a robust membrane stability. The integrity and stability of the iTFC NF membranes during the continuous operation must be evaluated, especially for those fabricated using the template method that have the possibility of template deformation or leaching. The long-term stability test for the optimized iTFC02 NF membrane reveals a proper operation stability on the basis of a 12 h cross-flow test under 5 bar on a feed stream containing 1000 ppm Na_2SO_4. As shown in **Figure 5-6e**, the water permeance remains stable at ~ 21 $L.m^{-2}.h^{-1}.bar^{-1}$, and salt rejection above 98%. Additionally, the pressure resistance of iTFC02 membrane has been investigated by NF performance test at different pressures (1-5 bar). As shown in **Figure 5-6f**, the rejection of Na_2SO_4 decreases slightly as the operating pressure increases, which could be due to the concentration polarization at higher pressure. Also, the permeance changes only negligibly when the pressure is raised. Furthermore, the relationship between water flux and pressure remains roughly linear, which could be due to the presence of the GONR template that offsets some of the compaction at the interface of the composite membrane. The long-term stability and pressure resistance of iTFC02 results suggests that a robust interfacial adhesion strength between the hybrid GONR/PA top selective layer, GONR template interlayer, and the PES support layer. This excellent stability properties suggest the practicality of GONR templates for NF industrial applications.

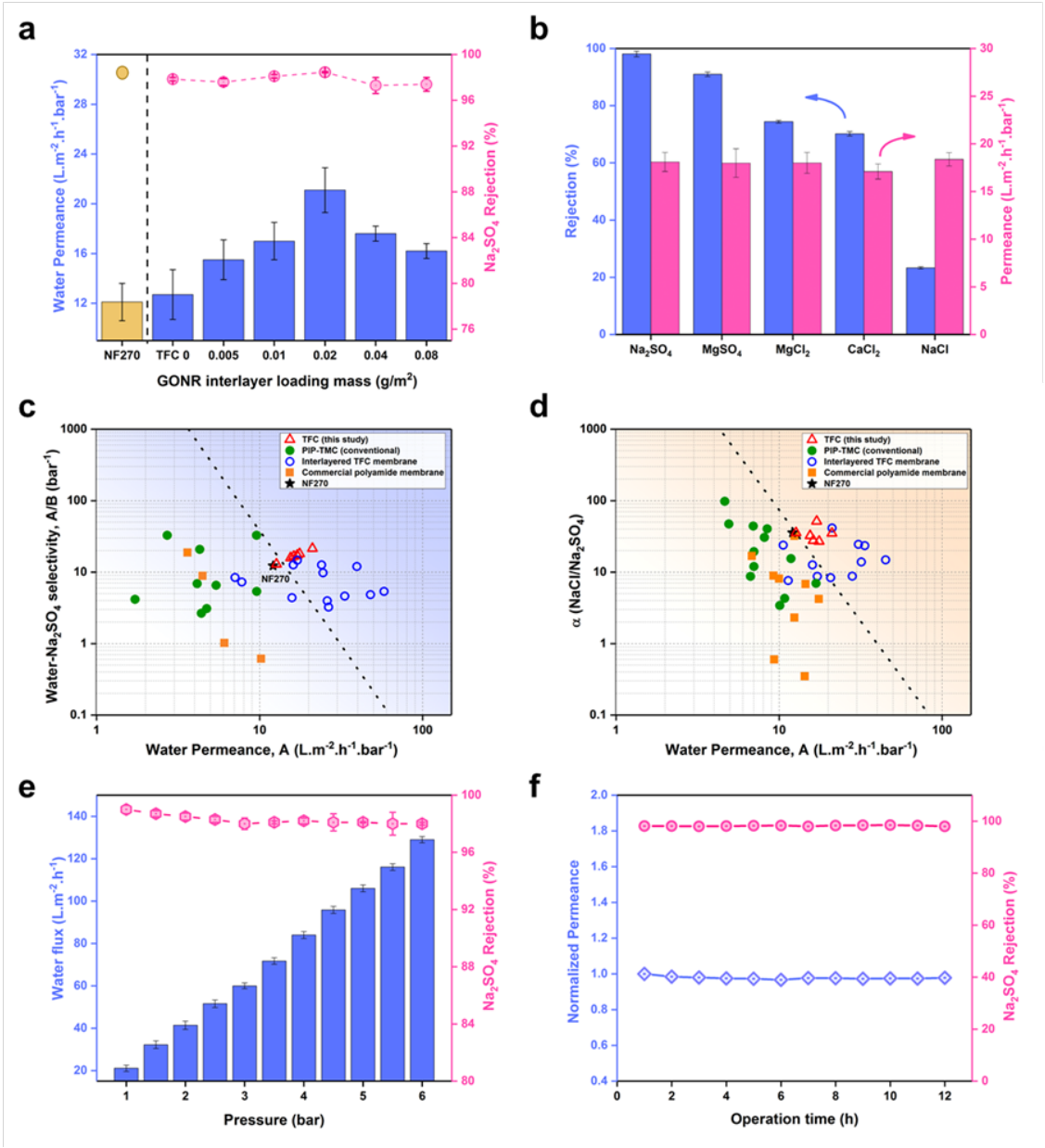

Figure 5-6. Separation performance of TFC and iTFC membranes: (a) Water permeance and Na_2SO_4 rejection of NF270 commercial membrane, pristine TFC, and iTFC NF membranes with different loading of GONR template. (b) Permeance and salt rejections of optimized NF membrane (iTFC02) (under 5 bar and 1000 ppm solution including single type of salt, Na_2SO_4, $MgSO_4$, $MgCl_2$, $CaCl_2$, NaCl), (c) Comparison of nanofiltration performance (water/Na_2SO_4 selectivity) and (d) ion sieving (NaCl/Na_2SO_4 selectivity) of iTFC membranes with hand-made polyamide TFC membrane and commercial NF membranes. The dashed black line is the upper-

bound line related permeability-selectivity trade-off, (e) The pressure resistance test and (f) long term stability during cross-flow filtration test of iTFC02 (test condition: pressure 5 bar, Na_2SO_4 concentration1000 ppm).

5.3.5 Dissecting the role of GONR on the IP reaction and exceptional permselectivity of iTFC02

To understand the relationship between the morphology and structure of PA film and the GONR IP template, we interpret the IP mechanism in the presence of the GONR network. After immersion of the substrate in the amine solution, the substrate including the GONR network and PES pores maintains the aqueous solution of PIP. Then, once the water saturated substrate is contacted with the organic solution, the IP reaction occurs. The fabrication of PA through IP reaction is a complex, exothermal, self-limiting and nonequilibrium hierarchical process comprising simultaneous and intensely coupled reaction and diffusion of monomeric species[35,146]. The IP reaction-diffusion mechanism includes three stages: monomer concentration profile development inside the boundary layer, beginning of the nascent film formation, and diffusion-limited film growth[35]. The GONR template is incorporated to improve the IP reaction via manipulation of the three stages to achieve an ultrathin selective NF membrane. We hypothesize that the presence of hydrophilic GONR template has combined impacts on the stages of the IP reaction: (i) promotes the IP reaction due to enhanced availability of amine monomers at the interface, (ii) reduces the release rate and diffusion of the amine monomers into the polymerization reaction zone due to electrostatic interaction and hydrogen bonding, (iii) accelerates the IP reaction by increased thermo- and solute-capillary instability and confinement effect.

Amine monomer availability plays a significant role in the IP reaction and growth of the PA network structure. i.e. a higher availability of amine monomer in the reaction zone promotes faster and tighter nascent film formation. Here, the presence of GONR, increases the monomer storage capacity and solution uptake from 245% to 256% (**Figure 5-7a)**. Also, from the capillary effect view, the absorbed aqueous PIP solution migrates from the bottom of the substrate via the capillary force. Amine monomer may be transported through vertical tortuous nanochannels formed by the confined spaces between GONR network in addition to intrinsic physical defects (holes) of GONR. The height of the capillary rise, calculated via the Lucas-Wesburn equation[243,255], increases from 5.43E-04 $\sqrt{t(s)}$ (m) for the PES support membrane to 9.1PES-GE-04 $\sqrt{t(s)}$ (m) for the PES-GONR02 template (**Figure 5-7b)**. Therefore, higher PIP enrichment through the GONR template accelerates the formation of dense and

cross-linked incipient film and produces a less permeable film with PIP monomer at the "diffusion-limited growth" stage.

The transport of amine monomers into the IP reaction zone is essential for PA film formation, i.e. slower diffusion leads to a thinner and more permeable PA layer. Since the diffusion of the PIP monomer to hexane is greater than the diffusion of TMC to water, the PIP molecules (0.7 nm) diffuse from the aqueous phase into the organic phase to form the PA nanofilm in the organic phase near the interface. The affinity and interaction between the substrate and PIP monomer has been evaluated by measuring the zeta-potential of the substrate. As shown in **Figure 5-7c**, substrate becomes more negatively charged with the increase of pH. Since PIP protonation offers a hydroxyl-rich environment (pH=9.5-10), the PES-GONR02 would also be negatively charged when immersed in the PIP-containing solution. Consequently, the charge density of PES-GONR at pH=9.5 may reflect its ability to attract positively charged PIP molecules in the aqueous phase. The presence of GONR, increases the charge density of the substrate surface (i.e., PES: -8.78 $C.m^{-2}$, PES-GONR02: -12.48 $C.m^{-2}$) and increased the electrostatic attraction between the IP template and PIP monomers which result in the reduction in monomer transport across the interface.

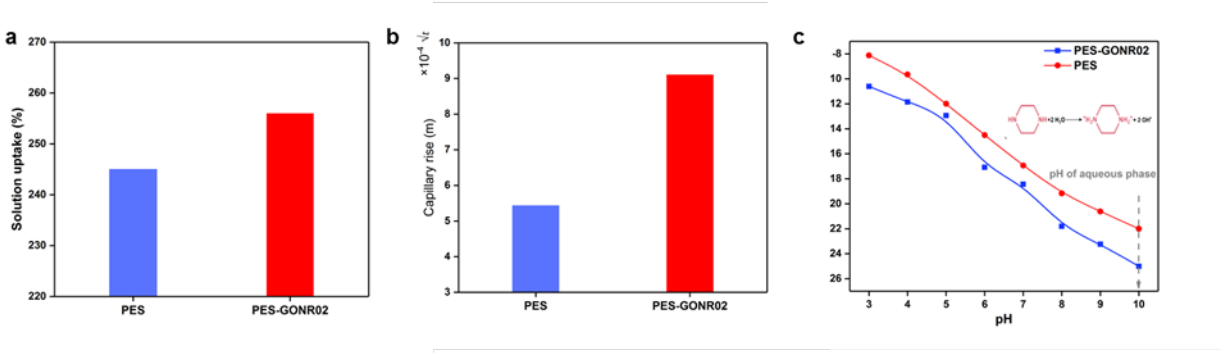

Figure 5-7. (a)Solution uptake, (b)capillary rise, (c)zeta potential of IP template with/without GONR

To further investigate this effect, molecular dynamic (MD) simulations have been applied to validate our assumption regarding amine monomer (PIP) diffusion toward the organic phase through the water/hexane interface in the presence/absence of GONR on the PES substrate. The simulated diffusion coefficient of PIP monomer with and without GONR has been calculated by linear curve fitting of the MSD data depicted in **Figure 5-8d**. As can be observed in **Figure 5-8e**, the calculated diffusion coefficient of PIP molecules drops significantly (around 60%) when the GONR particle is introduced into the simulation box. The decrement clearly demonstrates that the intermolecular interaction between

PIP molecules and GONR particle which restricts the mobility of PIP monomers. Quantitative evaluation of the interactions supports the claim since the intermolecular interaction between PIP molecules and other parts of the system jumped from -148.59 kcal/mol to -162.68 kcal/mol when the GONR particle is applied in the aqueous phase. These quantities obtained from molecular dynamic simulations are reported in **Table 5-2**. On the other hand, **Figure 5-8c** shows the hydrogen bonds formed among different substances in the presence of GONR. Therefore, adding GONR particle can give rise to an affinity for PIP molecules (this affinity is about -14 kcal/mol) which is due mainly to hydrogen bonding through functional groups of the GONR particle illustrated in **Figure 5-8c**. It is worth mentioning that the maximum hydrogen-acceptor distance is adjusted to 3 Å during the H-bond detection which means the detected H-bonds are categorized as strong hydrogen bonds with electrostatic nature [256]. The aforementioned hydrogen bonds with an electrostatic nature (based on Jeffrey's classification [256]) can also be concluded from zeta potential analysis which demonstrated the partial charge of sublayer surface after modification by GONR particles. The confinement effect has a significant role in the instability of the IP reaction and thereby affects the morphology and structure of the PA. i.e. the better confined IP template, improves both nanofoaming and interfacial instability[35] that result in a rough cross-linked PA layer with crumpled structure.

The addition of GONR template intensify the thermos and solute-capillary flows, called Marangoni flow, by increasing the chemical composition gradient and local temperature in the reaction zone[35,146]. On the one hand, the PIP adsorption affinity for GONR establishes a gradient of PIP monomers when the aqueous PIP solution moves up during the capillary rise. The gradient of PIP concentration in the reaction zone leads to the chemo-hydrodynamic instabilities in IP reaction and promotes the IP reaction and the amine diffusion toward the organic phase. On the other hand, the confined GONR network can better trap the generated heat and gas bubble between GONR template and PA film during the IP reaction, which leads to a rougher polyamide film.

Table 5-2. The energy quantities obtained from MD simulation.

Energy (kcal/mol)	E_{System}	E_X	E_{PIP}	$E_{Interaction}$
Without GONR	-3383.15	-3441.05	206.49	-148.59
With GONR	-3416.31	-3473.47	219.84	-162.68

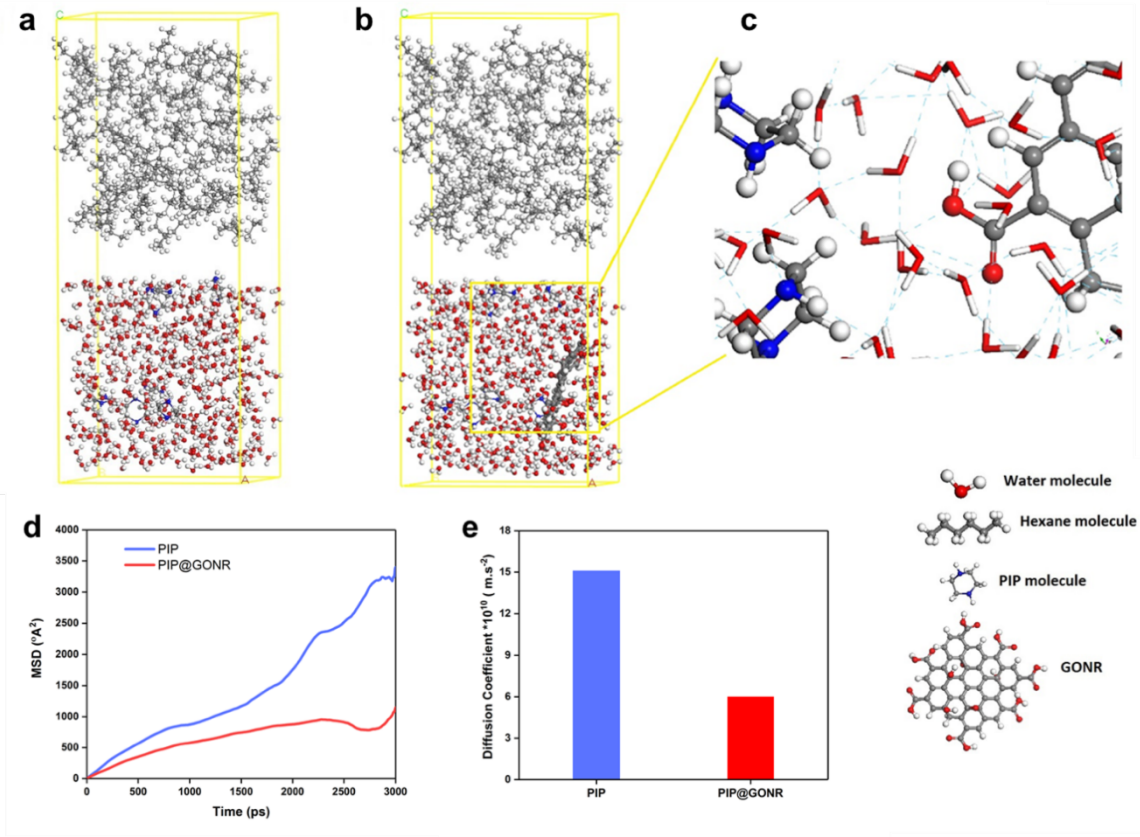

Figure 5-8. Molecular structure and considered simulation boxes in the MD simulation (a) hexane-water, (b) hexane-water-GONR systems, (c) hydrogen bonds formed among different molecules in hexane-water-GONR system, (d) obtained MSD data related to the mobility of PIP molecules, and (e) calculated diffusion coefficient of PIP with/without GONR.

5.4 Conclusion

In summary, in this work, we presented a novel IP template, GONR ultrathin network, could successfully meet two essential needs, gutter layer effect and IP reaction optimization. The GONR template properly optimized the IP process via regulation the capillary rise, electrostatic interactions, and nanoconfinement of IP reaction. The combined factors, of tuning the trans-interface transport of amine monomers, limiting the heat and gas bubbles formed in situ, intensifying the solute-capillary flows, promoting the IP reaction toward fabrication of more hydrophilic, highly cross-linked, ultrathin, crumpled selective layer with the potential of extra nanochannel water passage. The optimized loading of GONR at 0.02 $g.m^{-2}$ resulted in a desired hybrid GONR/PA TFC NF membrane with a nanostriped crumpled structure beyond the PA context, ultrathin PA nanofilm with a thickness of 15 nm, and a

narrow pore size distribution and high crosslinking degree of 80% that simultaneously improve the permeability and selectivity, and successfully pass the upper bound trade-off with permeance of 21.3 $L.m^{-2}.h^{-1}.bar^{-1}$ and excellent rejection of 98% for Na_2SO_4 under 5 bar of pressure.

This research should inspire the development of a novel hybrid selective nanofilm through template method to break the upper-bound line of the permeability and selectivity performance of membranes in different applications and provide cost efficient and energy efficient separation processes such as organic solvent nanofiltration, pervaporation, sea water desalination, wastewater treatment, etc.

Chapter 6: **Conclusion and Future work**

6.1 General conclusions and contributions

The main objective of this dissertation was the tailored design and fabrication of advanced polyamide thin film composite (PA-TFC) membranes for reverse osmosis (RO) and nanofiltration (NF) applications. General contribution of the dissertation is to considerably enhance knowledge about the application of nanotechnology tools (ALD) and novel nanomaterials (MXene, and GONR) in PA-TFC membrane and their impact on the properties and performance of TFC membranes.

In **chapter 2**, the reverse osmosis and nanofiltration processes as dominant technologies for desalination and ion separation applications, and transport mechanism in these processes were reviewed. Then, the thin film composite (TFC) membrane which is the most common membrane for RO and NF applications, and interfacial polymerization reaction and different approaches to optimize the interfacial polymerization reaction to improve the permselectivity of membrane were reviewed.

In **Chapter 3**, based on the importance of sublayer on interfacial polymerization reaction and its role on PA-TFC membrane properties and performance, for the first time, atomic layer deposition (ALD) used to engineer the conventional sublayer and overcome its limitations. This functional TiO_2 nanofilm increases the affinity between modified sublayer and amine monomer to promote the efficient and subtle tuning of the adsorption and diffusion of amine monomer during the interfacial polymerization process. The obtained TFC membrane with optimal ALD TiO_2 coverage demonstrates improved RO performance in terms of high permeance of 1.8 $L.m^{-2}.h^{-1}.bar^{-1}$ and high salt rejection rate of 96.1% in a dead-end process. This work reveals that coating functional nanomaterials by ALD is a practical manipulation technique toward the controllable fabrication of promising TFC membrane and the optimization of sublayer materials.

In **Chapter 4**, inspired by using nanomaterials as a filler to improve the performance of thin film composite membranes, and by understanding the desired properties of novel multifunctional 2D materials (Transition-metal carbides - MXenes), a novel TFN membrane was fabricated and investigated. In this part, at first, to address the challenges of MXene including low ambient stability, facile restacking and agglomeration, and poor compatibility and processability, we proposed a facile, green, and cost-efficient approach to coat a stable layer of plant-derived polyphenol tannic acid (TA) on the surface of MXene ($Ti_3C_2T_x$) nanosheets. Then, high-performance reverse osmosis polyamide thin film nanocomposite (RO-PA-TFN) membranes were fabricated by the incorporation of modified

MXene ($Ti_3C_2T_x$–TA) nanosheets in the polyamide selective layer through interfacial polymerization. The strong negative charge and hydrophilic multifunctional properties of TA not only boosted the chemical compatibility between $Ti_3C_2T_x$ MXene nanosheets and the polyamide matrix to overcome the formation of nonselective voids but also generated a tight network with selective interfacial pathways for efficient monovalent salt rejection and water permeation. In comparison to the neat thin film composite membrane, the optimum TFN ($Ti_3C_2T_x$–TA) membrane with a loading of 0.008 wt % nanofiller revealed a 1.4-fold enhancement in water permeability, a well-maintained high NaCl rejection rate of 96% in a dead-end process and enhanced anti-fouling tendency. This research offers a facile way for the development of modified MXene nanosheets to be successfully integrated into the polyamide-selective layer to improve the performance and fouling resistance of TFN membranes.

Finally, in **Chapter 5**, inspiring by interlayered-TFC membranes approach and understanding the IP template importance, a novel interlayer, graphene oxide nanoribbon (GONR) was proposed to tune the interfacial polymerization and to design a defect-free ultrathin hybrid PA/GONR membrane for NF application. Controlling the concentration of GONR loading enabled tuning of the structure and physicochemical properties (crosslinking degree, surface charge, pore size, hydrophilicity, morphology, roughness, and thickness) of the polyamide selective layer. The optimized loading of GONR was coated on the surface of polyether sulfone support layer, then the ultrathin hybrid polyamide/GONR nanofilm (< 30 nm) was formed through the IP at low concentration of monomers. The optimized ultrathin TFC membrane surpassed the upper bound line of the permeability-selectivity performance of the existing conventional and industrial PA membranes. This research provides a new way with modulating the interfacial polymerization reaction by using features of graphene oxide nanoribbon to develop ultrathin hydride membranes.

6.2 Future work

Based on the studies and investigations of this dissertation, the following recommendations are provided here.

- **Interfacial polymerization template design**.
    - Aside from graphene oxide nanoribbon as an example for an interlayer in this thesis, and the other materials which were used in the literature, a wide range of materials and new structures (hydrogels, 3D structure materials, so on) could be explored as

the tailored template for tuning the IP reaction to fabricate the high-performance PA-TFC membrane.

- A better understanding of the mechanism of the IP and PA formation in the presence of interlayer is needed through advanced techniques for membrane characterization (positron annihilation lifetime spectroscopy, 3D TEM, electrochemical impedance spectroscopy, and so on). In this way, the interlayer interactions and binding with the sublayer and top layer, the entire membrane integrity, influence of pattern and orientation of nanofillers as an interlayer, their impact on the transport behavior (solute transport and water-solute selectivity) should be investigated systematically.
- The importance of gutter effect on the transport paths in the interlayered-TFC membranes, and the role of the substrate pore size as an impactful factor on the transport behavior, warrants to more modeling and experimental investigation.

- **Scale-up interlayered-TFC membrane.**

  The fabrication method for the nanomaterials or nanocomposite interlayer on substrate are limited at this stage, mostly to vacuum filtration and co-deposition. The scalability of current methods for interlayer needs to be explored. Most of the interlayer preparation methods have been developed for flat sheet membranes. A step forward to extend the interlayer to commercial hollow fibers and spiral wound membranes requires more research effort.

- **Interlayered-TFN membranes; combination of two approaches (incorporation of nanomaterials as a filler and interlayer at the same time).**

  Despite the significant increase in membrane perm-selectivity due to the presence of nanomaterials in the top selective layer and interlayer, both approaches and design a high performance iTFN membrane can be applied. In addition, an opportunity exists to conduct systematic research on the influence of nanofillers on the fouling and chlorine resistance of iTFN membrane to facilitate it for a varied range of real applications.

Bibliography

[1] D.M. Stevens, J.Y. Shu, M. Reichert, A. Roy, Next-Generation Nanoporous Materials: Progress and Prospects for Reverse Osmosis and Nanofiltration, Ind. Eng. Chem. Res. 56 (2017) 10526–10551. https://doi.org/10.1021/acs.iecr.7b02411.

[2] M. Elimelech, W.A. Phillip, The Future of Seawater Desalination: Energy, Technology, and the Environment, Science (80-.). 333 (2011) 712–717. https://doi.org/10.1126/science.1200488.

[3] C.Y. Tang, Z. Yang, H. Guo, J.J. Wen, L.D. Nghiem, E. Cornelissen, Potable Water Reuse through Advanced Membrane Technology, Environ. Sci. Technol. 52 (2018) 10215–10223. https://doi.org/10.1021/acs.est.8b00562.

[4] S. Jiang, Y. Li, B.P. Ladewig, A review of reverse osmosis membrane fouling and control strategies, Sci. Total Environ. 595 (2017) 567–583. https://doi.org/10.1016/j.scitotenv.2017.03.235.

[5] J.E. Cadotte, R.J. Petersen, R.E. Larson, E.E. Erickson, A new thin-film composite seawater reverse osmosis membrane, Desalination. 32 (1980) 25–31. https://doi.org/10.1016/S0011-9164(00)86003-8.

[6] P.W. Morgan, S.L. Kwolek, Interfacial polycondensation. II. Fundamentals of polymer formation at liquid interfaces, J. Polym. Sci. Part A Polym. Chem. 34 (1996) 531–559. https://doi.org/10.1002/pola.1996.816.

[7] A.K. Ghosh, E.M.V. Hoek, Impacts of support membrane structure and chemistry on polyamide-polysulfone interfacial composite membranes, J. Memb. Sci. 336 (2009) 140–148. https://doi.org/10.1016/j.memsci.2009.03.024.

[8] X. Lu, L.H. Arias Chavez, S. Romero-Vargas Castrillón, J. Ma, M. Elimelech, Influence of active layer and support layer surface structures on organic fouling propensity of thin-film composite forward osmosis membranes, Environ. Sci. Technol. 49 (2015) 1436–1444. https://doi.org/10.1021/es5044062.

[9] S. Karan, Z. Jiang, A.G. Livingston, A. Jarry, R. Kostecki, G. Chen, D.J. Bacon, J. Newman, J. Park, A.M. Sastry, W. Lu, A.L. Greer, R.S. Lakes, T. Rouxel, F. Aguesse, N.M. Alford, A. Alderson, S. Karan, Z. Jiang, A.G. Livingston, Sub-10 nm polyamide nanofilms with ultrafast

solvent transport for molecular separation, Science (80-.). 348 (2015) 1347–1351. https://doi.org/10.1126/science.aaa5058.

[10] D. Cohen-Tanugi, R.K. McGovern, S.H. Dave, J.H. Lienhard, J.C. Grossman, Quantifying the potential of ultra-permeable membranes for water desalination, Energy Environ. Sci. 7 (2014) 1134–1141. https://doi.org/10.1039/c3ee43221a.

[11] J.R. Werber, A. Deshmukh, M. Elimelech, The Critical Need for Increased Selectivity, Not Increased Water Permeability, for Desalination Membranes, Environ. Sci. Technol. Lett. 3 (2016) 112–120. https://doi.org/https://doi.org/10.1021/acs.estlett.6b00050.

[12] B. Khorshidi, T. Thundat, B.A. Fleck, M. Sadrzadeh, RSC Advances Thin fi lm composite polyamide membranes : parametric study on the in fl uence of synthesis conditions, (2015) 54985–54997. https://doi.org/10.1039/C5RA08317F.

[13] B. Khorshidi, T. Thundat, D. Pernitsky, M. Sadrzadeh, A parametric study on the synergistic impacts of chemical additives on permeation properties of thin film composite polyamide membrane, J. Memb. Sci. 535 (2017) 248–257. https://doi.org/10.1016/j.memsci.2017.04.052.

[14] M.F. Jimenez-Solomon, P. Gorgojo, M. Munoz-Ibanez, A.G. Livingston, Beneath the surface: Influence of supports on thin film composite membranes by interfacial polymerization for organic solvent nanofiltration, J. Memb. Sci. 448 (2013) 102–113. https://doi.org/10.1016/j.memsci.2013.06.030.

[15] Q. Zhang, Z. Zhang, L. Dai, H. Wang, S. Li, S. Zhang, Novel insights into the interplay between support and active layer in the thin film composite polyamide membranes, J. Memb. Sci. 537 (2017) 372–383. https://doi.org/10.1016/j.memsci.2017.05.033.

[16] J.R. McCutcheon, M. Elimelech, Influence of membrane support layer hydrophobicity on water flux in osmotically driven membrane processes, J. Memb. Sci. 318 (2008) 458–466. https://doi.org/10.1016/j.memsci.2008.03.021.

[17] G.Z. Ramon, M.C.Y. Wong, E.M.V. Hoek, Transport through composite membrane, part 1: Is there an optimal support membrane?, J. Memb. Sci. 415–416 (2012) 298–305. https://doi.org/10.1016/j.memsci.2012.05.013.

[18] J. Wang, R. Xu, F. Yang, J. Kang, Y. Cao, M. Xiang, Probing influences of support layer on the morphology of polyamide selective layer of thin film composite membrane, J. Memb. Sci.

556 (2018) 374–383. https://doi.org/10.1016/j.memsci.2018.04.011.

[19] K. Wang, X. Wang, B. Januszewski, Y. Liu, D. Li, R. Fu, M. Elimelech, X. Huang, Tailored design of nanofiltration membranes for water treatment based on synthesis–property–performance relationships, Chem. Soc. Rev. 51 (2022) 672–719. https://doi.org/10.1039/d0cs01599g.

[20] R. Zhang, J. Tian, S. Gao, B. Van der Bruggen, How to coordinate the trade-off between water permeability and salt rejection in nanofiltration?, J. Mater. Chem. A. 8 (2020) 8831–8847. https://doi.org/10.1039/D0TA02510K.

[21] Z. Wang, S. Liang, Y. Kang, W. Zhao, Y. Xia, J. Yang, H. Wang, X. Zhang, Manipulating interfacial polymerization for polymeric nanofilms of composite separation membranes, Prog. Polym. Sci. 122 (2021) 101450. https://doi.org/10.1016/j.progpolymsci.2021.101450.

[22] Marcel Mulder, Basic principles of membrane technology, n.d.

[23] RICHARD W. BAKER, Membrane Technology and Applications, 2012. https://doi.org/10.1016/B978-1-85617-389-6.50003-5.

[24] P. Marchetti, M.F. Jimenez Solomon, G. Szekely, A.G. Livingston, Molecular Separation with Organic Solvent Nanofiltration: A Critical Review, Chem. Rev. 114 (2014) 10735–10806. https://doi.org/10.1021/cr500006j.

[25] A. Alkhatib, Reverse-Osmosis Desalination of Water Powered by Photo-Voltaic Modules, Comput. Water, Energy, Environ. Eng. 03 (2014) 22–29. https://doi.org/10.4236/cweee.2014.31003.

[26] Y.J. Lim, K. Goh, M. Kurihara, R. Wang, Seawater desalination by reverse osmosis: Current development and future challenges in membrane fabrication – A review, J. Memb. Sci. 629 (2021) 119292. https://doi.org/10.1016/j.memsci.2021.119292.

[27] WHO, Chapter 10 Acceptability aspects : Taste , odour and appearance, Guidel. Drink. Qual. (2017) 219–230.

[28] Z. Yang, L. Long, C. Wu, C.Y. Tang, High Permeance or High Selectivity? Optimization of System-Scale Nanofiltration Performance Constrained by the Upper Bound, ACS ES&T Eng. 2 (2022) 377–390. https://doi.org/10.1021/acsestengg.1c00237.

[29] S.H. Maruf, D.U. Ahn, A.R. Greenberg, Y. Ding, Glass transition behaviors of interfacially

polymerized polyamide barrier layers on thin film composite membranes via nano-thermal analysis, Polymer (Guildf). 52 (2011) 2643–2649. https://doi.org/10.1016/j.polymer.2011.04.022.

[30] A.P. Korikov, P.B. Kosaraju, K.K. Sirkar, Interfacially polymerized hydrophilic microporous thin film composite membranes on porous polypropylene hollow fibers and flat films, J. Memb. Sci. 279 (2006) 588–600. https://doi.org/10.1016/j.memsci.2005.12.051.

[31] S. Veríssimo, K. V. Peinemann, J. Bordado, Thin-film composite hollow fiber membranes: An optimized manufacturing method, J. Memb. Sci. 264 (2005) 48–55. https://doi.org/10.1016/j.memsci.2005.04.020.

[32] I.C. Kim, J. Jegal, K.H. Lee, Effect of Aqueous and Organic Solutions on the Performance of Polyamide Thin-Film-Composite Nanofiltration Membranes, J. Polym. Sci. Part B Polym. Phys. 40 (2002) 2151–2163. https://doi.org/10.1002/polb.10265.

[33] J. Wei, X. Jian, C. Wu, S. Zhang, C. Yan, Influence of polymer structure on thermal stability of composite membranes, J. Memb. Sci. 256 (2005) 116–121. https://doi.org/10.1016/j.memsci.2005.02.012.

[34] F. Liu, L. Wang, D. Li, Q. Liu, B. Deng, A review: The effect of the microporous support during interfacial polymerization on the morphology and performances of a thin film composite membrane for liquid purification, RSC Adv. 9 (2019) 35417–35428. https://doi.org/10.1039/c9ra07114h.

[35] V. Freger, G.Z. Ramon, Polyamide desalination membranes: Formation, structure, and properties, Elsevier B.V., 2021. https://doi.org/10.1016/j.progpolymsci.2021.101451.

[36] W.J. Lau, A.F. Ismail, N. Misdan, M.A. Kassim, A recent progress in thin film composite membrane: A review, Desalination. 287 (2012) 190–199. https://doi.org/10.1016/j.desal.2011.04.004.

[37] S. Shao, F. Zeng, L. Long, X. Zhu, L.E. Peng, F. Wang, Z. Yang, C.Y. Tang, Nanofiltration Membranes with Crumpled Polyamide Films: A Critical Review on Mechanisms, Performances, and Environmental Applications, Environ. Sci. Technol. 56 (2022) 12811–12827. https://doi.org/10.1021/acs.est.2c04736.

[38] B.-H. Jeong, E.M.V. Hoek, Y. Yan, A. Subramani, X. Huang, G. Hurwitz, A.K. Ghosh, A.

Jawor, Interfacial polymerization of thin film nanocomposites: A new concept for reverse osmosis membranes, J. Memb. Sci. 294 (2007) 1–7. https://doi.org/10.1016/j.memsci.2007.02.025.

[39] J.E. Gu, S. Lee, C.M. Stafford, J.S. Lee, W. Choi, B.Y. Kim, K.Y. Baek, E.P. Chan, J.Y. Chung, J. Bang, J.H. Lee, Molecular layer-by-layer assembled thin-film composite membranes for water desalination, Adv. Mater. 25 (2013) 4778–4782. https://doi.org/10.1002/adma.201302030.

[40] M.R. Chowdhury, J. Steffes, B.D. Huey, J.R. McCutcheon, 3D printed polyamide membranes for desalination, Science (80-.). 361 (2018) 682–686. https://doi.org/10.1126/science.aar2122.

[41] Z. Tan, S. Chen, X. Peng, L. Zhang, C. Gao, Polyamide membranes with nanoscale Turing structures for water purification, Science (80-.). 360 (2018) 518–521. https://doi.org/10.1126/science.aar6308.

[42] Y. Liang, Y. Zhu, C. Liu, K.-R.R. Lee, W.-S.S. Hung, Z. Wang, Y. Li, M. Elimelech, J. Jin, S. Lin, Polyamide nanofiltration membrane with highly uniform sub-nanometre pores for sub-1 Å precision separation, Nat. Commun. 11 (2020) 2015. https://doi.org/10.1038/s41467-020-15771-2.

[43] L. Shen, R. Cheng, M. Yi, W.S. Hung, S. Japip, L. Tian, X. Zhang, S. Jiang, S. Li, Y. Wang, Polyamide-based membranes with structural homogeneity for ultrafast molecular sieving, Nat. Commun. 13 (2022) 1–11. https://doi.org/10.1038/s41467-022-28183-1.

[44] M. Shi, Z. Wang, S. Zhao, J. Wang, S. Wang, A support surface pore structure re-construction method to enhance the flux of TFC RO membrane, J. Memb. Sci. 541 (2017) 39–52. https://doi.org/10.1016/j.memsci.2017.06.087.

[45] T.H. Lee, M.Y. Lee, H.D. Lee, J.S. Roh, H.W. Kim, H.B. Park, Highly porous carbon nanotube / polysulfone nanocomposite supports for high- fl ux polyamide reverse osmosis membranes, J. Memb. Sci. 539 (2017) 441–450. https://doi.org/10.1016/j.memsci.2017.06.027.

[46] H.M. Park, K.Y. Jee, Y.T. Lee, Preparation and characterization of a thin- fi lm composite reverse osmosis membrane using a polysulfone membrane including metal-organic frameworks, J. Memb. Sci. 541 (2017) 510–518.

https://doi.org/10.1016/j.memsci.2017.07.034.

[47] M. Shi, Z. Wang, S. Zhao, J. Wang, P. Zhang, X. Cao, A novel pathway for high performance RO membrane: Preparing active layer with decreased thickness and enhanced compactness by incorporating tannic acid into the support, J. Memb. Sci. 555 (2018) 157–168. https://doi.org/10.1016/j.memsci.2018.03.025.

[48] A. Sotto, A. Rashed, R.X. Zhang, A. Martínez, L. Braken, P. Luis, B. Van der Bruggen, Improved membrane structures for seawater desalination by studying the influence of sublayers, Desalination. 287 (2012) 317–325. https://doi.org/10.1016/j.desal.2011.09.024.

[49] D. Emadzadeh, W.J. Lau, T. Matsuura, M. Rahbari-Sisakht, A.F. Ismail, A novel thin film composite forward osmosis membrane prepared from PSf-TiO2 nanocomposite substrate for water desalination, Chem. Eng. J. 237 (2014) 70–80. https://doi.org/10.1016/j.cej.2013.09.081.

[50] L.F. Liu, X.L. Gu, X. Xie, R.H. Li, C.Y. Yu, X.X. Song, C.J. Gao, Modification of PSf/SPSf blended porous support for improving the reverse osmosis performance of aromatic polyamide thin film composite membranes, Polymers (Basel). 10 (2018). https://doi.org/10.3390/polym10060686.

[51] H. Il Kim, S.S. Kim, Plasma treatment of polypropylene and polysulfone supports for thin film composite reverse osmosis membrane, J. Memb. Sci. 286 (2006) 193–201. https://doi.org/10.1016/j.memsci.2006.09.037.

[52] J.T. Arena, B. Mccloskey, B.D. Freeman, J.R. Mccutcheon, Surface modification of thin film composite membrane support layers with polydopamine: Enabling use of reverse osmosis membranes in pressure retarded osmosis, J. Memb. Sci. 375 (2011) 55–62. https://doi.org/10.1016/j.memsci.2011.01.060.

[53] K. Pan, P. Fang, B. Cao, Novel composite membranes prepared by interfacial polymerization on polypropylene fiber supports pretreated by ozone-induced polymerization, Desalination. 294 (2012) 36–43. https://doi.org/10.1016/j.desal.2012.03.007.

[54] Z.Z. Wang, Z.Z. Wang, S. Lin, H. Jin, S. Gao, Y. Zhu, J. Jin, Nanoparticle-templated nanofiltration membranes for ultrahigh performance desalination, Nat. Commun. 9 (2018) 2004. https://doi.org/10.1038/s41467-018-04467-3.

[55] Z. Zhang, X. Shi, R. Wang, A. Xiao, Y. Wang, Ultra-permeable polyamide membranes

harvested by covalent organic framework nanofiber scaffolds: a two-in-one strategy, Chem. Sci. 10 (2019) 9077–9083. https://doi.org/10.1039/C9SC03088C.

[56] Z. Yang, F. Wang, H. Guo, L.E. Peng, X.-H. Ma, X.-X. Song, Z. Wang, C.Y. Tang, Mechanistic Insights into the Role of Polydopamine Interlayer toward Improved Separation Performance of Polyamide Nanofiltration Membranes, Environ. Sci. Technol. 54 (2020) 11611–11621. https://doi.org/10.1021/acs.est.0c03589.

[57] M. Kattula, K. Ponnuru, L. Zhu, W. Jia, H. Lin, E.P. Furlani, Designing ultrathin film composite membranes: The impact of a gutter layer, Sci. Rep. 5 (2015) 1–9. https://doi.org/10.1038/srep15016.

[58] J.-J.J. Wang, H.C. Yang, M.-B.B. Wu, X. Zhang, Z.K. Xu, Nanofiltration membranes with cellulose nanocrystals as an interlayer for unprecedented performance, J. Mater. Chem. A. 5 (2017) 16289–16295. https://doi.org/10.1039/C7TA00501F.

[59] S. Gao, Y. Zhu, Y. Gong, Z. Wang, W. Fang, J. Jin, Ultrathin Polyamide Nanofiltration Membrane Fabricated on Brush-Painted Single-Walled Carbon Nanotube Network Support for Ion Sieving, ACS Nano. 13 (2019) 5278–5290. https://doi.org/10.1021/acsnano.8b09761.

[60] X. Wu, M. Ding, H. Xu, W. Yang, K. Zhang, H. Tian, H. Wang, Z. Xie, Scalable Ti3C2TxMXene Interlayered Forward Osmosis Membranes for Enhanced Water Purification and Organic Solvent Recovery, ACS Nano. 14 (2020) 9125–9135. https://doi.org/10.1021/acsnano.0c04471.

[61] Z. Zhou, Y. Hu, C. Boo, Z. Liu, J. Li, L. Deng, X. An, High-Performance Thin-Film Composite Membrane with an Ultrathin Spray-Coated Carbon Nanotube Interlayer, Environ. Sci. Technol. Lett. 5 (2018) 243–248. https://doi.org/10.1021/acs.estlett.8b00169.

[62] H. gyu Choi, A.A. Shah, S.-E.E. Nam, Y.-I.I. Park, H. Park, Thin-film composite membranes comprising ultrathin hydrophilic polydopamine interlayer with graphene oxide for forward osmosis, Desalination. 449 (2019) 41–49. https://doi.org/10.1016/j.desal.2018.10.012.

[63] Y. Hao, Q. Li, B. He, B. Liao, X. Li, M. Hu, Y. Ji, Z. Cui, M. Younas, J. Li, An ultrahighly permeable-selective nanofiltration membrane mediated by an in situ formed interlayer, J. Mater. Chem. A. 8 (2020) 5275–5283. https://doi.org/10.1039/C9TA12258C.

[64] Y. Li, C. Li, S. Li, B. Su, L. Han, B. Mandal, Graphene oxide (GO)-interlayered thin-film

nanocomposite (TFN) membranes with high solvent resistance for organic solvent nanofiltration (OSN), J. Mater. Chem. A. 7 (2019) 13315–13330. https://doi.org/10.1039/C9TA01915D.

[65] C. Li, S. Li, J. Zhang, C. Yang, B. Su, L. Han, X. Gao, Emerging sandwich-like reverse osmosis membrane with interfacial assembled covalent organic frameworks interlayer for highly-efficient desalination, J. Memb. Sci. 604 (2020) 118065. https://doi.org/10.1016/j.memsci.2020.118065.

[66] X. Zhang, Y. Lv, H.-C.C. Yang, Y. Du, Z.-K.K. Xu, Polyphenol coating as an interlayer for thin-film composite membranes with enhanced nanofiltration performance, ACS Appl. Mater. Interfaces. 8 (2016) 32512–32519. https://doi.org/10.1021/acsami.6b10693.

[67] M.-B.B. Wu, Y. Lv, H.-C.C. Yang, L.-F.F. Liu, X. Zhang, Z.-K.K. Xu, Thin film composite membranes combining carbon nanotube intermediate layer and microfiltration support for high nanofiltration performances, J. Memb. Sci. 515 (2016) 238–244. https://doi.org/10.1016/j.memsci.2016.05.056.

[68] L. Wang, M. Fang, J. Liu, J. He, J. Li, J. Lei, Layer-by-Layer Fabrication of High-Performance Polyamide/ZIF-8 Nanocomposite Membrane for Nanofiltration Applications, ACS Appl. Mater. Interfaces. 7 (2015) 24082–24093. https://doi.org/10.1021/acsami.5b07128.

[69] F. Yu, H. Shi, J. Shi, K. Teng, Z. Xu, X. Qian, High-performance forward osmosis membrane with ultra-fast water transport channel and ultra-thin polyamide layer, J. Memb. Sci. 616 (2020) 118611. https://doi.org/10.1016/j.memsci.2020.118611.

[70] X.W. Liu, Y. Cao, Y.X. Li, Z.L. Xu, Z. Li, M. Wang, X.H. Ma, High-performance polyamide/ceramic hollow fiber TFC membranes with TiO 2 interlayer for pervaporation dehydration of isopropanol solution, J. Memb. Sci. 576 (2019) 26–35. https://doi.org/10.1016/j.memsci.2019.01.023.

[71] Y. Zhu, W. Xie, S. Gao, F. Zhang, W. Zhang, Z. Liu, J. Jin, Single-Walled Carbon Nanotube Film Supported Nanofiltration Membrane with a Nearly 10 nm Thick Polyamide Selective Layer for High-Flux and High-Rejection Desalination, Small. 12 (2016) 5034–5041. https://doi.org/10.1002/smll.201601253.

[72] Z. Yang, Z.W. Zhou, H. Guo, Z. Yao, X.H. Ma, X. Song, S.P. Feng, C.Y. Tang, Tannic

Acid/Fe 3+ Nanoscaffold for Interfacial Polymerization: Toward Enhanced Nanofiltration Performance, Environ. Sci. Technol. 52 (2018) 9341–9349. https://doi.org/10.1021/acs.est.8b02425.

[73] M. Wu, J. Yuan, H. Wu, Y. Su, H. Yang, X. You, R. Zhang, X. He, N.A. Khan, R. Kasher, Z. Jiang, Ultrathin nanofiltration membrane with polydopamine-covalent organic framework interlayer for enhanced permeability and structural stability, J. Memb. Sci. 576 (2019) 131–141. https://doi.org/10.1016/j.memsci.2019.01.040.

[74] J. Yuan, M. Wu, H. Wu, Y. Liu, X. You, R. Zhang, Y. Su, H. Yang, J. Shen, Z. Jiang, Covalent organic framework-modulated interfacial polymerization for ultrathin desalination membranes, J. Mater. Chem. A. 7 (2019) 25641–25649. https://doi.org/10.1039/C9TA08163A.

[75] G. Gong, P. Wang, Z. Zhou, Y. Hu, New Insights into the Role of an Interlayer for the Fabrication of Highly Selective and Permeable Thin-Film Composite Nanofiltration Membrane, ACS Appl. Mater. Interfaces. 11 (2019) 7349–7356. https://doi.org/10.1021/acsami.8b18719.

[76] F. Luo, J. Wang, Z. Yao, L. Zhang, H. Chen, Polydopamine nanoparticles modified nanofiber supported thin film composite membrane with enhanced adhesion strength for forward osmosis, J. Memb. Sci. 618 (2021) 118673. https://doi.org/10.1016/j.memsci.2020.118673.

[77] X. Yang, Y. Du, X. Zhang, A. He, Z.K. Xu, Nanofiltration Membrane with a Mussel-Inspired Interlayer for Improved Permeation Performance, Langmuir. 33 (2017) 2318–2324. https://doi.org/10.1021/acs.langmuir.6b04465.

[78] Z. Wang, W. Fang, F. Zhang, Y. Zhu, J. Jin, Ultrathin Nanofiltration Membrane from Confined Polymerization within the Nanowire Network for High Efficiency Divalent Cation Removal, ACS Macro Lett. 8 (2019) 1240–1246. https://doi.org/10.1021/acsmacrolett.9b00624.

[79] Y. Ji, M. Zhang, K. Guan, J. Zhao, G. Liu, W. Jin, High-Performance CO_2 Capture through Polymer-Based Ultrathin Membranes, Adv. Funct. Mater. 29 (2019) 1900735. https://doi.org/10.1002/adfm.201900735.

[80] Y. Li, E. Wong, A. Volodine, C. Van Haesendonck, K. Zhang, B. Van Der Bruggen,

Nanofibrous hydrogel composite membranes with ultrafast transport performance for molecular separation in organic solvents, J. Mater. Chem. A. 7 (2019) 19269–19279. https://doi.org/10.1039/c9ta06169j.

[81] L. Gui, J. Dong, W. Fang, S. Zhang, K. Zhou, Y. Zhu, Y. Zhang, J. Jin, [ASAP] Ultrafast Ion Sieving from Honeycomb-like Polyamide Membranes Formed Using Porous Protein Assemblies, Nano Lett. (n.d.). https://doi.org/10.1021/acs.nanolett.0c01350.

[82] M. Weber, A. Julbe, A. Ayral, P. Miele, M. Bechelany, Atomic Layer Deposition for Membranes: Basics, Challenges, and Opportunities, Chem. Mater. 30 (2018) 7368–7390. https://doi.org/10.1021/acs.chemmater.8b02687.

[83] Q. Xu, Y. Yang, X. Wang, Z. Wang, W. Jin, J. Huang, Y. Wang, Atomic layer deposition of alumina on porous polytetrafluoroethylene membranes for enhanced hydrophilicity and separation performances, J. Memb. Sci. 415–416 (2012) 435–443. https://doi.org/10.1016/j.memsci.2012.05.031.

[84] H. Chen, S. Wu, X. Jia, S. Xiong, Y. Wang, Atomic layer deposition fabricating of ceramic nanofiltration membranes for efficient separation of dyes from water, AIChE J. 64 (2018) 2670–2678. https://doi.org/10.1002/aic.16097.

[85] J. Feng, S. Xiong, Z. Wang, Z. Cui, S. Sun, Y. Wang, Atomic layer deposition of metal oxides on carbon nanotube fabrics for robust , hydrophilic ultra fi ltration membranes, J. Memb. Sci. 550 (2018) 246–253. https://doi.org/10.1016/j.memsci.2018.01.003.

[86] F. Li, Y. Yang, Y. Fan, W. Xing, Y. Wang, Modification of ceramic membranes for pore structure tailoring : The atomic layer deposition route, J. Memb. Sci. 397–398 (2012) 17–23. https://doi.org/10.1016/j.memsci.2012.01.005.

[87] X. Zhou, Y.Y. Zhao, S.-R.R. Kim, M. Elimelech, S. Hu, J.H. Kim, Controlled TiO 2 Growth on Reverse Osmosis and Nanofiltration Membranes by Atomic Layer Deposition: Mechanisms and Potential Applications, Environ. Sci. Technol. 52 (2018) 14311–14320. https://doi.org/10.1021/acs.est.8b03967.

[88] P. Juholin, M. Kääriäinen, M. Riihimäki, R. Sliz, J.L. Aguirre, M. Pirilä, T. Fabritius, D. Cameron, R.L. Keiski, Comparison of ALD coated nanofiltration membranes to unmodified commercial membranes in mine wastewater treatment, Sep. Purif. Technol. 192 (2018) 69–77.

https://doi.org/10.1016/j.seppur.2017.09.005.

[89] J. Nikkola, J. Sievänen, M. Raulio, J. Wei, J. Vuorinen, C.Y. Tang, Surface modification of thin film composite polyamide membrane using atomic layer deposition method, J. Memb. Sci. 450 (2014) 174–180. https://doi.org/10.1016/j.memsci.2013.09.005.

[90] H. Wang, M. Wei, Z. Zhong, Y. Wang, Atomic-layer-deposition-enabled thin-film composite membranes of polyimide supported on nanoporous anodized alumina, J. Memb. Sci. 535 (2017) 56–62. https://doi.org/10.1016/j.memsci.2017.04.026.

[91] D.L. Zhao, S. Japip, Y. Zhang, M. Weber, C. Maletzko, T.S. Chung, Emerging thin-film nanocomposite (TFN) membranes for reverse osmosis: A review, Water Res. 173 (2020) 115557. https://doi.org/10.1016/j.watres.2020.115557.

[92] Y. Cheng, Y. Ying, S. Japip, S.-D. Jiang, T.-S. Chung, S. Zhang, D. Zhao, Advanced Porous Materials in Mixed Matrix Membranes, Adv. Mater. 30 (2018) 1802401. https://doi.org/10.1002/adma.201802401.

[93] D. Ling, S. Japip, Y. Zhang, M. Weber, C. Maletzko, T. Chung, Emerging thin- fi lm nanocomposite (TFN) membranes for reverse osmosis : A review, Water Res. 173 (2020) 115557. https://doi.org/10.1016/j.watres.2020.115557.

[94] B. Khorshidi, I. Biswas, T. Ghosh, T. Thundat, M. Sadrzadeh, Robust fabrication of thin film polyamide-TiO2 nanocomposite membranes with enhanced thermal stability and anti-biofouling propensity, Sci. Rep. 8 (2018) 784. https://doi.org/10.1038/s41598-017-18724-w.

[95] H. Saleem, S.J. Zaidi, Nanoparticles in reverse osmosis membranes for desalination : A state of the art review, Desalination. 475 (2020) 114171. https://doi.org/10.1016/j.desal.2019.114171.

[96] H. Huang, X. Qu, H. Dong, L. Zhang, H. Chen, Role of NaA zeolites in the interfacial polymerization process towards a polyamide nanocomposite reverse osmosis membrane, RSC Adv. 3 (2013) 8203–8207. https://doi.org/10.1039/c3ra40960k.

[97] M. Kumar, M. Grzelakowski, J. Zilles, M. Clark, W. Meier, Highly permeable polymeric membranes based on the incorporation of the functional water channel protein Aquaporin Z, Proc. Natl. Acad. Sci. U. S. A. 104 (2007) 20719–20724. https://doi.org/10.1073/pnas.0708762104.

[98] G. Zhu, D.O. Nolan, R.P. Lively, Molecularly Mixed Composite Membranes : Challenges and Opportunities, (2020) 3464–3473. https://doi.org/10.1002/chem.201903519.

[99] W. Caseri, Nanocomposites of polymers and metals or semiconductors: Historical background and optical properties, Macromol. Rapid Commun. 21 (2000) 705–722. https://doi.org/10.1002/1521-3927(20000701)21:11<705::AID-MARC705>3.0.CO;2-3.

[100] M. Kumar, M.A. Khan, H.A. Arafat, Recent Developments in the Rational Fabrication of Thin Film Nanocomposite Membranes for Water Purification and Desalination, ACS Omega. 5 (2020) 3792–3800. https://doi.org/10.1021/acsomega.9b03975.

[101] W.J. Lau, S. Gray, T. Matsuura, D. Emadzadeh, J.P. Chen, A.F. Ismail, J. Paul Chen, A.F. Ismail, J.P. Chen, A.F. Ismail, J. Paul Chen, A.F. Ismail, A review on polyamide thin film nanocomposite (TFN) membranes: History, applications, challenges and approaches, Water Res. 80 (2015) 306–324. https://doi.org/10.1016/j.watres.2015.04.037.

[102] W.J. Lau, A.F. Ismail, P.S. Goh, N. Hilal, B.S. Ooi, Characterization methods of thin film composite nanofiltration membranes, Sep. Purif. Rev. 44 (2015) 135–156. https://doi.org/10.1080/15422119.2014.882355.

[103] J. Zhao, G. He, G. Liu, F. Pan, H. Wu, Progress in Polymer Science Manipulation of interactions at membrane interfaces for energy and environmental applications, Prog. Polym. Sci. 80 (2018) 125–152. https://doi.org/10.1016/j.progpolymsci.2017.12.002.

[104] H. Zhang, X.Y. Gong, W.X. Li, X.H. Ma, C.Y. Tang, Z.-L.L. Xu, Thin-film nanocomposite membranes containing tannic acid-Fe3+ modified MoS2 nanosheets with enhanced nanofiltration performance, J. Memb. Sci. 616 (2020) 118605. https://doi.org/10.1016/j.memsci.2020.118605.

[105] M. Ma, C. Zhang, C. Zhu, S. Huang, J. Yang, Z. Xu, Nanocomposite membranes embedded with functionalized MoS2 nanosheets for enhanced interfacial compatibility and nanofiltration performance, J. Memb. Sci. 591 (2019) 117316. https://doi.org/10.1016/j.memsci.2019.117316.

[106] M. Namvar-Mahboub, M. Pakizeh, S. Davari, Preparation and characterization of UZM-5/polyamide thin film nanocomposite membrane for dewaxing solvent recovery, J. Memb. Sci. 459 (2014) 22–32. https://doi.org/10.1016/j.memsci.2014.02.014.

[107] B. Rajaeian, A. Rahimpour, M.O. Tade, S. Liu, Fabrication and characterization of polyamide thin film nanocomposite (TFN) nanofiltration membrane impregnated with TiO2 nanoparticles, Desalination. 313 (2013) 176–188. https://doi.org/10.1016/j.desal.2012.12.012.

[108] C. Kong, T. Shintani, T. Tsuru, "Pre-seeding"-assisted synthesis of a high performance polyamide-zeolite nanocomposite membrane for water purification, New J. Chem. 34 (2010) 2101–2104. https://doi.org/10.1039/c0nj00581a.

[109] S. Jeon, J. Lee, Rationally designed in-situ fabrication of thin film nanocomposite membranes with enhanced desalination and anti-biofouling performance, J. Memb. Sci. (2020) 118542. https://doi.org/10.1016/j.memsci.2020.118542.

[110] W. Choi, S. Jeon, S.J. Kwon, H. Park, Y.I. Park, S.E. Nam, P.S. Lee, J.S. Lee, J. Choi, S. Hong, E.P. Chan, J.H. Lee, Thin film composite reverse osmosis membranes prepared via layered interfacial polymerization, J. Memb. Sci. 527 (2017) 121–128. https://doi.org/10.1016/j.memsci.2016.12.066.

[111] B. Wu, X. Li, D. An, S. Zhao, Y. Wang, Electro-casting aligned MWCNTs/polystyrene composite membranes for enhanced gas separation performance, J. Memb. Sci. 462 (2014) 62–68. https://doi.org/10.1016/j.memsci.2014.03.015.

[112] L. Wang, M.S.H. Boutilier, P.R. Kidambi, D. Jang, N.G. Hadjiconstantinou, R. Karnik, Fundamental transport mechanisms, fabrication and potential applications of nanoporous atomically thin membranes, Nat. Nanotechnol. 12 (2017) 509–522. https://doi.org/10.1038/nnano.2017.72.

[113] S.F. Anis, R. Hashaikeh, N. Hilal, Reverse osmosis pretreatment technologies and future trends: A comprehensive review, Desalination. 452 (2019) 159–195. https://doi.org/10.1016/j.desal.2018.11.006.

[114] S.S. Shenvi, A.M. Isloor, A.F.F. Ismail, A review on RO membrane technology: Developments and challenges, Desalination. 368 (2015) 10–26. https://doi.org/10.1016/j.desal.2014.12.042.

[115] G.R. Xu, J.M. Xu, H.J. Feng, H.L. Zhao, S.B. Wu, Tailoring structures and performance of polyamide thin film composite (PA-TFC) desalination membranes via sublayers adjustment-a review, Desalination. 417 (2017) 19–35. https://doi.org/10.1016/j.desal.2017.05.011.

[116] A.F.F. Ismail, M. Padaki, N. Hilal, T. Matsuura, W.J.J. Lau, Thin film composite membrane - Recent development and future potential, Desalination. 356 (2015) 140–148. https://doi.org/10.1016/j.desal.2014.10.042.

[117] J. Lee, R. Wang, T.H. Bae, High-performance reverse osmosis membranes fabricated on highly porous microstructured supports, Desalination. 436 (2018) 48–55. https://doi.org/10.1016/j.desal.2018.01.037.

[118] X. Zhao, J. Li, C. Liu, A novel TFC-type FO membrane with inserted sublayer of carbon nanotube networks exhibiting the improved separation performance, Desalination. 413 (2017) 176–183. https://doi.org/10.1016/j.desal.2017.03.021.

[119] S.F. Anis, R. Hashaikeh, N. Hilal, Functional materials in desalination: A review, Desalination. 468 (2019) 114077. https://doi.org/10.1016/j.desal.2019.114077.

[120] Q. Shi, L. Ni, Y. Zhang, X. Feng, Q. Chang, J. Meng, Poly(p-phenylene terephthamide) embedded in a polysulfone as the substrate for improving compaction resistance and adhesion of a thin film composite polyamide membrane, J. Mater. Chem. A. 5 (2017) 13610–13624. https://doi.org/10.1039/C7TA02552A.

[121] W. Zhao, H. Liu, Y. Liu, M. Jian, L. Gao, H. Wang, X. Zhang, Thin-Film Nanocomposite Forward-Osmosis Membranes on Hydrophilic Microfiltration Support with an Intermediate Layer of Graphene Oxide and Multiwall Carbon Nanotube, ACS Appl. Mater. Interfaces. 10 (2018) 34464–34474. https://doi.org/10.1021/acsami.8b10550.

[122] N.P. Dasgupta, L. Li, X. Sun, Atomic Layer Deposition for Energy and Environmental Applications, Adv. Mater. Interfaces. 3 (2016) 2–3. https://doi.org/10.1002/admi.201600914.

[123] R.W. Johnson, A. Hultqvist, S.F. Bent, A brief review of atomic layer deposition : from fundamentals to applications, Biochem. Pharmacol. 17 (2014) 236–246. https://doi.org/10.1016/j.mattod.2014.04.026.

[124] H. Yang, R.Z. Waldman, Z. Chen, S.B. Darling, Atomic layer deposition for membrane interface engineering, Nanoscale. 10 (2018) 20505–20513. https://doi.org/10.1039/C8NR08114J.

[125] K. Kaliyappan, Z. Chen, Atomic-scale manipulation of electrode surface to construct extremely stable high-performance sodium ion capacitor, Nano Energy. 48 (2018) 107–116.

https://doi.org/10.1016/j.nanoen.2018.03.021.

[126] E. Bet-Moushoul, Y. Mansourpanah, K. Farhadi, M. Tabatabaei, TiO<inf>2</inf> nanocomposite based polymeric membranes: A review on performance improvement for various applications in chemical engineering processes, Chem. Eng. J. 283 (2016) 29–46. https://doi.org/10.1016/j.cej.2015.06.124.

[127] J. Sekulić, J.E. ten Elshof, D.H. A. Blank, A Microporous Titania Membrane for Nanofiltration and Pervaporation, Adv. Mater. 16 (2004) 1546–1550. https://doi.org/10.1002/adma.200306472.

[128] T. Tsuru, D. Hironaka, T. Yoshioka, M. Asaeda, Titania membranes for liquid phase separation: effect of surface charge on flux, Sep. Purif. Technol. 25 (2001) 307–314. https://doi.org/10.1016/S1383-5866(01)00057-0.

[129] Z. Song, M. Fathizadeh, Y. Huang, K.H. Chu, Y. Yoon, L. Wang, W.L. Xu, M. Yu, TiO2 nanofiltration membranes prepared by molecular layer deposition for water purification, J. Memb. Sci. 510 (2016) 72–78. https://doi.org/10.1016/j.memsci.2016.03.011.

[130] G. Lui, G. Li, X. Wang, G. Jiang, E. Lin, M. Fowler, A. Yu, Z. Chen, Flexible, three-dimensional ordered macroporous TiO 2 electrode with enhanced electrode–electrolyte interaction in high-power Li-ion batteries, Nano Energy. 24 (2016) 72–77. https://doi.org/10.1016/j.nanoen.2016.03.019.

[131] J. Alam, M. Alhoshan, L.A. Dass, A.K. Shukla, M.R. Muthumareeswaran, M. Hussain, A.S. Aldwayyan, Atomic layer deposition of TiO2 film on a polyethersulfone membrane: separation applications, J. Polym. Res. 23 (2016) 183. https://doi.org/10.1007/s10965-016-1063-9.

[132] G.S. Lai, W.J. Lau, P.S. Goh, Y.H. Tan, B.C. Ng, A.F. Ismail, A novel interfacial polymerization approach towards synthesis of graphene oxide-incorporated thin film nanocomposite membrane with improved surface properties, Arab. J. Chem. 12 (2019) 75–87. https://doi.org/10.1016/j.arabjc.2017.12.009.

[133] L. Huang, J.R. McCutcheon, Impact of support layer pore size on performance of thin film composite membranes for forward osmosis, J. Memb. Sci. 483 (2015) 25–33. https://doi.org/10.1016/j.memsci.2015.01.025.

[134] W.H.J. Vaes, E.U. Ramos, H.J.M. Verhaar, C.J. Cramer, J.L.M. Hermens, Understanding and estimating membrane/water partition coefficients: Approaches to derive quantitative structure property relationships, Chem. Res. Toxicol. 11 (1998) 847–854. https://doi.org/10.1021/tx970210y.

[135] Y. Jun, H. Zarrin, M. Fowler, Z. Chen, Functionalized titania nanotube composite membranes for high temperature proton exchange membrane fuel cells, Int. J. Hydrogen Energy. 36 (2011) 6073–6081. https://doi.org/10.1016/j.ijhydene.2011.02.030.

[136] Z. Jiang, S. Karan, A.G. Livingston, Water Transport through Ultrathin Polyamide Nanofilms Used for Reverse Osmosis, Adv. Mater. 30 (2018) 1705973. https://doi.org/10.1002/adma.201705973.

[137] X. Liang, L.F. Hakim, G.D. Zhan, J.A. McCormick, S.M. George, A.W. Weimer, J.A. Spencer, K.J. Buechler, J. Blackson, C.J. Wood, J.R. Dorgan, Novel processing to produce polymer/ceramic nanocomposites by atomic layer deposition, J. Am. Ceram. Soc. 90 (2007) 57–63. https://doi.org/10.1111/j.1551-2916.2006.01359.x.

[138] X. Liang, D.M. King, P. Li, A.W. Weimer, Low-temperature atomic layer-deposited TiO 2 films with low photoactivity, J. Am. Ceram. Soc. 92 (2009) 649–654. https://doi.org/10.1111/j.1551-2916.2009.02940.x.

[139] H.C. Guo, E. Ye, Z. Li, M.Y. Han, X.J. Loh, Recent progress of atomic layer deposition on polymeric materials, Mater. Sci. Eng. C. 70 (2017) 1182–1191. https://doi.org/10.1016/j.msec.2016.01.093.

[140] A. Spende, N. Sobel, M. Lukas, R. Zierold, J.C. Riedl, L. Gura, I. Schubert, J.M.M. Moreno, K. Nielsch, B. Stühn, C. Hess, C. Trautmann, M.E. Toimil-Molares, TiO 2 , SiO 2 , and Al 2 O 3 coated nanopores and nanotubes produced by ALD in etched ion-track membranes for transport measurements, Nanotechnology. 26 (2015) 335301. https://doi.org/10.1088/0957-4484/26/33/335301.

[141] A. Rahtu, M. Ritala, Reaction mechanism studies on the zirconium chloride-water atomic layer deposition process, J. Mater. Chem. 12 (2002) 1484–1489. https://doi.org/10.1039/b109846b.

[142] R. Hussin, K.L. Choy, X. Hou, Deposited Tio2 thin films by atomic layer deposition (ALD)

for optical properties, ARPN J. Eng. Appl. Sci. 11 (2016) 7529–7533. http://www.arpnjournals.org/jeas/research_papers/rp_2016/jeas_0616_4470.pdf.

[143] J. Aarik, A. Aidla, T. Uustare, M. Ritala, M. Leskelä, Titanium isopropoxide as a precursor for atomic layer deposition: characterization of titanium dioxide growth process, Appl. Surf. Sci. 161 (2000) 385–395. https://doi.org/10.1016/S0169-4332(00)00274-9.

[144] P. Vouros, K. Biemann, The structural significance of doubly charged ion spectra. Phenylenediamine derivatives, Org. Mass Spectrom. 2 (1969) 375–386. https://doi.org/10.1002/oms.1210020406.

[145] A. Nowbahar, V. Mansard, J.M. Mecca, M. Paul, T. Arrowood, T.M. Squires, Measuring Interfacial Polymerization Kinetics Using Microfluidic Interferometry, J. Am. Chem. Soc. 140 (2018) 3173–3176. https://doi.org/10.1021/jacs.7b12121.

[146] V. Freger, Kinetics of Film Formation by Interfacial Polycondensation, Langmuir. 21 (2005) 1884–1894. https://doi.org/10.1021/la048085v.

[147] V. Freger, Nanoscale heterogeneity of polyamide membranes formed by interfacial polymerization, Langmuir. 19 (2003) 4791–4797. https://doi.org/10.1021/la020920q.

[148] Z.X. Low, Y.T. Chua, B.M. Ray, D. Mattia, I.S. Metcalfe, D.A. Patterson, Perspective on 3D printing of separation membranes and comparison to related unconventional fabrication techniques, J. Memb. Sci. 523 (2017) 596–613. https://doi.org/10.1016/j.memsci.2016.10.006.

[149] M. Fathizadeh, A. Aroujalian, A. Raisi, Effect of added NaX nano-zeolite into polyamide as a top thin layer of membrane on water flux and salt rejection in a reverse osmosis process, J. Memb. Sci. 375 (2011) 88–95. https://doi.org/10.1016/j.memsci.2011.03.017.

[150] H. Zhao, S. Qiu, L. Wu, L. Zhang, H. Chen, C. Gao, Improving the performance of polyamide reverse osmosis membrane by incorporation of modified multi-walled carbon nanotubes, J. Memb. Sci. 450 (2014) 249–256. https://doi.org/10.1016/j.memsci.2013.09.014.

[151] X. Gao, Y. Li, X. Yang, Y. Shang, Y. Wang, B. Gao, Z. Wang, Highly permeable and antifouling reverse osmosis membranes with acidified graphitic carbon nitride nanosheets as nanofillers, J. Mater. Chem. A. 5 (2017) 19875–19883. https://doi.org/10.1039/C7TA06348B.

[152] X. Song, Q. Zhou, T. Zhang, H. Xu, Z. Wang, Pressure-assisted preparation of graphene oxide quantum dot-incorporated reverse osmosis membranes: antifouling and chlorine resistance

potentials, J. Mater. Chem. A. 4 (2016) 16896–16905. https://doi.org/10.1039/C6TA06636D.

[153] J. Yin, G. Zhu, B. Deng, Graphene oxide (GO) enhanced polyamide (PA) thin-film nanocomposite (TFN) membrane for water purification, Desalination. 379 (2016) 93–101. https://doi.org/10.1016/j.desal.2015.11.001.

[154] J. Zhu, J. Hou, S. Yuan, Y. Zhao, Y. Li, R. Zhang, M. Tian, J. Li, J. Wang, B. Van der Bruggen, MOF-positioned polyamide membranes with a fishnet-like structure for elevated nanofiltration performance, J. Mater. Chem. A. 7 (2019) 16313–16322. https://doi.org/10.1039/C9TA02299F.

[155] N.A. Khan, J. Yuan, H. Wu, T. Huang, X. You, A.U. Rahman, C.S. Azad, M.A. Olson, Z. Jiang, Covalent Organic Framework Nanosheets as Reactive Fillers To Fabricate Free-Standing Polyamide Membranes for Efficient Desalination, ACS Appl. Mater. Interfaces. 12 (2020) 27777–27785. https://doi.org/10.1021/acsami.0c06417.

[156] H. Dou, M. Xu, B. Wang, Z. Zhang, G. Wen, Y. Zheng, D. Luo, L. Zhao, A. Yu, L. Zhang, Z. Jiang, Z. Chen, Microporous framework membranes for precise molecule/ion separations, Chem. Soc. Rev. 50 (2021) 986–1029. https://doi.org/10.1039/d0cs00552e.

[157] Y.T. Chew, W.F. Yong, Recent advances of thin film nanocomposite membranes: Effects of shape/structure of nanomaterials and interfacial polymerization methods, Chem. Eng. Res. Des. 172 (2021) 135–158. https://doi.org/10.1016/j.cherd.2021.06.003.

[158] Z.C. Ng, W.J. Lau, T. Matsuura, A.F. Ismail, Thin film nanocomposite RO membranes: Review on fabrication techniques and impacts of nanofiller characteristics on membrane properties, Chem. Eng. Res. Des. 165 (2021) 81–105. https://doi.org/10.1016/j.cherd.2020.10.003.

[159] N. Akther, S. Phuntsho, Y. Chen, N. Ghaffour, H.K. Shon, Recent advances in nanomaterial-modified polyamide thin-film composite membranes for forward osmosis processes, J. Memb. Sci. 584 (2019) 20–45. https://doi.org/10.1016/j.memsci.2019.04.064.

[160] J. Yin, B. Deng, Polymer-matrix nanocomposite membranes for water treatment, J. Memb. Sci. 479 (2015) 256–275. https://doi.org/10.1016/j.memsci.2014.11.019.

[161] K. Liu, C. Kei, M. Mishra, P. Chen, W. Liu, T. Perng, Uniform coating of TiO 2 on high aspect ratio substrates with complex morphology by vertical forced- fl ow atomic layer

deposition, (2017) 34730–34735. https://doi.org/10.1039/c7ra04853j.

[162] Z. Liao, J. Zhu, X. Li, B. Van der Bruggen, Regulating composition and structure of nanofillers in thin film nanocomposite (TFN) membranes for enhanced separation performance: A critical review, Sep. Purif. Technol. 266 (2021) 118567. https://doi.org/10.1016/j.seppur.2021.118567.

[163] H.E. Karahan, K. Goh, C. (John) Zhang, E. Yang, C. Yıldırım, C.Y. Chuah, M.G. Ahunbay, J. Lee, Ş.B. Tantekin-Ersolmaz, Y. Chen, T. Bae, MXene Materials for Designing Advanced Separation Membranes, Adv. Mater. 32 (2020) 1906697. https://doi.org/10.1002/adma.201906697.

[164] M. Mozafari, A. Arabi Shamsabadi, A. Rahimpour, M. Soroush, Ion-Selective MXene-Based Membranes: Current Status and Prospects, Adv. Mater. Technol. 2001189 (2021) 1–28. https://doi.org/10.1002/admt.202001189.

[165] H. Riazi, S.K. Nemani, M.C. Grady, B. Anasori, M. Soroush, Ti 3 C 2 MXene–polymer nanocomposites and their applications, J. Mater. Chem. A. (2021). https://doi.org/10.1039/D0TA08023C.

[166] X. Wang, Q. Li, J. Zhang, H. Huang, S. Wu, Y. Yang, Novel thin-film reverse osmosis membrane with MXene Ti3C2Tx embedded in polyamide to enhance the water flux, anti-fouling and chlorine resistance for water desalination, J. Memb. Sci. 603 (2020) 118036. https://doi.org/10.1016/j.memsci.2020.118036.

[167] X. Wu, L. Hao, J. Zhang, X. Zhang, J. Wang, J. Liu, Polymer-Ti3C2Tx composite membranes to overcome the trade-off in solvent resistant nanofiltration for alcohol-based system, J. Memb. Sci. 515 (2016) 175–188. https://doi.org/10.1016/j.memsci.2016.05.048.

[168] Z. Lu, Y. Wei, J. Deng, L. Ding, Z.K. Li, H. Wang, Self-Crosslinked MXene (Ti3C2Tx) Membranes with Good Antiswelling Property for Monovalent Metal Ion Exclusion, ACS Nano. 13 (2019) 10535–10544. https://doi.org/10.1021/acsnano.9b04612.

[169] L. Ding, Y. Wei, Y. Wang, H. Chen, J. Caro, H. Wang, A Two-Dimensional Lamellar Membrane: MXene Nanosheet Stacks, Angew. Chemie - Int. Ed. 56 (2017) 1825–1829. https://doi.org/10.1002/anie.201609306.

[170] L. Gao, C. Li, W. Huang, S. Mei, H. Lin, Q. Ou, Y. Zhang, J. Guo, F. Zhang, S. Xu, H. Zhang,

MXene/Polymer Membranes: Synthesis, Properties, and Emerging Applications, Chem. Mater. 32 (2020) 1703–1747. https://doi.org/10.1021/acs.chemmater.9b04408.

[171] A.A. Shamsabadi, A.P. Isfahani, S.K. Salestan, A. Rahimpour, B. Ghalei, E. Sivaniah, M. Soroush, Pushing Rubbery Polymer Membranes to Be Economic for CO2 Separation: Embedment with Ti3C2Tx MXene Nanosheets, ACS Appl. Mater. Interfaces. 12 (2020) 3984–3992. https://doi.org/10.1021/acsami.9b19960.

[172] M.C. Krecker, D. Bukharina, C.B. Hatter, Y. Gogotsi, V. V. Tsukruk, Bioencapsulated MXene Flakes for Enhanced Stability and Composite Precursors, Adv. Funct. Mater. 30 (2020) 1–10. https://doi.org/10.1002/adfm.202004554.

[173] J. Fei, S.W. Koh, W. Tu, J. Ge, H. Rezaeyan, S. Hou, H. Duan, Y.C. Lam, H. Li, Functionalized MXene Enabled Sustainable Water Harvesting and Desalination, Adv. Sustain. Syst. 4 (2020) 1–9. https://doi.org/10.1002/adsu.202000102.

[174] D. Wang, Y. Xin, Y. Wang, X. Li, H. Wu, W. Zhang, D. Yao, H. Wang, Y. Zheng, Z. He, Z. Yang, X. Lei, A general way to transform Ti3C2Tx MXene into solvent-free fluids for filler phase applications, Chem. Eng. J. 409 (2021). https://doi.org/10.1016/j.cej.2020.128082.

[175] W.Y. Chen, S.N. Lai, C.C. Yen, X. Jiang, D. Peroulis, L.A. Stanciu, Surface Functionalization of Ti3C2TxMXene with Highly Reliable Superhydrophobic Protection for Volatile Organic Compounds Sensing, ACS Nano. 14 (2020) 11490–11501. https://doi.org/10.1021/acsnano.0c03896.

[176] H. Riazi, M. Anayee, K. Hantanasirisakul, A.A. Shamsabadi, B. Anasori, Y. Gogotsi, M. Soroush, Surface Modification of a MXene by an Aminosilane Coupling Agent, Adv. Mater. Interfaces. 7 (2020) 1902008. https://doi.org/10.1002/admi.201902008.

[177] L. Hao, H. Zhang, X. Wu, J. Zhang, J. Wang, Y. Li, Novel thin-film nanocomposite membranes filled with multi-functional Ti 3 C 2 T x nanosheets for task-specific solvent transport, Compos. Part A Appl. Sci. Manuf. 100 (2017) 139–149. https://doi.org/10.1016/j.compositesa.2017.05.003.

[178] G. Liu, J. Shen, Y. Ji, Q. Liu, G. Liu, J. Yang, W. Jin, Two-dimensional Ti2CT: X MXene membranes with integrated and ordered nanochannels for efficient solvent dehydration, J. Mater. Chem. A. 7 (2019) 12095–12104. https://doi.org/10.1039/c9ta01507h.

[179] W. Yan, M. Shi, C. Dong, L. Liu, C. Gao, Applications of tannic acid in membrane technologies: A review, Adv. Colloid Interface Sci. 284 (2020) 102267. https://doi.org/10.1016/j.cis.2020.102267.

[180] M.P. Li, X. Zhang, H. Zhang, W.L. Liu, Z.H. Huang, F. Xie, X.H. Ma, Z.L. Xu, Hydrophilic yolk-shell ZIF-8 modified polyamide thin-film nanocomposite membrane with improved permeability and selectivity, Sep. Purif. Technol. 247 (2020) 116990. https://doi.org/10.1016/j.seppur.2020.116990.

[181] H.M. Hegab, A. Elmekawy, T.G. Barclay, A. Michelmore, L. Zou, D. Losic, C.P. Saint, M. Ginic-markovic, A Novel Fabrication Approach for Multifunctional Graphene-based Thin Film Nano-composite Membranes with Enhanced Desalination and Antibacterial Characteristics, Sci. Rep. 7 (2017) 1–10. https://doi.org/10.1038/s41598-017-07531-y.

[182] C. Zhang, K. Wei, W. Zhang, Y. Bai, Y. Sun, J. Gu, Graphene Oxide Quantum Dots Incorporated into a Thin Film Nanocomposite Membrane with High Flux and Antifouling Properties for Low-Pressure Nanofiltration, ACS Appl. Mater. Interfaces. 9 (2017) 11082–11094. https://doi.org/10.1021/acsami.6b12826.

[183] H.J. Kim, Y.S. Choi, M.Y. Lim, K.H. Jung, D.-G.G. Kim, J.J. Kim, H. Kang, J.C. Lee, Reverse osmosis nanocomposite membranes containing graphene oxides coated by tannic acid with chlorine-tolerant and antimicrobial properties, J. Memb. Sci. 514 (2016) 25–34. https://doi.org/10.1016/j.memsci.2016.04.026.

[184] L. Liu, C. Ge, Y. Zhang, W. Ma, X. Su, L. Chen, S. Li, L. Wang, X. Mu, Y. Xu, Tannic acid-modified silver nanoparticles for enhancing anti-biofilm activities and modulating biofilm formation, Biomater. Sci. 8 (2020) 4852–4860. https://doi.org/10.1039/d0bm00648c.

[185] H. Wu, H. Sun, W. Hong, L. Mao, Y. Liu, Improvement of Polyamide Thin Film Nanocomposite Membrane Assisted by Tannic Acid-FeIII Functionalized Multiwall Carbon Nanotubes, ACS Appl. Mater. Interfaces. 9 (2017) 32255–32263. https://doi.org/10.1021/acsami.7b09680.

[186] Z. Liao, X. Fang, J. Xie, Q. Li, D. Wang, X. Sun, L. Wang, J. Li, Hydrophilic Hollow Nanocube-Functionalized Thin Film Nanocomposite Membrane with Enhanced Nanofiltration Performance, ACS Appl. Mater. Interfaces. 11 (2019) 5344–5352. https://doi.org/10.1021/acsami.8b19121.

[187] X. Zhao, A. Vashisth, E. Prehn, W. Sun, S.A. Shah, T. Habib, Y. Chen, Z. Tan, J.L. Lutkenhaus, M. Radovic, M.J. Green, Antioxidants Unlock Shelf-Stable Ti3C2Tx (MXene) Nanosheet Dispersions, Matter. 1 (2019) 513–526. https://doi.org/10.1016/j.matt.2019.05.020.

[188] G.S. Lee, T. Yun, H. Kim, I.H. Kim, J. Choi, S.H. Lee, H.M.H.J.H.M. Lee, H.S. Hwang, J.G. Kim, D.W. Kim, H.M.H.J.H.M. Lee, C.M. Koo, S.O. Kim, Mussel Inspired Highly Aligned Ti3C2TxMXene Film with Synergistic Enhancement of Mechanical Strength and Ambient Stability, ACS Nano. 14 (2020) 11722–11732. https://doi.org/10.1021/acsnano.0c04411.

[189] K. Zarshenas, G. Jiang, J. Zhang, M.A.M.A. Jauhar, Z. Chen, Atomic scale manipulation of sublayer with functional TiO2 nanofilm toward high-performance reverse osmosis membrane, Desalination. 480 (2020) 114342. https://doi.org/10.1016/j.desal.2020.114342.

[190] B. Khorshidi, T. Thundat, D. Pernitsky, M. Sadrzadeh, permeation properties of thin fi lm composite polyamide membrane, J. Memb. Sci. 535 (2017) 248–257. https://doi.org/10.1016/j.memsci.2017.04.052.

[191] H. Ejima, J.J. Richardson, K. Liang, J.P. Best, M.P. Van Koeverden, G.K. Such, J. Cui, F. Caruso, One-step assembly of coordination complexes for versatile film and particle engineering, Science (80-.). 341 (2013) 154–157. https://doi.org/10.1126/science.1237265.

[192] M. Shin, H.A. Lee, M. Lee, Y. Shin, J.J. Song, S.W. Kang, D.H. Nam, E.J. Jeon, M. Cho, M. Do, S. Park, M.S. Lee, J.H. Jang, S.W. Cho, K.S. Kim, H. Lee, Targeting protein and peptide therapeutics to the heart via tannic acid modification, Nat. Biomed. Eng. 2 (2018) 304–317. https://doi.org/10.1038/s41551-018-0227-9.

[193] D. Wu, J. Zhou, M.N. Creyer, W. Yim, Z. Chen, P.B. Messersmith, J. V. Jokerst, Phenolic-enabled nanotechnology: versatile particle engineering for biomedicine, Chem. Soc. Rev. (2021). https://doi.org/10.1039/d0cs00908c.

[194] J. Saiz-Poseu, J. Mancebo-Aracil, F. Nador, F. Busqué, D. Ruiz-Molina, The Chemistry behind Catechol-Based Adhesion, Angew. Chemie - Int. Ed. 58 (2019) 696–714. https://doi.org/10.1002/anie.201801063.

[195] C. Doe, S.-M. Choi, S.R. Kline, H.-S. Jang, T.-H. Kim, Charged Rod-Like Nanoparticles Assisting Single-Walled Carbon Nanotube Dispersion in Water, Adv. Funct. Mater. 18 (2008) 2685–2691. https://doi.org/10.1002/adfm.200800321.

[196] C. Guibert, V. Dupuis, J. Fresnais, V. Peyre, Controlling nanoparticles dispersion in ionic liquids by tuning the pH, J. Colloid Interface Sci. 454 (2015) 105–111. https://doi.org/10.1016/j.jcis.2015.04.059.

[197] H. Abdel-shafy, M.S. Mohamed-mansour, Polyphenols: Properties, Occurrence, Content in Food and Potential Effects, Toxicology. 6 (2017) 232–261.

[198] G. Cheraghian, L. Hendraningrat, A review on applications of nanotechnology in the enhanced oil recovery part A: effects of nanoparticles on interfacial tension, Int. Nano Lett. 6 (2016) 129–138. https://doi.org/10.1007/s40089-015-0173-4.

[199] C. Klaysom, S. Hermans, A. Gahlaut, S. Van Craenenbroeck, I.F.J. Vankelecom, Polyamide/Polyacrylonitrile (PA/PAN) thin film composite osmosis membranes: Film optimization, characterization and performance evaluation, J. Memb. Sci. 445 (2013) 25–33. https://doi.org/10.1016/j.memsci.2013.05.037.

[200] X. Li, K.Y. Wang, B. Helmer, T.-S. Chung, Thin-Film Composite Membranes and Formation Mechanism of Thin-Film Layers on Hydrophilic Cellulose Acetate Propionate Substrates for Forward Osmosis Processes, Ind. Eng. Chem. Res. 51 (2012) 10039–10050. https://doi.org/10.1021/ie2027052.

[201] S. Abdikheibari, W. Lei, L.F. Dumée, N. Milne, K. Baskaran, Thin film nanocomposite nanofiltration membranes from amine functionalized-boron nitride/polypiperazine amide with enhanced flux and fouling resistance, J. Mater. Chem. A. 6 (2018) 12066–12081. https://doi.org/10.1039/c8ta03446j.

[202] B. Li, S. Japip, T.-S.S. Chung, Molecularly tunable thin-film nanocomposite membranes with enhanced molecular sieving for organic solvent forward osmosis, Nat. Commun. 11 (2020) 1–10. https://doi.org/10.1038/s41467-020-15070-w.

[203] X.-H.H. Ma, Z.K. Yao, Z. Yang, H. Guo, Z.L. Xu, C.Y. Tang, M. Elimelech, Nanofoaming of Polyamide Desalination Membranes to Tune Permeability and Selectivity, Environ. Sci. Technol. Lett. 5 (2018) 123–130. https://doi.org/10.1021/acs.estlett.8b00016.

[204] M.F. Ismail, B. Khorshidi, M. Sadrzadeh, New insights into the impact of nanoscale surface heterogeneity on the wettability of polymeric membranes, J. Memb. Sci. 590 (2019) 117270. https://doi.org/10.1016/j.memsci.2019.117270.

[205] C.Y. Tang, Y.-N.N. Kwon, J.O. Leckie, Effect of membrane chemistry and coating layer on physiochemical properties of thin film composite polyamide RO and NF membranes, Desalination. 242 (2009) 149–167. https://doi.org/10.1016/j.desal.2008.04.003.

[206] G.N.B. Baroña, J. Lim, M. Choi, B. Jung, Interfacial polymerization of polyamide-aluminosilicate SWNT nanocomposite membranes for reverse osmosis, Desalination. 325 (2013) 138–147. https://doi.org/10.1016/j.desal.2013.06.026.

[207] G.S. Lai, W.J. Lau, S.R. Gray, T. Matsuura, R. Jamshidi Gohari, M.N. Subramanian, S.O. Lai, C.S. Ong, A.F. Ismail, D. Emazadah, M. Ghanbari, A practical approach to synthesize polyamide thin film nanocomposite (TFN) membranes with improved separation properties for water/wastewater treatment, J. Mater. Chem. A. 4 (2016) 4134–4144. https://doi.org/10.1039/c5ta09252c.

[208] P. Karami, B. Khorshidi, L. Shamaei, E. Beaulieu, J.B.P. Soares, M. Sadrzadeh, Nanodiamond-Enabled Thin-Film Nanocomposite Polyamide Membranes for High-Temperature Water Treatment, ACS Appl. Mater. Interfaces. 12 (2020) 53274–53285. https://doi.org/10.1021/acsami.0c15194.

[209] C. Buechner, S.M. Gericke, L. Trotochaud, O. Karslloğlu, J. Raso, H. Bluhm, Quantitative Characterization of a Desalination Membrane Model System by X-ray Photoelectron Spectroscopy, Langmuir. 35 (2019) 11315–11321. https://doi.org/10.1021/acs.langmuir.9b01838.

[210] H. Zheng, Z. Mou, K. Zhou, Incorporation of Core-Shell-Structured Zwitterionic Carbon Dots in Thin-Film Nanocomposite Membranes for Simultaneously Improved Perm-Selectivity and Antifouling Properties, ACS Appl. Mater. Interfaces. 12 (2020) 53215–53229. https://doi.org/10.1021/acsami.0c13386.

[211] K. Shen, W. Hua, S. Ding, X. Wang, Customizing versatile polyamide nanofiltration membrane by the incorporation of a novel glycolic acid inhibitor, Sep. Purif. Technol. 255 (2021) 117632. https://doi.org/10.1016/j.seppur.2020.117632.

[212] Y. Zhang, Y. Su, J. Peng, X. Zhao, J. Liu, J. Zhao, Z. Jiang, Composite nanofiltration membranes prepared by interfacial polymerization with natural material tannic acid and trimesoyl chloride, J. Memb. Sci. 429 (2013) 235–242. https://doi.org/10.1016/j.memsci.2012.11.059.

[213] H. Dou, M. Xu, B. Wang, Z. Zhang, D. Luo, B. Shi, G. Wen, M. Mousavi, A. Yu, Z. Bai, Z. Jiang, Z. Chen, Analogous Mixed Matrix Membranes with Self-Assembled Interface Pathways, Angew. Chemie - Int. Ed. 60 (2020) 5864–5870. https://doi.org/10.1002/anie.202014893.

[214] S.H. Kim, S.Y. Kwak, T. Suzuki, Positron annihilation spectroscopic evidence to demonstrate the flux-enhancement mechanism in morphology-controlled thin-film-composite (TFC) membrane, Environ. Sci. Technol. 39 (2005) 1764–1770. https://doi.org/10.1021/es049453k.

[215] D. Dutta, A. Bhattacharyya, B.N. Ganguly, Microstructural study of aromatic polyamide membrane material, J. Memb. Sci. 224 (2003) 127–135. https://doi.org/10.1016/j.memsci.2003.08.001.

[216] R.R. Sharma, S. Chellam, Temperature effects on the morphology of porous thin film composite nanofiltration membranes, Environ. Sci. Technol. 39 (2005) 5022–5030. https://doi.org/10.1021/es0501363.

[217] R. Zhang, Y. Liu, M. He, Y. Su, X. Zhao, M. Elimelech, Z. Jiang, Antifouling membranes for sustainable water purification: Strategies and mechanisms, Chem. Soc. Rev. 45 (2016) 5888–5924. https://doi.org/10.1039/c5cs00579e.

[218] R.R. Choudhury, J.M. Gohil, S. Mohanty, S.K. Nayak, Antifouling, fouling release and antimicrobial materials for surface modification of reverse osmosis and nanofiltration membranes, J. Mater. Chem. A. 6 (2018) 313–333. https://doi.org/10.1039/c7ta08627j.

[219] C. He, Z. Liu, J. Wu, X. Pan, Z. Fang, J. Li, B.A. Bryan, Future global urban water scarcity and potential solutions, Nat. Commun. 12 (2021) 1–11. https://doi.org/10.1038/s41467-021-25026-3.

[220] J.R. Werber, C.O. Osuji, M. Elimelech, Materials for next-generation desalination and water purification membranes, Nat. Rev. Mater. 1 (2016) 16018. https://doi.org/10.1038/natrevmats.2016.18.

[221] H.B. Park, J. Kamcev, L.M. Robeson, M. Elimelech, B.D. Freeman, Maximizing the right stuff: The trade-off between membrane permeability and selectivity, Science (80-.). 356 (2017) eaab0530. https://doi.org/10.1126/science.aab0530.

[222] Q. Gan, L.E. Peng, H. Guo, Z. Yang, C.Y. Tang, Cosolvent-Assisted Interfacial

Polymerization toward Regulating the Morphology and Performance of Polyamide Reverse Osmosis Membranes: Increased m-Phenylenediamine Solubility or Enhanced Interfacial Vaporization?, Environ. Sci. Technol. 56 (2022) 10308–10316. https://doi.org/10.1021/acs.est.2c01140.

[223] C. Kong, T. Shintani, T. Kamada, V. Freger, T. Tsuru, Co-solvent-mediated synthesis of thin polyamide membranes, J. Memb. Sci. 384 (2011) 10–16. https://doi.org/10.1016/j.memsci.2011.08.055.

[224] X.-H. Ma, Z. Yang, Z. Yao, H. Guo, Z. Xu, C.Y. Tang, Interfacial Polymerization with Electrosprayed Microdroplets: Toward Controllable and Ultrathin Polyamide Membranes, Environ. Sci. Technol. Lett. 5 (2018) 117–122. https://doi.org/10.1021/acs.estlett.7b00566.

[225] W. Choi, J.E. Gu, S.H. Park, S. Kim, J. Bang, K.Y. Baek, B. Park, J.S. Lee, E.P. Chan, J.H. Lee, Tailor-made polyamide membranes for water desalination, ACS Nano. 9 (2015) 345–355. https://doi.org/10.1021/nn505318v.

[226] S. Han, J. Zhu, A.A. Uliana, D. Li, Y. Zhang, L. Zhang, Y. Wang, T. He, M. Elimelech, Microporous organic nanotube assisted design of high performance nanofiltration membranes, Nat. Commun. 13 (2022) 7954. https://doi.org/10.1038/s41467-022-35681-9.

[227] Y. Wen, R. Dai, X. Li, X. Zhang, X. Cao, Z. Wu, S. Lin, C.Y. Tang, Z. Wang, Metal-organic framework enables ultraselective polyamide membrane for desalination and water reuse, Sci. Adv. 8 (2022) 1–12. https://doi.org/10.1126/sciadv.abm4149.

[228] S. Xue, C.W. Lin, C. Ji, Y. Guo, L. Liu, Z. Yang, S. Zhao, X. Cai, Q.J. Niu, R.B. Kaner, Thin-Film Composite Membranes with a Hybrid Dimensional Titania Interlayer for Ultrapermeable Nanofiltration, Nano Lett. 22 (2022) 1039–1046. https://doi.org/10.1021/acs.nanolett.1c04000.

[229] Z. Yang, P.F. Sun, X. Li, B. Gan, L. Wang, X. Song, H.D. Park, C.Y. Tang, A Critical Review on Thin-Film Nanocomposite Membranes with Interlayered Structure: Mechanisms, Recent Developments, and Environmental Applications, Environ. Sci. Technol. 54 (2020) 15563–15583. https://doi.org/10.1021/acs.est.0c05377.

[230] Y. Lu, R. Wang, Y. Zhu, Z. Wang, W. Fang, S. Lin, J. Jin, Two-dimensional fractal nanocrystals templating for substantial performance enhancement of polyamide nanofiltration membrane, Proc. Natl. Acad. Sci. U. S. A. 118 (2021) 1–7.

https://doi.org/10.1073/pnas.2019891118.

[231] B. Yuan, S. Zhao, P. Hu, J. Cui, Q.J. Niu, Asymmetric polyamide nanofilms with highly ordered nanovoids for water purification, Nat. Commun. 11 (2020) 1–12. https://doi.org/10.1038/s41467-020-19809-3.

[232] Q. Li, Z. Liao, J. Xie, L. Ni, C. Wang, J. Qi, X. Sun, L. Wang, J. Li, Enhancing nanofiltration performance by incorporating tannic acid modified metal-organic frameworks into thin-film nanocomposite membrane, Environ. Res. 191 (2020) 110215. https://doi.org/10.1016/j.envres.2020.110215.

[233] Y. Wen, X. Zhang, X. Li, Z. Wang, C.Y. Tang, Metal-Organic Framework Nanosheets for Thin-Film Composite Membranes with Enhanced Permeability and Selectivity, ACS Appl. Nano Mater. 3 (2020) 9238–9248. https://doi.org/10.1021/acsanm.0c01860.

[234] S. Cao, A. Deshmukh, L. Wang, Q. Han, Y. Shu, H.Y. Ng, Z. Wang, J.H. Lienhard, Enhancing the Permselectivity of Thin-Film Composite Membranes Interlayered with MoS2Nanosheets via Precise Thickness Control, Environ. Sci. Technol. 56 (2022) 8807–8818. https://doi.org/10.1021/acs.est.2c00551.

[235] X. Song, Y. Zhang, H.M. Abdel-Ghafar, E.S.A. Abdel-Aal, M. Huang, S. Gul, H. Jiang, Polyamide membrane with an ultrathin GO interlayer on macroporous substrate for minimizing internal concentration polarization in forward osmosis, Chem. Eng. J. 412 (2021) 128607. https://doi.org/10.1016/j.cej.2021.128607.

[236] L. Long, C. Wu, Z. Yang, C.Y. Tang, Carbon Nanotube Interlayer Enhances Water Permeance and Antifouling Performance of Nanofiltration Membranes: Mechanisms and Experimental Evidence, Environ. Sci. Technol. 56 (2022) 2656–2664. https://doi.org/10.1021/acs.est.1c07332.

[237] C. Xiang, W. Lu, Y. Zhu, Z. Sun, Z. Yan, C.C. Hwang, J.M. Tour, Carbon nanotube and graphene nanoribbon-coated conductive Kevlar fibers, ACS Appl. Mater. Interfaces. 4 (2012) 131–136. https://doi.org/10.1021/am201153b.

[238] E.Y. Jang, J. Carretero-González, A. Choi, W.J. Kim, M.E. Kozlov, T. Kim, T.J. Kang, S.J. Baek, D.W. Kim, Y.W. Park, R.H. Baughman, Y.H. Kim, Fibers of reduced graphene oxide nanoribbons, Nanotechnology. 23 (2012) 235601. https://doi.org/10.1088/0957-

4484/23/23/235601.

[239] E. Choi, S.J. Hong, Y.J. Kim, S.E. Choi, Y. Choi, J.H. Kim, J. Kang, O. Kwon, K. Eum, B. Han, D.W. Kim, Pore Tuning of Metal-Organic Framework Membrane Anchored on Graphene-Oxide Nanoribbon, Adv. Funct. Mater. 31 (2021) 1–8. https://doi.org/10.1002/adfm.202011146.

[240] Y. Choi, S.S. Kim, J.H. Kim, J. Kang, E. Choi, S.E. Choi, J.P. Kim, O. Kwon, D.W. Kim, Graphene Oxide Nanoribbon Hydrogel: Viscoelastic Behavior and Use as a Molecular Separation Membrane, ACS Nano. 14 (2020) 12195–12202. https://doi.org/10.1021/acsnano.0c05902.

[241] D.W. Kim, I. Kim, J. Jang, Y.T. Nam, K. Park, K.O. Kwon, K.M. Cho, J. Choi, D. Kim, K.M. Kang, S.J. Kim, Y. Jung, H.-T. Jung, (ESI) One Dimensional Building Block for Molecular Separation: Laminated Graphitic Nanoribbons Materials and methods, Nanoscale. (2017). http://www.rsc.org/suppdata/c7/nr/c7nr05737g/c7nr05737g1.pdf.

[242] D.K. James, J.M. Tour, The chemical synthesis of graphene nanoribbons-A tutorial review, Macromol. Chem. Phys. 213 (2012) 1033–1050. https://doi.org/10.1002/macp.201200001.

[243] J. Cai, T. Jin, J. Kou, S. Zou, J. Xiao, Q. Meng, Lucas-Washburn Equation-Based Modeling of Capillary-Driven Flow in Porous Systems, Langmuir. 37 (2021) 1623–1636. https://doi.org/10.1021/acs.langmuir.0c03134.

[244] M. Nasr, N. Alfryyan, S.S. Ali, H.M. Abd El-Salam, M. Shaban, Preparation, characterization, and performance of PES/GO woven mixed matrix nanocomposite forward osmosis membrane for water desalination, RSC Adv. 12 (2022) 25654–25668. https://doi.org/10.1039/d2ra03832c.

[245] H. Sun, COMPASS: An ab initio force-field optimized for condensed-phase applications. Overview with details on alkane and benzene compounds, J. Phys. Chem. B. 102 (1998) 7338.

[246] L. Jiao, L. Zhang, X. Wang, G. Diankov, H. Dai, Narrow graphene nanoribbons from carbon nanotubes, Nature. 458 (2009) 877–880. https://doi.org/10.1038/nature07919.

[247] X. You, K. Xiao, H. Wu, Y. Li, R. Li, J. Yuan, R. Zhang, Z. Zhang, X. Liang, J. Shen, Z. Jiang, Electrostatic-modulated interfacial polymerization toward ultra-permselective nanofiltration membranes, IScience. 24 (2021) 102369.

https://doi.org/10.1016/j.isci.2021.102369.

[248] C. Casiraghi, D. Prezzi, Raman Spectroscopy of Graphene Nanoribbons: A Review, Carbon Nanostructures. 0 (2017) 19–30. https://doi.org/10.1007/978-3-319-58134-7_2.

[249] S. Habibpour, J.G. Um, Y. seok Jun, P. Bhargava, C.B. Park, A. Yu, Structural Impact of Graphene Nanoribbon on Mechanical Properties and Anti-corrosion Performance of Polyurethane Nanocomposites, Chem. Eng. J. 405 (2021) 126858. https://doi.org/10.1016/j.cej.2020.126858.

[250] S.J. Kim, S. Kook, B.E. O'Rourke, J. Lee, M. Hwang, Y. Kobayashi, R. Suzuki, I.S. Kim, Characterization of pore size distribution (PSD) in cellulose triacetate (CTA) and polyamide (PA) thin active layers by positron annihilation lifetime spectroscopy (PALS) and fractional rejection (FR) method, J. Memb. Sci. 527 (2017) 143–151. https://doi.org/10.1016/j.memsci.2016.12.064.

[251] L.E. Peng, Z. Yao, Z. Yang, H. Guo, C.Y. Tang, Dissecting the Role of Substrate on the Morphology and Separation Properties of Thin Film Composite Polyamide Membranes: Seeing Is Believing, Environ. Sci. Technol. 54 (2020) 6978–6986. https://doi.org/10.1021/acs.est.0c01427.

[252] K.M. Cho, H.J. Lee, Y.T. Nam, Y.J. Kim, C. Kim, K.M. Kang, C.A. Ruiz Torres, D.W. Kim, H.T. Jung, Ultrafast-Selective Nanofiltration of an Hybrid Membrane Comprising Laminated Reduced Graphene Oxide/Graphene Oxide Nanoribbons, ACS Appl. Mater. Interfaces. 11 (2019) 27004–27010. https://doi.org/10.1021/acsami.9b09037.

[253] D.W. Kim, I. Kim, J. Jang, Y.T. Nam, K. Park, K.O. Kwon, K.M. Cho, J. Choi, D. Kim, K.M. Kang, S.J. Kim, Y. Jung, H.T. Jung, One dimensional building blocks for molecular separation: Laminated graphitic nanoribbons, Nanoscale. 9 (2017) 19114–19123. https://doi.org/10.1039/c7nr05737g.

[254] B. Tylkowski, I. Tsibranska, Overview of main techniques used for membrane characterization, J. Chem. Technol. Metall. 50 (2015) 3–12.

[255] Y. Zhao, X. Tong, J. Kim, T. Tong, C.H. Huang, Y. Chen, Capillary-Assisted Fabrication of Thin-Film Nanocomposite Membranes for Improved Solute-Solute Separation, Environ. Sci. Technol. 56 (2022) 5849–5859. https://doi.org/10.1021/acs.est.2c01728.

[256] G.A.J. Jeffrey, G.A. Jeffrey, An Introduction to Hydrogen Bonding, Oxford University Press, 1997.

[257] B. Khorshidi, T. Thundat, B.A. Fleck, M. Sadrzadeh, A novel approach toward fabrication of high performance thin film composite polyamide membranes, Sci. Rep. 6 (2016) 1–10. https://doi.org/10.1038/srep22069.

[258] M. Son, H.H. gyu Choi, L. Liu, E. Celik, H. Park, H.H. gyu Choi, Efficacy of carbon nanotube positioning in the polyethersulfone support layer on the performance of thin-film composite membrane for desalination, Chem. Eng. J. 266 (2015) 376–384. https://doi.org/10.1016/j.cej.2014.12.108.

[259] M. Fathizadeh, H.N. Tien, K. Khivantsev, Z. Song, F. Zhou, M. Yu, Polyamide/nitrogen-doped graphene oxide quantum dots (N-GOQD) thin film nanocomposite reverse osmosis membranes for high flux desalination, Desalination. 451 (2017) 1–8. https://doi.org/10.1016/j.desal.2017.07.014.

[260] W. Ma, A. Soroush, T.V.A. Luong, M.S. Rahaman, Cysteamine- and graphene oxide-mediated copper nanoparticle decoration on reverse osmosis membrane for enhanced anti-microbial performance, J. Colloid Interface Sci. 501 (2017) 330–340. https://doi.org/10.1016/j.jcis.2017.04.069.

[261] M. Ben-Sasson, X. Lu, E. Bar-Zeev, K.R. Zodrow, S. Nejati, G. Qi, E.P. Giannelis, M. Elimelech, In situ formation of silver nanoparticles on thin-film composite reverse osmosis membranes for biofouling mitigation, Water Res. 62 (2014) 260–270. https://doi.org/10.1016/j.watres.2014.05.049.

[262] G.L. Jadav, P.S. Singh, Synthesis of novel silica-polyamide nanocomposite membrane with enhanced properties, J. Memb. Sci. 328 (2009) 257–267. https://doi.org/10.1016/j.memsci.2008.12.014.

[263] H.R. Chae, J. Lee, C.H. Lee, I.C. Kim, P.K. Park, Graphene oxide-embedded thin-film composite reverse osmosis membrane with high flux, anti-biofouling, and chlorine resistance, J. Memb. Sci. 483 (2015) 128–135. https://doi.org/10.1016/j.memsci.2015.02.045.

[264] H. Mahdavi, A. Rahimi, Zwitterion functionalized graphene oxide / polyamide thin fi lm nanocomposite membrane : Towards improved anti-fouling performance for reverse osmosis

G RA P H I C A L AB S T R A C T, Desalination. 433 (2018) 94–107. https://doi.org/10.1016/j.desal.2018.01.031.

[265] L. Liu, G. Zhu, Z. Liu, C. Gao, Effect of MCM-48 nanoparticles on the performance of thin film nanocomposite membranes for reverse osmosis application, Desalination. 394 (2016) 72–82. https://doi.org/10.1016/j.desal.2016.04.028.

[266] L. Yu, W. Zhou, Y. Li, Q. Zhou, H. Xu, B. Gao, Z. Wang, Antibacterial Thin-Film Nanocomposite Membranes Incorporated with Graphene Oxide Quantum Dot-Mediated Silver Nanoparticles for Reverse Osmosis Application, ACS Sustain. Chem. Eng. 7 (2019) 8724–8734. https://doi.org/10.1021/acssuschemeng.9b00598.

Appendices

Appendix A. Supplementary material for chapter 3

a) Supplementary Figures

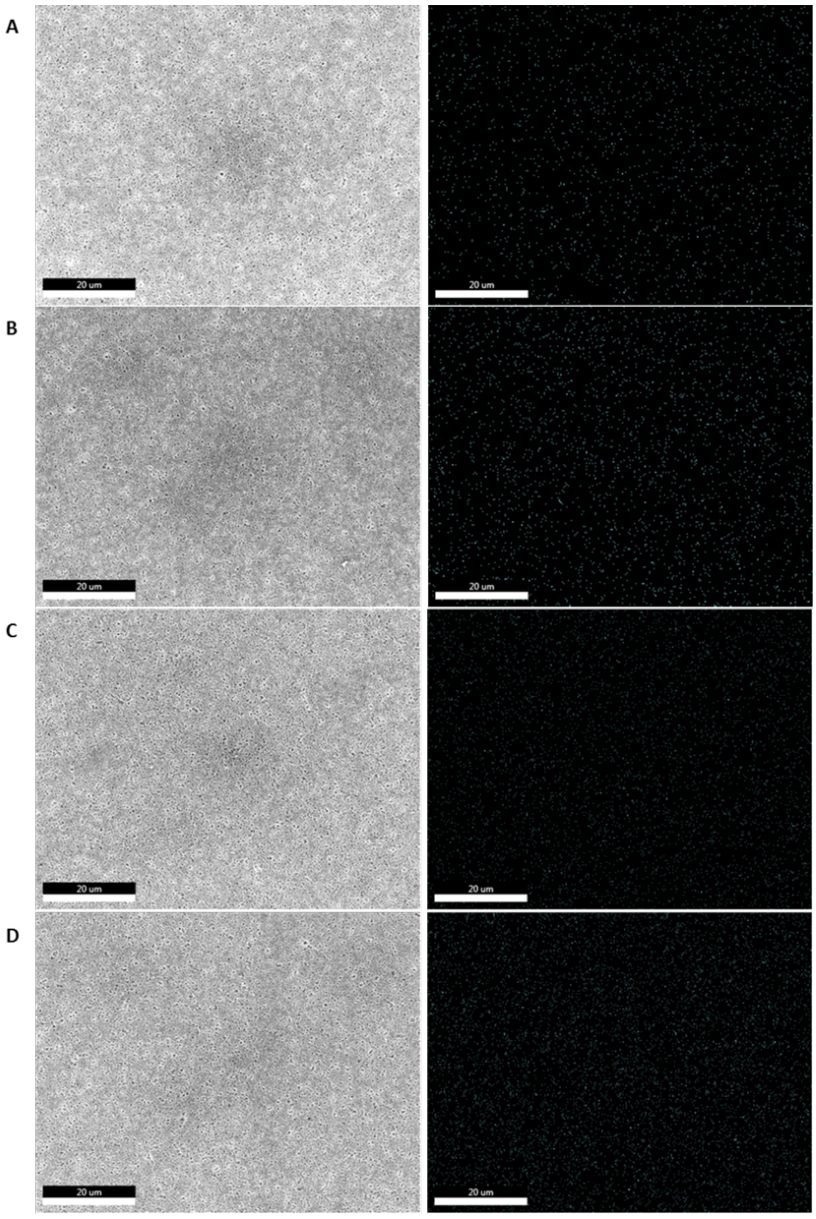

Figure S0-1. SEM image and EDX map scanning images of membrane surfaces: (A) ALD-10-TiO2@PES, (B) ALD-50-TiO2@PES, (C) ALD-100-TiO2@PES, (D) ALD-200-TiO2@PES.

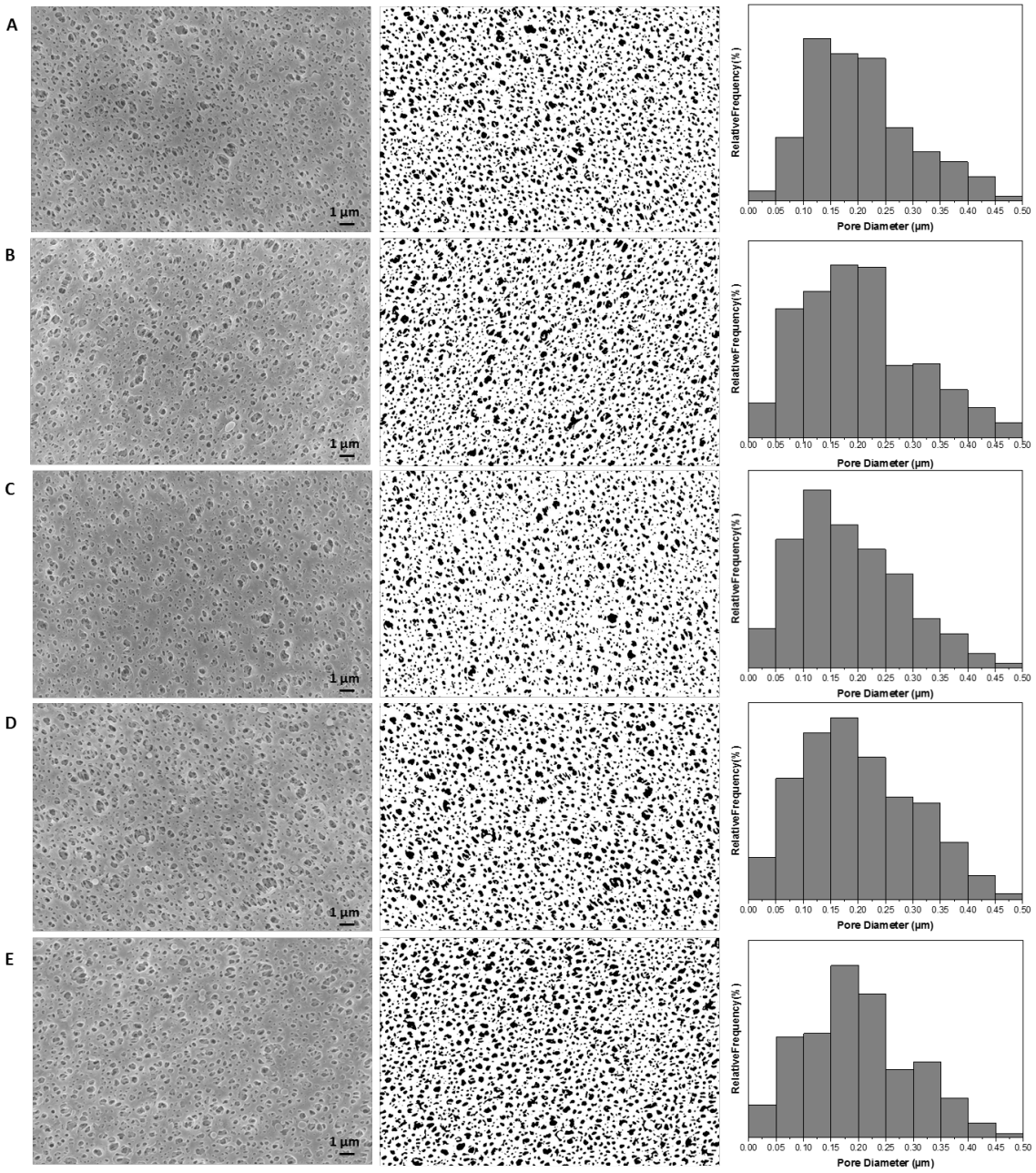

Figure S0-2. SEM surface images, the threshold images for SEM images, and pore size distribution of the sublayers (A)PES, (B)ALD-10-TiO2@PES, (C)ALD-50-TiO2@PES, (D)ALD-100-TiO2@PES, (E)ALD-200-TiO2@PES

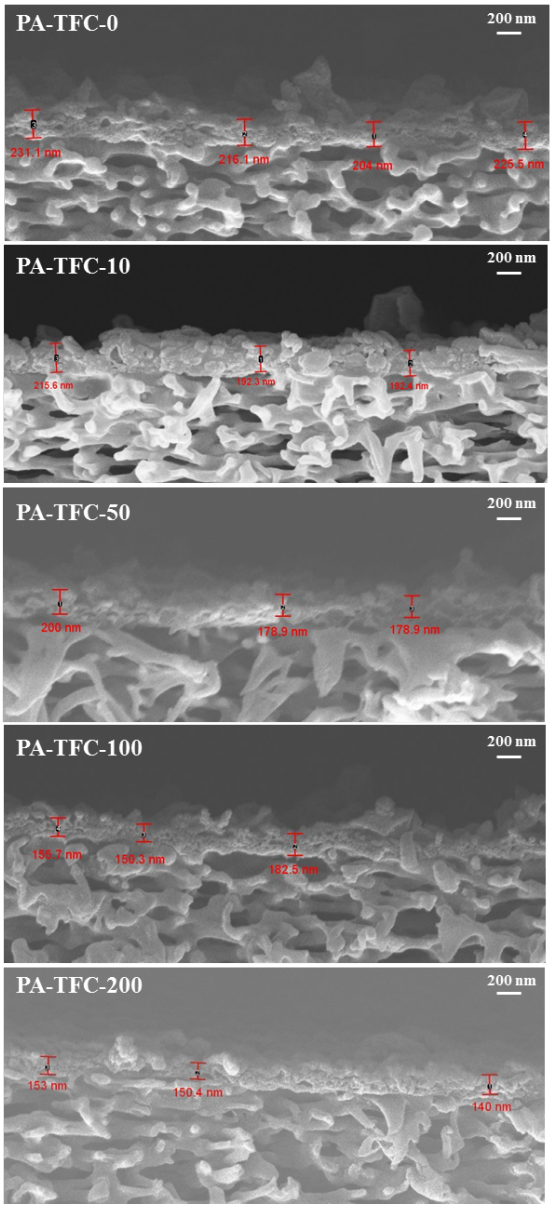

Figure S0-3. Cross-sectional SEM images of the PA-TFC membrane fabricated on substrates with different cycles of ALD.

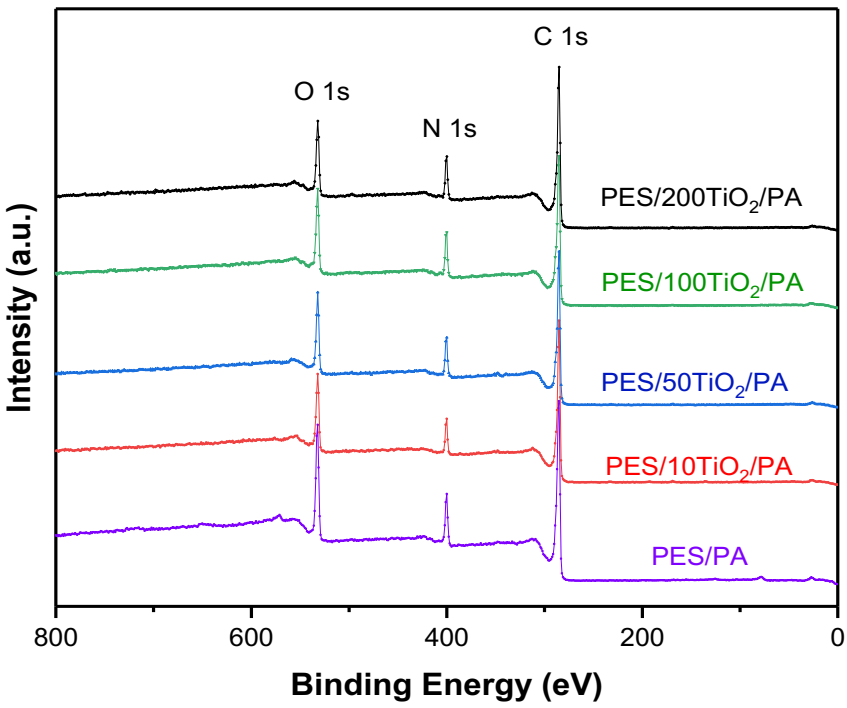

Figure S0-4. XPS survey spectra of the different TFC membranes.

b) Supplementary Tables

Table S0-1: Summary of properties of sublayer.

Sample	ALD cycle	Contact Angle (°)	Roughness	
			Ra (nm)	Rq (nm)
PES	0	62 ± 2	53.7 ± 8.1	73.2 ± 13.2
ALD-10-TiO_2@PES	10	40 ± 3	49.3 ± 6.3	66.1 ± 5.5
ALD-50-TiO_2@PES	50	36 ± 3	46.7 ± 2.8	64.8 ± 6.4
ALD-100-TiO_2@PES	100	27 ± 2	41.5 ± 4.9	57.9 ± 7.7
ALD-200-TiO_2@PES	200	11 ± 2	37.2 ± 5.8	47.7 ± 7.6

Table S0-2: Pure water flux of sublayers.

Sample	Flux ($L.m^{-2}.hr^{-1}.bar$)
PES	3375
ALD 100-TiO2 @ PES	3672
ALD 200-TiO2 @ PES	4119

Table S0-3: Physical properties of TFC membranes.

Sample	ALD cycle	Thickness (nm)	Roughness	
			R_a (nm)	R_q (nm)
PES	0	216.2 ± 12.57	81.76 ± 14.74	104.53 ± 17.25
ALD-10-TiO_2@PES	10	201 ± 10.8	74.96 ± 4.2	99.56 ± 6.27
ALD-50-TiO_2@PES	50	191.7 ± 10.2	70.46 ± 5.35	93.93 ± 7.08
ALD-100-TiO_2@PES	100	173.6 ± 10.7	69.02 ± 5.71	89.26 ± 8.04
ALD-200-TiO_2@PES	200	153.6 ± 9.6	54 ± 4.32	69 ± 5.04

Table S0-4: XPS analysis of TFC membranes.

sample	C1s (%)	N1s (%)	O1s (%)	O/N ratio	Crosslinking degree (%)
PA-TFC-0	70.13	11.28	17.47	1.55	35
PA-TFC-10	74.54	10.07	15.39	1.52	37
PA-TFC-50	73.32	11.35	15.33	1.35	55
PA-TFC-100	71.44	12.38	16.19	1.3	59
PA-TFC-200	73.78	11.92	14.3	1.2	72

Table S0-5: Performance of commercial and lab made RO membrane.

Membrane type	Permeability ($L.m^{-2}.h^{-1}.bar^{-1}$)	Salt Rejection (%)	Reference
Dow-SWHR	0.936	92	[38]
Dow-SW30	0.7	93.8	[136]
GE AG	2.45	90.2	[136]
TriSep X-20	2.7	93.2	[257]
Lab-made TFC	0.756	93.4	[38]
Lab-made fTFC	1.21	96.1	[258]
Lab-made TFC	0.72	93.1	[259]
PA-TFC-0	1.4	92.6	This work
PA-TFC-100	1.77	95.8	This work

Appendix B. Supplementary material for chapter 4

a) Supplementary Figures

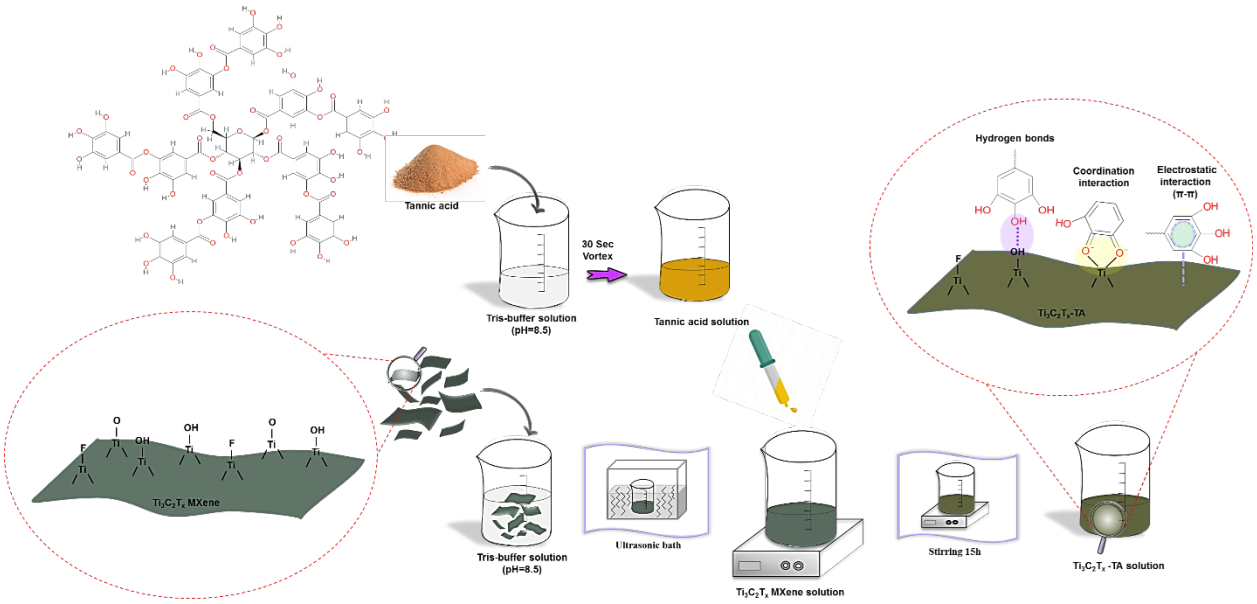

Figure S0-5. Schematic of modification procedure of $Ti_3C_2T_x$ MXene nanosheets by TA.

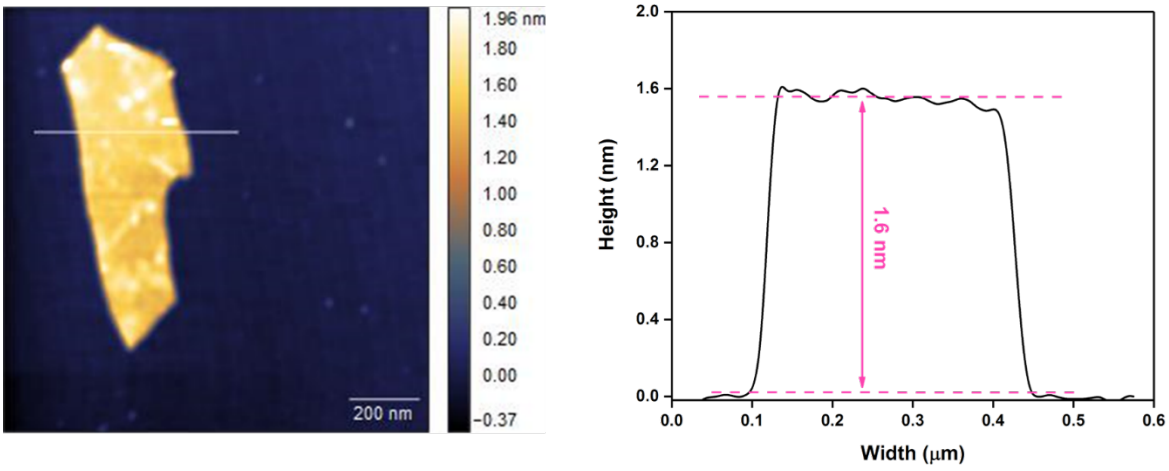

Figure S0-6. AFM image and height profile of $Ti_3C_2T_x$ MXene naosheet before ultrasonication.

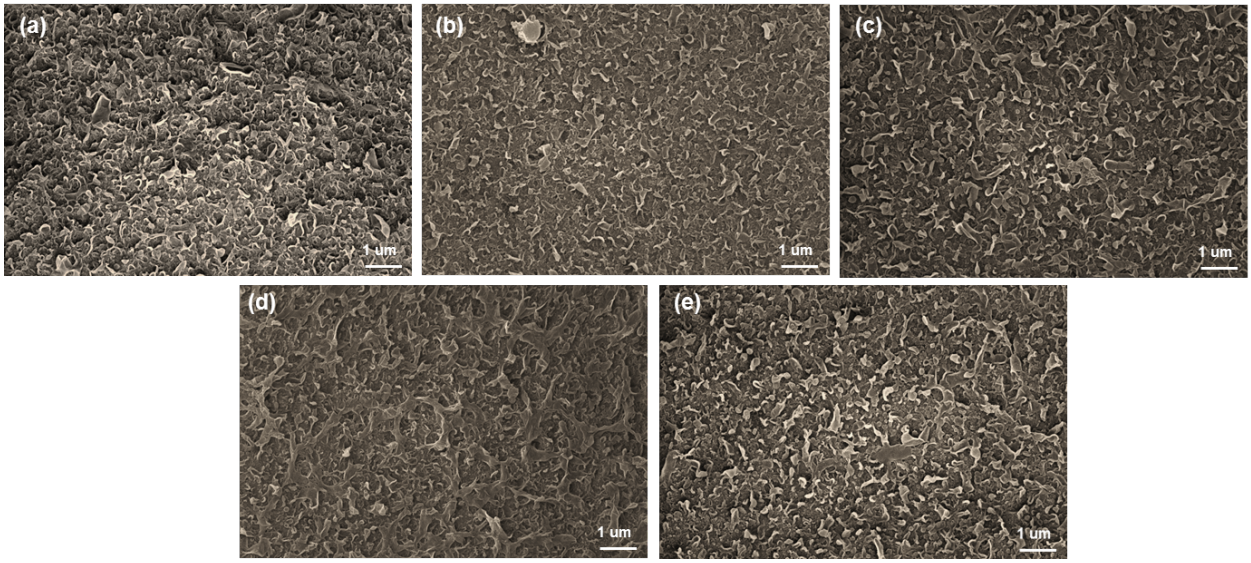

Figure S0-7. FESEM images (Mag = 10 KX) of pristine TFC and TFNs with different $Ti_3C_2T_x$-TA loading: (a) TFC, (b)TFN($Ti_3C_2T_x$-TA-002), (c) TFN($Ti_3C_2T_x$-TA-004), (d) TFN($Ti_3C_2T_x$-TA-008), (e) TFN($Ti_3C_2T_x$-TA-016).

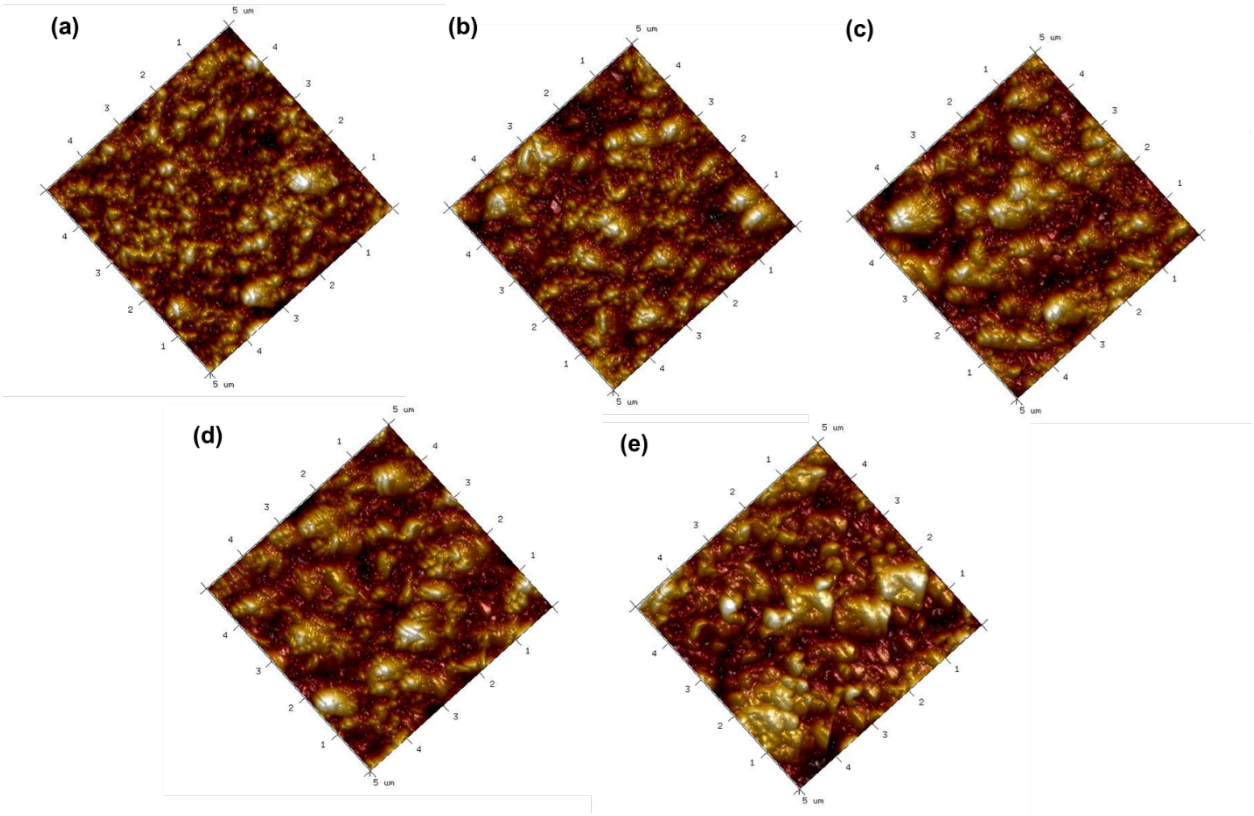

Figure S0-8. AFM images of neat TFC and TFNs with different $Ti_3C_2T_x$-TA loading: (a)TFC, (b) TFN($Ti_3C_2T_x$-TA-002), (c) TFN($Ti_3C_2T_x$-TA-004), (d) TFN($Ti_3C_2T_x$-TA-008), (e) TFN($Ti_3C_2T_x$-TA-016).

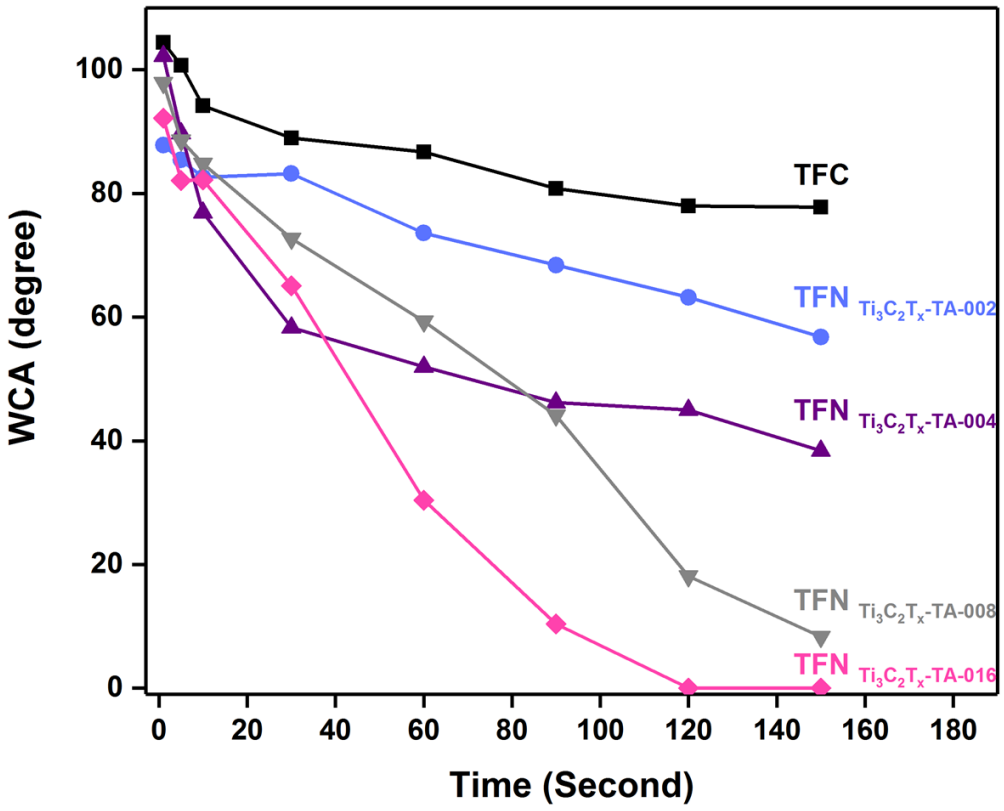

Figure S0-9. Dynamic contact angle of TFC and TFN with different concentration of $Ti_3C_2T_x$-TA.

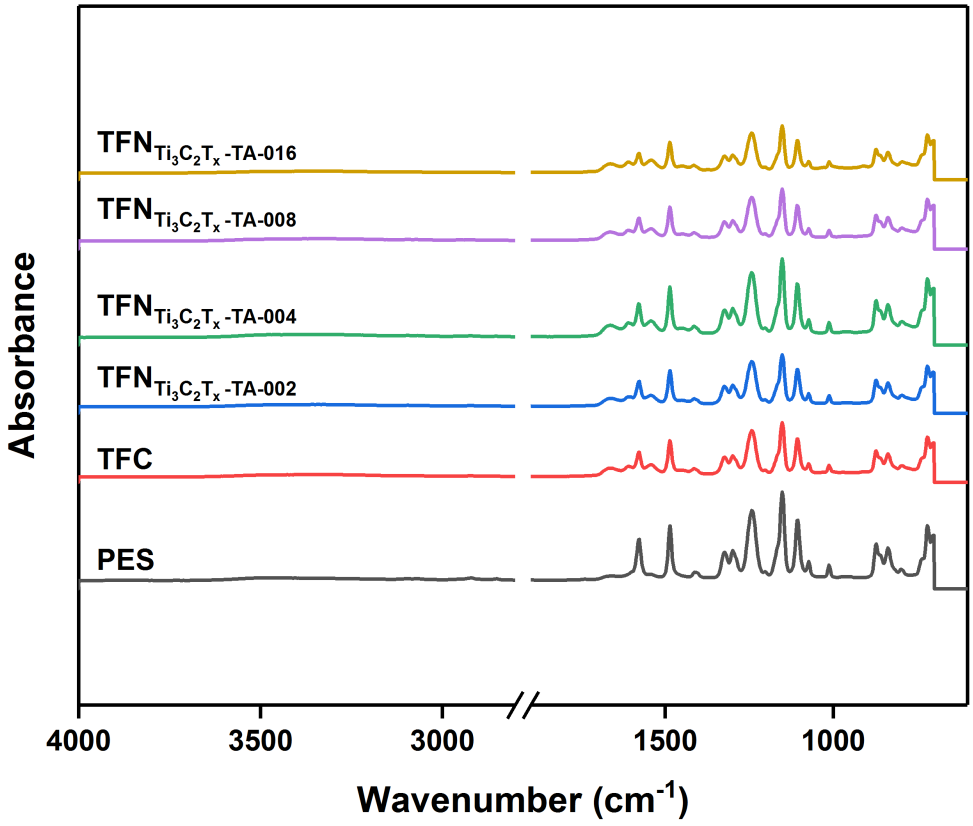

Figure S0-10. FTIR-ATR spectra of PES, TFC, and TFN with different concentration of $Ti_3C_2T_x$-TA.

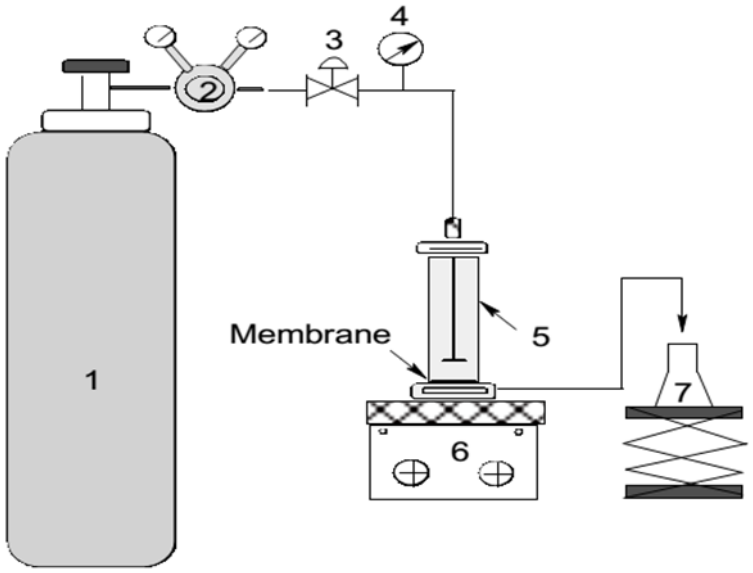

Figure S0-11. Experimental dead-end set up for membrane separation tests: (1) N_2 cylinder, (2) gas regulator, (3) controlling valve, (4) pressure gauge, (5) feed tank and membrane test cell (Sterlitech HP4750), (6) magnetic stirrer, (7) permeate collector.

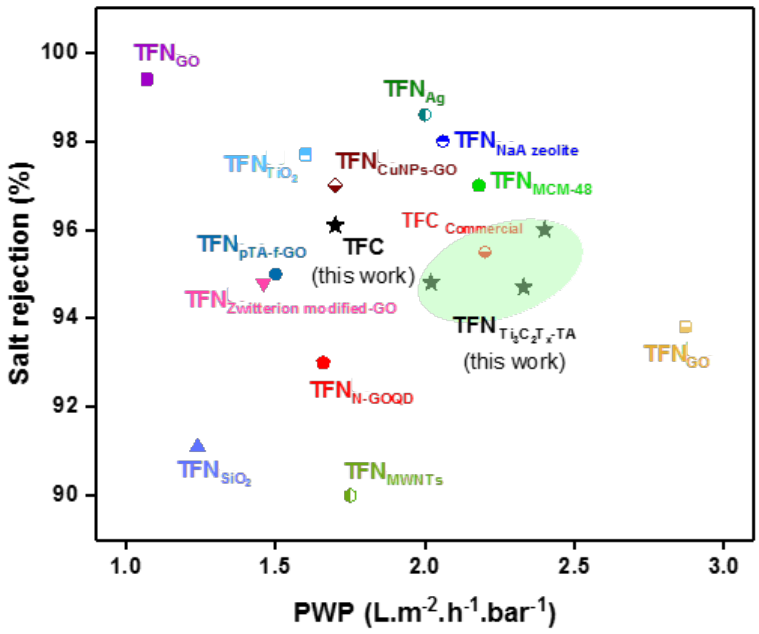

Figure S0-12. Performance comparison (pure water permeability and salt rejection) of the RO membranes in this study and literature [94,96,265,266,150,181,259–264]**.**

b) Supplementary Tables

Table S0-6: Surface roughness of the pristine TFC and TFNs with different $Ti_3C_2T_x$-TA loading.

Membrane	Ra (nm)	Rq (nm)
TFC	40.37 ± 5.25	52.43±7.32
TFN ($Ti_3C_2T_x$-TA-002)	43.63±3.59	54.9±4.11
TFN ($Ti_3C_2T_x$-TA-004)	47.73±3.42	60.13±3.58
TFN ($Ti_3C_2T_x$-TA-008)	49.8±3.68	63.37±5.15
TFN ($Ti_3C_2T_x$-TA-016)	45.5±3.32	57.63±3.79

Table S0-7: Surface composition of the pristine TFC and TFNs with different $Ti_3C_2T_x$-TA loading.

Membrane	C 1s (At%)	O 1s (At%)	N 1s (At%)	O / N ratio
TFC	73.3	14.9	10.7	1.39
TFN ($Ti_3C_2T_x$-TA-002)	72.3	15	11.1	1.36
TFN ($Ti_3C_2T_x$-TA-004)	76.1	12.5	10.3	1.21
TFN ($Ti_3C_2T_x$-TA-008)	76.6	12.2	10.3	1.19
TFN ($Ti_3C_2T_x$-TA-016)	76.3	13.5	9.3	1.46

Table S0-8: Peak area percentage of O1s and N1s for TFC and TFN($Ti_3C_2T_x$-TA-008) membrane.

Membrane	O1s (At %)			N 1s (At %)			
	-NH-C=O	O-C=O	$\frac{O-C=O}{N-C=O}$	$R\text{-}NH_2$	N-C=O	$-NH_3^+$	$\frac{R-NH2}{N-C=O}$
TFC	46	54	1.17	7	89	4	0.078
TFN ($Ti_3C_2T_x$-TA-008)	53	47	0.88	2	92	6	0.017

Table S0-9: Filtration performance of TFC and TFN membranes for separation NaCl solution (2000 ppm, under a pressure of 20 bar at 25 ˚C).

Membrane	Permeance ($L.m^{2}.h^{-1}.bar^{-1}$)	Rejection (%)
TFC	1.7 ± 0.21	96.1 ± 0.58
TFN ($Ti_3C_2T_x$-TA-002)	2.02 ± 0.12	94.8 ± 0.8
TFN ($Ti_3C_2T_x$-TA-004)	2.33 ± 0.15	94.7 ± 0.4
TFN ($Ti_3C_2T_x$-TA-008)	2.4 ± 0.1	96 ± 0.55
TFN ($Ti_3C_2T_x$-TA-016)	2.64 ± 0.05	90.5 ± 2.5
TFN ($Ti_3C_2T_x$-002)	2.21 ± 0.18	94.1 ± 0.6
TFN ($Ti_3C_2T_x$-004)	2.28 ± 0.13	91.9 ± 0.3
TFN ($Ti_3C_2T_x$-008)	2.8 ± 0.25	80.1 ± 1.5

Appendix C. Supplementary material for chapter 5

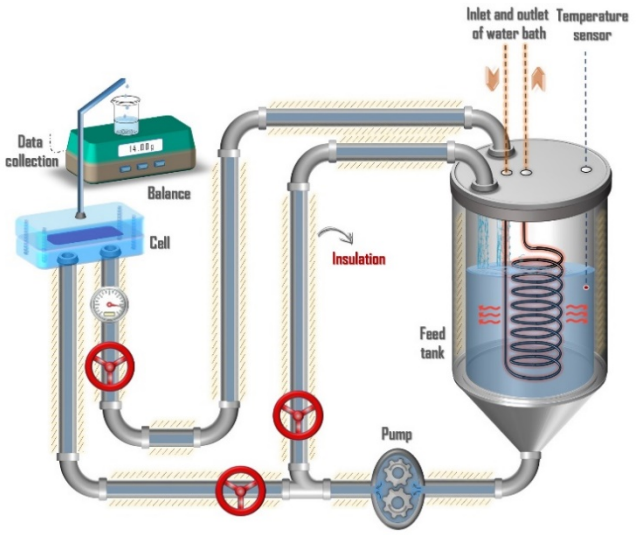

Figure S0-13. Schematic of cross-flow filtration setup.

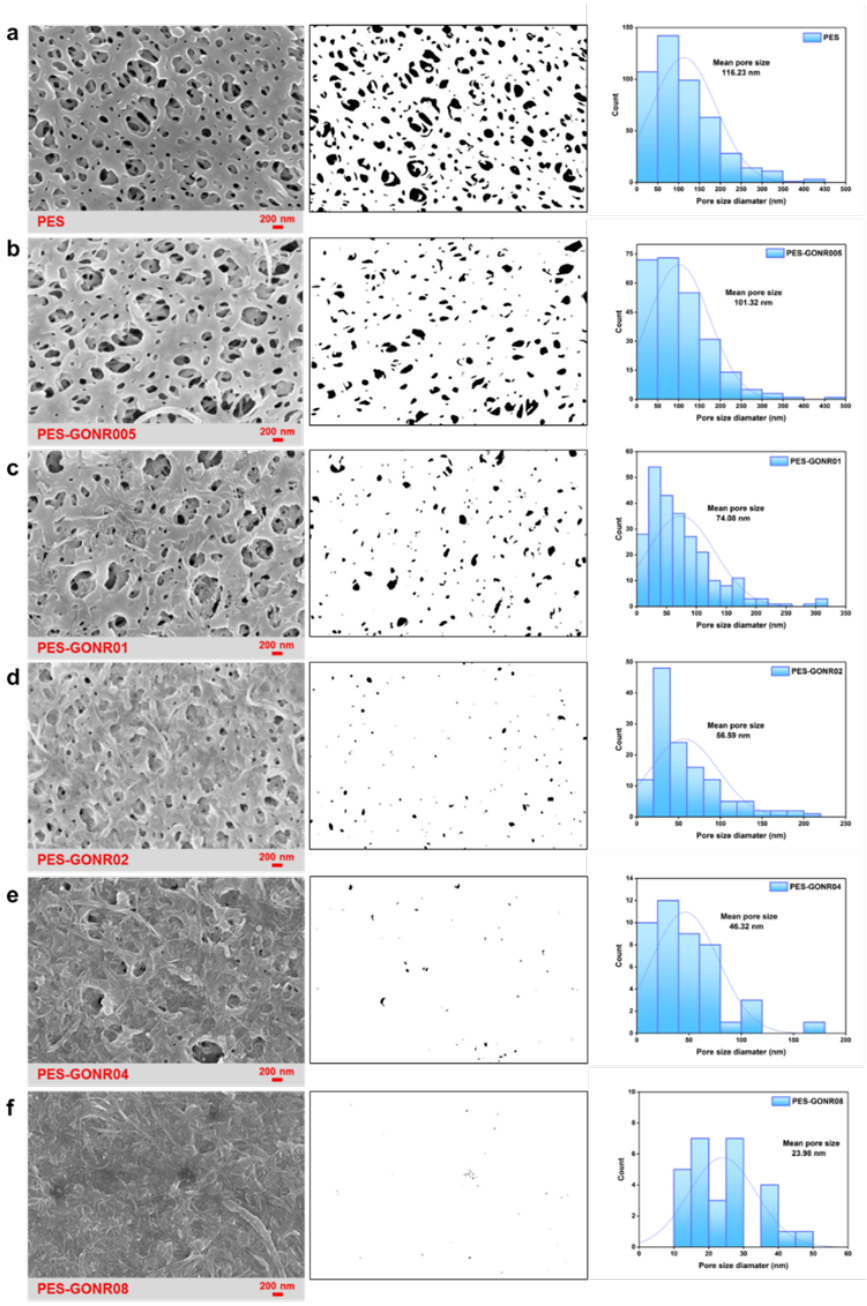

Figure S0-14. Surface SEM images, operated images, and pore size distribution of GONR/PES substrate; (a)PES, (b)PES-GONR005, (c)PES-GONR01, (d)PES-GONR02, (e)PES-GONR04, (f)PES-GONR08.

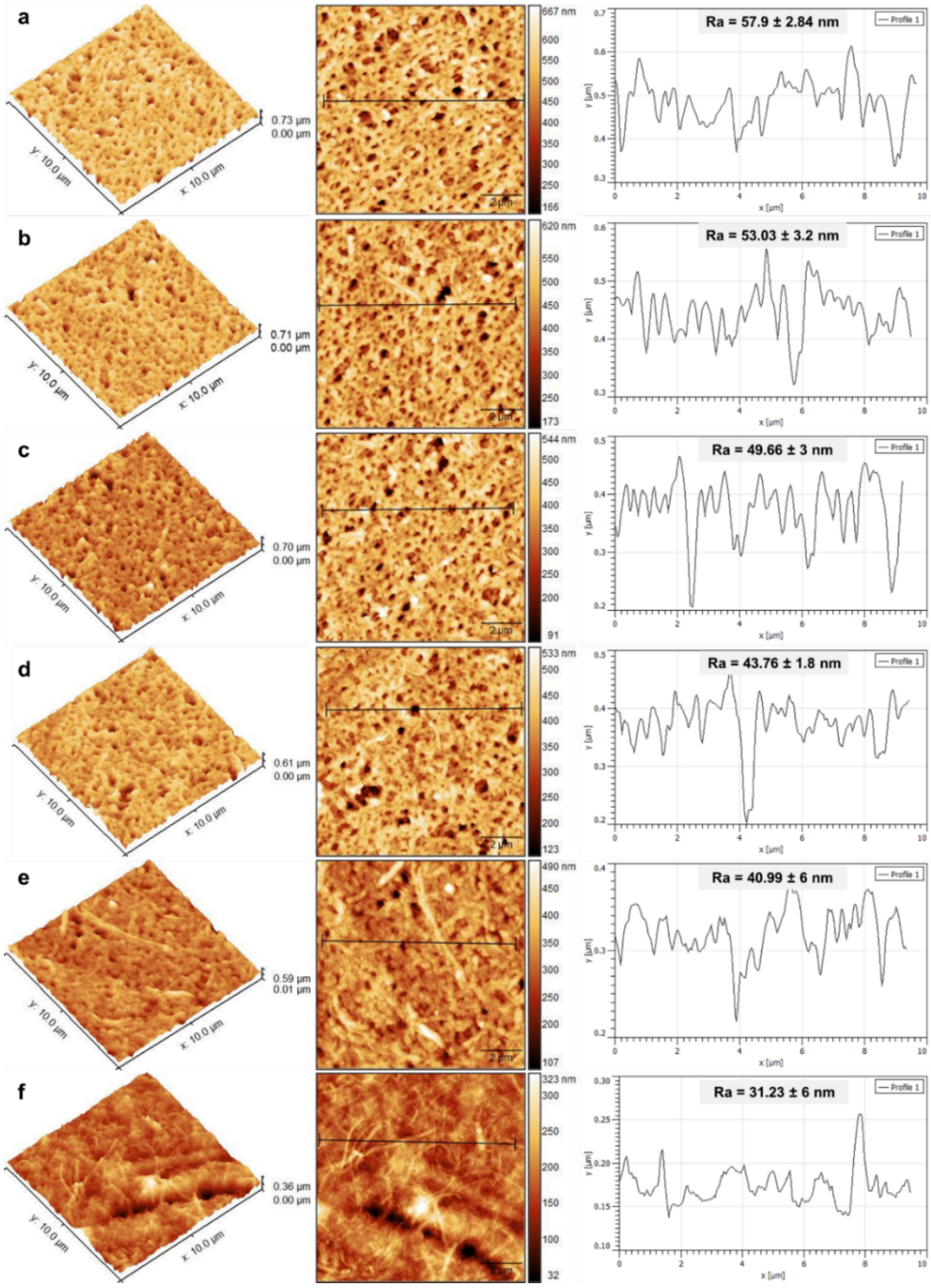

Figure S0-15. AFM images (2D, and 3D) and mean roughness (Ra) of GONR/PES substrates; (a) pristine PES, (b)PES-GONR005, (c)PES-GONR01, (d)PES-GONR02, (e)PES-GONR04, (f)PES-GONR08.

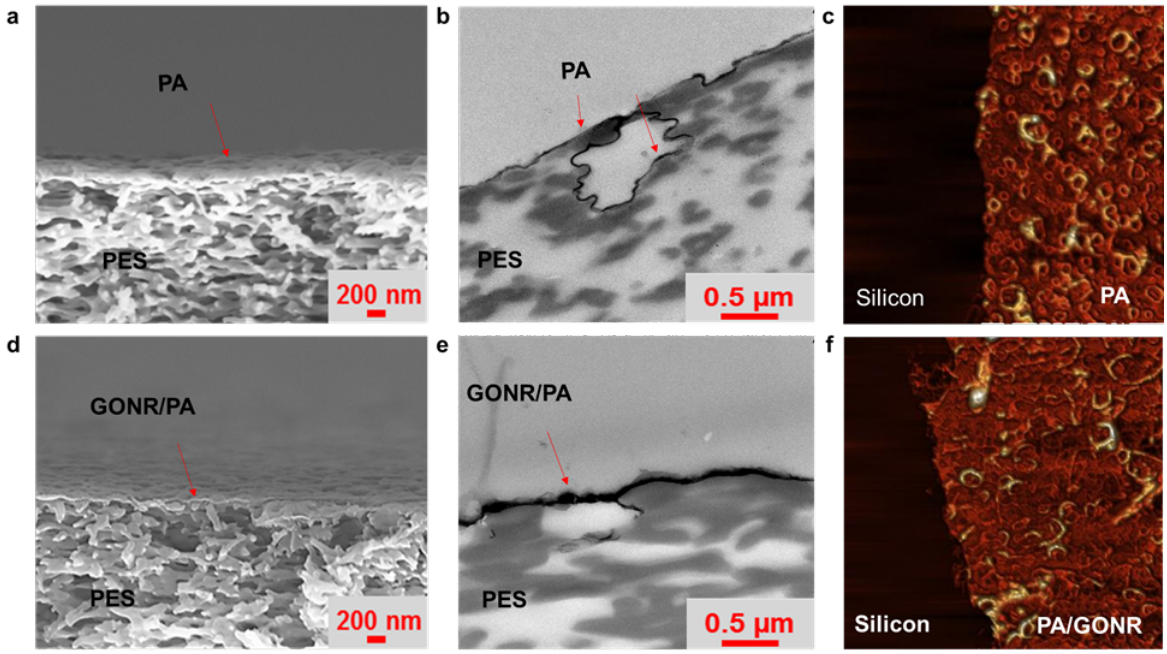

Figure S0-16. Morphology and structure of TFC and iTFC02 membranes: (a, d) SEM cross section, (b, e) TEM cross section, (c, f) AFM back side.

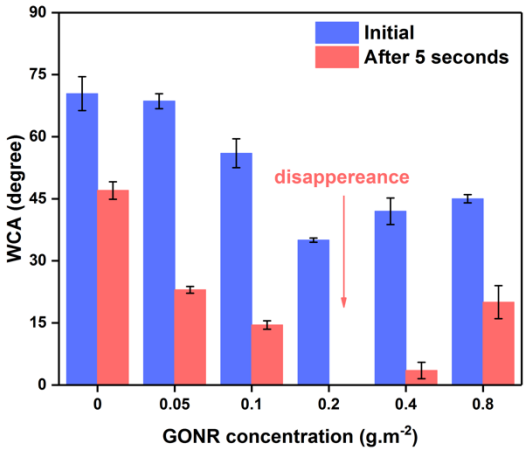

Figure S0-17. Initial and after 5 seconds average water contact angles measurement of DI water for GONR/PES substrate with different loading of GONR.